OPTICAL AND SURFACE ANALYSIS OF DNA MICROARRAYS

TO ASSESS PRINTED SPOT HETEROGENEITY

by

Archana Nagaraja Rao

A dissertation submitted to the faculty of
The University of Utah
in partial fulfillment of the requirements for the degree of

Doctor of Philosophy

Department of Pharmaceutics and Pharmaceutical Chemistry

The University of Utah

May 2013

The University of Utah Graduate School

STATEMENT OF DISSERTATION APPROVAL

The dissertation of **Archana Nagaraja Rao**

has been approved by the following supervisory committee members:

David W. Grainger	, Chair	**03/09/13** Date Approved
Jindrich H. Kopecek	, Member	**03/07/13** Date Approved
James N. Herron	, Member	**03/07/13** Date Approved
Valdimir Hlady	, Member	**03/07/13** Date Approved
Bruce K. Gale	, Member	**03/12/13** Date Approved

and by **David W. Grainger** , Chair of

the Department of **Pharmaceutics and Pharmaceutical Chemistry**

and by Donna M. White, Interim Dean of The Graduate School.

ABSTRACT

DNA microarrays have been plagued with analytical problems with quantitation, metrics, figures of merit, and reliability and reproducibility issues, hindering their acceptance in clinical and diagnostic settings. The main deficiency in the printed DNA format is the microspot heterogeneity occurring during array fabrication and further amplified during target hybridization.

Work described in this dissertation focuses on assessment of DNA microarray spots generated with conventional pin-type contact printing of fluorescently labeled DNA probes, on industry-standard commercial polymer-coated array slides and their hybridization with complementary oligomer DNA target. Printing of probe DNA microspots shares many features of commonly reported droplet evaporation dynamics that lead to different drying patterns and spot morphologies. This study directly identifies and analyzes different DNA probe chemical and spatial microenvironments within spots, analyzed with high-resolution time-of-flight secondary ion mass spectrometry (TOF-SIMS) chemical imaging, confocal epifluorescence, and probe microscopy force imaging methods. Drying of DNA probe spots shows Marangoni flow effects with high densities of probe DNA-Cy3 located in spot centers and nonhomogeneous DNA distributed radially within printed spots with both TOF-SIMS imaging and epifluorescence microscopy. Target hybridization kinetics and duplex formation were assessed using real-time *in situ* confocal imaging, and confirmed radial hemispherical diffusion-mediated distribution of target capture from spot edge to its interior. Kinetic modeling indicates pseudo-first order kinetics due to transport limitations and local density-dependent probe interactions with diffusing target. Fluorescence resonance energy transfer (FRET) and photobleaching results show that the high-density probe overcrowding in spots facilitates a broad range of target binding interactions regardless of dye orientations. Moreover, lateral probe density heterogeneity observed with high-resolution imaging techniques confirmed with confocal microscopy produces equally

heterogeneous target capture under normal assay conditions, showing how spot drying produces signal variability.

These methods are the first to interrogate single printed array spots providing new support that microspot signal heterogeneity is not purely a result of target hybridization but is initially sourced during immobilization of probes with droplet printing techniques. This will guide new thinking on immobilized density influence on assay performance and how to approach assay endpoints, either kinetically or at equilibrium binding, by modifying spot molecular environments to reliably capture their signal.

TABLE OF CONTENTS

ACKNOWLEDGEMENTS

This dissertation personifies the four and a half wonderful years of my graduate research experience in the Grainger group. I would like to express my sincere gratitude to my advisor, Prof. David W. Grainger, for his exemplary mentorship and unceasing motivation. Honing my technical skill sets, research abilities, and my overall development has been the outcome of Dr. Grainger's patience, guidance, energy, encouragement, and knowledge. I would like to also thank his wife, Holly Grainger, for her moral and emotional support during my four years of Ph.D.

I would like to thank my distinguished supervisory committee members, Dr. Jindrich Kopecek, Dr. Jim Herron, Dr. Vladmir Hlady, and Dr. Bruce Gale, for their valuable guidance, knowledge, and advice on my research project.

My gratitude goes to the members of the Grainger research group (previous group members: Lisa Chamberlin, Hiro Takashashi, Gregory Habers, Shawn Bevers, and Ping Gong; my-timers: Dr. Amanda Brooks, Paul Hogerbe, Dolly Holt, Anna Asthaskina, Clinton Jones, Yuwei Wang, Dorina, Joesph Amodttt, and Jonathan) who were very supportive, encouraging, and very friendly during my research. I would like to thank all the coauthors on my manuscripts for their scientific contribution and valuable collaboration. I would like to also thank Dr. Grainger for providing me an opportunity to collaborate and work on an innovative project with Mahender Avula, Dr. Florian Solzbacher, and Dr. Larry McGill. I would like to thank Mahender for being a great friend and support during my Ph.D.

I am incredibly grateful to my family for their faith in me and their unconditional support. My father: Nagaraja Rao, my mother: Vijayalakshmi, my sister and brother-in-law: Shalini and Madhusudhana, my brother and sister-in-law: Raghavendra and Sharada, my niece: Sanjana, and my nephew: Aditya.

PREFACE

Work in this dissertation attempts to address a major analytical reliability and reproducibility challenge in microprinted fabrication of DNA microarray devices related to: (1) DNA probe immobilization using contact microdroplet printing and drying techniques that compromise spot uniformity and lead to spot-spot heterogeneity and signal variation, and (2) target hybridization efficiencies and capture kinetics known to be affected by heterogeneous probe density and distribution in printed spots. The studies are the first to analyze single printed array spots with high-resolution imaging methods, and results provide multiple reasons for array signal variation. The work presented in this dissertation is motivated by the failure of this technology, originally developed nearly 2 decades ago, to penetrate clinical applications: only four FDA-approved microarrays are currently clinically available. Limitations in array-based assay signals such as poor reliability and reproducibility, poor sensitivity with clinical samples, lack of correlation of signal with absolute analyte abundance, and false positives all result in the inability of the assay format to accurately inform clinical decision-making. The overarching hypothesis governing these studies is that **microarray spot drying affects the spot quality and probe lateral heterogeneity, influencing the target hybridization (kinetics, spot-spot variability/signal intensity, and sensitivity) and thereby the microarray assay answer.** Significance lies in the wide variety of applications for DNA microarray technology in genomics analysis and diagnostics, exploiting its high-throughput screening capabilities for thousands of genetic components on a single platform. Extensions of the conclusions and methods to emerging arrays in peptides, sugars, and proteins are also impacting.

Self-fabricated, so-called “home-brew” microarrays have been historically the most versatile and favored microarray platforms because of the ability to 1) tailor array content to each user, 2) fabricate arrays on-site, and 3) avoid shelf-life issues for printed arrays in storage or shipment. Various fluidic-based inkjet and microjet deposition methods and spotting technologies

are used to fabricate such arrays. Both contact (e.g., pin deposition) and noncontact (e.g., piezo) printing results in nonuniform spots, spot-spot variation, and heterogeneous distributions of probe density throughout the dried spot. Fluorescent signals recorded by conventional fluorescence scanners typically used in genomics centers and routine methods use an integrated intensity for each spot. Often, such a signal has no fiduciary calibration with a known on-array, spiked standard, and is also not commensurate with analyte abundance. That is, analyte signal reflects some magnitude of complementary gene target presence in the sample matching the probe identity, but not much more quantitative information content. Because the probe immobilization and its molecular environment within each spot impacts target uptake kinetics and thermodynamics, the signal in each spot could depend more upon probe density than analyte abundance in a sample. Studies were designed to address these issues.

Chapter 2 (Rao, A. N.; Vandencasteele, N.; Gamble, L. J.; Grainger, D. W., Analytical Chemistry 2012, 84 (24), 10628-10636) presents new work on high-resolution analysis of single, dye-labeled printed spots made with contact printing on commercial polymer-coated reactive microarray slides. Studies were designed to recognize the cause of spot variabilities and how target responds to these spot density issues. Fluorescence scanning fails to report absolute quantitation of immobilized probe amounts with low pixel/micron resolutions compared to the high-resolution data obtained from epifluorescence and TOF-SIMS techniques. Analysis of DNA printed spot heterogeneity and spot-to-spot variation for printed dye-labeled DNA microspots often shows higher DNA density at the centers of printed DNA microspots than spot edges. High-resolution epifluorescence optical imaging of DNA-Cy3 and TOF-SIMS chemical imaging of different DNA or Cy3 chemical fragment ion species within spots together provide complementary information for assessing dried DNA density and distributions on coated glass commercial microarray substrates. High-density DNA regions in spot centers obtained from epifluorescence imaging compare very well to those obtained with TOF-SIMS chemical state imaging. Routine, conventional fluorescence scanner images provide information for integrated spot pixel intensity, shape, and morphology, but lack all details for intraspot DNA heterogeneity and intraspot structural issues known to affect target capture and duplex hybridization kinetics critical to this

assay's answer development and diagnostic reliability. Comparative spot-spot assessment with multiple complementary analytical techniques consistently detected DNA spot-spot variability, heterogeneity within individual DNA spots, and DNA density distributions.

Dried DNA spot nonuniformities obtained using contact printing techniques are attributed to array fabrication process parameters, including nonequilibrium drying under influences of buffers, humidity, and evaporation during microarray fabrication. Marangoni drying under these evaporative conditions produces chemical and physical interactions between DNA and nonvolatile solutes in the spot, yielding DNA aggregation and surface deposition within the original spotted, wetted footprint. Direct side-by-side comparisons of dried DNA spot dimensions, DNA density distributions, lateral heterogeneities, and trends in variations in spot DNA densities with varying DNA print concentrations are consistent in asserting these influences on dried spot morphologies. Nonuniform DNA probe distributions produce nonlinear changes in integrated spot fluorescence intensities with increasing DNA-Cy3 printed content. Significantly, probe spot heterogeneities also affect DNA target capture efficiencies and reliabilities, and ultimately the entire microarray assay signal generation. Hence, variations in DNA target capture duplexes both within spots and spot-to-spot have origins in probe print drying artifacts. Improved assay consistency and "answer" reliability and reproducibility therefore should focus on probe printing controls and consistent surface, buffer, and drying properties in order to limit stochastic variability. Study results justify necessary improvements in methods and quality controls for DNA surface immobilization processes that influence analyte (i.e., DNA target) capture and that affect microarray assay signal reliability, reproducibility and clinical translation.

Chapter 3 (published as Rao, A. N.; Rodesch, C. K.; Grainger, D. W., Analytical Chemistry 2012, 84 (21), 9379-9387) compares single printed spot confocal optical heterogeneity with high-resolution time-of-flight secondary ion mass spectrometry (TOF-SIMS) chemical state imaging heterogeneity. Fluorescence analysis of individual array-printed DNA microspots using fluorophore-labeled DNA probe-target pairings with confocal microscopy provides important new information regarding the spot molecular environment of immobilized probes, target hybridization processes to substrate-bound probe, and incubation time periods for duplex-forming assays.

Single spot image analysis and intensity measurements for immobilized Cy3-oligo DNA probe and Cy5-oligo DNA target compared for two different dye positions on the duplex showed few differences in real-time hybridization time points. The detailed image analysis of real-time hybridization for target DNA confirmed the mass transfer-limited diffusion of target binding to immobilized probe in highly dense but heterogeneous DNA spots. Though real-time hybridization (duplex formation) detection of probe-target is challenging for surface-bound assays, fluorescence resonance energy transfer (FRET) enables real-time monitoring of duplex formation and hybridization rates by monitoring Cy3/Cy5 signal intensities during hybridization processes. Hybridization in solution produced different FRET effects for the two different duplexed dye positions in contrast to DNA surface-capture assays that facilitate FRET in both positions in single DNA hybridized spots, attributed to high probe densities. *In situ* photobleaching of Cy3 and Cy5 within the spot's cross-section supports heterogeneous probe-target distribution in multilayered-thick printed spots. Overall, new confocal DNA hybridization data provide important new information supporting spot fluorescence signal intensity variations resulting from spot probe printing and drying. Real-time *in situ* fluorescence image analysis of hybridization supports nonuniform probe distribution density within each spot as a key influence on target binding kinetics and fluorescence signal ambiguities. Microarray assays based on spot printing and target capture should consider these sources of intrinsic variability, and their influence on assay answer reliability.

As observed in Chapter 2, heterogeneous probe immobilization leads to nonuniform target distribution and binding throughout the spot, Chapter 3 presents the work on real-time *in-situ* hybridization kinetics of target binding on printed-blocked-rinsed dried spots to assess the modes of target hybridization with confocal microscopy. The advantage of real-time hybridization is the detection of target binding in the probe spot. The real-time hybridization studies gave important insights: (1) target diffusion in a radial hemispherical pattern from the outside edge moving towards the spot's interior, complementing the well-known models of target hybridization in nonuniform spots, (2) kinetic modeling analysis shows a pseudo-first order kinetics of duplex reaction, (3) spot heterogeneity was observed before (probe only spot) and after hybridization

spot, and (4) hybridization at low density regions of the spot (outer edges) were observed compared to the high probe density in spot centers. Additionally, FRET analysis of bound probe-Cy3 hybridizing with target-Cy5 forming duplex (parallel: Cy3-Cy5 close proximity and antiparallel: Cy3-Cy5 apart) showed no difference in FRET signal due to overcrowding of the probe during immobilization and target binding to the overcrowded probe density. These studies indicate printed probe only spot have probe lateral heterogeneity and are few layers thick.

Finally, Chapter 4 describes printing processes for PNA probes as a DNA probe surrogate but without confounding issues of coulombic charge blockade for hybridizing target. The neutral PNA probe design was used to rationally change the duplex electrostatic interactions involved in DNA probe-target capture without changing the target or the sequence. Printed PNA spots in combination with different additives and surfactants did not show improvements in spot morphology or uniform probe density. PNA spot heterogeneity was comparable to results obtained with DNA spots. Additives and surfactant systems had lesser impact over the spot morphology than the evaporation process in printed spots.

Overall, the dissertation provides an improved understanding of microarray failures using high-resolution surface analytical and optical techniques. Routine fluorescence scanners recognized as a gold standard for microarray end point analysis are limited in their assessment of integrated spot pixel intensity, shape, and morphology. Our current study (1) correlates high resolution optical fluorescence imaging with surface analytical tools for molecular analysis, specifically to quantify immobilized probes, printed probe morphology, heterogeneity, chemical spatial distribution, and intensities across the arrayed surfaces. Also, the examination of printed spot-to-spot with surface analysis showed the variabilities which cannot be achieved with conventional scanners due to lack of resolution for intraspot DNA heterogeneity and intraspot structural issues; (2) real-time hybridization kinetics using high-resolution optical studies indicate nonuniform probe immobilization densities and distribution impacts target hybridization and signal efficiency; (3) DNA spot heterogeneity was comparable with PNA spot for a similar print condition emphasizing the dominant effect of the droplet evaporation process. Thus, our study emphasizes the importance of achieving uniform probe immobilization with spot printing for efficient target

hybridization and accuracy in the end point detection. The limitations are due to various physicochemical properties associated with the printing technique which should be overcome to obtain uniform distribution of probes in printed spots.

CHAPTER-1

BIOPHYSICAL ASPECTS OF NUCLEIC ACIDS AT SURFACES RELEVANT TO DNA MICROARRAYS

Archana N. Rao[1] and David W. Grainger[1,2*]

[1]Department of Pharmaceutics and Pharmaceutical Chemistry, University of Utah, Salt Lake City, UT 84112-5820 USA

[2]Department of Bioengineering, University of Utah, Salt Lake City, UT 84112 USA

**to whom correspondence should be addressed:* David W. Grainger, david.grainger@utah.edu

Keywords: DNA microarray, DNA biophysics, radius of gyration, persistence length, kinetics and thermodynamics of DNA hybridization, DNA flexibility and bending, DNA configurations, Coulombic blockage, Marangoni, coffee-ring

---

Submitted to RSC, Biomaterials, March 2013

1.1 Abstract

Both clinical and analytical metrics produced by DNA microarray technology have recognized problems in reproducibility, reliability, and sensitivity. These issues are often attributed to poor understanding and control of nucleic acid behaviors and properties at solid-liquid interfaces. DNA hybridization, central to DNA microarray formats, depends on the behavior of single strand (ss) DNA bound to surfaces. DNA's persistence length, radius of gyration, electrostatics, conformation on different surfaces, chain flexibility and curvature, charging effects in ionic solutions, and fluorescent labeling all influence its physical chemistry. DNA target interactions with the immobilized ssDNA strand are naturally also highly impacted. Furthermore, the kinetics, thermodynamics, enthalpic, and entropic contributions involved in DNA hybridization reflect global probe/target structure and dynamics. Here we review the biophysical issues relevant to DNA molecular behaviors at surfaces and their influences on duplex formation in microarray performance. By correlating biophysical aspects of ssDNA/dsDNA at surfaces with abundant microarray analysis now published, we seek to offer insight into DNA microarray challenges that have hindered clinical adoption as diagnostics and research reliability as genomics tools.

1.2 Introduction

DNA microarray technology enables gene expression profiling for thousands of genes in parallel in a single assay.[1] Information from DNA microarray-based assay is used in genotyping,[2] DNA–protein interactions,[3] genome sequencing,[4] pharmacogenomics and drug discovery,[5] infectious and genetic disease,[6] cancer diagnostics,[7] forensic and genetic identification,[8] toxicology,[9] and many other applications. Though a powerful high-throughput tool with assorted applications, the microarrays analytical accuracy and assay reliability in assessing clinical samples, producing analyte quantitation, and in clinical decision making is questionable.[10] Data analysis and interpretation have provided unique challenges and "the transition from bedside to bench to bedside" has been slower than expected due to various pitfalls in using diagnostic and prognostic insight.[11] Only four FDA-approved microarray based diagnostics of clinical relevance are currently marketed.[12] Requirements for assay standardization and validation for each

microarray experimental step, emphasizing quality control in array fabrication, scanner calibration, and data verification have proven difficult to surmount. The USA FDA's initiative of Microarray Quality Control I, II, and III (MAQC) consortia are charged with identifying and assessing critical factors affecting array data quality and to optimize and standardize microarray procedures.[13] This effort has focused on resolving procedural discrepancies and improving assay and data repeatability and reproducibility among various platforms but has not really addressed fundamental root causes of assay issues to date.[14, 15] Given the various dimensions to this assay problem, at their basis commonly lies the understanding of biophysical aspects of short single-strand nucleic acids as probes, and their behavior at surfaces in producing hybridization with target analytes. Certainly improved bioinformatics and biostatistics in assessing the target capture data for accurate interpretation of signal remain critical to a meaningful relevant medical outcome.[16-18] Nonetheless, a first-principles perspective of DNA at surfaces and its central control of the molecular interactions controlling these data are essential.

Recent advancements in technologies, analysis methods, and sophisticated experimental tools such as optical (spectroscopic), surface analytical, and molecular force approaches have facilitated new information on the dynamic behaviors of nucleic acids both in bulk states and on surfaces. Parameters regarding DNA molecular conformations, structural transitions, and dynamics at nanometer scales and in short (i.e., millisecond) time frames, provide data for DNA relevant to understanding certain behaviors on microchips and array surfaces. Additionally, new in silico computational models, molecular dynamics simulations, and software tools have produced correlations with experimental data as well as with accuracy in predicting certain DNA structural phenomena. While simulations and modeling are recognized to have some discrepancies with experimental data, they should be capable of providing insight into understanding certain, relevant biophysical properties.[19] Table 1.1 summarizes some of the major obstacles to be addressed for successful designs of improved DNA microarrays.

The DNA microarray strategy exploits surface-tethered complementary oligonucleotides on solid supports, often dense, surface-grafted, or printed short nucleotide ensembles, to capture other complementary nucleotides from a sample. Figure 1.1 shows schematics for the working

principles of DNA microarrays. The ssDNA oligomer probe immobilization initially at a solid-liquid, then subsequently a solid-air interface (upon drying) produces a unique state for DNA not found naturally. Probes are typically short 20-70 base single-stranded DNA (ssDNA). These unconventional processing steps and resulting DNA surface microenvironments have profound influences on subsequent ssDNA-surface interactions and coupled dsDNA hybridization responses with incoming DNA targets. Therefore, understanding DNA interfacial behavior during this processing is critical in asserting control over assay performance and designing rational steps for improvements that address certain needs in Table 1.1.

Various strategies are used for realizing DNA microarray construction, as shown in Figure 1.1, on a wide range of solid substrate chemistries and forms.[20, 21] ssDNA probe immobilization on a surface has three fundamental approaches that can be broadly characterized as: 1) DNA "grafting to"; 2) DNA "grafting from"; and 3) DNA nanodroplet printing/drying. In the first approach, anionic polyphosphate DNA probe oligomers are either electrostatically adsorbed to cationic surfaces, or by combinations of polar and hydrophobic interactions (i.e., to nitrocellulose, silicon oxide, or polypropylene). In the second "grafting from" approach, fluidics, photolithography, and photochemistry are combined with automated microprocessing to sequentially add and spatially direct each individual DNA nucleotide to growing ssDNA probe chain ends across a patterned surface. In the third strategy, automated dispensing equipment places DNA probe solution droplets in specified surface locations and allows them to rapidly dry by evaporation. These are summarized in Figure 1.2.

Many amine-terminated organosilane-coated and poly(L-lysine)-modified slides provide cationic surfaces for electrostatically binding anionic DNA probes, the basis for several popular commercial glass microarrays ("grafting to" approach, Figure 2A).[22, 23] Covalent "grafting to" approaches for DNA probes are diverse, but many use terminally amine-modified DNA and amine-reactive surface chemistries, including aldehyde, isothiocyanate, isocyanate chemistry, and also reactive esters, including *p*-nitro- and perfluoro-phenyl and N-hydroxysuccinimide (NHS) terminal groups on coated slides.[24] "Grafting from" strategies are also known for fabrication of commercial DNA microarrays. Affymetrix combines photolithography and combinatorial chemistry

to synthesize very high-density DNA chips. Hydroxylated, silanized fused silica wafers are derivatized with a linker molecule and a light-sensitive protecting group. Photolithographic masks then illuminate specific locations on the silanized wafer at sites with UV exposure, causing deprotection to activate that couples free nucleotides onto the silica wafer where irradiated (Figure 1.2B). Additional capping steps prevent unattached molecules from becoming probes. Nucleotide side chains are protected to prevent branched-chain formation. Photo-induced deprotection, coupling, and capping steps are sequentially continued until full-length probes are fabricated on chip at high density.[25] In an alternative commercial approach, NimbleGen builds arrays using photo-deposition chemistry based on a mask-less array synthesizer (MAS), specifically a mask-less light projector acting as a 'virtual mask' instead of the physical chromium photomasks used by Affymetrix. Patterns of metal films produce patterned DNA as chemisorbed adlayers.[26] Figure 1.2C shows thiolated DNA probes that react with clean gold, copper, platinum, and silver metallic surfaces via metal-thiolate bond formation spontaneously from solution to yield immobilized DNA probes.

This solution-based chemistry has been widely studied as a fundamental method for accessing DNA single-point attached films as well as commercialized for array use.[27, 28] Figure 1.2D depicts microarray fabrication using droplet deposition and evaporation based on high definition spatial deposition of nanoliter amounts of probe solution. Dispensing can be based on contact precision pins, inkjet, bubblejet, or piezo actuation technology dispensing 100 pL to 2 mL. Contact pin printing usually results in spot densities of 2000–4000 spots/cm^2 of ~100 micron diameters, while noncontact (i.e., piezo) printing yields slightly higher spot density with smaller spot diameters. Reliable fabrication of printed microspot microarrays is a multiparameter optimization problem. Spot performance in assay is a function of final spot morphology, and probe density and distribution within the spots affecting target hybridized density and signal distribution.[29-31] Little methods standardization is currently present, meaning that each spotting recipe, instrument, and print protocol produces different DNA probe spot properties with different probe/target hybridization capabilities, therefore different signals. Given all of these DNA array fabrication methods, all but droplet spotting methods are expected to yield immobilized

monolayers of nucleic acids on supports. Additionally, microarray “grafting to” immobilization methods (Figure 1.2A, C, D) all use presynthesized oligonucleotide probes purified by capillary electrophoresis or high-performance liquid chromatography prior to array deposition of nearly homogeneous probe samples, increasing assay specificity. By contrast, *in situ* probe synthesis (Figure 1.2B) is not 100% accurate, and ready validation of the fidelity of the final probe synthesis on the surface is difficult.[32] These photo-generated “grafting from” microarrays therefore contain significant nucleotide chain defects distinct from the desired sequence.[33] A consequence of high probe density is slow hybridization kinetics that remains incomplete in practical assay timelines, resulting in a low hybridization efficiency and low concentration of hybridized target analyte. On the contrary: low surface probe densities lead to relatively fast kinetics but with absolute hybridized target signal limited by the reduced surface probe density.[34] Table 1.2 shows resulting features sizes, spot densities, as well as probe density per feature for the various immobilization methods.[26, 35, 36]

Knowledge and control of DNA probe density and its physical state is fundamentally important to interpreting changes in assay signal from label-free or labeled microarray assays, and to design highly efficient, reproducible assay formats. Importantly, each DNA probe immobilization approach yields distinctly different molecular fates for the resulting DNA duplex event on surfaces. For example, physi- or chemi-sorption of oligo-ssDNA probe chains to surfaces in the “grafting to” approach (Figure 1.2A) provides little control over immobilized ssDNA chain densities and chain segmental conformations, where relative amounts of ssDNA probe loops, trains, and tails (see Figure 1.3)[37, 38] are stochastic endpoints from the adsorption process and drying and distances between adsorbed chains are unknown, and perhaps entangled. A critical physicochemical distinction from other ssDNA probe immobilization methods is the largely unproven presumption that such adsorbed ssDNA chains are largely horizontal on the surface due to the multiplicity of adsorption sites and polyvalent DNA chain segments.

By contrast, end-point DNA immobilization resulting from both photochemical *in situ* patterning/reaction approaches, as well as metal-thiolate probe chemisorption and covalent chain-end reaction chemistry (Figure 1.2B,C), is presumed to produce brush-like chain

conformations oriented largely orthogonal to the surface. These important differences in immobilized probe DNA chain orientations should be reflected in their kinetics, thermodynamics, and efficiencies of target capture during duplex formation under assay conditions. These can be appreciated by inspection of idealized DNA chain physical states on surfaces, shown in Figure1.3. Uncontrolled DNA-surface interactions yield adsorbed DNA chains with multiple surface-binding states, leading to the classic surface-immobilized polymer "loop-trains-tails" surface configurational scenario (Figure 1.3A).[39] How DNA-DNA duplexes form from this random surface- adsorbed state in microarray assays, presuming that short ssDNA probe oligomers of 20-30 base pairs (bp) require substantial complementary base pairing to form stable duplexes with targets, is not known. Yet, many long-standing DNA array platforms utilize this adsorption approach (e.g., FAST™ slides) to create arrays for DNA assays that bind DNA targets.[40, 41] End-point grafted probes (Figure 1.3B) produce different immobilized probe states that depend upon ssDNA chain lateral density as a function of the chain Flory radius, R_F: high-density DNA brushes contrasted with low-density mushroom layers. Each is characterized by segmental density distributions normal to the surface and resulting DNA layer thickness, L, that produce significant steric and electrostatic barriers to target hybridization.[42]

Low-density probe immobilization can also allow DNA probe-surface adsorption in certain cases that can hinder hybridization.[35, 43] This is reversible in some cases when competing adsorbing space-filling diluents are used to displace weak DNA-surface adsorption, causing grafted chain desorption and reorientation.[43, 44] DNA chain-surface adsorption makes the probe unavailable for target duplex formation, compromising assay performance. Schematics of mushroom and brush structures of ssDNA immobilized on substrates are shown in Figure 1.3B. In the ''mushroom'' regime, immobilized chains are considered as occupying hemispheres with radius comparable to the Flory radius of the free DNA chain, R_F. When the DNA surface density increases $L \leq R_F^2$, the chains begin to crowd each other, extending from the surface to reduce segment crowding, thus forming a ''brush'' of extended chains.[42] In the brush regime, the chains stretch out normal to the surface so as to decrease the monomer concentration and the number of repulsive monomer-monomer contacts.[42] The DNA brush thus formed affects the hybridization

isotherm and the duplex rate equations. In particular, the brush lowers both the hybridization rate and the attainable hybridization efficiency (yield) for a given concentration of DNA targets.[42] Therefore, DNA microarray design should consider this probe density regime in formulating protocols for array preparation and hybridization as well as in the analysis of assay results.

Specifically designed surface chemistries for DNA probe binding improve DNA surface coupling efficiency and minimize nonspecific binding from undesired cross-reactive groups intrinsic to many DNA combinations with surfaces.[45] Importantly, various surface modifications to improve DNA binding have evolved from original affinity reagent printing and desiccation on intrinsically adhesive surface chemistries (i.e., nitrocellulose, glass), thicker, three-dimensional reactive films (i.e., immobilized hydrogels, sol-gels) coated over solid glass supports, and photochemical and electrochemical immobilization methods.[46] Detailed descriptions for strategies for microarray and design fabrication, as well as detection methods are available.[24, 47] Despite the diversity and development of DNA array immobilization methods and substrate chemistries, the conventional detection method for screening duplexed arrays has largely remained the conventional fluorescent scanner. This signal derives from dye-labeled DNA targets from samples that are PCR-amplified using dye-labeled nucleotides and then captured by immobilized arrayed complementary probes, producing surface-bound fluorescent signals that reflect the fidelity of probe-target recognition across the various probes immobilized in different spatial locations. Importantly, integrated fluorescent intensity within each spot becomes the assay “answer” for gene presence and abundance in such assays. Nonetheless, microarray fluorescence data generally do not quantify each gene’s abundance represented in the microarray. This is due to affects of different rates and efficiencies for different strand sequences and base contents, as well as both the steric and electrostatic features for densely printed probes at surfaces. Assay fluorescent signal from a given array microspot is generally judged to be significantly when more or less than two log orders of spot intensity (increase or decrease) different (i.e., 2log *S*) over a given baseline assay control, usually a fiduciary gene marker set or ‘normal’ gene expression sample.[48] Assay detection limits vary, depending on substrate, probe length, target length,

detection milieu, and spotting method, with femtomolar DNA target fluorescent detection frequently reported from saline solutions (but not from cell lysate, tissue, or clinical specimens).

Significantly, the integration of spot fluorescent intensity to report assay signal using commonly used fluorescence scanners demonstrates that the typical fluorescence scanner cannot discern microspot optical heterogeneity and fluorescence intensity variation in single printed spots to yield a reliable metric.[49] High-resolution chemical state imaging mass spectrometry (TOF-SIMS) studies of printed DNA microspots confirm that fluorescence scanning methods fail to report absolute, reliable quantitation of immobilized DNA probe amounts. Inaccuracy in the fluorescent metric can be attributed to fluorescent dye-dye, dye-surface, and dye-dye stacking, leading to quenching of surface fluorescence signal.[50] Routine conventional fluorescence scanner images provide information for integrated spot pixel intensity, shape, and morphology, but lack important details for incorporating intraspot DNA immobilized heterogeneity and intraspot structural issues known to affect both target capture signals and duplex hybridization kinetics critical to this assay's answer development and diagnostic reliability. Additionally, signal quantitation is affected by numerous, known surface issues and background noise sources that confound reliable, quantitative correlations of spot-to-spot fluorescent assay signals and experiment-to-experiment comparisons.[17, 51]

Many factors affect DNA microarray performance quality (Table 1.1) aside from the stringency that affects analytical figures of merit (sensitivity, specificity) through probe design, sequence selection, and target affinity (shown in Figures 1.2 and 1.3). A major influence comes from the ssDNA immobilization states that affect "availability" to target binding at the surface. Hybridization processes and DNA duplex formation (i.e., duplex kinetics, thermodynamics, and efficiency) are a direct result of DNA chain physical states on surfaces. Factors such as ssDNA length, sequence, grafted probe density, electrostatic interactions, segment conformational states, and steric hindrance are critically important to assay signal generation.[49, 52] These intrinsic properties of DNA chains at surfaces are reflected in physical manifestations of DNA chain persistence length, radius of gyration, conformation of ssDNA both on surfaces and in solutions with various ionic strengths, surfactants in buffers, and dye labels which then further dictate the

biophysical properties of tethered ssDNA on surfaces and resulting interactions with targets. Additionally, target fluorescent labels necessary for fluorescent DNA assay can produce dye-dye, dye-surface, and dye-DNA aggregation nonidealities that also influence fluorescent signal generation.[53, 54] It is therefore important in this regard that nonequilibrium drying of printed DNA solution spots during immobilization methods (Figure 1.2D) often leads to coffee ring and Marangoni convection flow drying effects that alter DNA density and distributions within dried DNA probe spots.[30, 55] These flow effects result in varying probe distribution and density that both affect target capture to these spots, kinetically, spatially, and spot-to-spot. This classic spot drying issue represents a source of DNA assay variability with a fundamental and well-studied history.[56,57]

Assessment of variables in the chemistry and physics of ssDNA immobilization and resulting properties at surfaces are correlated to currently observed limitations in the information content and reliability of DNA microarray assays. Understanding and control over ssDNA-surface interactions are therefore key for improving microarray reliability, quantitative capability, and detection limits for current microarray assays as well as for developing new microarray surfaces more effective in performing in complex biomedical media. Nonetheless, careful analysis linking known bulk DNA biophysical properties to DNA-surface behavior is rarely reported. This review seeks to digest the current knowledge base in this theme to help identify the fundamental issues affecting DNA-DNA recognition and binding at surfaces to attempt to move more of these technologies to clinical applications. A further benefit is a more general extension of this critical review process and analytical rationale to emerging, analogous opportunities in saccharide, cell-based, high-throughput drug screening arrays, and protein-based capture assays.

1.3 DNA biophysics

Because DNA oligomers are densely immobilized at surfaces in microarray formats, their chain-chain interactions, chain-surface interactions, hydration, response to changing ionic strength, drying, and other hybridization conditions all impose forces that alter DNA chain conformations and segmental densities at surfaces different from DNA in bulk solution. These

influences on DNA affect its availability and efficiency as immobilized probe to recognize transported target DNA to form duplexes at assay surfaces.

1.3.1 DNA chain structure and conformational forms

DNA oligomers of 20-70 nucleotides are routinely used in arrays and bead-based assays.[58] As surface-tethered systems, immobilized ssDNA chains will assume an array-dependent equilibrium conformational state at surfaces that results from their immobilization state and local thermodynamic stimuli. ssDNA chains can be described as highly negatively charged, long, semiflexible or short, rigid polymers based on their length. As a polyphosphate with regular anionic group repeats bridging each nucleotide monomer, they have some properties characteristic of a typical polyanion. While longer ssDNA chains can be considered to be semiflexible polymers, shorter chains are rigid rod-like structures. For lengths > 150bp, the ssDNA chain is generally recognized to exist as a flexible polymer and for lengths < 150bp, it is considered as rod-like (based on the persistence length for DNA in physiological conditions: L_P=50nm or ~150bp). As a strongly charged polyelectrolyte, DNA's electrostatic interactions are screened by counterion condensation represented by $\rho > Z_e/l_B$ where $l_B = e^2/\varepsilon K_B T$; where l_B is the Bjerrum length, corresponding to the length scale where the thermal energy is comparable to Coulombic interactions. The worm-like chain (WLC) model is often used to describe the intermediate behavior between a rigid rod and a random coil to account for the striking local stiffness but long-range flexibility of ssDNA.[59, 60] The WLC model describes DNA molecules at low applied forces as an entropic spring and an inextensible worm-like chain, and at higher applied forces (i.e., 6pN to ~70pN) as behaving like an elastic rod.[61, 62] Development of this model for DNA and other semiflexible (or semistiff) polymer chains has been an important contribution of polymer theory. The WLC model describes behavior intermediate between a rigid rod and a random coil and can be modified in various forms to account for other theoretical and experimental variables. DNA's flexible chains form diffuse adsorbed layers extending from the surface into bulk solution in contrast to typical semiflexible or rigid chains forming dense and compact surface-adsorbed layers. DNA chain coiling (chain flexibility based on ,Kuhn length, i.e., two times the chain persistence length), conformational degrees of freedom based on solvent

conditions (Flory theory of polymer-solvent interactions), repulsive interactions between DNA electrostatic components, and the chain spring constant reflecting the chain elasticity all describe the DNA chain conformation states when tethered at the liquid-solid interface.

1.3.2 Parameters used to describe DNA physical properities

Physical properties of ssDNA and dsDNA are primarily a function of their chain lengths and solution conditions. Flexibility of DNA chains depends on persistence length (L_p), radius of gyration (R_g), and chain flexibility angle (θ), as shown in Figure1.4.

Persistence length is a measure of the rigidity of a linear polymer and is evaluated by determining how quickly the orientation of a polymer backbone changes as its chain contour is traversed. Shorter persistence lengths reflect greater chain conformational freedom. Polymer radius of gyration (R_g) is a measure of the volume occupied by the linear polymer under equilibrium conformational conditions and is evaluated by calculating the time average of the root-mean-square distance of the polymer components from its centroid. The chain flexibility angle (θ) is a fixed bond angle constraining the rotational flexibility around the chain backbone, resulting in chain stiffness. As the bond angle is reduced, the persistence length increases dramatically. Figure 1.4 schematically correlates chain contour length (L) and its persistence length (L_p), radius of gyration (R_g), and the angle of flexibility (θ) for ssDNA and dsDNA tethered to a substrate.

For a ssDNA which is a semiflexible chain characterized by a persistence length L_p, the Flory radius is $R_F \approx (Na/L_p)\ 3/5L_p$ where L_p/a is the number of monomers in a persistent segment (a = radius of spherical monomers hard core repulsion). Theoretically, the Kuhn length (b) is related to the radius of gyration by $R_g=b^2\ N/6$ where N= the number of segments with the chain length of L. Also, the radius of gyration of a circular chain is smaller than the linear chain of a same counter length by a factor of $\sqrt{2}$, based on the relationship of polymer with an excluded volume, represented by equation (1) where ζ is the excluded volume parameter defined by $\zeta=2\nu-1$ and ν is the Flory exponent. Also with Zimm model $R_g \approx 1.2R_H$

$$\langle \mathbf{R_g^2} \rangle_{\mathbf{circular}} = \langle \mathbf{R_g^2} \rangle_{\mathbf{linear}} \frac{\left(1+\frac{\zeta}{3+2\zeta}\right)}{2} \qquad (1)$$

Araki et al. experimentally verified that the hydrodynamic radius (R_H) of a circular DNA is larger than that of linear DNA. The radius of gyration depends on the number of bases(N) in the DNA chain and is described by de Gennes scaling theory as $Rg \propto N^v$ where N^v depends on the salt concentration of the DNA solution, and the scaling coefficient v depends of the flexibility of the chain.

1.3.3 Persistence length of DNA

Persistence length is an important parameter used to characterize the flexibility of linear macromolecules and their conformations in the absence of excluded volume interactions. Persistence length provides an estimate for the typical curvature radius of the polymer chain under thermal fluctuations.[63] Various models (WLC, Monte Carlo simulations) and experimental methods have been used to report persistence length for ssDNA and dsDNA. The WLC model characterizes the bending length scale of a semiflexible polymer as persistence length, (L_p), mathematically defined by the decay length of tangent-tangent correlations of the chain. The energy required to bend a semiflexible polymer over an angle (θ) over length (L) depends on the temperature and persistence length, L_p of the polymer.[64] The rod's local direction de-correlates at distance(s*)* along the curve according to e^{-s/L_P}. For contour lengths $L \geq L_p$, DNA can be described as a flexible polymer (essentially a self-avoiding freely jointed chain) whose entropic component of energy is dominant. In contrast, for contour lengths $L \leq L_p$, DNA can be imagined as more rod-like with an elastic-dominated energy (Figure 1.4); the stiffer the chain, the longer the persistence length. As per equation (2) the bond angle (θ) and persistence length (L_p) are inversely related.

$$\mathbf{E_{WLC}} = \left(\frac{\mathbf{k_B T L_p}}{\mathbf{2L_p}}\right)\boldsymbol{\theta}^{\mathbf{2}} \qquad (2)$$

DNA's bending rigidity is also described by the WLC model for a polyelectrolyte. The electrostatic influence on persistence length originally expressed in Odijk-Skolnick-Fixman (OSF) theory is the sum of bare persistence length (L_{Pi}) resulting from the intrinsic rigidity of the chain, and an electrostatic contribution (L_{Pe}) depending on ionic strength ($L_P = L_{Pi} + L_{Pe}$)[65]. Single molecule experiments such as optical[62] and laser [66] tweezers in various buffer conditions have been used

to study DNA rigidity. In monovalent salt (e.g., $Na^{+}_{(aq)}$), the measured persistence length is consistent with an electrostatic contribution that varies inversely with the ionic strength.[67, 68] In this case, L_{Pe} is related to the Debye–Hückel screening length (κ^{-1}) and Bjerrum length (l_b) (0.7 nm in water/monovalent ions) as $L_{Pe} = \kappa^{-1}/4l_b$. However, this model fails with multivalent cations like $Co(NH_3)_6^{3+}{}_{(aq)}$ and $spermidine^{3+}{}_{(aq)}$. Measurements with these ions gave L_{Pe} values some 25–30 nm lower than the 'intrinsic' persistence length, L_{Pi}, as the DNA locally bends towards the transiently bound multivalent ions, shortening the intrinsic persistence length.[66]

1.3.4 Radius of gyration (R_g) and DNA conformation

Free DNA in aqueous solution is a relatively well-behaved polymer based on conventional polymer physics models.[62] Early experiments deducing DNA's root-mean-square radius of gyration (R_g) in buffered aqueous solutions showed R_g to be a function of weight-average molecular weight (M_w).[69] This relation between R_g and M_w was derived from experimental data and Monte Carlo simulations incorporating the Kratky and Porod persistence chain model. Long ssDNA under high salt conditions also behaves as a flexible coil-like polymer.[70] These chains were shown to adsorb side by side on surfaces with no lateral interpenetration between coils, with R_g estimated as 0.38 $N^{1/2}$nm, where N is the number of ssDNA nucleotide bases. At higher probe density, the radius of gyration is influenced by the ionic strength. In high salt concentration, the ssDNA probe surface density is proportional to the reciprocal of the effective cross-section of a DNA probe coil, $1/Rg^2$, corresponding to an inverse dependence on its length, N, i.e., probe surface density ~ 1/N.[52, 71] For thiolated ssDNA probes on gold with N less than 24 bp, probe density was independent of N. However, longer DNA probes exhibit flexible coil behavior (i.e., $R_g \sim N^{1/2}$) in solution, measured for ssDNA (280 to 5380 nucleotides long) in high ionic strength solutions where the Debye length is on the order of a few Angstroms.[71] The thiol-gold bond formation is a strong driving force for immobilization and ordering of shorter probes with the cross-sectional radius of a ssDNA linear chain is estimated to be 0.6 to 0.7 nm.[72, 73] Surface coverage decreases with N over the entire range investigated, dropping by nearly an order of magnitude from ~6 $\times 10^{12}$ probes/cm^2 for 8-mer ssDNA probes to ~7$\times 10^{11}$ probes/cm^2 for 48-mers.[52] Latulippe et al. deduced a model for R_g for supercoiled

plasmid DNA based on linear DNA using an effective contour length equal to a fraction of the total contour length.[74] Only a few direct measurements of this root mean square R_g are reported for different plasmid isoforms over a broad range of plasmid sizes, but these are double-stranded systems with longer lengths, secondary and higher order structures, and low relevance to microarray behaviors.

The presence of an impenetrable substrate profoundly affects DNA chain conformation and segment distribution with N segments attached by one end at a tethered surface density (σ). Surface forces resulting in enthalpic interactions dictate this conformation in each case, balancing long-range electrostatic, medium range dipolar and hydration forces, and short range dispersion forces between DNA and substrate chemistry versus DNA and solution in ideal terms. However, this does not consider the unusual history of DNA-surface interactions during array fabrication that often includes DNA nanodroplet solution deposition onto a substrate, nonequilibrium spot drying onto the solid substrate under increasing ionic strength, desiccation, subsequent aqueous rinsing in high ionic strength media, and desiccation again. This produces considerable opportunities for DNA-surface interactions and adsorbed states beyond consideration in classical 2-body treatments. In DNA microarray, the ssDNA probes tethered to one end of the solid substrate is an impenetrable surface influencing the confirmation and the segment distribution of the DNA chains. When interactions between DNA segments and the substrate are repulsive, scaling theory for isolated end-tethered polymers predicts a depletion zone of DNA segments near the surface in the absence of DNA-surface adsorption enthalpy, characterized by chain segment distribution $\rho(z)$ increasing as $\rho(z) \sim z^{\xi}$ with the distance *z* from the substrate. ξ is related to the critical (Flory) exponent γ by $\xi = (1-\gamma)/\gamma$ which in a good solvent ($\gamma = 0.588$) takes the value $\xi = 0.7$.[75] At larger z distances, the influence of the surface weakens and the chain segment distribution approaches a maximum value $\rho(R_g) \cong \sigma(Na)R_g$ -- the average segment density within the polymer layer whose height is approximately given by R_g of the free, unperturbed chain.[42, 76] The DNA segments distribution as a function of distance of different scenarios of the DNA chain chemisorbed and physisorbed to the surface is shown in Figure 1.5.

The slow increase of chain segment distribution close to the substrate, together with its faster decay for distances $z \geq R_g$ suggests that the segment distribution of an end-tethered polymer in the low-density limit ($\sigma R^2_g \leq 1$) is strongly asymmetric, resembling the shape of a mushroom.[77] Although the ‘‘mushroom’’ conformation for an isolated end-tethered polymer (see Figure 1.3) represents the simplest situation of a broken symmetry for polymer statistics, detailed experimental tests of the theoretical predictions for $\rho(s)$ in the low-density limit are lacking. Lehner et al. measured the segment distributions of end-tethered polymers with uniform chain length in a good solvent, using confocal fluorescence microscopy on single DNA labeled with dye to evaluate the chain conformations. The segment distribution $\rho(z)$ as a function of distance from the substrate, z, measured for chains with contour lengths of $15.4\mu m \leq L \leq 59.4\mu m$ measured R_g which scales with persistence length as $Rg \sim L_p^{0:57\pm0:05}$ showing the presence of excluded-volume interactions between charged DNA segments.[78]

1.3.5 Electrostatic effects on DNA

Manning’s counterion condensation theory of highly charged polyelectrolytes, including DNA, essentially condenses counterions near the polymer surface.[79] The condensed counterion layer is sufficient to neutralize ~76% of DNA charge, reducing the charge of each phosphate to -0.24e; divalent and trivalent counterions reduce residual phosphate charges to -0.12e and -0.08e.[79] In doing so, the electrostatic contribution to DNA stiffness is reduced by phosphate backbone charge screening from counterion condensation. Cation binding to DNA is an ion-exchange reaction, releasing other counterions into bulk solvent and providing favorable entropic sources of binding energy. Schurr et al. complemented this theory by experimental and modeling experiments with polyelectrolyte showing the effects of counterion condensation on DNA configuration at surfaces. Supercoiled DNAs in solution are deformed farther from the minimum energy configuration than the corresponding surface-confined DNAs, with the number of configurations available in solution DNA vastly greater than surface-confined DNA.[80-82] Optical tweezers experiments showed decreasing DNA persistence length for increasing counterion valence,[66] meaning that DNA is more flexible with increased counter cation valency.

Manning also proposed contributions of DNA's phosphate charge to DNA stiffness; dsDNA represents an equilibrium between stretching forces caused by interphosphate repulsion and compressive forces caused by attractive interactions between Hoogsten or Watson-Crick paired nucleotides.[83] Thus, through the Debye length (κ^{-1}), a dependence of DNA's persistence length on salt concentration is evident. However, the effects of DNA charge on the molecular rigidity of DNA is debatable.[84] Theoretical and experimental results have shown that DNA conformation depends on the local molecular-level charge balance.[85] X-ray crystallography experiments involving tethering of cations in the major groove of DNA (directed radially outward) suggested that these cations mediate their effects on chain bending and DNA collapse through electrostatics and that they do not disrupt base stacking.[19] Thus, both phosphate neutralization and adduction (cations bound to major grove) induce spontaneous DNA bending.[85, 86]

Dramatic reductions often observed in immobilized DNA hybridization efficiency and thermal denaturation curve broadening as the probe surface density increases are attributed to the so-called Coulomb blockade.[87] The intrachain Coulombic repulsion in like-charged DNA nucleotides in probes in a highly crowded surface packing results in a more extended and swollen chain conformation. Interchain repulsion is a natural consequence of laterally immoblized DNA, producing DNA stretching away from the surface and local chain rigidity and conformational limitations. Local field strengths are expected from these high charge densities fixed on surfaces via DNA arraying. On metal surfaces (e.g., thiolated DNa on gold) this also generates image charges.[85] This considerable negative electrostatic barrier leads to surface repulsion of incoming DNA target. These local opposing surface potentials must be mitigated to enable duplex formation with incoming targets of like charge density. This necessitates use of high ionic strength hybridization buffers and solutions to screen charge density and enable shorter range hydrogen bonding through base complementary. Additionally, steric barriers to duplex formation are introduced by the local rigid, dense ssDNA chains arrayed on surfaces. The electrostatic contribution to DNA stiffness is reduced by phosphate screening owing to counterion condensation.[88] Also, the binding of cationic ligands to DNA is an ion-exchange reaction in which condensed counterions are released into bulk solvent, providing an important favorable entropic

source of binding energy. DNA-surface interactions that result in multiple DNA surface-adsorbed states (i.e., loops, trains, and tails) or induction of DNA secondary structures confound this ideal situation further. The cations DNA bending using electrostatic theory for phosphate neutralization indicates that excess cation binding to the major grove of DNA induces spontaneous bending.[85] The local DNA deformability (softness) with respect to bending and twisting is also attributed to both chain conformation and DNA sequence.[89, 90]

Experiments on DNA arrays have revealed substantial differences in hybridization thermodynamics and hybridization efficiency of DNA free in solution and surface-tethered DNA (i.e., for both glass and gold surfaces) due to dominate electrostatics effects. In 2D microarray systems, as the target-probe binding increases, the hybridization efficiency decreases due to Coulomb blockage due to hybridization. There is a sufficient amount of electrostatic repulsion of target-probe layer to the incoming target. This effect suppresses further hybridization with the Columbic blockage reducing the microarray sensitivity. However, Coulombic screening using multivalent counterion enhancement and use of 3D arrays using probe immobilization in gels, mimicking solution hybridization, can reduce this effect due to coaxial stacking effect of two bases localized in one strand of DNA duplexes.[91] Additionally, reduced DNA chain-chain repulsion and enhanced hybridization kinetics at surfaces have been achieved by applying a positive electrostatic potential to ssDNA-immobilized surfaces, leading to claims for increasing assay sensitivity.[92,93] Schematics showing coulombic blockade by ssDNA on surfaces and the dependence of R_g on ionic strength (ion valence: Z) are shown in Figure 1.6. Two different scenarios emerge in the charged brush regime characterized by two length scales: the average vertical extension of DNA chains from the surface L, and the typical extent of the counterion cloud, denoted by H shown in Figure 1.6. The counterions can either extend outside the brush, $H \gg L$, as shown, or be confined inside the brush, $H \approx L$ in the weak-charge limit where the counterion cloud has a thickness H larger than the thickness of the brush layer, L, for strong-charge limit, where all counterions are contained inside the brush and a single length scale $L \approx H$ exists. High salts are used to screen the electrostatic repulsion and increase the surface DNA hybridization efficiency. At high salt limit, the only length characterizing the exponential decay of

electrostatic potential close to the surface is the Debye-Hückel screening length.[94] The influence of ionic strength on the flexible chain R_g is depicted in Figure 1.6. The ionic strength (Z) and R_g have inverse relations due to chain condensation with added salt, affecting the probe and target chain conformations, and with R_g for the probe influencing duplex formation.

Different buffer salts influence probe immobilization efficiencies and kinetics. Buffers with divalent salts dramatically increase the efficiency of immobilization and result in high immobilized surface densities that may only be possible if the divalent counterions induce strong attractive intermolecular interactions. In contrast with previous reports of alkanethiol adsorption kinetics on gold, ssDNA immobilization in 1M phosphate buffer does not occur with expected Langmuir kinetics, a result attributable to rearrangement within the film that follows the initial probe adsorption.

1.3.6 DNA bending

The stiffness of DNA opposes processes requiring bending, twisting, and looping typical for hybridization.[95, 96] As both accessibility and binding affinity of DNA are key parameters affecting the hybridization efficiency in surface-based biosensor technologies, better chain accessibility and flexibility will result in higher hybridization efficiency.[97] The classic framework for understanding long-range DNA shape and resistance to bending is explained by the WLC model of DNA flexibility.[19] Marko and Sigga described the free energy required to deform a stiff helical, symmetrical DNA molecule to explain the bending and twisting of DNA with elastic theory.[98] However, fundamental forces responsible for the remarkable resistance of DNA to bending and twisting remain controversial. Experiments by Cluzel et al. to measure the bending of DNA with the movement of the micropipette tip by measuring applied force is proportional to the bending.[99] The stretching of the DNA molecule tethered between the optical fiber and the bead caused bending. Willam and Maher proposed a cause of DNA bending using electrostatic theory for phosphate neutralization and excess cation binding to the major grove of DNA, inducing spontaneous bending.[85] The local DNA deformability (softness) with respect to bending and twisting is also attributed to both chain conformation and DNA sequence.[89, 90] Both models of kinked WLC (KWLC) and single-stranded bubble propose local distortions that could strongly

enhance bending and bidirectional torsional flexibility.[100] However, dsDNA distortion such as formation of circles smaller than ~85bp which include shaper bending or kinking of DNA cannot be explained with the WLC model. Thus, the force (or, likely, balance of forces) responsible for the bending stiffness of DNA remains unresolved,[19] also for immobilized strands at surfaces.

Nonetheless, due to its chain flexibility, ssDNA in solution is often described using statistical approaches such as flexibly jointed or WLC models.[101] Also, DNA persistence length is in good agreement with different approaches; for example, oligo-dT in a moderate salt concentration decreases from 3 nm in 25mM NaCl to 1.5 nm in 2M NaCl. Zhang et al. studied the elasticity of ssDNA through Monte Carlo implementation of a modified freely jointed chain (FJC) model with electrostatic, base-pairing, and base-pair stacking interactions.[102] In low-salt solution, electrostatic interaction dominates, and at low forces, the molecule can be more easily aligned than an unmodified FJC. In high-salt solution, a secondary hairpin structure appears in ssDNA by formation of base pairs between complementary bases, and external stretching causes a hairpin-coil structural transition, which is continuous for ssDNA made of random sequences. Their comparison of modeling calculations with experimental data suggests that base pairing of ssDNA tends to form a nested, independent planar hairpin structure rather than a random intersecting pattern in solution.[102] Zhang et al. demonstrated that increased DNA accessibility increased DNA hybridization efficiency through variations in pH-driven mechanical chain bending of ssDNA probes.

1.3.7 Factors influencing DNA persistence length

Persistence length varies depending on whether chains are bound or unbound to surfaces, surface interactions, in bulk solution, temperature, type of buffer, divalent or multivalent ions present, and also on the method of measurement.[103] For example, the apparent persistence length (L_{pa}) of dsDNA assessed using AFM is much shorter on 3-aminopropylsilane (AP-mica) than on bare mica. The same surface effect has also been shown qualitatively for plasmid DNA with L_{pa} of dsDNA varied from 55 to 100 nm on bare mica and from 20 to 40 nm on AP-mica.[104] Persistence lengths measured by different methods vary considerably: the dsDNA value measured by electron microscopy is 150 nm in 30mM ammonium acetate[105] in minimum salt

concentration, whereas it is 35–50 nm in solutions with Mg^{2+} cation concentrations above 0.1mM.[106] Additionally, the experimental persistence length does not match well with simulations (consistently less than experiment) since the persistence length is highly sensitive to factors such as base sequence, hairpin loops, experimental methods such as fluorescence spectroscopy, laser tweezers, and gel electrophoresis. Under physiological conditions, conventional ssDNA values for L_p are near 50 nm or ~150 bp. Evidence also suggests that sequence-dependent differences in base stacking forces can measurably influence DNA persistence length. However, the scale of these stacking effects has never been experimentally compared with electrostatic effects.[107, 108]

1.3.8 Persistence length of ssDNA tethered to surfaces

Understanding the structure of single-stranded DNA (ssDNA) tethered to surfaces is critical for optimizing its accessibility and binding to target DNA, influencing hybridization rates and efficiencies. While there is enormous literature on the persistence length of ssDNA in solution, very few measurements of ssDNA persistence lengths tethered to surfaces are reported. The ssDNA persistence length based on the coarse-grained model its dependence on chain length.[109] For a small number of bases, ssDNA has a longer end-to-end distance given its 0.64 nm distance between bases compared to dsDNA (e.g., 0.34 nm interbase distance for coiled base-paired duplexes). However, with more bases, ssDNA yields a shorter end-to-end distance than dsDNA because it curls over on itself much more on average, reflecting its shorter persistence length ($\leq$1.48 nm).[110] Various experimental and simulation approaches have been performed to evaluate DNA persistence length as a function of temperature, salt concentration, base sequence, interaction potential strength, and local position along the chain. The persistence length of single-stranded DNA (ssDNA) tethered to a modified graphite surface using atomic force microscopy at very low ionic strength was L_p = 9.1 nm and this decreases with increasing ionic strength to 6.7 nm and 4.6nm at 1mM and 10mM NaCl, respectively.[71, 111] Murphy et al. used FRET to deduce persistence lengths for ssDNA (oligodeoxythymidylates, dT_N) of chain lengths ($10 \leq N \leq 70$ nucleotides) over a wide range of salt concentrations. Persistence length varied from 1.5nm in 2M NaCl to 3nm in 25mM NaCl. The ssDNA was not bound to the surface directly but

attached to dsDNA immobilized on a streptavidin-coated quartz surface. Chen et al. measured persistence length of dT_{40} tethered to a glass surface at the same ionic strengths as Murphy et al. but with SAXS and smFRET. They found that persistence lengths were 50% less for tethered DNA, possibly due to glass surface interactions on chain conformations. Crozier et al. reported persistence length of ssDNA with molecular dynamics (MD) simulations with a coarse-grained method for single polyelectrolyte chains grafted to a solid surface. This revealed a small intrinsic persistence length that is highly extended in zero salt simulations. Added salt does shrink the chain as salt ions enter the volume near the chain.[112] The persistence length of ssDNA predicted with the coarse-grained DNA model (with bases modeled as rigid-body ellipsoids to capture their anisotropic stereochemistry) initially decreases with increasing temperature in accord with the WLC model; however, at higher temperatures where nonlocal interactions become important, the persistence length shows an increasing trend over a large range of temperature, while the R_g for the DNA globule expands through a collapse-transition temperature. Below the crossover temperature, the base stacking interactions stiffen the chains and increase the persistence length, while above this temperature, nonlocal base-base van der Waals interactions (which are inseparable from stacking interactions) soften the chain and decrease the persistence length.[109] The persistence length for a homogeneous single-strand of adenine as large as ~50 bases is more than the corresponding homogenous strand of thymine bases ($L_P \approx 2$ bases) at low temperature due to the large enthalpic costs for hairpin formation in poly(A) over poly (T).[89] Temperature has a drastic influence on persistence length and R_g for both ss-poly(A) and ss-poly(T). At lower temperature, ss-poly(A) stacks significantly more strongly than ss-poly(T); however, at higher temperature, nonlocal interactions between bases govern the persistence length and the poly(A) forms a collapsed globule with shorter persistence length and poly(T) form an expanded globule.[109] Thus, ssDNA persistence length tethered to surfaces varies with temperature, ionic strength, sequence, and type of surface immobilization -- all important factors influencing further binding of target DNA and important for considering probe accessibility and mobility in the microarray chip design.

1.3.9 Persistence length of dsDNA at surfaces

Hybridization of ssDNA to form dsDNA is a necessary event required of two complementary DNA strands (probe and target) in a microarray assay. The physical properties of each DNA partner change upon hybridization: dsDNA is much more rigid than ssDNA.[113] This difference in chain rigidity can be described in terms of persistence length.[114] Persistence length of dsDNA has been shown to be approximately 50 nm in environments containing a salt concentration greater than 10 mM, while that of ssDNA has been shown to be only about 1 nm.[106] As discussed (vida supra), ssDNA molecules of lengths less than 50 nm have very different chain rigidities compared to dsDNA molecules of the same lengths. Stretching persistence length of dsDNA has also been measured using single-molecule techniques.[115,116] Abels et al. measured individual dsDNA molecules attached at one end to a glass cover slip and at the other end to a magnetic bead, yielding values of 54 nm, in agreement with values reported.[63, 115, 117] Brinkers et al. measured persistence length for a lone dsDNA using dark field microscopy by capturing the projected positions of attached nanoparticles undergoing constrained Brownian motion.[64] A nanoparticle is tethered to a substrate using a single dsDNA molecule and immersed in buffer with no force exerted on the DNA, then hybridized. With Monte Carlo simulation and experimental evidence, the authors evaluated persistence lengths of 45 single molecules of four different lengths of dsDNA measured under at high salt concentration. These had a mean value of 35 nm (standard error of 2.8 nm). In contrast, Mastroianni et al. measured the persistence length of short dsDNA chains in solutions with dsDNA-linked dimers of gold nanoparticles using small-angle x-ray scattering without requiring any external forces or binding to a substrate.[118] These results for dsDNA comprising 42–94 basepairs were consistent with a simple WLC model of dsDNA elasticity and comparable to results from Monte Carlo simulations. A persistence length of 50 nm (150 base pairs) is consistent with results of single-molecule force-extension experiments on much longer dsDNA chains. These results produced contrast to recent suggestions of enhanced DNA flexibility at these length scales.[118] dsDNA persistence length also depends on media ionic strength, similar to ssDNA. Decreased DNA persistence length was also observed for increasing counterion valency.[9] The persistence lengths of both ssDNA and dsDNA have the same

functional dependence on ionic concentration. Notably, dsDNA is roughly 55 times stiffer at 0.02M, 25 times stiffer at 0.04M, and 52 times stiffer at 0.13M than ssDNA.[71] Extra stability is provided by hybridization since weakening base-base interactions with increasing ionic strength only modestly reduces chain stiffness due to stacking.[109]

1.3.10 DNA elasticity

DNA chain mechanical properties include force extension, DNA elasticity, torque as a function of twist for stretched DNA, and torsional strain.[119] Chain flexibility and conformational adaptation are important factors for duplex formation. Various theories are proposed to understand DNA elasticity. The classic framework for understanding long-range DNA chain shape and resistance to bending is embodied in the WLC model of DNA flexibility in a Kratky & Porod chain (simple polymer chain with no torsional stress).[120] The elasticity of DNA including looping, distance-dependent flexibility[121] and J-factor (ring-closure probability for a given DNA length, an experimentally accessible measure of polymer stiffness) are explained by the WLC model.[122]

AFM and optical tweezers have successfully measured DNA stretching under applied forces.[65] Measuring DNA elasticity by tethering DNA to a surface and applying various loads to determine chain elongation and yield points is also well known.[123] Various experimental methods and instruments with newer technologies have aimed at determining DNA's molecular elasticity. However, dsDNA elasticity is highly influenced by factors such as the type of surface anchor, a duplex terminal anchored to the material, type of substrate material (e.g., hydrophilic or hydrophobic), and media ionic strength.[124,125] Changes in ionic strength predict DNA elasticity based on persistence length and elastic modulus determinations. Lowering ionic strength increases persistence length and reduces DNA elastic stretch modulus.[65]

The finite worm-like chain (FWLC) model modifies the classical WLC model by including finite chain length, chain-end boundary conditions, and bead rotational fluctuations (inherent in optical trapping assays where beads are used to apply forces).[126] The FWLC solution provides a significant improvement to the theoretical framework used to analyze single-molecule experiments over a broad range of experimentally accessible DNA lengths, including both short contour length (a few hundred nanometers) and very long (microns in contour length)

molecules.[126] The freely jointed chain (FJC) model reliably predicts properties for a polymer chain whose segments are unrestricted in their orientation, corresponding to freely rotating segments of the Kuhn length (i.e., $2L_p$). However, the FJC model is not a good approximation for the elastic behavior of DNA molecule exhibited at large extensions (i.e., $L > R_g$).[95] The WLC model is much better for describing the behavior of oligo-DNA, particularly at large extensions (i.e., for DNA fragments 105–130 bp in length, $L > R_g$). However, DNA cyclization studies have revealed the nonapplicability of the WLC model to DNA bending on biologically relevant length scales (~85 bp in length). The WLC model cannot describe the force of extension, solution scattering, and long-contour-length cyclization experiments, and therefore, alteration of the WLC model is required to include sharp bending or kinking of DNA.[127]

1.3.11 DNA stretching

The elastic properties of both short and long ssDNA and dsDNA tethered to charged and uncharged supports under aqueous conditions are important in defining probe interfacial properties affecting the kinetics, thermodynamics, and binding efficiency of DNA target in microarrays. Electrical manipulation studies by Rant et al. of ssDNA and dsDNA end-tethered to gold surfaces in electrolyte solutions showed dissimilar kinetic behaviors attributed to elasticity of the bound DNA.[128] Stiff polymers undergo rotation around the anchoring pivot point; flexible polymers, by contrast, are pulled onto the attracting surface, segment by segment. These features are important determinants of the accessibility and ability of self-assembled probes to bind to complementary target sequence.

Studies of DNA mechanical properties indicate that DNA's elasticity is similar to that of synthetic polyamide, nylon.[129] Recently, Eijck et al. used neutron scattering through aligned fibers of DNA to gauge the speed of sound waves vibrating along DNA helices, yielding a force constant of 83 N/m. Using a computer simulation model of DNA's vibrations, the authors explained the large variation in previously reported DNA elasticities ranging from 0.3 to 133 N/m.[130] Studies of mechanical properties as early as 1995 by Marko and Siggia analyzing stretching of dsDNA tethered at one end and stretched by a force applied directly to the free end by an electric field or by hydrodynamic flow have been compared with a statistical mechanical treatment of the WLC

model. All experiments display a strong stretching regime where end-to-end distance approaches the DNA contour length as l/(force)$^{1/2}$, indicating WLC elasticity.[98, 131]

Experiments with torsionally constrained single molecules provided the first direct measurements for coupling twists and stretches in dsDNA.[132] A strong twist-stretch coupling in torsionally constrained DNA stretching experiments reflects the intrinsic elasticity of the DNA duplex, consistent with classical WLC elasticity theory. Experiments using torsionally constrained DNA have permitted determination of coupling between DNA twist and stretch.[60, 133, 134] Results are consistent with fundamental principles from classical WLC elasticity theory. A constrained twist of a DNA strand manifests itself as a link, twist, or writhe due to DNA's elastic entropy.[132] Single-molecule stretch experiments indicate that dsDNA deviates from the inextensible WLC model up to forces of10 pN. Beyond 65pN, dsDNA suddenly changes its form, from B to S, stretching up to 70% beyond its canonical B-form contour length. The S form of DNA is stable in high salt up to forces of between approximately 150 pN (for random sequence). Some 300 pN above this force, S-DNA melts into single strands that exhibit the characteristic force/extension behavior of ssDNA.[133] The simplest extensible WLC with twist rigidity is considered a model for DNA under tension. However, dsDNA is chiral, which demands that helix stretching coupled with twisting leads to a structural transition. The dependence of DNA's elasticity on such structural transitions[115] within a single stretched and supercoiled DNA molecule.[55] Force–extension curves for torsionally constrained DNA. Force–extension curves when single DNA molecules are twisted in either direction and pulled to high force,[135] and phase boundaries, all correspond to the structural states of DNA in coexistence with adjacent pure phases.[136] Stretching of helical dsDNA twists the DNA, perturbing its twist degree of freedom and leading to its supercoiling as it relaxes -- a distinct phenomenon occurring in DNA compared to other polymers.

When dsDNA is stretched beyond its contour length, a highly cooperative overstretching transition is observed, dependent on the concentration of buffer/salt. Wenner et al. performed measurements of DNA elasticity and overstretching transition by stretching single dsDNA molecules as a function of monovalent salt concentration with optical tweezers measurement. The persistence length measurement with change in ionic strength of sodium ion concentration

decreases from 1000 to 2.57 mM, shown to increase from 46 to 59 nm with the elastic stretch modulus remaining constant. However, as salt concentration decreased further, the overstretching transition force decreased from 68 to 52 pN. This reduction in force is attributed to decreases in DNA double helix stability with decreasing salt concentration. Although the Watson-Crick base-paired hydrogen bonds break as helical DNA is overstretched, these data indicate that both DNA strands remain close together during the transition.[137] Punkkinen et al. theoretically described the salt-dependent over-stretching transition of DNA by coupling the two-state model and the elasticity theory proposed for monovalent salt effects on elastic modulus during the transition.[138] In dsDNA, the effective chain length per unit charge varies with salt in agreement with the Manning[139] and Poisson-Boltzmann models for thin polyelectrolyte rods,[140] whereas the other model parameters describing structural features exhibit little salt dependence.[139] Thus, electrostatic components of force-induced DNA overstretching are mediated mesoscopically via elasticity.[138] This is an important factor since DNA microarray duplexing assays are conducted in typically high ionic strength buffer and salt systems to minimize electrostatic repulsions while maximizing ssDNA elasticity, extension, and accessibility known to impact the efficiency of target binding and the stability of resulting dsDNA.

The pH of DNA solutions also affects chain extension, efficient hybridization, and the stability of the resulting DNA duplex via influences on DNA conformation and duplex stability. Single molecule dsDNA exhibits a highly cooperative overstretching transition under varying pH at high ionic strength.[85] Williams et al. showed that as the solution pH was increased from pH 6.0 to 10.6 in 250mM NaCl, overstretching transition forces decreased from 67.0±0.8 pN to 56.2±0.8 pN, while the transition width remained nearly constant.[141] As the pH was lowered from pH 6.0 to 3.1, the overstretching force decreased from 67.0±0.8 pN to 47.0±1.0pN, but the transition width increased from 3.0±0.6 pN to 16.0±3pN. These results quantitatively support that DNA strand dissociation, or melting, occurs during the overstretching transition.[141] However, other data suggest that DNA should unwind under tension as it is pulled towards a denatured structure.[60, 99, 133, 142] Gore et al. used rotor bead tracking to directly measure twist–stretch coupling in single dsDNA molecules. dsDNA overwinds under tension, reaching a maximum twist at a tension of

~30pN, and when increased above this critical value, the DNA begins to unwind.[143] The observed twist–stretch coupling predicts that DNA should also lengthen when overwound under constant tension. This property would possibly explain the anomalously large torsional rigidity of dsDNA[143] and might also have implications for surface-tethered DNA since ssDNA must stretch and twist to form dsDNA when duplexing new target to compensate for variability in chain dimensionalities at encounter, and to align bases for optimal hydrogen bonding in duplexes. dsDNA is well-described as a worm-like chain at concentrations of trivalent cations capable of inducing condensation but when condensation is prevented by keeping the dsDNA molecule stretched. A retractile force appears in the presence of multivalent cations at molecular extensions that allows intramolecular contacts, suggesting that condensation in stretched DNA occurs by a ‘‘thermal ratchet’’ mechanism.[66] Using designed sequences of DNA with nearly identical DNA curvatures (based on same length of base pairs, e.g., 132bp) but with different elasticities and varied AT base pair (i.e., duplex melting point) content, Raghunath et al. showed that dsDNA persistence length varies by almost 30% between sequences containing 61% AT and 45% AT.[144]

DNA, like other biopolymers, differs from classical polymers in its intrinsic torsional stiffness. The force of extension, torque, and angle of DNA for structural and elastic parameters of torsionally melted DNA single molecules was measured by Sheinin et al. using an angular optical trap.[145] Under moderate forces, melted DNA assumes a left-handed structure and is highly torsionally compliant. For lower forces, melted DNA properties are highly dependent on DNA sequence.[145] Moroz and Nelson studied DNA force extension as a function of overtwist over a wide range of applied force with a theoretical model. The statistical character of DNA conformations under tension changes from a classical random walk to “torsional random walk” whose random variables are the direction of each step relative to its predecessor, together with a relative axial twist.[96] The similarity between Metropolis Monte Carlo simulation[146] and experimental measurement of torsionally stretched DNA by Strick et al.[60] strongly suggests that correlations observed between base stacking and permanent hydrogen bond constraints play an important role in understanding supercoiled DNA elasticity. Bryant et al. measured torque as a

function of twist for stretched dsDNA: that is, torsional strain in over- or under-wound molecules to power the rotation of submicrometer beads serving as calibrated loads. With DNA's twist elasticity, the torsional modulus shows an over- or under-wound dsDNA molecule behaving as a constant-torque wind-up motor capable of repeatedly producing thousands of rotations, and that an overstretched molecule acts as a force–torque converter.[119] These results indicate the importance of external forces on DNA. However, such forces of DNA elasticity and mechanics occurring at the microarray surface are not directly comparable to these results and need to be evaluated further. Properties such as flexibility and elasticity of unbound, free DNA under an external force as described above can help us understand the behavior of DNA tethered to surfaces influenced by external factors such as ionic strength.

In summary, absence of the application of external forces, short ssDNA maintains a compact conformation; its chain extension per base pair is shorter than that of dsDNA for forces smaller than ~6 pN. At higher forces, however, the situation is reversed. As the DNA single strand is not constrained to follow a helical path in extension, it becomes nearly twice as long as dsDNA as it is pulled in tension, forming brush-like extension on the surface under applied force (i.e., shear, tensile, electrical).[115] These chain tensile properties seem to be affected by their surface environment when tethered.[147] However, without external forces, ssDNA chain conformational adaptations in a tethered-state must accommodate DNA target binding on surfaces by overcoming these local higher chain energies to extend spontaneously from a surface and form an accessible chain capable of rapid dsDNA encounter and duplex formation that is then stiff. dsDNA chains are generally helical with twisted conformations that contain complex torsional and elastic energies exhibiting nonlinear chain extension responses to external forces. Rather than extending fully to a brush-like state with forced extension, dsDNA is separated into ssDNA unimers by stretching forces strong enough to cleave chain-chain base-paired hydrogen bonds after torsional and helical elastically stabilized conformational changes are completed.[148] The longer the DNA chains, the higher the chain polyphosphate negative charge density at physiological pH which affects the efficiency of hybridization.[97] Also, longer ssDNA and dsDNA chains respond to ionic strengths and applied electrical forces differently than shorter DNA

chains. The longer ssDNA chains forms secondary structures and affect the hybridization efficiency; however, with shorter chains the sensitivity of detection is reduced. The accessibility and binding affinity of DNA affect the hybridization of microarrays and hence, an optimum length of the DNA is desired.

1.3.12 Extending the behavior of ssDNA and dsDNA tethered to surfaces to microarray applications

The determination of tethered DNA conformations on surfaces and correlated hybridization behaviors with incoming DNA targets provides empirical information required to understand barriers to DNA duplex formation in arrays and to move DNA interfacial applications forward. This should impact their reliability and adaptation for clinical and biotechnological utility in many surface-bound formats. Immobilized DNA monolayers are widely used in both fundamental and applied genomics and are also versatile experimental models for elucidating the behavior of charged polymers at interfaces. The physical behavior of these assay systems is to a large extent governed by their internal ionic microenvironment of layers of end-tethered, polyanionic, single-stranded DNA oligonucleotides and fundamental intermolecular forces to yield duplexes in complex surface states.

DNA molecular conformation tethered to a microarray surface likely significantly affects the rates and efficiencies of hybridization. Although a number of methods have been applied to determine the structure of the immobilized DNA layer, such optical or contact methods as ellipsometry,[149] optical reflectivity,[150] neutron reflectivity,[151] x-ray photoelectron spectroscopy,[152] FRET,[101] SPR,[153] and AFM[154] are not very sensitive to variations in DNA chain conformation or chain density on surfaces, shown to influence its molecular behavior (vida supra). The DNA adlayer response to alternating repulsive and attractive electric surface fields studied by time-resolved fluorescence measurements of ssDNA and dsDNA end-tethered to gold surfaces in electrolyte solutions shows distinct dynamics for flexible single-stranded oligoDNA probes versus stiff dsDNA. Hydrodynamic simulations rationalize this finding to disclose two different kinetic mechanisms: stiff polymers undergo rotation around the anchoring pivot point while flexible ssDNA polymers are pulled onto the attracting surface segment by segment.[155]

To assess conformations of surface-bound DNA molecules by evaluating the average location of a fluorescent label in a DNA layer relative to the surface, Moiseev et al. used an optical interferometric technique (spectral self-interference fluorescence microscopy) for precise polymer extension measurements.[156] This method estimated the shape of coiled single-stranded DNA, the average tilt of double-stranded DNA of different lengths, and the amount of hybridization. The molecular disposition of DNA varied on surfaces based on differences in DNA length, whether dye labeling was at the proximal or distal end of the probe and the dye labeling position on the target.[156] There were interesting observations such as an unlabeled strand hybridized with labeled probes (at the distal end) resulting in an extended duplex formation. Additionally, the conformation of a surface-bound 50-nt labeled oligonucleotide changed when duplexed with a 21-mer complimentary target strand, and the position of the distal end increased from 5.5 to 6.5 nm. A different situation was observed when an ssDNA–dsDNA construct has the double stranded part proximal to the surface. These important observations emphasize the importance of length of the ssDNA and its confirmation, hybridization efficiency of different lengths, and dye labeling influencing the DNA probes accessibility to the target DNA.

The ionic environment within a tethered DNA surface layer differs strikingly from that in solution and is relevant to DNA arrays and related technologies based on monitoring interfacial electrostatics in nucleic acid films. Electrochemical techniques were used to probe the ionic microenvironment inside monolayers of end-attached ssDNA oligonucleotides (as DNA brushes). Retention of counterions by the DNA brush manifests as lowered susceptibility of the interfacial capacitance to external salt conditions. The charging response exhibited signatures of structural reorganization whereby the DNA strands stretch or relax with changes in solution ionic strength, consistent with expected physical behavior of charged polymer layers. The quantity of bound DNA and strand coverage can be evaluated based on the shift in reduction potential for redox counterions associated with the DNA monolayer.[157] The physical behavior of the ssDNA at surfaces is largely governed by the ionic environments providing important information of organization of the DNA layer at the surface and its polymer charging behavior at the interface providing guidance for the development of DNA microarray diagnostics.

1.3.13 Kinetics of microarray surface-capture assays

When the surface density of ssDNA oligonucleotide probes increases, DNA hybridization decreases.[42, 158] The free energy penalty associated with dense probe layers modifies both the hybridization isotherms and the duplex rate equations: the attainable ssDNA hybridization fractional completion and rate of DNA hybridization are both reduced.[42] The hybridization behavior, kinetics and thermodynamics of microarrays are influenced by aspects of chip design (probe design) and hybridization (target design). Langmuir isotherm treatment and their corresponding duplex kinetics is a starting model for noninteractive probes and when ssDNA probe density is sufficiently low; at higher probe densities, the Langmuir model requires modification.[49]

Longer targets lead to reduced duplex equilibrium binding constants on surfaces due to the nonoverlap of target strands, incurring an entropic penalty at the impenetrable surface.[42] This chain crowding leads to a polymer brush (of probe), modifying the Langmuir isotherm and kinetics due to free energy penalty associated with brush capture of target compared to less dense, constrained mushroom densities. The brush penalty reflects both the electrostatic interactions with the probe layer and the entropic price due to the extension of crowded chains, leading to slower hybridization. Guo et al. observed that the maximum attainable hybridization fraction increases at higher probe density (Σ_0) when the number of bases in the target (n) increases.[159] However, Su et al. reported slower hybridization as the number of bases in the target increases at fixed probe density.[160] Surface diluents are used to overcome these complications by providing space between crowded ssDNA chains. For example, surface diluents spacers reactive to gold are mixed into thiolated DNA ssDNA probes, or used to displace ssDNA after gold assembly (e.g., mercaptohexanol,[114] 11-mercapto-1-undecanol,[43] oligoethylene glycols).[43] Additionally, small molecule spacers are used to modify the effects of increased steric hindrance occurring when lateral distances between anchored probes (i.e., crowding) ensure low probe-target interaction energy and drastic reductions in the number of accessible chain configurations in the vicinity of an impenetrable planar surface.

The array chip design and interfacial characteristics are important parameters for improved performance of the microarray. Possible design parameters include two important factors: 1) the nature of the surface (i.e., the treatment used to minimize nonspecific adsorption and maximize DNA tethering and accessibility), and 2) ssDNA probe design (i.e., length, charge, lack of secondary structure, hydrophobicity, and the chemical design/length of spacer chains joining the probe to the surface). Additionally, probe surface area (Σ_0) and the number of bases per probe chain become important features in electrostatic field and steric properties in crowded array spots. Probe density in a typical array spot varies from 1.2×10^{10} and 4×10^{13} probes per cm^2, corresponding to 2.5×10^{2} $nm^2 \leq \Sigma_0 \leq 8.3\times10^{4}$ nm^2.[54] The labeling of probe and target with signal molecules (e.g., Cy3 or Cy5 dyes) can also affect the hybridization behavior and signal intensity (discussed in detail in another section). Hybridization conditions include the composition of the hybridization solution, the hybridization temperature, and the hybridization time (incubation time). Typical hybridization temperatures vary over the range 30 to $60\,^{0}C$ depending on the GC base fractions (i.e., duplex chain melt point). The assay incubation time (i.e., time to hybridization endpoint stabilization) can be very long (i.e., up to 2h to 16h reported[27, 161, 162]) depending on bulk composition, target concentration, ionic strength, and probe grafting density. Incubation times often vary, different even for similar concentration of probe and target, but depending on study conditions and largely influenced by ssDNA probe density distributions.[163, 164]

Deviations or extension of the Langmuir model should be explored during microarray fabrication. Livshits and Mirzabekov focused on target diffusion into DNA chips with probes bound into thin pads of water-soluble gels.[165] Chan et al. considered DNA chips with probes attached to impenetrable surfaces, allowing for study of lateral two-dimensional diffusion of physisorbed targets.[166] These two articles considered the case of a given spot contacted with a solution containing a single target. Vainrub and Pettitt first considered the role of electrostatic interactions within the probe layer.[93] Bhanot et. al first analyzed in a numerical study the effect of competitive surface hybridization, for hybridization at a number of spots contacted with a multicomponent solutions of targets with no bulk hybridization.[158] Importantly, this demonstrates that microchip performance is best when equilibrium is attained. Forman et al. analyzed observable selectivity in

hybridization and the ability to distinguish perfectly matched and mismatched target sequences that are affected by surface interactions.[167] Hagan and Chakraborty discussed the initial hybridization rate constants when the unhybridized probes form a brush.[168] The effect of bulky fluorescent labels on the hybridization was first considered theoretically by Naef and Magnasco[169] who recognized the difference in hybridization between surface hybridization and solution hybridization. Additionally, Moiseev et al.[156] and Unruh et al. studied the influence of the nature of dye-DNA interactions using fluorescence methods in the study of biomolecular dynamics, the extent to which a fluorescent dye influences the mobility and chain confirmation of labeled ssDNA. The dye labeled ssDNA influencing the confirmation and the chain length before and after hybridization with dye labeled and unlabeled targets is different and affects the hybridization efficiency.[170]

Sensitivity and specificity of hybridization isotherms of DNA chips is an important aspect in the kinetics of hybridization affecting various surface and bulk properties. Competitive hybridization, at the surface and in the bulk, lowers the sensitivity of DNA chips.[164] Competitive surface hybridization occurs when different targets can hybridize with the same probe. Competitive bulk hybridization takes place when the targets can hybridize with free complementary chains in the solution. The hybridization isotherm emerges as a Langmuir isotherm modified for electrostatic interactions within the probe layer. The effects of competitive hybridization are important for the quantitative analysis of DNA chip results, especially when used to study point mutations. The hybridization isotherms of DNA chips provide a natural starting point for the analysis of their sensitivity and specificity. Vainrub and Pettitt developed a thermodynamic theory of association to a molecule immobilized in an electric double layer and applied this to a DNA chip at high 1M NaCl and low 0.01M NaCl ionic strength for dielectric and metallic substrates.[93] They predicted strong electrostatic effects and suggested the feasibility of electronic control of DNA hybridization and design of chips to avoid the DNA folding problem. They used linear Poisson–Boltzmann theory of the electric double-layer interaction between an ion-penetrable sphere and a hard plate with variables including binding enthalpy, entropy, and equilibrium reaction constant for an immobilized complex. They also developed a mean field

model of the Coulomb effects in two-dimensional DNA arrays to understand the binding isotherms and thermal denaturation of the double helix.[87] These studies on DNA microarrays have revealed substantial differences in hybridization thermodynamics between DNA free in solution and surface-tethered DNA. The electrostatic repulsion of the assayed nucleic acid from the array of DNA probes dominates the binding thermodynamics, and causes the Coulomb blockage of the hybridization. This explains the observed dramatic decrease in hybridization efficiency and the thermal denaturation curve broadening as the probe surface density grows in DNA microarrays. Chen et al. investigated how substrate–DNA interaction influences both thermodynamics and kinetics of DNA hybridization of DNA-modified gold nanoparticles (GNPs).[171] They proposed that during hybridization, the target DNA in solution does not directly react with the immobilized probe, but rather it is first adsorbed onto the GNP surface, followed by two-dimensional diffusion until it finally hybridizes with an immobilized probe DNA. Different duplex melting properties between hairpin and random-coil sequence DNAs come from the structure-influenced interaction between the bases and GNPs. Steric hindrance induced by the compact configuration in a DNA hairpin probe prevents its bases from interacting with the surface and leads to a higher stability of hairpin-formed duplexes on the GNPs.

1.3.14 Spacers in DNA surface immobilization

Flexible spacer chains (PEGs, alkanes, oligo(dT) are frequently utilized as an alternative to direct ssDNA probe surface coupling in order to enhance the hybridization of terminally anchored oligonucleotide probes in DNA microarrays.[76] For low grafting densities where probes lie flat on the solid surface, a reduction in the number of accessible ssDNA probe chain configurations results. At higher grafting densities, different DNA brush regimes introduce an extra hybridization penalty. A unique brush regime is obtained for long neutral spacers (e.g., PEO) and short targets at intermediate media ionic strengths where DNA chain stretching is due to electrostatic interactions between immobilized probes.[76] When the surface density of immobilized probes is low, the dominant chain conformational effect is due to the ssDNA interactions with the impenetrable solid surface, reducing the number of accessible chain trajectories of terminally anchored mushrooms, affecting the entropy of the reactants and the

products. Long spacers weaken this surface effect, and hybridization behavior can approach more bulk-like characteristics.[76] However, the effect also depends strongly on DNA target length. Analogously, increases in spacer lengths when targets are short (to overcome steric limitations at the grafting site) have detrimental effects. In contrast to the advantages of relieving steric strain at the grafting site, a nonmonotonic effect of spacer length is observed when targets are short. At higher grafting densities, probe chains crowd each other, producing a polymer brush, higher ssDNA surface charge density, possible Coulombic blockade, steric hindrance to approaching targets, and resulting poor duplex efficiency.[76]

Probe brush or mushroom regimes can be formed on surfaces when ssDNA is tethered with spacers depending on the number of bases in the probe and spacer lengths. The stretching elasticity of the spacers and electrostatic interactions between the probes is influenced by the ionic strength. For DNA chips, the configurational statistics of the chains, probe target, and in duplexes also play a role. Furthermore, while the probe and target sequence and length can be controlled, the area per probe site (density) cannot be readily controlled at high resolution (only at a statistical average over macroscales). The effect of spacers on the hybridization constant K_{spt} (equilibrium constant due to spacers) provides experimental characterization of the surface exponent γ_s (surface reaction).[27, 33] ssDNA brushes with long spacers carrying short probes provide a possibility of labeling the free ends to allow for experimental determination of their spatial distribution. Assessing the DNA polymer brush or mushroom structure on array substrates is important to the control of probe density on substrates to optimize further probe-target binding kinetics in microarray applications. With the advent of structured probe sensors, such as those incorporating deliberate secondary structures such as hairpins as in molecular beacons or aptamers,[172, 173] it becomes more important to understand these surface-mediated structural effects. The intramolecular base pairs involved in secondary structure, stabilizing single-strand conformations create a higher energy barrier to intermolecular hybridization, slowing hybridization kinetics. Comparative studies of DNA hybridization kinetics both in solution and on the surface with SPR, UV absorbance, and QCM indicate that both probe and target secondary structure affects hybridization kinetics.[172] Although planar gold surfaces and conventional ssDNA probe

layer environments suppress the measured duplex rates 20- to 40- fold, the effects of secondary structure are similar in solution and surface environments.[172] Probe and target pairs containing large amounts of secondary structure were shown to hybridize by a more complex mechanism than traditional two-state DNA duplex formation. On the surface, the reduction in kinetics is likely caused by steric and electrostatic hindrance present in the DNA probe film as well as conformational restriction of the surface-tethered strands caused by the confinement of ssDNA on the surface. Both size and rigidity of hairpin loops have been shown to affect thermodynamic stability and could also affect duplex formation rates. Additionally, the length of hairpin 'tail' can be site for duplex nucleation.[172]

1.3.15 DNA spot drying phenomena and immobilized DNA heterogeneity

Fabrication of DNA probe printed spots on commercial array slides in repeated hundreds to thousands of spotted features involves spatially controlled deposition of nanoliter drops of complex DNA solutions onto reactively coated glass substrates using a robotic spotter, followed by evaporation of deposited liquid droplets within seconds.[57, 174] Noncontact inkjet printing and contact (pin) spotting of DNA generally all yield submicroliter droplet volumes on surfaces as the basis for DNA microspot formation in arraying. Unfortunately, droplet drying at this size scale and with typical arraying conditions most frequently results in inhomogeneous solute deposition upon droplet drying.[36, 174] For assay purposes, this resulting DNA dried spot heterogeneity is undesired, but is difficult to control from the combined phenomena of droplet solution composition, deposition wetting, spreading, evaporation, and subsequent DNA drying patterns. Evaporation from sessile droplets induces radial convection within the drop, producing the well-known ''coffee ring'' effect.[175, 176] The evaporation also induces a gradient in temperature across the droplet and consequently a gradient in surface tension, generating Marangoni flow.[57] Deegan et al. pointed out that the physical origin of the coffee stain effect is due to a combination of pinning of the three-phase contact line and a convective flux driven by the evaporation.[177] The occurrence of "coffee stain like" droplets is caused by a combination of solvent evaporation and contact line pinning: whenever the contact line of an evaporating drop is prevented from receding, a convective flux is generated from the center towards the edge of the drop in order to

sustain the solvent evaporation.[178] This flux carries solute from the bulk of the drop towards the contact line, leading to a local increase in concentration and eventually to precipitation of the solute. The Marangoni effect or convection phenomenon associated with the surface tension of the droplet is caused by solute concentration variation from local solvent evaporation.[179] In a sessile evaporating drop, Marangoni stress (surface tension gradient over the droplet) can be induced by the presence of temperature variation near fluid interface or concentration variation caused by solvent evaporation.[175] The circulating convective flows leads to intensive mixing of the analyte during evaporation, helping to overcome mass transport limitations and can be the counter force to the coffee stain forming Marangoni droplet drying pattern.[180] The rapid evaporative process produces increased solution ionic strength and solute concentrations in the drying DNA film, resulting in distinct differences in immobilized DNA structure, density, and chemistry compared to bulk solution coupling reactions between DNA and surfaces.[181] The spot drying thus commonly leads to “halo” or “doughnut” shaped spots which are not identifiable or reliable in the conventional fluorescence scanner readings. However, extensive high-resolution imaging techniques such as confocal epifluorescence can be combined with other more exotic surface analytical tools (e.g., TOF-SIMS and XPS imaging) to evaluate the distribution of DNA within dried spots and probe effects due to drying artifacts.[50, 57, 182]

Studies by Pappaert et al. reported the hybridization process as being the main reason causing doughnut shaped DNA dried spots.[183] A combination of computer simulations, theoretical, and optical techniques have shown that the ring-shaped hybridization pattern occurs due to diffusion-limited conditions present during hybridization process. Large amounts of binding molecules reach the spot center from the sides, leading to a preferential binding on the rims of the spot resulting in larger intensities obtained on the edges compared to center of spot. They also hypothesized that these patterns occur during hybridization, especially with short oligonucleotides that have a very high binding probability and fast hybridization kinetics. Longer target DNA molecules lead to a more evenly distributed intensity signals. Studies by Dandy et al. indicate that near the spot center, target is delivered to the probe surface solely through the linear normal diffusion component, whereas toward the outer edge, a lateral (radial) component of

diffusive flux augments the normal linear transport component, producing hemispherical diffusion.[26] These effects result collectively in the outer spot edges accumulating more DNA targets through greater proximate fluid volume transport versus spot centers. This was further verified by real-time hybridization kinetics studies using imaging with confocal fluorescence microscopy.[30] Signal accumulates at the spot periphery initially, increasing radially towards the spot center over time. Target mass transport also depends on target concentration, diffusion coefficients of target solutions, and probe-target combinations.[184, 185] This validates the radial planar diffusion mechanism kinetically. However, recent studies have indicated that the droplet drying artifacts are caused initially during probe immobilization (specifically during printing), further influencing target hybridization.[30, 50] Improving the uniformity of probe coverage across each spot feature could improve assay signal consistency at any given assay endpoint, even prior to target saturation.

Drying conditions for printed DNA droplets on a surface are proposed to result from competition between the dominant effects of coffee ring versus Marangoni droplet drying patterns.[50] Dugas et al. studied the effect of DNA droplet drying on hydrophobic flat surfaces and proposed that droplets flatten with a constant contact area, and then the droplet shrinks at a constant contact angle.[57] These results produce variations in diameters and morphologies for thousands of spots deposited on microarray surfaces that are not uniform since their local wetting/spreading and resulting drying behaviors are nonuniform from submicron variabilities in solid support chemistry. If surfaces exhibit sufficiently uniform chemistry, then control of some physicochemical properties (wetting, evaporation rate) of the droplet allows formation of well-controlled spots compatible with DNA grafting.

Further intraspot and spot-to-spot heterogeneity with different concentrations of both total DNA and fraction of dye-labeled DNA can be explained from spot drying behavior in the presence of DNA-bound signal dyes, surfactants, and dissolved salts.[57, 99] Evaporation kinetics for droplets containing DNA varied as a function of DNA concentration. Drops containing very low DNA concentrations dried by maintaining a constant base area (pinning),[56] whereas those with high concentration dried with a constant contact angle.[96] Fang et al. showed with confocal and

rheologic studies that in the case of high concentration droplets, the DNA droplet formed a shell and low DNA concentrations resulted in isolated island formation.[56] Various efforts to resolve the discrepancy in interspot DNA dried spots to increase the relative humidity from 40-80% and also varying the surfactant such as betaine and co-solvent DMSO. McQuain et al. optimized the concentration of the surfactant to 1.5M betaine and maintaining the relative humidity at 60%, reduced interspot and intraspot variations.[186] More specifically, addition of anionic surfactant (e.g., SDS) initially facilitates uniform droplet spreading and stabilizes the drop evaporation, drastically altering the “coffee ring effect”. Surfactant-driven Marangoni flows arise when the local surfactant concentration at the pinned contact line increases due to the coffee ring effect, thereby decreasing the local surface tension and inducing Marangoni flow towards the spot center.[187] The extent of circular Marangoni flow is influenced by variation of SDS concentration along the air-water interface.[188] The mode of evaporation can be influenced by the presence of salts with the DNA probe deposition patterns following the salting trace.[57] Schematics of DNA droplet drying in the presence of salt and buffer leading to either coffee-ring or Marangoni droplet drying phenomena are shown in Figure 1.6.

Phase separation upon drying, producing salt crystallization in evaporating droplets of DNA solutions containing salts, occurs as well.[189, 190] Exceeding the local solubility limit of salts in evaporating droplets leads to rich morphologies of deposited salt crystals and DNA. Formation of radially varying salt concentration yields deposited rings with spacing between the concentric rings that depends on the DNA concentration and ion species concentration.[190] Marangoni inward flow of solution produces various salt patterns with deposition of the DNA-dye in concentric pattern in the spot.[191] The physicochemical properties of the evaporating DNA solution are influenced by the dynamic changes in DNA concentration, ionic strength, and surfactant concentration, influencing the final dried DNA patterns.[57] Theoretical and experimental results conclude that at low concentrations of salt, the deposit becomes more uniform, covering the entire surface beneath the droplet, whereas at higher concentration, salt deposits appear predominantly along the outer rim of the spot.[190] At lower DNA concentration, DNA at the liquid-vapor interface is deposited at the droplet edge during initial evaporation stages, and eventually

under developing Marangoni flow, transitions to deposition of DNA aggregates at the spot centers. Hence, periodic patterning is less dominant at very low concentrations due to reduced spreading. Nonetheless, drying of many DNA droplets containing mixtures of DNA, surfactants, and dissolved salts undergo phase separation. Despite the use of nonionic/zwitterionic surfactants to limit DNA probe interactions, DNA segregation[57] can occur into two phases on drying: one enriched in DNA and another in surfactant, leading to another form of phase segregation upon drying and formation of a DNA precipitate with increasing electrolyte and surfactant concentration upon evaporation.[191-193] Furthermore, supersaturated salt conditions promote DNA phase separation.[57, 190] Precipitation occurs at very low concentrations of both DNA and surfactant, and is further enhanced in the presence of electrolytes.[182, 193-195] Similar aggregation is predominant at higher DNA concentrations (i.e., micromolar to molar)[53] and with dye labeled DNA oligomers.[196] It is likely that such concentrations are achieved within droplets within a few seconds of printing due to water evaporation with rapid drying.

Furthermore, cyanine dyes analogous to Cy-3 are known to readily form molecular aggregates in aqueous media.[197] Cyanine dyes are also known to interact with dsDNA in aqueous media through various interactions, either by intercalation, minor groove binding between base pairs, or dye-dye aggregation.[53, 197, 198] Cyanine dye aggregation is also reported in Langmuir-Blodgett monolayer of amphiphilic nucleic acids during evaporation rates controlled by mass transfer across the aqueous-film-air interface.[199] In cyanine dye-labeled single-strand probe DNA, dye–dye interactions and dye–nucleotide aggregations in the presence of increasing ionic strength and surfactant concentrations reduce probe stability and quench fluorescence.[88, 170, 196] Singly labeled fluorescent DNA probes exhibit dye–DNA interactions as studied by fluorescence anisotropy and lifetime assays.[196] As Cy3-DNA content increases in print solutions up to 100% DNA mass fraction, DNA aggregation is seen to be much more predominant, increasing dye quenching and reducing fluorescence intensity. Hence, DNA-dye aggregates are found predominately at spot centers, and fewer Cy3-DNA probes deposit at droplet edges.

As various factors affect droplet drying morphology such as DNA concentration, temperature, humidity, buffer, salts, and dye-labels, efforts to alter microdroplet footprint shape on

surfaces have recently gained attention. Yunker et al.[178] and Weon et al.[179] altered droplet shape to obtain uniform droplet drying. Polymer "liftoff" arrays combine the hydrophobic surface properties of di-p-xylylene (Parylene) with photolithographically etched hydrophilic openings within the polymer to control the spot morphology [200] and uniformity of deposition.[201] Manipulating the surface wetting properties, mixing of the droplet with frequency dependent oscillating flow[202] to alter flow pattern of the evaporating droplet, and the electrowetting[203] technique driven microfluidic flows allow suppression of the coffee ring for colloidal suspensions of variable concentration and particle size. The global objective of these strategies is to modify and perhaps control DNA probe deposition physics on surfaces, specifically to affect immobilization density and lateral distributions within dried DNA spots for assay.

The spatial distribution of probes is heterogeneous and chemical imaging now enables the local density of probes should be monitored. The physical properties of an ensemble of same sequence strands of nucleic acids may show a range of hybridization phases, dependent on the density of probes, the ionic concentration, electrostatic distributions, and other characteristics.[204] Therefore, understanding of DNA grafting density and DNA probe chain conformation is important in the design of microarray for efficient target binding. Furthermore, the behavior of grafted chains affect the chain confirmation due to neighbor interactions should be accounted. The assay signal generation is an important end point result is highly dependent on careful design of the probe density, probe length and spacing and target hybridization with their partners. The important aspect of lesser probe density leading to lower signal and at higher grafting density due to Coulombic blockade leading to lower signal should be optimized with appropriate density based on signal and hybridization parameter (kinetics, and thermodynamics). The understanding of the bulk-to-surface behavior of the probes and the hybridization thermodynamics and kinetics is the vital factor in designing microarrays. Extensive theoretical, experimental, and computational comparisons are known for DNA hybridization in solutions, but substantially less is known or practically available for modeling in various DNA tethered states.

1.4 Conclusions

DNA microarrays have been used extensively for more than a decade in numerous forms. However, the high variability in the design parameters of probes, surfaces, targets, and types of immobilization (different platforms) has led to challenges in obtaining reproducible and reliable assay results, particularly those that produce reliable answer directly from samples without PCR amplification, or whose signals reflect target absolute abundance (i.e., quantitative output). The coordinated probe and substrate design techniques for “grafting to”, and “grafting from” ssDNA probes, and spot deposition methods have their limitations in attaining uniform ssDNA probe grafting efficiency and probe density. These result in microarrays with deficiencies in the resulting assay metrics, reproducibility, and reliability as a diagnostic format. The biophysical aspects of DNA molecular mechanics, conformations, control, and stability of surface-tethered states in local environments, interactions with the surface and with neighboring probes, and with high ionic strength environments in duplex formations all impacts the array behavior and assay answer. These factors need to be thoroughly evaluated in surface spotted format since there is no direct translation of bulk DNA characteristics to surface-tethered DNA properties. Common polymer physical parameters such as radius of gyration, persistence length, DNA elasticity, flexibility, and chain conformational mechanics have not been investigated in detail for either surface-tethered ssDNA or dsDNA. ssDNA chain accessibility on surfaces that determines target binding and ultimately array performance is determined by local tethered flexibility and conformations based on DNA sequence, electrostatic interactions, media influences, and surface immobilization technique.

Though various theoretical and experimental approaches seek to explain DNA surface behavior with optical, fluorescent, and force spectroscopies, several discrepancies persist for explaining DNA flexibility vs. stiffness at surfaces. DNA chain conformations effects due to phosphate backbone charges and base stacking are still unresolved. WLC remains the widely accepted classic model for understanding DNA molecular mechanics despite its several shortcomings. Extensive improvements have been made to the WLC model to accommodate DNA bending angles and chain flexibility. Various molecular dynamics simulations and other

models have been developed to attempt to correlate and supplement the shortcomings of WLC. The newly developed coarse-grained approach is widely accepted for treating DNA as an inextensible elastic rod, and despite lacking atomic details, is accurate for thousands of base pairs down to few hundred. However, its applicability remains controversial for short DNA molecules with persistence lengths of less than 1nm.

Studies of physical structure and biophysical properties of DNA as well as their extensions to short immobilized ssDNA probes at surfaces have proven useful in understanding current issues. The process of DNA hybridization at surfaces is a critical part of DNA-based array technology. Addressing the future improvements, development, and fabrication of microarrays, also in designing new applications will require further knowledge of DNA as tethered chains and how its duplexation behavior is controlled kinetically and thermodynamically under assay conditions. The complexity of this more fundamental task is compounded by the large number of reported protocols for preparing and functionalizing surfaces for DNA microarray use in practical assay deployment. Polyelectrolyte brush theories help elucidate target-probe interactions, media, and substrate effects, providing additional information to analyze the effects of immobilized DNA probe density on the thermodynamics and kinetics of DNA hybridization on array surfaces. As the kinetics and thermodynamics of immobilized molecules located farther away from the solid support can approach those in solution states, the utility of introducing spacer chains for ssDNA immobilization is exploited but largely from an empirical perspective. The beneficial role of spacers is generally recognized, but a coherent view of their optimal design and underlying physics has not been presented. Accurate measurement of probe surface coverage, a parameter crucial for determination of efficiencies of immobilization and hybridization protocols, is extremely difficult. More careful evaluation for hybridization isotherms and hybridization rate constants for different platforms are required to understand DNA microarray performance. Only with clear elucidation of molecular mechanisms surrounding DNA duplex formation on tethering surfaces and sources of its variability will the nucleic acid microarray approach move to standardization, and even toward rigorous quantitative answers required for their clinical translation.

1.5 Acknowledgments

The authors acknowledge support for this work from NIH R01 EB001473 and technical input from V. Hlady and J. Herron (University of Utah).

Table 1.1 Important considerations for improving the design and development of nucleic acid microarrays

Microarray Methods	Major hurdles	Ref
Microarray design	Addressing the biological question with selection of proper controls, fiduciary markers, internal calibrations, quality controls	58, 205, 206
Experimental processing	Probe immobilization, target preparation from complex milieu and reliable hybridization, sample-to-answer time efficiencies, signal: noise challenges	1, 17, 21
Data extraction	Assay (e.g., fluorescence) signal translation for quantification of gene of interest, absolute abundance correlations, reliable quantitation, platform-platform correlation	207-210
Data analysis and modeling	Standardized, validated bioinformatics and biostatistics algorithms	211-213
Data repeatability and reproducibility	MAQC-I,-II and -III-identified optimization, reliability, intra- and interplatform reproducibility issues	1313, 214, 215
Limited database access	access to web-based data-mining platforms aimed at facilitating discovery from genome-wide expression analyses	10, 216, 217

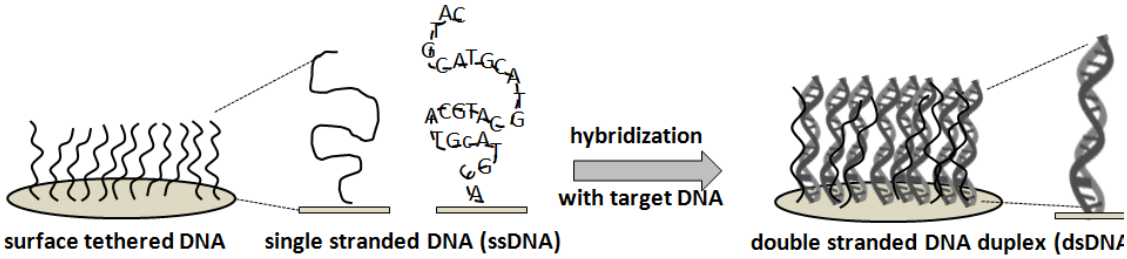

Figure 1.1 Single-strand DNA-probe immobilization and double strand target hybridization at surfaces: the working principle for DNA microarrays as surface-capture assays. (Reference 23)

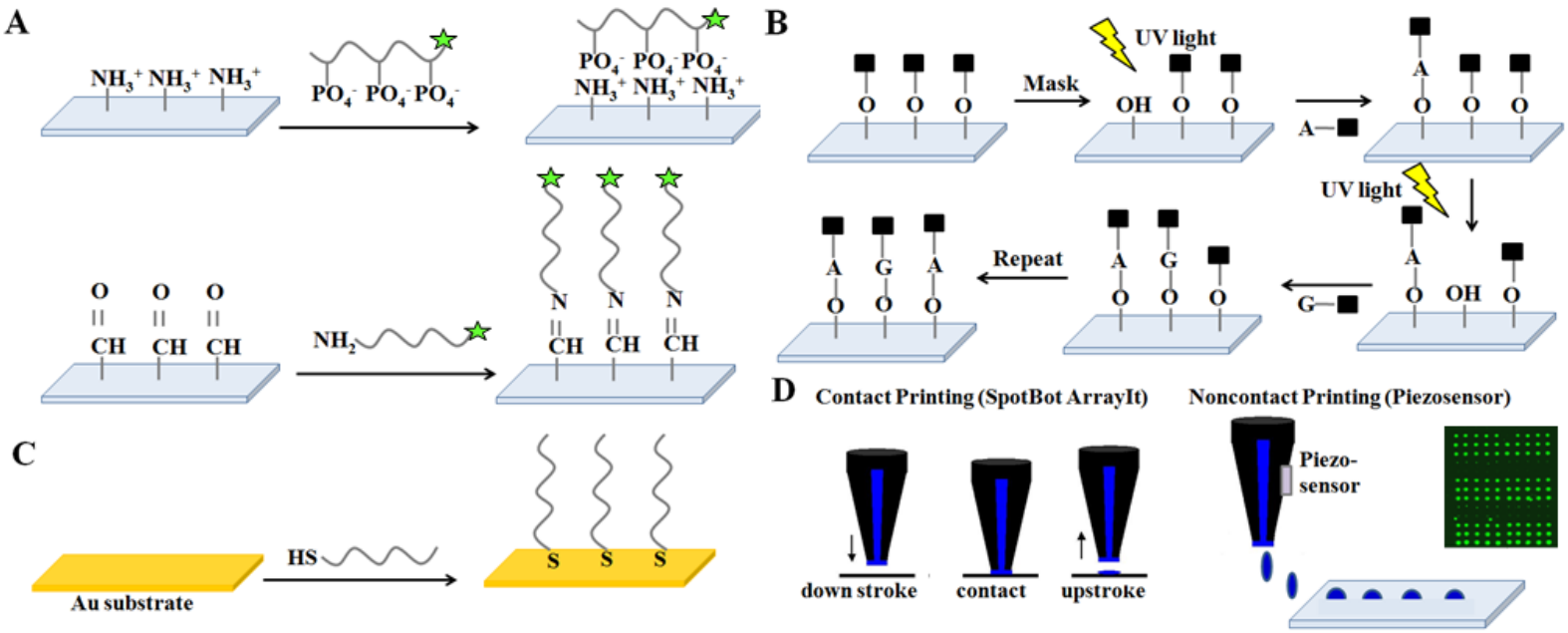

Figure 1.2. General methods to fabricate DNA arrays. A) "Grafting to": probe DNA surface immobilization by electrostatic interactions: DNA binding to amine-derivatized surfaces by ionic interactions between cationic primary amine surface groups and anionic DNA phosphate groups. Alternatively, covalent "grafting to": probe DNA immobilization by Schiff base reactions using amine-modified DNA and aldehyde-derivatized surfaces. Other amine-reactive chemistries are also popular. B) "Grafting from": photochemical, spatially controlled (e.g., Affymetrix Genechip™, NimbleGen) probe fabrication by *in situ* synthesis using sequential photoactivation and deprotection of nucleic acids. Photomask or maskless UV irradiation over localized surface regions selectively activates nucleotides that react with growing chains ends on surfaces, producing patterned arrays with predetermined DNA chain chemical diversity, and at high density. C) "Grafting to" using chemisorption of thiolated DNA probe oligomers on coinage metal substrates via metal-thiolate bonds. D) Micro/nano droplet contact and noncontact (e.g., piezo) printing of DNA probe solutions in defined array patterns, with subsequent droplet drying and immobilization by both physical and chemical reactions with surfaces.

Table 1.2. DNA feature sizes and probe densities for the various array fabrication methods

Surface	Area	Probe density/cm^2
Gold	100 μm diameter spot	5×10^{12}
Amine modified surface	4.5mm diameter spot	2.5×10^{12}
Photolithography	5-10 μm	10^6

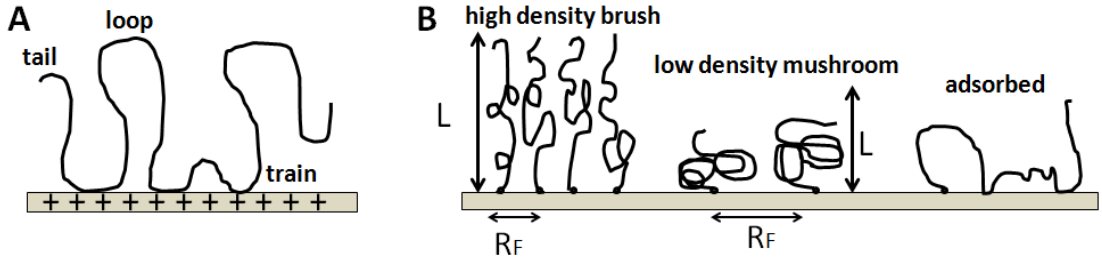

Figure 1.3. Schematics of DNA chain adsorption conformation on surfaces. A) Interaction of DNA with the substrate leading to tail, loop, and train sections of the adsorbed chain; B) Surface-tethered DNA chains can form either "mushroom"-like or "brush"-like molecular conformations, depending on grafting density. For very low grafting density, the DNA chain lies flat on the surface.

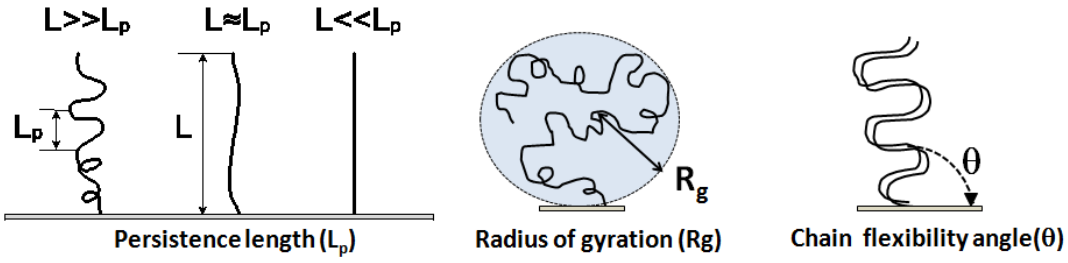

Figure 1.4. Persistence length, radius of gyration, and chain flexibility angle for immobilized ssDNA and dsDNA tethered ideally on surfaces.

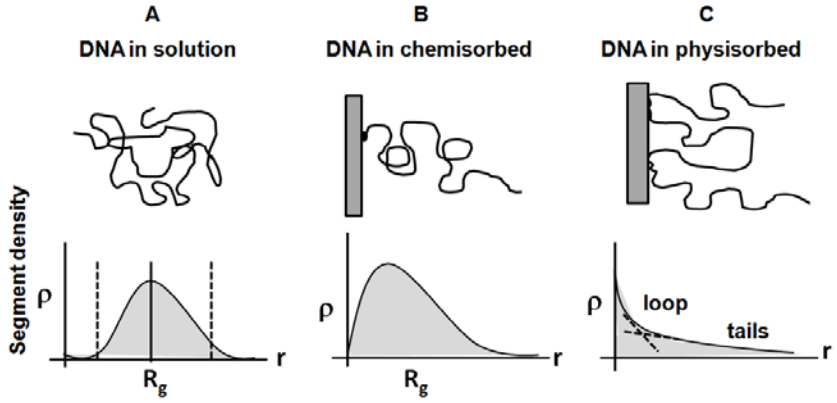

Figure 1.5. Schematic description of DNA segmental distribution as a function of distance from the surface. A) DNA in solution. B) DNA chemisorbed (chemically end-tethered) and DNA physisorbed forming tails, loops, and trains. (Reference 34)

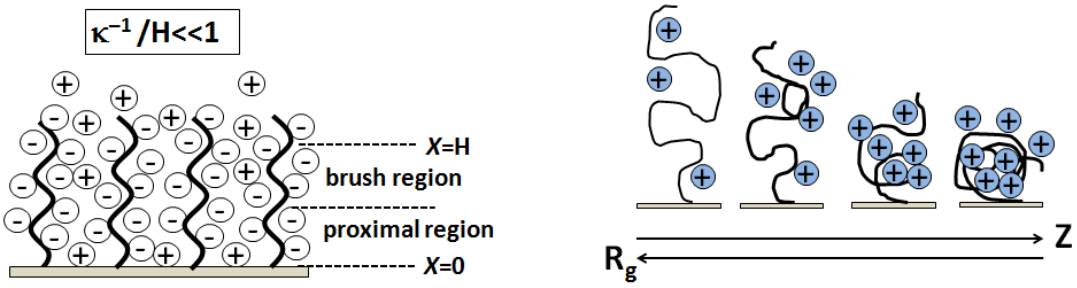

Figure 1.6. Surface coulombic blockade of target DNA by immobilized ssDNA (polyanion theory) due to DNA nucleotide phosphate anions and their Debye length dependence (κ^{-1}) (left), and the effect of increasing ionic strength on the DNA polyanion radius of gyration (R_g) (right). (Reference 95)

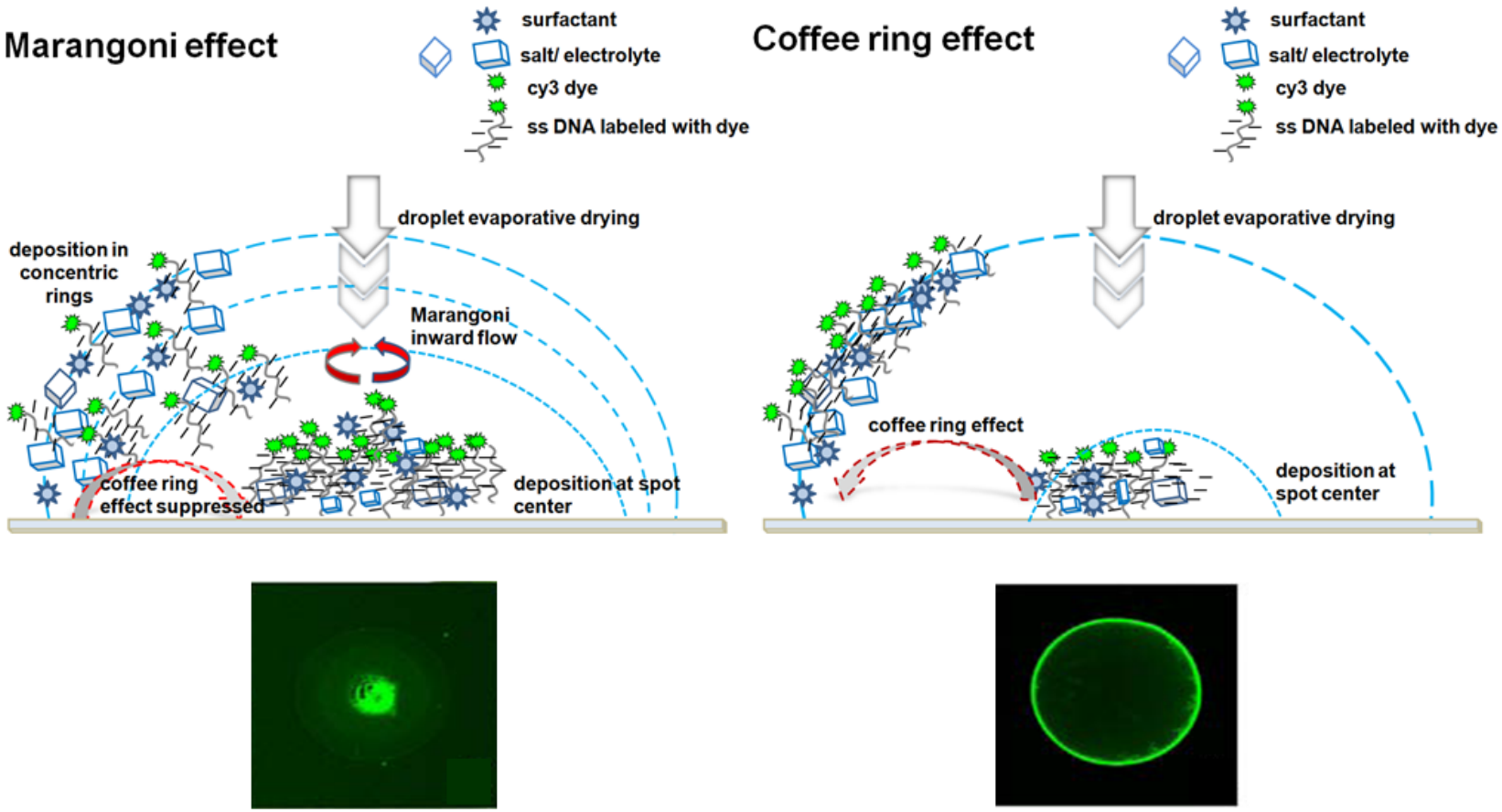

Figure 1.7. DNA droplet drying phenomena: Marangoni (left) vs. coffee ring effect (right) for printed spots. Fluorescent images of the respective effects are shown below.

1.6 References

1. Heller, M. J., DNA microarray technology: Devices, systems, and applications. 2002; Vol. 4, pp 129-153.

2. Hoheisel, J. D., *Nature Reviews Genetics* **2006,** *7* (3), 200-210.

3. Bulyk, M. L., *Current Opinion in Biotechnology* **2006,** *17* (4), 422-430.

4. Gresham, D.; Dunham, M. J.; Botstein, D., *Nature Reviews Genetics* **2008,** *9* (4), 291-302.

5. Evans, W. E.; Relling, M. V., *Nature* **2004,** *429* (6990), 464-468.

6. Bryant, P. A.; Venter, D.; Robins-Browne, R.; Curtis, N., *Lancet Infectious Diseases* **2004,** *4* (2), 100-111.

7. Kononen, J.; Bubendorf, L.; Kallioniemi, A.; Bärlund, M.; Schraml, P.; Leighton, S.; Torhorst, J.; Mihatsch, M. J.; Sauter, G.; Kallioniemi, O. P., *Nature Medicine* **1998,** *4* (7), 844-847.

8. Sobrino, B.; Brión, M.; Carracedo, A., *Forensic Science International* **2005,** *154* (2-3), 181-194.

9. Lobenhofer, E. K.; Bushel, P. R.; Afshari, C. A.; Hamadeh, H. K., *Environmental Health Perspectives* **2001,** *109* (9), 881-892.

10. Stears, R. L.; Martinsky, T.; Schena, M., *Nature Medicine* **2003,** *9* (1), 140-145.

11. Pusztai, L., *Clinical Cancer Research* **2006,** *12* (24), 7209-7214.

12. Li, X.; Quigg, R. J.; Zhou, J.; Gu, W.; Nagesh Rao, P.; Reed, E. F., *Current Genomics* **2008,** *9* (7), 466-474.

13. Shi, L., *Nature Biotechnology* **2006,** *24* (9), 1151-1161.

14. Ji, H.; Davis, R. W., *Nature Biotechnology* **2006,** *24* (9), 1112-1113.

15. Lundeberg, J.; Klevebring, D.; Gry, M.; Lindberg, J.; Eidefors, A., *Journal of Biomedicine and Biotechnology* **2009,** *2009*.

16. Šášik, R.; Woelk, C. H.; Corbeil, J., *Journal of Molecular Endocrinology* **2004,** *33* (1), 1-9.

17. Tseng, G. C.; Oh, M. K.; Rohlin, L.; Liao, J. C.; Wong, W. H., *Nucleic Acids Research* **2001,** *29* (12), 2549-2557.

18. Hess, K. R.; Zhang, W.; Baggerly, K. A.; Stivers, D. N.; Coombes, K. R.; Zhang, W., *Trends in Biotechnology* **2001,** *19* (11), 463-468.

19. Peters, J. P.; Maher, L. J., *Quarterly Reviews of Biophysics* **2010,** *43* (1), 23-63.

20. Schena, M., *Microarray analysis*. Wiley-Liss Hoboken, NJ: 2003.

21. Barbulovic-Nad, I.; Lucente, M.; Sun, Y.; Zhang, M.; Wheeler, A. R.; Bussmann, M., *Critical Reviews in Biotechnology* **2006,** *26* (4), 237-259.

22. Gong, P.; Grainger, D. W., *Microarrays: Methods in Molecular Biology-Methods and Protocols*. 2007.

23. Duggan, D. J.; Bittner, M.; Chen, Y.; Meltzer, P.; Trent, J. M., *Nature Genetics* **1999,** *21* (1 SUPPL.), 10-14.

24. Wu, P.; Castner, D. G.; Grainger, D. W., *Journal of Biomaterials Science, Polymer Edition* **2008,** *19* (6), 725-753.

25. Chowdhury, E. H.; Akaike, T., *Case studies-Development of oligonucleotides*. Wiley-interscience: Cary, North Carolina, 2007.

26. Dandy, D. S.; Wu, P.; Grainger, D. W., *Proceedings of the National Academy of Sciences of the United States of America* **2007,** *104* (20), 8223-8228.

27. Peterson, A. W.; Heaton, R. J.; Georgiadis, R. M., *Nucleic Acids Research* **2001,** *29* (24), 5163-5168.

28. Liu, R. H.; Yang, J.; Lenigk, R.; Bonanno, J.; Grodzinski, P., *Analytical Chemistry* **2004,** *76* (7), 1824-1831.

29. Gong, P.; Grainger, D. W., *Surface Science* **2004,** *570* (1-2), 67-77.

30. Rao, A. N.; Rodesch, C. K.; Grainger, D. W., *Analytical Chemistry* **2012,** *84* (21), 9379-9387.

31. Rao, A. N.; Vandencasteele, N.; Gamble, L. J.; Grainger, D. W., *Analytical Chemistry* **2012,** *84* (24), 10628-10636.

32. Ramakrishnan, R.; Dorris, D.; Lublinsky, A.; Nguyen, A.; Domanus, M.; Prokhorova, A.; Gieser, L.; Touma, E.; Lockner, R.; Tata, M.; Zhu, X.; Patterson, M.; Shippy, R.; Sendera, T. J.; Mazumder, A., *Nucleic Acids Research* **2002,** *30* (7).

33. Dai, H.; Meyer, M.; Stepaniants, S.; Ziman, M.; Stoughton, R., *Nucleic Acids Research* **2002,** *30* (16).

34. Halperin, A.; Buhot, A.; Zhulina, E. B., *Journal of Physics Condensed Matter* **2006,** *18* (18), S463-S490.

35. Gong, P.; Lee, C. Y.; Gamble, L. J.; Castner, D. G.; Grainger, D. W., *Analytical Chemistry* **2006,** *78* (10), 3326-3334.

36. Venkatasubbarao, S., *Trends Biotechnol* **2004,** *22* (12), 630-7.

37. Conti, M.; Bustanji, Y.; Falini, G.; Ferruti, P.; Stefoni, S.; Samorì, B., *ChemPhysChem* **2001,** *2* (10), 610-613.

38. Paleček, E., *Bioelectrochemistry and Bioenergetics* **1986,** *15* (2), 275-295.

39. Dias, R. S.; Pais, A. A. C. C.; Linse, P.; Miguel, M. G.; Lindman, B., *Journal of Physical Chemistry B* **2005,** *109* (23), 11781-11788.

40. Stillman, B. A.; Tonkinson, J. L., *BioTechniques* **2000,** *29* (3), 630-635.

41. Grainger, D. W.; Greef, C. H.; Gong, P.; Lochhead, M. J., Current Microarray Surface chemistry. In *Microarrays Volume-1 Synthesis Methods*, Rampal, J. B., Ed. Humana Press: 2007; pp 37-58.

42. Halperin, A.; Buhot, A.; Zhulina, E. B., *Biophysical Journal* **2005,** *89* (2), 796-811.

43. Lee, C. Y.; Gong, P.; Harbers, G. M.; Grainger, D. W.; Castner, D. G.; Gamble, L. J., *Analytical Chemistry* **2006,** *78* (10), 3316-3325.

44. Cheng, F.; Gamble, L. J.; Castner, D. G., *Analytical Chemistry* **2008,** *80* (7), 2564-2573.

45. Steven W. Metzger, M. J. L., and David W. Grainger, **2002**.

46. Sassolas, A.; Leca-Bouvier, B. D.; Blum, L. J., *Chemical Reviews* **2008,** *108* (1), 109-139.

47. Dufva, M., *Biomolecular Engineering* **2005,** *22* (5-6), 173-184.

48. Fielden, M. R.; Halgren, R. G.; Dere, E.; Zacharewski, T. R., *Bioinformatics* **2002,** *18* (5), 771-773.

49. Levicky, R.; Horgan, A., *Trends in Biotechnology* **2005,** *23* (3), 143-149.

50. Rao, A. N.; Vandencasteele, N.; Gamble, L. J.; Grainger, D. W., *Analytical Chemistry* **2012**, Just accepted.

51. Dudley, A. M.; Aach, J.; Steffen, M. A.; Church, G. M., *Proceedings of the National Academy of Sciences of the United States of America* **2002,** *99* (11), 7554-7559.

52. Steel, A. B.; Levicky, R. L.; Herne, T. M.; Tarlov, M. J., *Biophysical Journal* **2000,** *79* (2), 975-981.

53. Seifert, J. L.; Connor, R. E.; Kushon, S. A.; Wang, M.; Armitage, B. A., *Journal of the American Chemical Society* **1999,** *121* (13), 2987-2995.

54. Randolph, J. B.; Waggoner, A. S., *Nucleic Acids Research* **1997,** *25* (14), 2923-2929.

55. Allemand, J. F.; Bensimon, D.; Lavery, R.; Croquette, V., *Proceedings of the National Academy of Sciences of the United States of America* **1998,** *95* (24), 14152-14157.

56. Fang, X.; Li, B.; Petersen, E.; Seo, Y. S.; Samuilov, V. A.; Chen, Y.; Sokolov, J. C.; Shew, C. Y.; Rafailovich, M. H., *Langmuir* **2006,** *22* (14), 6308-6312.

57. Dugas, V.; Broutin, J.; Souteyrand, E., *Langmuir* **2005,** *21* (20), 9130-9136.

58. Schena, M.; Heller, R. A.; Theriault, T. P.; Konrad, K.; Lachenmeier, E.; Davis, R. W., *Trends in Biotechnology* **1998,** *16* (7), 301-306.

59. Strick, T. R.; Allemand, J. F.; Bensimon, D.; Croquette, V., *Biophysical Journal* **1998,** *74* (4), 2016-2028.

60. Strick, T. R.; Allemand, J. F.; Bensimon, D.; Bensimon, A.; Croquette, V., *Science* **1996,** *271* (5257), 1835-1837.

61. Smith, S. B.; Cui, Y.; Bustamante, C., *Science* **1996,** *271* (5250), 795-9.

62. Wang, M. D.; Yin, H.; Landick, R.; Gelles, J.; Block, S. M., *Biophys J* **1997,** *72* (3), 1335-46.

63. Bouchiat, C.; Wang, M. D.; Allemand, J. F.; Strick, T.; Block, S. M.; Croquette, V., *Biophysical Journal* **1999,** *76* (1 I), 409-413.

64. Brinkers, S.; Dietrich, H. R. C.; De Groote, F. H.; Young, I. T.; Rieger, B., *Journal of Chemical Physics* **2009,** *130* (21).

65. Bustamante, C.; Smith, S. B.; Liphardt, J.; Smith, D., *Current Opinion in Structural Biology* **2000,** *10* (3), 279-285.

66. Baumann, C. G.; Smith, S. B.; Bloomfield, V. A.; Bustamante, C., *Proceedings of the National Academy of Sciences of the United States of America* **1997,** *94* (12), 6185-6190.

67. Odijk, T., *J Polym Sci Polym Phys Ed* **1977,** *15* (3), 477-483.

68. Skolnick, J.; Fixman, M., *Macromolecules* **1977,** *10* (5), 944-948.

69. Kirste, R. G., *Discussions of the Faraday Society* **1970,** *49*, 51-59.

70. Kuznetsov, S. V.; Shen, Y.; Benight, A. S.; Ansari, A., *Biophysical Journal* **2001,** *81* (5), 2864-2875.

71. Tinland, B.; Pluen, A.; Sturm, J.; Weill, G., *Macromolecules* **1997,** *30* (19), 5763-5765.

72. Rekesh, D.; Lyubchenko, Y.; Shlyakhtenko, L. S.; Lindsay, S. M., *Biophysical Journal* **1996,** *71* (2), 1079-1086.

73. Mucic, R. C.; Herrlein, M. K.; Mirkin, C. A.; Letsinger, R. L., *Chemical Communications* **1996,** (4), 555-557.

74. Latulippe, D. R.; Zydney, A. L., *Biotechnology and Bioengineering* **2010,** *107* (1), 134-142.

75. De Gennes, P. G., *Macromolecules* **1980,** *13* (5), 1069-1075.

76. Halperin, A.; Buhot, A.; Zhulina, E. B., *Langmuir* **2006,** *22* (26), 11290-11304.

77. Adamuti-Trache, M.; McMullen, W. E.; Douglas, J. F., *Journal of Chemical Physics* **1996,** *105* (11), 4798-4811.

78. Lehner, R.; Koota, J.; Maret, G.; Gisler, T., *Physical review letters* **2006,** *96* (10).

79. Manning, G. S., *Quarterly Reviews of Biophysics* **1978,** *11* (2), 179-246.

80. Schurr, J. M.; Allison, S. A., *Biopolymers - Peptide Science Section* **1981,** *20* (2), 251-268.

81. Schurr, J. M.; Fujimoto, B. S., *Biophysical Chemistry* **2002,** *101-102*, 425-445.

82. Schurr, J. M., *RSC Biomolecular Sciences* **2009,** (Nucleic Acid–Metal Ion Interactions), 307–349.

83. Manning, G. S.; Ebralidse, K. K.; Mirzabekov, A. D.; Rich, A., *Journal of Biomolecular Structure and Dynamics* **1989,** *6* (5), 877-889.

84. Savelyev, A.; Materese, C. K.; Papoian, G. A., *Journal of the American Chemical Society* **2011,** *133* (48), 19290-19293.

85. Williams, L. D.; Maher Iii, L. J., Electrostatic mechanisms of DNA deformation. 2000; Vol. 29, pp 497-521.

86. Moulaei, T.; Maehigashi, T.; Lountos, G. T.; Komeda, S.; Watkins, D.; Stone, M. P.; Marky, L. A.; Li, J. S.; Gold, B.; Williams, L. D., *Biochemistry* **2005,** *44* (20), 7458-7468.

87. Vainrub, A.; Pettitt, B. M., *Physical Review E - Statistical, Nonlinear, and Soft Matter Physics* **2002,** *66* (4), 041905/1-041905/4.

88. Nazarenko, I.; Pires, R.; Lowe, B.; Obaidy, M.; Rashtchian, A., *Nucleic Acids Research* **2002,** *30* (9), 2089-2095.

89. Goddard, N. L.; Bonnet, G.; Krichevsky, O.; Libchaber, A., *Physical review letters* **2000,** *85* (11), 2400-2403.

90. Coleman, B. D.; Olson, W. K.; Swigon, D., *Journal of Chemical Physics* **2003,** *118* (15), 7127-7140.

91. Vasiliskov, V. A.; Prokopenko, D. V.; Mirzabekov, A. D., *Nucleic Acids Research* **2001,** *29* (11), 2303-2313.

92. Nguyen, T. T.; Grosberg, A. Y.; Shklovskii, B. I., *Journal of Chemical Physics* **2000,** *113* (3), 1110-1125.

93. Vainrub, A.; Pettitt, B. M., *Chemical Physics Letters* **2000,** *323* (1-2), 160-166.

94. Netz, R. R.; Andelman, D., *Physics Reports* **2003,** *380* (1-2), 1-95.

95. Strick, T.; Allemand, J. F.; Croquette, V.; Bensimon, D., *Progress in Biophysics and Molecular Biology* **2000,** *74* (1-2), 115-140.

96. Moroz, J. D.; Nelson, P., *Proceedings of the National Academy of Sciences of the United States of America* **1997,** *94* (26), 14418-14422.

97. Zhang, J.; Lang, H. P.; Yoshikawa, G.; Gerber, C., *Langmuir* **2012,** *28* (15), 6494-6501.

98. Marko, J. F.; Siggia, E. D., *Macromolecules* **1995,** *28* (26), 8759-8770.

99. Cluzel, P.; Lebrun, A.; Heller, C.; Lavery, R.; Viovy, J. L.; Chatenay, D.; Caron, F., *Science* **1996,** *271* (5250), 792-794.

100. Cloutier, T. E.; Widom, J., *Proceedings of the National Academy of Sciences of the United States of America* **2005,** *102* (10), 3645-3650.

101. Murphy, M. C.; Rasnik, I.; Cheng, W.; Lohman, T. M.; Ha, T., *Biophysical Journal* **2004,** *86* (4), 2530-2537.

102. Zhang, Y.; Zhou, H.; Ou-Yang, Z. C., *Biophysical Journal* **2001,** *81* (2), 1133-1143.

103. Hansma, H. G.; Kim, K. J.; Laney, D. E.; Garcia, R. A.; Argaman, M.; Allen, M. J.; Parsons, S. M., *Journal of Structural Biology* **1997,** *119* (2), 99-108.

104. Bezanilla, M.; Manne, S.; Laney, D. E.; Lyubchenko, Y. L.; Hansma, H. G., *Langmuir* **1995,** *11* (2), 655-659.

105. Frontali, C.; Dore, E.; Ferrauto, A.; Gratton, E.; Bettini, A.; Pozzan, M. R.; Valdevit, E., *Biopolymers - Peptide Science Section* **1979,** *18* (6), 1353-1373.

106. Hagerman, P. J., *Annual review of biophysics and biophysical chemistry* **1988,** *17*, 265-286.

107. Protozanova, E.; Yakovchuk, P.; Frank-Kamenetskii, M. D., *Journal of Molecular Biology* **2004,** *342* (3), 775-785.

108. Caserta, M.; Agricola, E.; Churcher, M.; Hiriart, E.; Verdone, L.; Di mauro, E.; Travers, A., *Nucleic Acids Research* **2009,** *37* (16), 5309-5321.

109. Morriss-Andrews, A.; Rottler, J.; Plotkin, S. S., *Journal of Chemical Physics* **2010,** *132* (3).

110. Ambia-Garrido, J.; Vainrub, A.; Pettitt, B. M., *Computer Physics Communications* **2010,** *181* (12), 2001-2007.

111. Rechendorff, K.; Witz, G.; Adamcik, J.; Dietler, G., *Journal of Chemical Physics* **2009,** *131* (9).

112. Crozier, P. S.; Stevens, M. J., *Journal of Chemical Physics* **2003,** *118* (8), 3855-3860.

113. Erts, D.; Polyakov, B.; Olin, H.; Tuite, E., *Journal of Physical Chemistry B* **2003,** *107* (15), 3591-3597.

114. Levicky, R.; Herne, T. M.; Tarlov, M. J.; Satija, S. K., *Journal of the American Chemical Society* **1998,** *120* (38), 9787-9792.

115. Bustamante, C.; Bryant, Z.; Smith, S. B., *Nature* **2003,** *421* (6921), 423-427.

116. Wang, J.; Rivas, G.; Cai, X.; Chicharro, M.; Parrado, C.; Dontha, N.; Begleiter, A.; Mowat, M.; Palecek, E.; Nielsen, P. E., *Analytica Chimica Acta* **1997,** *344* (1-2), 111-118.

117. Abels, J. A.; Moreno-Herrero, F.; Van Der Heijden, T.; Dekker, C.; Dekker, N. H., *Biophysical Journal* **2005,** *88* (4), 2737-2744.

118. Mastroianni, A. J.; Sivak, D. A.; Geissler, P. L.; Alivisatos, A. P., *Biophysical Journal* **2009,** *97* (5), 1408-1417.

119. Bryant, Z.; Stone, M. D.; Gore, J.; Smith, S. B.; Cozzarelli, N. R.; Bustamante, C., *Nature* **2003,** *424* (6946), 338-41.

120. Kratky, O.; Porod, G., *Journal of Colloid Science* **1949,** *4* (1), 35-70.

121. Rippe, K.; Von Hippel, P. H.; Langowski, J., *Trends in Biochemical Sciences* **1995,** *20* (12), 500-506.

122. Shimada, J.; Yamakawa, H., *Macromolecules* **1984,** *17* (4), 689-698.

123. Maddox, J., *Nature* **1995,** *375* (6526), 11.

124. Bensimon, D.; Simon, A. J.; Croquette, V. V.; Bensimon, A., *Physical review letters* **1995,** *74* (23), 4754-4757.

125. Van mameren, J.; Peterman, E. J. G.; Wuite, G. J. L., *Nucleic Acids Research* **2008,** *36* (13), 4381-4389.

126. Seol, Y.; Li, J.; Nelson, P. C.; Perkins, T. T.; Betterton, M. D., *Biophysical Journal* **2007,** *93* (12), 4360-4373.

127. Wiggins, P. A.; Nelson, P. C., *Physical Review E - Statistical, Nonlinear, and Soft Matter Physics* **2006,** *73* (3).

128. Rant, U.; Arinaga, K.; Scherer, S.; Pringsheim, E.; Fujita, S.; Yokoyama, N.; Tornow, M.; Abstreiter, G., *Proceedings of the National Academy of Sciences of the United States of America* **2007,** *104* (44), 17364-17369.

129. *Nature* **2011,** *477* (7365), 372-372.

130. Van Eijck, L.; Merzel, F.; Rols, S.; Ollivier, J.; Forsyth, V. T.; Johnson, M. R., *Physical review letters* **2011,** *107* (8).

131. Morii, T.; Mizuno, R.; Haruta, H.; Okada, T., *Thin Solid Films* **2004,** *464-465*, 456-458.

132. Nelson, P., *Biophysical Journal* **1998,** *74* (5), 2501-2503.

133. Marko, J. F., *Europhysics Letters* **1997,** *38* (3), 183-188.

134. Stasiak, A.; Di Capua, E., *Nature* **1982,** *299* (5879), 185-186.

135. Léger, J. F.; Romano, G.; Sarkar, A.; Robert, J.; Bourdieu, L.; Chatenay, D.; Marko, J. F., *Physical review letters* **1999,** *83* (5), 1066-1069.

136. Sarkar, A.; Léger, J. F.; Chatenay, D.; Marko, J. F., *Physical Review E - Statistical, Nonlinear, and Soft Matter Physics* **2001,** *63* (5 I), 519031-5190310.

137. Wenner, J. R.; Williams, M. C.; Rouzina, I.; Bloomfield, V. A., *Biophysical Journal* **2002,** *82* (6), 3160-3169.

138. Punkkinen, O.; Hansen, P. L.; Miao, L.; Vattulainen, I., *Biophysical Journal* **2005,** *89* (2), 967-978.

139. Manning, G. S., *The Journal of Chemical Physics* **1969,** *51* (3), 924-933.

140. Le Bret, M.; Zimm, B. H., *Biopolymers - Peptide Science Section* **1984,** *23* (2), 271-285.

141. Williams, M. C.; Wenner, J. R.; Rouzina, I.; Bloomfield, V. A., *Biophysical Journal* **2001,** *80* (2), 874-881.

142. Kamien, R. D.; Lubensky, T. C.; Nelson, P.; O'Hern, C. S., *Europhysics Letters* **1997,** *38* (3), 237-242.

143. Gore, J.; Bryant, Z.; Nöllmann, M.; Le, M. U.; Cozzarelli, N. R.; Bustamante, C., *Nature* **2006,** *442* (7104), 836-839.

144. Raghunathan, K.; Chenc, Y. F.; Blaty, J.; Juliar, B. A.; Milstein, J.; Meiners, J. C. In *Mechanics of DNA: Sequence dependent elasticity*, San Diego, CA, San Diego, CA, 2011.

145. Sheinin, M. Y.; Forth, S.; Marko, J. F.; Wang, M. D., *Physical review letters* **2011,** *107* (10).

146. Yang, Z.; Haijun, Z.; Zhong-Can, O. Y., *Biophysical Journal* **2000,** *78* (4), 1979-1987.

147. Hansma, H. G.; Laney, D. E.; Bezanilla, M.; Sinsheimer, R. L.; Hansma, P. K., *Biophysical Journal* **1995,** *68* (5), 1672-1677.

148. Gao, L.; Wu, J.; Gao, D.; Wu, J., *Applied Physics Letters* **2007,** *91* (11).

149. Gray, D. E.; Case-Green, S. C.; Fell, T. S.; Dobson, P. J.; Southern, E. M., *Langmuir* **1997,** *13* (10), 2833-2842.

150. Chrisey, L. A.; O'Ferrall, C. E.; Spargo, B. J.; Dulcey, C. S.; Calvert, J. M., *Nucleic Acids Research* **1996,** *24* (15), 3040-3047.

151. Levicky, R.; Koneripalli, N.; Tirrell, M.; Satija, S. K., *Macromolecules* **1998,** *31* (8), 2616-2621.

152. Herne, T. M.; Tarlov, M. J., *Journal of the American Chemical Society* **1997,** *119* (38), 8916-8920.

153. Peterlinz, K. A.; Georgiadis, R. M.; Herne, T. M.; Tarlov, M. J., *Journal of the American Chemical Society* **1997,** *119* (14), 3401-3402.

154. Kelley, S. O.; Barton, J. K.; Jackson, N. M.; McPherson, L. D.; Potter, A. B.; Spain, E. M.; Allen, M. J.; Hill, M. G., *Langmuir* **1998,** *14* (24), 6781-6784.

155. Rant, U.; Arinaga, K.; Tornow, M.; Yong, W. K.; Netz, R. R.; Fujita, S.; Yokoyama, N.; Abstreiter, G., *Biophysical Journal* **2006,** *90* (10), 3666-3671.

156. Moiseev, L.; Ünlü, M. S.; Swan, A. K.; Goldberg, B. B.; Cantor, C. R., *Proceedings of the National Academy of Sciences of the United States of America* **2006,** *103* (8), 2623-2628.

157. Shen, G.; Tercero, N.; Gaspard, M. A.; Varughese, B.; Shepard, K.; Levicky, R., *Journal of the American Chemical Society* **2006,** *128* (26), 8427-8433.

158. Bhanot, G.; Louzoun, Y.; Zhu, J.; DeLisi, C., *Biophysical Journal* **2003,** *84* (1), 124-135.

159. Guo, Z.; Guilfoyle, R. A.; Thiel, A. J.; Wang, R.; Smith, L. M., *Nucleic Acids Research* **1994,** *22* (24), 5456-5465.

160. Su, H. J.; Surrey, S.; McKenzie, S. E.; Fortina, P.; Graves, D. J., *Electrophoresis* **2002,** *23* (10), 1551-1557.

161. Hassibi, A.; Vikalo, H.; Riechmann, J. L.; Hassibi, B., *Nucleic Acids Res.* **2009,** *37* (20).

162. Toegl, A.; Kirchner, R.; Gauer, C.; Wixforth, A., *J. Biomol. Tech.* **2003,** *14* (3), 197-204.

163. Carletti, E.; Guerra, E.; Alberti, S., *Trends Biotechnol.* **2006,** *24* (10), 443-448.

164. Halperin, A. S.; Buhot, A.; Zhulina, E. B., *Biophysical Journal* **2004,** *86* (2), 718-730.

165. Livshits, M. A.; Mirzabekov, A. D., *Biophysical Journal* **1996,** *71* (5), 2795-2801.

166. Chan, V.; Graves, D. J.; McKenzie, S. E., *Biophysical Journal* **1995,** *69* (6), 2243-2255.

167. Forman, J. E.; Walton, I. D.; Stern, D.; Rava, R. P.; Trulson, M. O., Thermodynamics of Duplex Formation and Mismatch Discrimination on Photolithographically Synthesized Oligonucleotide Arrays. 1998; Vol. 682, pp 206-228.

168. Hagan, M. F.; Chakraborty, A. K., *Journal of Chemical Physics* **2004,** *120* (10), 4958-4968.

169. Naef, F.; Magnasco, M. O., *Physical Review E - Statistical, Nonlinear, and Soft Matter Physics* **2003,** *68* (1 1), 119061-119064.

170. Unruh, J. R.; Gokulrangan, G.; Lushington, G. H.; Johnson, C. K.; Wilson, G. S., *Biophysical Journal* **2005,** *88* (5), 3455-3465.

171. Chen, C.; Wang, W.; Ge, J.; Zhao, X. S., *Nucleic Acids Research* **2009,** *37* (11), 3756-3765.

172. Gao, Y.; Wolf, L. K.; Georgiadis, R. M., *Nucleic Acids Research* **2006,** *34* (11), 3370-3377.

173. Nguyen, T. H.; Hilton, J. P.; Lin, Q., *Microfluidics and Nanofluidics* **2009,** *6* (3), 347-362.

174. Perelaer, J.; Smith, P. J.; Wijnen, M. M. P.; Van Den Bosch, E.; Eckardt, R.; Ketelaars, P. H. J. M.; Schubert, U. S., *Macromolecular Chemistry and Physics* **2009,** *210* (5), 387-393.

175. Hu, H.; Larson, R. G., *Journal of Physical Chemistry B* **2006,** *110* (14), 7090-7094.

176. Bietsch, A.; Hegner, M.; Lang, H. P.; Gerber, C., *Langmuir* **2004,** *20* (12), 5119-5122.

177. Deegan, R. D.; Bakajin, O.; Dupont, T. F.; Huber, G.; Nagel, S. R.; Witten, T. A., *Nature* **1997,** *389* (6653), 827-829.

178. Yunker, P. J.; Still, T.; Lohr, M. A.; Yodh, A. G., *Nature* **2011,** *476* (7360), 308-311.

179. Weon, B. M.; Je, J. H., *Physical Review E - Statistical, Nonlinear, and Soft Matter Physics* **2010,** *82* (1).

180. Poulard, C.; Damman, P., *EPL (Europhysics Letters)* **2007,** *80*, 64001.

181. Gong, P.; Harbers, G. M.; Grainger, D. W., *Analytical Chemistry* **2006,** *78* (7), 2342-2351.

182. Lee, C. Y.; Harbers, G. M.; Grainger, D. W.; Gamble, L. J.; Castner, D. G., *Journal of the American Chemical Society* **2007,** *129* (30), 9429-9438.

183. Pappaert, K.; Ottevaere, H.; Thienpont, H.; Van Hummelen, P.; Desmet, G., *BioTechniques* **2006,** *41* (5), 609-616.

184. Erickson, D.; Liu, X.; Krull, U.; Li, D., *Analytical Chemistry* **2004,** *76* (24), 7269-7277.

185. Dandy, D. S.; Wu, P.; Grainger, D. W., *Proceedings of the National Academy of Sciences of the United States of America* **2007,** *104* (20), 8223-8228.

186. McQuain, M. K.; Seale, K.; Peek, J.; Levy, S.; Haselton, F. R., *Analytical Biochemistry* **2003,** *320* (2), 281-291.

187. Hu, H.; Larson, R. G., *The Journal of Physical Chemistry B* **2006,** *110* (14), 7090-7094.

188. Still, T.; Yunker, P. J.; Yodh, A., *Langmuir* **2012**.

189. Smalyukh, I. I.; Zribi, O. V.; Butler, J. C.; Lavrentovich, O. D.; Wong, G. C. L., *Physical review letters* **2006,** *96* (17), 177801.

190. Kaya, D.; Belyi, V.; Muthukumar, M., *The Journal of chemical physics* **2010,** *133*, 114905.

191. Truskett, V. N.; Stebe, K. J., *Langmuir* **2003,** *19* (20), 8271-8279.

192. Lee, K.; Ivanova, N.; Starov, V.; Hilal, N.; Dutschk, V., *Advances in colloid and interface science* **2008,** *144* (1-2), 54-65.

193. Dias, R.; Rosa, M.; Pais, A. C.; Miguel, M.; Lindman, B., *JOURNAL-CHINESE CHEMICAL SOCIETY TAIPEI* **2004,** *51* (3), 447-470.

194. Zanchetta, G.; Nakata, M.; Buscaglia, M.; Bellini, T.; Clark, N. A., *Proceedings of the National Academy of Sciences* **2008,** *105* (4), 1111.

195. Liu, F.; Yang, J.; Huang, L.; Liu, D., *Pharmaceutical Research* **1996,** *13* (11), 1642-1646.

196. Randolph, J. B.; Waggoner, A. S., *Nucleic Acids Research* **1997,** *25* (14), 2923.

197. Armitage, B. A., *DNA Binders and Related Subjects* **2005**, 55-76.

198. Ogul'chansky, T. Y.; Losytskyy, M. Y.; Kovalska, V.; Yashchuk, V.; Yarmoluk, S., *Spectrochimica Acta Part A: Molecular and Biomolecular Spectroscopy* **2001,** *57* (7), 1525-1532.

199. Lehmann, U., *Thin Solid Films* **1988,** *160* (1-2), 257-269.

200. Eral, H. B.; Augustine, D. M.; Duits, M. H. G.; Mugele, F., *Soft Matter* **2011,** *7* (10), 4954-4958.

201. Moran-Mirabal, J. M.; Tan, C. P.; Orth, R. N.; Williams, E. O.; Craighead, H. G.; Lin, D. M., *Analytical Chemistry* **2007,** *79* (3), 1109-1114.

202. Oh, J. M.; Legendre, D.; Mugele, F., *EPL* **2012,** *98* (3).

203. Larson, R. G., *Angewandte Chemie - International Edition* **2012,** *51* (11), 2546-2548.

204. Harrison, A.; Binder, H.; Buhot, A.; Burden, C. J.; Carlon, E.; Gibas, C.; Gamble, L. J.; Halperin, A.; Hooyberghs, J.; Kreil, D. P.; Levicky, R.; Noble, P. A.; Ott, A.; Pettitt, B. M.; Tautz, D.; Pozhitkov, A. E., *Nucleic Acids Research* **2013**.

205. Tomiuk, S.; Hofmann, K., *Briefings in bioinformatics* **2001,** *2* (4), 329-340.

206. Petricoin Iii, E. F.; Hackett, J. L.; Lesko, L. J.; Puri, R. K.; Gutman, S. I.; Chumakov, K.; Woodcock, J.; Feigal Jr, D. W.; Zoon, K. C.; Sistare, F. D., *Nature Genetics* **2002,** *32* (5 SUPPL. DEC.), 474-479.

207. Quackenbush, J., *Nature Reviews Genetics* **2001,** *2* (6), 418-427.

208. Brazma, A.; Hingamp, P.; Quackenbush, J.; Sherlock, G.; Spellman, P.; Stoeckert, C.; Aach, J.; Ansorge, W.; Ball, C. A.; Causton, H. C.; Gaasterland, T.; Glenisson, P.; Holstege, F. C. P.; Kim, I. F.; Markowitz, V.; Matese, J. C.; Parkinson, H.; Robinson, A.; Sarkans, U.; Schulze-Kremer, S.; Stewart, J.; Taylor, R.; Vilo, J.; Vingron, M., *Nature Genetics* **2001,** *29* (4), 365-371.

209. Rocke, D. M.; Durbin, B., *Journal of Computational Biology* **2001,** *8* (6), 557-569.

210. Canales, R. D.; Luo, Y.; Willey, J. C.; Austermiller, B.; Barbacioru, C. C.; Boysen, C.; Hunkapiller, K.; Jensen, R. V.; Knight, C. R.; Lee, K. Y.; Ma, Y.; Maqsodi, B.; Papallo, A.; Peters, E. H.; Poulter, K.; Ruppel, P. L.; Samaha, R. R.; Shi, L.; Yang, W.; Zhang, L.; Goodsaid, F. M., *Nature Biotechnology* **2006,** *24* (9), 1115-1122.

211. Leung, Y. F.; Cavalieri, D., *Trends in Genetics* **2003,** *19* (11), 649-659.

212. Simon, R.; Radmacher, M. D.; Dobbin, K.; McShane, L. M., *Journal of the National Cancer Institute* **2003,** *95* (1), 14-18.

213. Allison, D. B.; Cui, X.; Page, G. P.; Sabripour, M., *Nature Reviews Genetics* **2006,** *7* (1), 55-65.

214. Chuaqui, R. F.; Bonner, R. F.; Best, C. J. M.; Gillespie, J. W.; Flaig, M. J.; Hewitt, S. M.; Phillips, J. L.; Krizman, D. B.; Tangrea, M. A.; Ahram, M.; Linehan, W. M.; Knezevic, V.; Emmert-Buck, M. R., *Nature Genetics* **2002,** *32* (5 SUPPL. DEC.), 509-514.

215. Draghici, S.; Khatri, P.; Eklund, A. C.; Szallasi, Z., *Trends in Genetics* **2006,** *22* (2), 101-109.

216. Rhodes, D. R.; Yu, J.; Shanker, K.; Deshpande, N.; Varambally, R.; Ghosh, D.; Barrette, T.; Pandey, A.; Chinnaiyan, A. M., *Neoplasia* **2004,** *6* (1), 1-6.

217. Holloway, A. J.; Van Laar, R. K.; Tothill, R. W.; Bowtell, D. D. L., *Nature Genetics* **2002,** *32* (5 SUPPL. DEC.), 481-489.

CHAPTER-2

HIGH-RESOLUTION EPIFLUORESCENCE AND TOF-SIMS CHEMICAL IMAGING COMPARISONS OF SINGLE DNA MICROARRAY SPOTS

Archana N. Rao[1], Nicolas Vandencasteele[2,§], Lara J. Gamble,[2] and David W. Grainger[1,3*]

[1]Department of Pharmaceutics and Pharmaceutical Chemistry, University of Utah, Salt Lake City, UT 84112-5820 USA

[2]National ESCA and Surface Analysis Center for Biomedical Problems, Departments of Chemical Engineering and Bioengineering, Box 351750, University of Washington, Seattle, WA 98195-1750 USA

[3]Department of Bioengineering, University of Utah, Salt Lake City, UT 84112 USA

**to whom correspondence should be addressed:* David W. Grainger, david.grainger@utah.edu

[§]current address: Université Libre de Bruxelles, Belgium

Keywords: microarray, chemical imaging, fluorescence, mass spectrometry, surface analysis, nucleic acid, hybridization

---

Reprinted with kind permission from Analytical Chemistry: Anal.Chem., 2012 Dec 18;84(24): 10628-36.doi: 10.1021/ac3019334. Epub 2012 Dec 3.

analytical chemistry

Article

pubs.acs.org/ac

High-Resolution Epifluorescence and Time-of-Flight Secondary Ion Mass Spectrometry Chemical Imaging Comparisons of Single DNA Microarray Spots

Archana N. Rao,[†] Nicolas Vandencasteele,[‡,∥] Lara J. Gamble,[‡] and David W. Grainger*[,†,§]

[†]Department of Pharmaceutics and Pharmaceutical Chemistry, University of Utah, Salt Lake City, Utah 84112-5820, United States

[‡]National ESCA and Surface Analysis Center for Biomedical Problems, Departments of Chemical Engineering and Bioengineering, Box 351750, University of Washington, Seattle, Washington 98195-1750, United States

[§]Department of Bioengineering, University of Utah, Salt Lake City, Utah 84112, United States

Supporting Information

ABSTRACT: DNA microarray assay performance is commonly compromised by spot−spot probe and signal variations as well as heterogeneity within printed microspots. Accurate metrics for captured DNA target signal rely upon uniform spot distribution of both probe and target DNA to yield reliable hybridized signal. While often presumed, this is neither easily achieved nor often proven experimentally. High-resolution imaging techniques were used to determine spot heterogeneity in identical DNA array microspots comprising varied ratios of unlabeled and dye-labeled DNA probes contact-printed onto commercial arraying surfaces. Epifluorescence imaging data for individual array microspots were correlated with time-of-flight secondary ion mass spectrometry (TOF-SIMS) chemical state imaging of the same spots. Epifluorescence imaging intensity distinguished varying DNA density distributed both within a given spot and from spot to spot. TOF-SIMS chemical analysis confirmed these heterogeneous printed DNA distributions by tracking bound Cy3 dye, DNA base, and phosphate specific ion fragments often correlating to fluorescence patterns within identical spots. TOF-SIMS ion fragments originating from probe DNA and Cy3 dye are enriched in microspot centers, correlating with high fluorescence intensity regions. Both TOF-SIMS and epifluorescence support Marangoni flow effects on spot drying, with high-density DNA−Cy3 located in spot centers and nonhomogeneous DNA distribution within printed spots. Microspot image dimensional analysis results for DNA droplet spreading show differing DNA densities across printed spots. The study directly supports different DNA probe chemical and spatial microenvironments within spots that yield spot−spot signal variations known to affect DNA target hybridization efficiencies and kinetics. These variations critically affect probe−target duplex formation and DNA array signal generation.

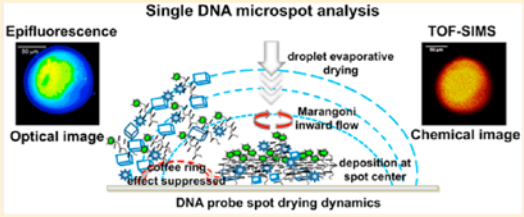

Despite years of development, microarray-based nucleic acid diagnostics continue to be plagued with numerous bioanalytical metric issues that block clinical translation. These include a recognized lack of direct correlation between absolute array spot fluorescent intensity—the common array signal readout—and absolute target abundance in a sample, difficulties in sensitivity and reliability in complex biological samples, and both lab-to-lab and platform-to-platform assay repeatability issues.[1,2] Printed probe spot heterogeneity and nonuniform immobilized DNA density result from procedures common to microarray preparation.[2] Significantly, immobilized DNA probe density is critical for target DNA duplex formation, affecting the resulting assay signal generation in array-based formats.[3−6] Control of printed DNA probe density is important to the reliability of this technology but very challenging to implement and assess.[7]

Both spot-to-spot and individual spot morphological heterogeneity arise from complex interactions between DNA probe microdroplets during printing onto substrates of highly variable interfacial properties (e.g., droplet wetting, sorption, and immobilization kinetics), as well as temperature and humidity during array fabrication that affect droplet drying kinetics.[8,9] The issues are a complex, interrelated set of parameters involving the intrinsic physical, chemical, kinetic, and thermodynamic properties of DNA at surfaces under both probe and target exposure conditions. In typical DNA probe printing to prepare microarrays, nanoliter-scale droplets of DNA solution are dispensed under ambient, nonequilibrium surface printing conditions, leading to rapid droplet evaporation (approximately a few seconds) on surfaces. Droplet evaporation rapidly increases droplet ionic strengths and DNA concentrations, forming distinct intraspot drying features as a consequence of mass transport-limited mixing and nonequilibrium evaporation kinetics.[10]

Received: July 25, 2012
Accepted: November 14, 2012
Published: November 14, 2012

Printed DNA spot drying is complicated due to the presence of complex mixtures of solutes in printed droplets and competing effects of simultaneous "coffee stain drying" and Marangoni flow effects within printed droplets.[11−14] Previous theoretical and experimental reports show that droplet evaporation induces nonuniform cooling along the droplet surface.[15,16] During evaporation, both diffusion and three-dimensional convection deposit solutes and particles in droplet centers.[17] The Marangoni effect is influenced by temperature-dependent solvent surface tension, viscosity, and fluid dynamics of the sessile drop.[18−20] Convective transport and circulation together yield local variations in droplet solute concentration, surface energies, contact angles, and mass distributions during the drying process. Deposition of materials at drying spot centers is due to recirculatory flow driven by surface tension gradients produced by latent heat of solvent evaporation.[20−22] This repeated event with increasing continuous evaporation leads to multiple concentric ring deposits of solute particles.[17,23,24] This precludes uniform distributions of DNA during spreading and drying of printed droplets in microarray fabrication. DNA spot drying phenomena leading to spot heterogeneity in the presence of different concentrations of DNA and fraction of dye-labeled DNA can be explained from spot drying behavior in the presence of DNA-bound dye, surfactant, and dissolved salts.[25] Addition of anionic surfactant [e.g., sodium dodecyl sulfate (SDS)] is known to initially facilitate uniform droplet spreading, stabilizing the evaporation and drastically altering the "coffee ring effect". Surfactant-driven Marangoni flows arise when the local surfactant concentration at the pinned contact line increases due to the coffee ring effect thereby decreasing the local surface tension and inducing Marangoni flow toward the spot center.[12] The extent of circular Marangoni flow is influenced by variation of SDS concentration along the air−water interface.[16] Also, the surfactant layers adsorbed at the liquid−solid interface creates different phases, envisaged to limit the accessibility of the reactive sites for the DNA immobilization. The mode of evaporation can be influenced by the presence of salts, with the DNA probe deposition patterns following the salting trace.[25] Phase separation producing salt crystallization in evaporating droplets of DNA solutions containing salts occurs during drying.[13,24] Exceeding the local solubility limit of salts in evaporating droplets leads to rich morphologies of salt crystal and DNA.[24] Formation of radially varying salt concentration has a spacing between the concentric rings that depends on the DNA concentration and ion species concentration.[24] Marangoni inward flow of solution produces various salt patterns with deposition of the DNA−dye in concentric pattern in the spot.[26] The physicochemical property of the evaporating DNA solution is influenced by the dynamic change in DNA concentration, ionic strength, and surfactant concentration influencing the final patterns.[25] Theoretical and experimental results conclude that, at low concentrations of salt, the deposit more uniformly covers the entire surface beneath the droplet, whereas at higher concentration, salt deposits appear predominantly along the spot's outer rim.[24] At lower DNA concentration, DNA at the liquid−vapor interface is deposited at the droplet edge during initial evaporation stages, and eventually, under developing Marangoni flow transitions, DNA aggregates at the spot centers.[27] Microdroplets containing DNA, surfactant, and dissolved salt undergo phase separation upon drying which is enhanced in the presence of cyanine dyes. Cyanine dyes are known to interact with dsDNA in aqueous media through various interactions, either by intercalation or minor groove binding between base pairs or dye−dye aggregation.[28−30]

Heterogeneity of DNA immobilized probe and bound target in microarrays has been characterized with optical imaging, surface topography, and many surface chemical analytical methods.[31] Surface fluorescence mapping and imaging has been the preferred clinical and biomedical data quantification tool for decades.[32] Fluorescence scanners, most frequently employed to quantify fluorescently labeled DNA patterns in arrays, are unable to quantify absolute amounts of probe or target DNA in spots and are affected by numerous known surface issues that confound reliable absolute quantitative correlations of fluorescent signals. Hence, this method is almost always a relative quantitation method[33−35] unable to report absolute density, biochemical or structural properties, or states for bound DNA.[36,37] Surface chemical methods such as X-ray photoelectron spectroscopy and time-of-flight secondary ion mass spectrometry (TOF-SIMS) provide information on nucleic acid elements, bonded structures, relative densities and coverage, and molecular fragments present in the top 2−10 nm of a surface—a dimension very appropriate to 20−40-mer DNA probes and targets in many arrays.[10,38] Furthermore, TOF-SIMS surface chemical state imaging of DNA features has proven merit in providing both spatially and mass resolved chemical state information on printed surface heterogeneity, DNA spot and printed contaminant compositional variability, and chemical changes between probe and hybridized substrates.[10] Importantly, processing of complex biomolecule TOF-SIMS data using multivariate methods such as principal component analysis (PCA) yields chemically informative images of different chemical species distributions within single printed spots at high sensitivity and submicrometer spatial resolution.[10,39−41] Salt presence affecting printed spot heterogeneity in carbohydrate microarrays has also been analyzed with TOF-SIMS.[42] Spot morphology and signal heterogeneity have been claimed to result from incomplete target hybridization.[43] However, that DNA capture spot and signal variations might have significant common origins in heterogeneous probe immobilization motivated these studies of single spots and spot−spot variabilities to elucidate sources of assay variability and approaches to improve hybridization consistency. Published literature provides substantial evidence that spot printing steps produce irreversible, unalterable surface patterns that determine subsequent DNA interactions.[10,44−46]

In this study, we sought to evaluate if variations in amounts of fluorescent label affect DNA/DNA−dye mixing in spots, their printed spot morphology, and fluorescence intensity. High-resolution epifluorescence imaging of single DNA printed rinsed-blocked and dried spots demonstrating fluorescence heterogeneity typical for printed DNA probe spots was compared to the identical spots analyzed using TOF-SIMS chemical state imaging.[46] This approach yields complementary molecular maps identifying specific chemical species in heterogeneous regions of a DNA spot. These new data provide a chemical basis for understanding DNA spot heterogeneity. Epifluorescence imaging of DNA spot morphologies, relative probe orientations and relative fluorescence unit (RFU) intensities exhibit intra- and interspot DNA density differences and heterogeneity. TOF-SIMS chemical imaging of identical spots provides unique chemical and spatial information on distributions of dye-labeled DNA in these printed spots. Together, these epifluorescence and TOF-SIMS techniques

dx.doi.org/10.1021/ac3019334 | Anal. Chem. 2012, 84, 10628−10636

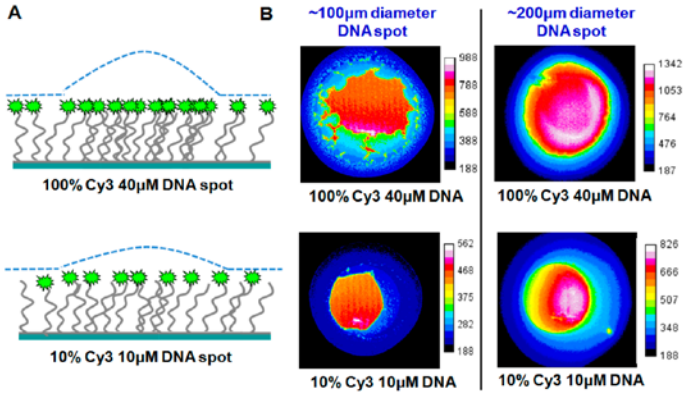

Figure 1. Spot heterogeneity in printed DNA microspots with varied DNA print concentrations and volumes. (A) Schematics of spot fluorescence high intensity with DNA Cy3 dye content at the spot center for two Cy3 concentrations (dotted line indicates fluorescence intensity variation with dye-labeled DNA present across the printed spot radius). (B) Comparison of single-spot epifluorescence images showing spot anisotropy with different contents of Cy3-labeled DNA probe with unlabeled DNA in ~100 μm (left images are 125 μm × 125 μm) and ~200 μm diameter (right images are 200 μm × 200 μm) spots (total DNA print concentrations of 40 and 10 μM for top and bottom rows, respectively). Note: all images are pseudocolored with contrast adjusted using the autoscale function in Image J.

identify DNA spot variability from nonuniform distribution of DNA in the microspot due to spot drying effects: higher DNA probe densities at spot centers, regardless of varied DNA–dye concentrations and spotting volumes. This is proposed to influence subsequent target uptake kinetics and distributions in the same spot, impacting the assay's answer.[44−46] Combining optical and chemical imaging techniques at micrometer resolution provides consistent and complementary information regarding spot heterogeneity and its impact on array signal generation.

■ MATERIALS AND METHODS

Materials. High-performance liquid chromatography (HPLC) purified (≥90%) DNA oligomer sequences, with and without terminal Cy3 dye labeling, and also with and without reactive primary amine termini (Table S-1, Supporting Information), were purchased from TriLink Biotechnologies (San Diego, U.S.A.). Polymer-coated commercial microarray slides (Slide H, amine-reactive polymer-coated slides,[47] Schott Nexterion, Louisville, U.S.A.) were used as received. Unused slides were stored in original packaging under nitrogen at 4 °C and used within 1 month of opening the package.

Microarray Printing. A SpotBot2 contact printer with Stealth SMP4 and SMP6 pins (Arrayit, Sunnyvale, U.S.A.) was used to print oligo-DNA probes onto commercial array surfaces. Microarrays (see the layout shown in Figure S-1 and printing methodology in the Supporting Information, similar to previous reporting[10]) were printed with multiple probe concentrations (10, 20, and 40 μM) and different molar ratios of Cy3 dye-labeled probe (Cy3−Oligo1−NH_2) to unlabeled probe (Oligo1−NH_2) (i.e., 0:1, 1:3, 3:1, and 1:0), yielding printed rows containing no Cy3-labeled probe (0:1) progressing to printed rows containing 100% Cy3-labeled probe (1:0). Nonspecific polymer surface interactions (i.e., residual substrate primary amine chemical reactivity) were then blocked on DNA-printed slides using a stepwise protocol per manufacturer's recommendations (see the Supporting Information). All spot analysis (TOF-SIMS, epifluorescence imaging) was performed on printed DNA microarrays that were rinsed-blocked and dried prior to analysis.

Fluorescence Imaging of DNA Microarrays. Probe-printed rinse-blocked and dried DNA microarrays were scanned for Cy3 (channel 535, GenePix 4100A scanner, version 6 software) before hybridization (after blocking) and prior to obtaining higher resolution fluorescent images with an epifluorescence microscope. For all scans, laser power was preset to 100%, brightness and contrast at 92%, PMT gain 400, the maximum pixel resolution is 5 μm/pixel, adjustable from 5 to 100 μm/pixel, and line average 3. Spots scanned before (data not shown) and after blocking have spot morphologies and patterns that are unchanged, indicating that spot heterogeneity occurs during droplet drying in the first step and remains for all steps thereafter.

Epifluorescence Imaging of Single DNA Spots. High-resolution fluorescent images of single DNA spots were acquired (Olympus IX81 epifluorescence microscope, Prior Scientific motorized *XYZ* environmental stage, motorized shutter/filter wheel, and Photometrics CoolSnap-ES scientific CCD camera in 36-bit color mode, controlled by Metamorph V6.2r6 software). Successive fluorescent images of individual DNA spots were captured under motorized *XYZ* stage control. Autofocus was set initially for the DNA spot containing the highest dye intensity (e.g., 40 μM DNA, 100% Cy3) to establish maximum image contrast and successively measured for all printed DNA spots in that array with the same optical parameters. On the basis of spot dye content, different microscope air objectives were used to maximize image information collection per spot (excitation filter 510−550 nm, dichroic long-pass filter from 510 nm, and emission band-pass filter at 575−600 nm used for Cy3 image capture). All images are pseudocolored, and image contrast was adjusted using the autoscale function in Image J. This processing can produce concentric rings of different colors with defined rings most often being artifactual, not real. Further description of DNA spot image analysis is provided in the Supporting Information.

TOF-SIMS Chemical Imaging and Analysis of DNA Microarray Spots. TOF-SIMS images were recorded on a

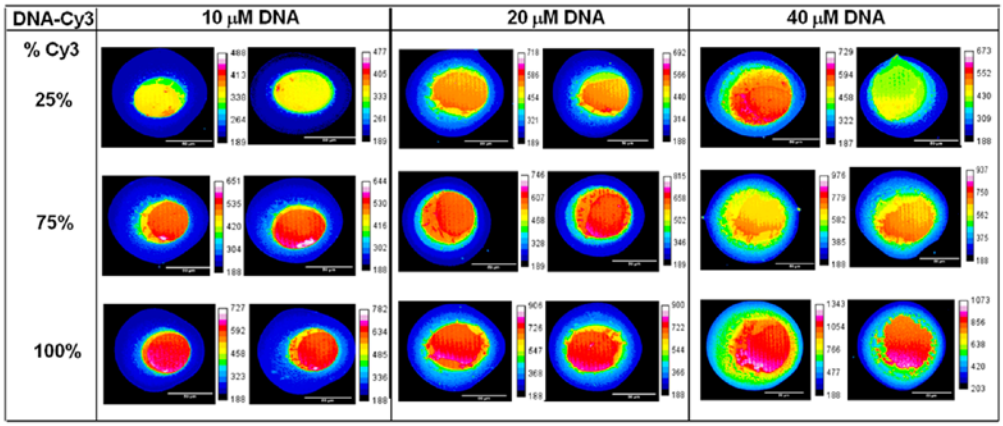

Figure 2. Epifluorescence images of printed DNA spots comparing two side-by-side dried spots each of identical DNA concentration and DNA–Cy3 content for 10, 20, and 40 μM. DNA print concentrations (rows across) and increasing 25–100% DNA–Cy3 ratios (columns down). Images are 125 μm × 125 μm. All images are pseudocolored with intensity contrast adjusted using the autoscale function in Image J to depict highest intensity of DNA–Cy3 dye at the spot's center.

TOF-SIMS V instrument (ION-TOF GmbH, Munster, Germany) using a Bi_3^+ cluster primary ion source. Each image has a resolution of 256 × 256 pixels; image sizes vary and are reported for each individual image. Positive and negative ion images were recorded using pulsed 25 keV, 0.18 pA primary ion beams in high-current bunched mode. Both positive and negative ion images were taken of the same spot. Positive spectra were calibrated using CH_3^+, $C_2H_2^+$, $C_4H_4^+$, $C_7H_9^+$, and negative spectra were calibrated using CH^-, $C_2H_3^-$, $C_2H_3^-$, CHO^-, and $C_2H_3O_2^-$. A low-energy electron beam was used for charge compensation. The mass resolution ($m/\Delta m$) was approximately 6000 for the m/z 26 peak in the positive spectra and 4000 for the m/z 25 peak in the negative spectra. TOF-SIMS image data were collected with primary ion dosing of 9.9×10^{11} ions/cm^2 for images taken with 50 scans and 2×10^{12} ions/cm^2 image taken with 100 scans (both doses are considered below the static limit).

■ RESULTS AND DISCUSSION

Printing-Dependent DNA Spot Heterogeneity. High-resolution epifluorescence images of individual printed rinsed-blocked and dried DNA microarray spots exhibit highly variable, nonuniform intraspot distributions of fluorescence intensity, reflecting heterogeneous distribution of dye-labeled DNA. Figure 1A schematically represents DNA spot heterogeneity observed by epifluorescence imaging, depicting higher Cy3-labeled DNA density at the spot center compared to the periphery at both high and low DNA–Cy3 concentrations (see Figure 1 cartoon depicting high-intensity regions in the spot center). Actual pseudocolored (Image J) single-spot epifluorescence intensity images in Figure 1B show dry DNA films for two printed diameters, each with high and low DNA–dye/DNA probe ratios at differing total DNA print concentrations. All images under all print conditions exhibit higher DNA dye densities in spot centers shown by the bright pseudocolored regions, irrespective of DNA concentration or Cy3 dye-labeled DNA probe ratio. Pseudocoloring of dried DNA showed in radial (circular) contours within each spot (i.e., ringlike deposits each of variable intensities); however, this was not observed in grayscale DNA spot images. Both the grayscale and pseudocolored images showed high intensity at the spot center with profile plots (Image J) indicating a dominant Marangoni inward flow during spreading and drying of DNA spots (see Supporting Information Figure S-2).[12,48] High Cy3 dye-labeled DNA intensities consistently seen in Figure 2 at spot centers support dominant Marangoni effects[25] during DNA spot drying on NHS slides.[47] Regardless of the printing method and deposited volume, heterogeneous dried spots result.[25,27,49−51] Intraspot DNA high-intensity center-type heterogeneity was consistently observed for both dried spot diameters of ~100 and ~200 μm (Figures 1 and 2), as shown in epifluorescence images for DNA spots (probe only) with different mixed probe DNA–Cy3/DNA ratios and different total printed DNA concentrations.

Epifluorescence Imaging to Assess DNA Spot Heterogeneity and Spot–Spot Variations. In addition to nonuniform probe distributions within single spots, spot–spot variations in DNA probe and target duplex densities are major sources of experimental variability in microarray-based analyses.[52,53] To enhance spot quality and reproducibility, surfactants are often used in probe immobilization buffers: nonionic Tween 20 and zwitterionic sarcosine surfactants were added to 300 mM sodium phosphate print buffer here, and anionic surfactant, SDS, was added to rinse buffer used after blocking. These have notable influence on droplet/drying physicochemical results (i.e., droplet wetting and evaporation rates) to produce well-controlled round, consistent diameter spots.[25] Figure 2 expands the examples of DNA heterogeneity shown in Figure 1 with epifluorescence images of printed DNA spots for a wide DNA spot compositional matrix involving different total DNA concentrations and highly varying DNA/DNA–Cy3 ratios. Drying phenomena seen in Figure 1 are consistently observed. Therefore, the Marangoni thermal stress must also dominate droplet drying across this broad DNA compositional matrix, causing spot heterogeneity. Maintaining 60% relative humidity during printing and drying did not alter this observed interspot or intraspot variability, as reported earlier.[54] Use of surfactants such as Tween and SDS commonly employed in various array fabrication steps (also here) creates

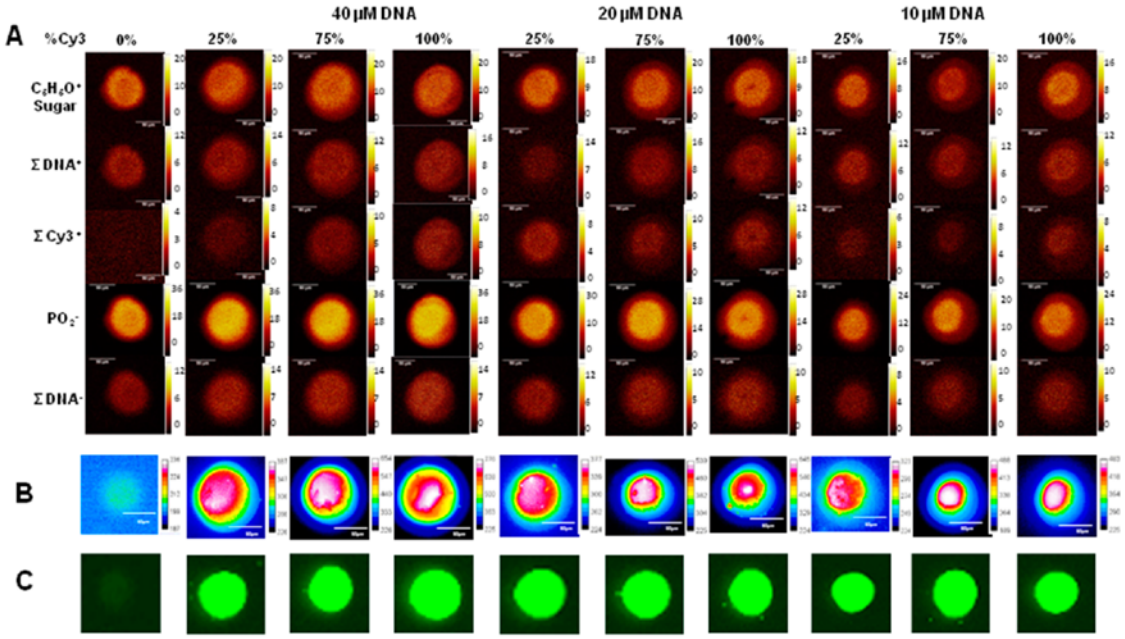

Figure 3. Comparison of TOF-SIMS, epifluorescence, and fluorescence scanner images of identical ~100 μm DNA spots (each vertical column) of varying total DNA concentration (major triplicate columns) and fractional DNA–Cy3 dye label content (each vertical column). (A) TOF-SIMS chemical images of different DNA chemical fragments: 10 and 20 μM DNA spot images were 150 μm × 150 μm and the 40 μM spots were 200 μm × 200 μm. (B) Epifluorescence images of DNA–Cy3, images are 125 μm × 125 μm, and (C) conventional fluorescence scanner images lacking spot features seen in panels A and B. DNA spots with 0% DNA–Cy3 in panel B are only visible with increasing exposure time in epifluorescence imaging. Corresponding fluorescence scanner image of the same 0% DNA–Cy3 spot (panel C) is only very faint with 100% laser intensity. Note: all images in panel B are pseudocolored with intensity contrast adjusted using the autoscale function in Image J.

Marangoni stress[48] conditions that otherwise are not generally favored in aqueous systems.[16,25,27,48]

Spot–spot variation for DNA microspots using identical printing conditions for five replicate sets during a single print run shows spot heterogeneities also observed for same-concentration DNA–dye printed spots using surface pixel intensity plots (Figure S-3, Supporting Information), consistent with the two-dimensional intensity plots shown in Figures 1 and 2. As both total printed DNA concentration and DNA–Cy3 content increase, spot–spot heterogeneity also increases in fluorescence intensity. Spots printed with higher DNA concentrations exhibit higher DNA fluorescence fractional distribution in spot centers. Also, increasing DNA concentration leads to comparative increases in printed dried spot diameters, contributed from initial droplet spreading. A steady increase in spot diameter is observed with increasing DNA concentration. Increasing DNA–dye labeling produced increasing spot diameters as seen in TOF-SIMS, epifluorescence, and fluorescence scanner images comparing 0% Cy3-labeled DNA spots with 25%, 75%, and 100% DNA–Cy3 content spots (see Figure 3, Supporting Information Table S-2, and Supporting Information Figure S-12). Despite much evidence for DNA aggregation upon drying, there is little evidence for nonideal mixing (i.e., DNA–Cy3 phase separation) of unlabeled DNA.

Use of nonionic/zwitterionic surfactants can produce two phases of DNA segregation:[25] one enriched in DNA and another in surfactant, promoting formation of DNA precipitates with increasing electrolyte and surfactant concentration with evaporation.[26,55,56] Furthermore, supersaturated salt conditions promote DNA phase separation,[24,25] at very low concentrations of both DNA and surfactant, and is further enhanced by electrolytes.[10,56–58] Similar aggregation is predominant at higher DNA concentrations (i.e., micromolar to molar)[28] and with dye-labeled DNA oligomers.[59] It is likely that such concentrations are achieved in droplets seconds after printing due to water evaporation with rapid drying. Furthermore, cyanine dyes analogous to Cy3 are known to readily form molecular aggregates in aqueous media.[29] Cyanine dye aggregation is also reported in Langmuir–Blodgett monolayers of amphiphilic nucleic acids during evaporation rates controlled by mass transfer across the aqueous-film–air interface.[60] In cyanine dye-labeled single-strand probe DNA, dye–dye interactions and dye–nucleotide[44] aggregation with increasing ionic strength and surfactant concentrations reduce probe stability and quench fluorescence.[59,67,70] Singly labeled fluorescent DNA probes exhibit dye–DNA interactions as studied by fluorescence anisotropy and lifetime assays.[59] As DNA–Cy3 content increases in print solutions up to 100% DNA mass fraction, DNA aggregation is much more predominant, increasing dye quenching and reducing fluorescence intensity (shown in a later section). Hence, DNA–dye aggregates predominately at spot centers,[13,48,61] and fewer DNA–Cy3 probes deposit at droplet edges, altering DNA chain interactions and density as the droplet evaporates.[27,50,61] (Figure S-4, Supporting Information, schematically summarizes DNA droplet drying phenomenon in the presence of salt and surfactant.)

dx.doi.org/10.1021/ac3019334 | Anal. Chem. 2012, 84, 10628–10636

TOF-SIMS Chemical Imaging of DNA–Dye Concentration-Dependent Printed Spot Heterogeneity. Further DNA-specific chemical evidence for printed spot heterogeneity comes from TOF-SIMS chemical imaging of single 100 μm diameter DNA printed spots containing various total DNA print and fractional DNA–Cy3 probe concentrations. Individual DNA spot chemical images obtained with TOF-SIMS for different mass fragments characteristic of different spot components are shown in Figure 3A. Selected chemical fragment images of individual printed DNA spots are displayed for the following: (Figure 3A, row 1) DNA ribose chemistry [m/z = 81, $C_5H_5O^+$]; (Figure 3A, row 2) all DNA-derived positive ions identified from TOF-SIMS spectra of deoxynucleoside controls [cytosine m/z 112 ($C_4H_6N_3O^+$), adenine 119 ($C_5H_3N_4^+$) and 136 ($C_5H_6N_5^+$), guanine m/z 135 ($C_5H_3N_4O^+$), 152 ($C_5H_6N_5O^+$), and 174 ($C_7H_4N_5O^+$)]; (Figure 3A, row 3) all positive ions associated with Cy3 [m/z 130 ($C_9H_8N^+$), 144 ($C_{10}H_{10}N^+$), 167 ($C_{12}H_9N^+$), and 180 ($C_{13}H_{10}N^+$)]; (Figure 3A, row 4) nucleotide phosphate fragment m/z 63 (PO_2^-); (Figure 3A, row 5) all DNA negative ions [thymine m/z 125 ($C_5H_5N_2O_2^-$), cytosine m/z 110 ($C_4H_4N_3O^-$), adenine m/z 134 ($C_5H_4N_5$), guanine m/z 133 ($C_5H_3N_5^-$), 150 ($C_5H_4N_5O^-$)].[40] It should be noted that TOF-SIMS image pixel intensities indicate relative differences in amounts of ions within that image but are not necessarily comparable between images. Collectively, all single-spot chemical images also show heterogeneity across the entire spot area, consistent with that seen in epifluorescence images of DNA spots (Figures 1 and 2).

In Figure 3, TOF-SIMS chemical fragment heterogeneity in Figure 3A is compared to epifluorescence images of the identical DNA spots in Figure 3B, as well as with the standard fluorescence scanner fluorescence pixel maps of the identical spots in Figure 3C. Because TOF-SIMS samples an ~15–20 Å depth into the surface while epifluorescence emits from much deeper zones (micrometer depths) within spots, there are some differences in the two different spot images and morphologies. However, regardless of differences in depth of analysis and pixel resolution, textures in images providing chemical information on spot heterogeneity shown in Figure 3A (TOF-SIMS) correlate well with pixel intensity heterogeneities for identical spots seen in Figure 3B (high-resolution epifluorescence images). Similarly, TOF-SIMS and epifluorescence images show similar spot heterogeneity with increased spot diameter (i.e., 200 μm diameter, increased spotting volume) as shown in Figure S-5 (Supporting Information) for 40 μM DNA spotting concentrations containing increasing amounts of Cy3 dye-labeled DNA

Significantly, neither of these higher resolution DNA spot heterogeneities is duplicated in the lower resolution fluorescent scanner images of the same spot shown in Figure 3C (pixel resolution with fluorescence scanner imaging is ~6 × 6 pixels, TOF-SIMS is 256 × 256 pixels, and epifluorescence is 572 × 512 pixels) (see Supporting Information Figure S-6). TOF-SIMS images of characteristic DNA and Cy3 dye fragments consistently exhibit Marangoni drying influences, producing higher density of both DNA and Cy3 dye chemical fragments in spot centers and reduced outward radial image intensity, comparable to high-resolution epifluorescence images (Figure 3B). Lower resolution scanner images cannot capture this radially heterogeneous pixel information and, instead, exhibit homogeneous spot intensities. Clearly, spot details important to DNA densities, amounts, and distributions as a function of spot radius are consistent using higher resolution imaging methods on single spots but are lost in the lower resolution fluorescence scanner image (Figure 3C).

Significantly for most microarray signal analysis, imaging technology used in Figure 3C represents the most commonly applied analytical method for commercial and clinical DNA arraying signal assays (i.e., fluorescence scanners). Importantly, integrated fluorescent intensity within each spot becomes the assay "answer" for gene presence and abundance in such assays. However, details obtained from high-resolution techniques for intraspot DNA spot heterogeneity and poor spot–spot reproducibility provide clear bases for suboptimal assay quality obtained using low-resolution scanner formats that cannot account for such variabilities or discern spot heterogeneity. Inconsistencies between these three different analytical imaging methods (on identical DNA spots) distinguish between the higher resolution of TOF-SIMS chemical imaging (Figure 3A), epifluorescence spot images (Figure 3B), and lower resolution spot fluorescence scanning.

More homogeneous fluorescence distribution, regardless of intensity differences, reflects DNA signal emanating from thicker spots from multiple depths. However, in most cases, spot morphology and density variations from epifluorescence imaging are comparable to TOF-SIMS chemical species imaging. Specifically, DNA–Cy3 dye fluorescence and relevant chemical fragment intensities are greatest at spot centers, decreasing outwardly with radius to spot edges. TOF-SIMS images provide direct evidence for Cy3 dye fragment distributions in single spots based on chemical fragment (m/z = 130, $C_9H_8N^+$) enhancement at spot centers. Additionally, images based on positive ion fragments derived from DNA ribose sugars (m/z = 81, $C_5H_5O^+$), negative ion phosphate peak (PO_2^-)—known DNA-derived positive and negative ion fragments—are consistently colocated with fluorescent high-intensity regions for DNA–Cy3 images. TOF-SIMS chemical species imaging corroborates epifluorescence images of DNA distribution for both intra- and interspot.

High-Resolution Epifluorescence and TOF-SIMS Image Comparisons of Individual DNA Microspots. Further single-spot analysis was used to compare prominent image features in spots, leveraging high-resolution imaging capabilities from both epifluorescence and TOF-SIMS against lower resolution scanner images. This provided more insight into sources of DNA printed spot morphological and density heterogeneity by direct comparisons of chemically and optically distinct spatial features within respective images. Identical spot comparisons in TOF-SIMS and epifluorescence must correlate and align image and slide orientation. Comparisons of printed probe DNA spots using high-resolution epifluorescence, TOF-SIMS image, and fluorescence scanner images are provided in Figure S-7 (Supporting Information).

Influence of DNA–Cy3 Spotting Concentrations on Spot Fluorescence Intensity. Plots of DNA–Cy3 probe fluorescent intensity with varying DNA–Cy3 and DNA–Cy3/total DNA probe print concentrations do not exhibit a linear correspondence of increasing spot RFU with commensurate increases in Cy3 dye label fraction. Figure S-8 (Supporting Information) shows that integrated spot RFU signals exhibit nonlinear intensity responses to increasing DNA–Cy3 additions. DNA–Cy3 dye content within each spot should increase the spot's RFU linearly and proportionally as long as dye–dye quenching or Cy3 quantum yield perturbations are negligible. Since the fluorescence intensity RFU value is the

dx.doi.org/10.1021/ac3019334 | Anal. Chem. 2012, 84, 10628–10636

assay "answer", spot morphology and spot fluorescent reporting fidelity is crucial to accurately determine experimental spot-to-spot variation and experimental assay "answer" validity.[62] Possible Cy3 aggregation, dimerization, DNA−Cy3[59,63,64] and dye−substrate surface interactions that reduce fluorescent intensity for printed ssDNA are offered as possible explanations for this nonlinearity observed. Lateral nonradiative energy transfer (self-quenching) is known between cyanine dyes (i.e., Cy3 and Cy5) at higher surface densities and bulk concentrations.[65] Quenching due to dye−dye and dye−surface interactions is predominant at short separation distances,[66−70] favored at higher DNA labeling densities and supported by lower-than-expected increases in spot-integrated RFUs as DNA−Cy3 fractions increase from 25% to 75% to 100%. Supporting Information Figure S-8 shows integrated spot fluorescence intensities from epifluorescence images of varying DNA−Cy3 concentrations not correlating with actual DNA probe concentrations. This presents a difficult validation issue for use of this format as an industry standard and clinically applied assay wherein low-resolution fluorescence scanners are expected to produce integrated spot RFU intensity as the assay "answer".

DNA Spot Morphology and Droplet Spreading Comparisons during Printing/Drying. Spot drying effects on both DNA−Cy3 distribution in printed spots and spot morphologies were evaluated by assessing printed spot dimensions and distinct spot drying features (e.g., DNA distribution in different DNA drying regions). Spot dimensions, areas, diameters, and high fluorescent intensity from DNA spreading/drying were measured for epifluorescence images of printed DNA spots. Supporting Information Figure S-9 shows gross printed spot dimensions measured from both epifluorescence and processed TOF-SIMS images of identical printed DNA spots. Image scaling measurements confirming DNA spot diameter and central high-intensity DNA−Cy3 regions in epifluorescence imaging are obtained by converting pixels to micrometers (Figure S-10, Supporting Information). Epifluorescence imaging provides higher resolution spot data compared to TOF-SIMS images, showing clearly the high-intensity central region of DNA−Cy3 distribution in the spot. Similarly, the dimensions of the high-intensity region of DNA spot images of ∼200 μm dried 40 μM DNA spots with 100% DNA−Cy3 dye were prominent and measurable for Cy3 dye distribution within the spot and were comparable using both techniques (Figure S-11, Supporting Information).

Uniform DNA spot morphologies and fluorescence intensities are important for accuracy, repeatability, and reproducibility of the DNA array assay RFU "answer", especially using common lower resolution scanner fluorescence image pixel integration. Both integrated spot intensity and relative spot size are important for reliable RFU analysis of DNA array spots.[71] As shown in Supporting Information Figures S-9 and S-11, spot sizes obtained from contact printing could be precisely determined from diameter measurements using both high-resolution imaging techniques. While low-resolution fluorescence scanner images of DNA spot size are uniform without notable bleeding/spreading of either DNA or printer buffer, this imaging method cannot consider spot nonuniformity and resulting changes in spot signal intensities as observed with high-resolution techniques. TOF-SIMS validates printed spot size by showing that all relevant DNA chemical signatures correlate to the same spot dimension as the same DNA spot's epifluorescence image signature. While this correlation confirms the accuracy of high-resolution epifluorescence to capture spot Cy3 fluorescent heterogeneity and signal accurately, lower-resolution scanners, while accurately determining actual spot size (Table S-2, Supporting Information), cannot provide sufficient resolution to resolve spot fluorescence heterogeneity. Hence, integrated spot RFU signal intensities, independent of instrumentation differences, will necessarily be unique for each method. This is supported by line scan analyses for corresponding spots (data not shown).

Epifluorescence and TOF-SIMS images also demonstrate increasing spot diameters and spread areas with increasing amounts of DNA and fractions of DNA−Cy3 for the 100 μm spot regimes (constant drop volume, Figure S-12A, Supporting Information). Supporting Information Figure S-12B compares both 100 and 200 μm spot diameters for 40 μM total printed probe DNA with increasing DNA−Cy3 content (different drop volumes). Both TOF-SIMS and epifluorescence imaging are closely comparable in demonstrating increased dried spot diameter with increasing DNA−Cy3 content. Common buffers such as PBS and SSC used for DNA spot printing lead to size and morphological inhomogeneities.[25] However, droplet evaporation induces DNA phase separation with increasing ionic strength, surfactant, and Cy3 dye-DNA concentrations, influencing spot drying patterns and DNA immobilized densities.[72−75] This is important since high-density DNA probe immobilization and DNA−DNA crowding influence DNA target surface capture (hybridization), hindering duplex formation at surfaces by both steric and Coulombic blockade repulsive barriers to incoming DNA targets.[3,6,72,73] This means that DNA target binding efficiency, dependent on local probe density,[76] will also be heterogeneous given wide variations in both intra- and interspot probe density shown to result from Cy3 dye-labeled DNA altered interactions with surfaces during printing and drying[77] and evaporatively induced DNA phase separation.[27] Notably, high amounts of probe dye labeling used here to monitor spot optical properties are not typical of most arraying experiments and are shown to lead to greater phase segregation and spot size alterations.[59] Additionally, DNA exhibits only modest drying-induced nonspecific surface binding upon printing and clearly reacts covalently in presence of NHS chemistry. Spots lacking DNA-specific chemical coupling or buffer-only spots can be imaged from residual DNA nonspecific binding in the former case and background autofluorescence generated from buffer spot wetting/drying in both cases.[44] Whether DNA surface coupling chemistry proceeds after print buffer evaporation is not known; however, it seems likely that residual amounts of DNA in printed spots areas (after evaporation) are primarily a nonspecific drying-induced physisorbed aggregation of noncoupled DNA mixed with surface-coupled DNA, leaving substantial amounts of noncoupled but drying-stabilized DNA on the surface despite rinsing.[78] This aggregated disorganized DNA film comprises the microspot that undergoes target capture, with a higher DNA density (high DNA concentration, substantially greater spot thickness[78]) at its center due to DNA transport under Marangoni drying.

■ CONCLUSIONS

Analysis of DNA printed spot heterogeneity and spot-to-spot variation for printed dye-labeled DNA microspots often shows higher DNA density at the centers of printed DNA microspots than spot edges. High-resolution epifluorescence optical imaging of DNA−Cy3 and TOF-SIMS chemical imaging of

different DNA or Cy3 chemical fragment ion species within spots together provide complementary information for assessing dried DNA density and distributions on coated glass commercial microarray substrates. High-density DNA regions in spot centers obtained from epifluorescence imaging compare very well to those obtained with TOF-SIMS chemical state imaging. Routine, conventional fluorescence scanner images provide information for integrated spot pixel intensity, shape, and morphology but lack all details for intraspot DNA heterogeneity and intraspot structural issues known to affect target capture and duplex hybridization kinetics critical to this assay's answer development and diagnostic reliability. Comparative spot−spot assessment with multiple complementary analytical techniques consistently detected DNA spot−spot variability, heterogeneity within individual DNA spots, and DNA density distributions.

Dried DNA spot nonuniformities obtained using contact printing techniques are attributed to array fabrication process parameters including nonequilibrium drying under influences of buffers, humidity, and evaporation during microarray fabrication. Marangoni drying under these evaporative conditions produces chemical and physical interactions between DNA and nonvolatile solutes in the spot, yielding DNA aggregation and surface deposition within the original spotted, wetted footprint. Direct side-by-side comparisons of dried DNA spot dimensions, DNA density distributions, lateral heterogeneities, and trends in variations in spot DNA densities with varying DNA print concentrations are consistent in asserting these influences on dried spot morphologies. Nonuniform DNA probe distributions produce nonlinear changes in integrated spot fluorescence intensities with increasing DNA−Cy3 printed content. Significantly, probe spot heterogeneities also affect DNA target capture efficiencies and reliabilities and, ultimately, the entire microarray assay signal generation. Hence, variations in DNA target capture duplexes both within spots and spot to spot have origins in probe print drying artifacts. Improved assay consistency and "answer" reliability and reproducibility therefore should focus on probe printing controls and consistent surface, buffer, and drying properties in order to limit stochastic variability. Study results justify necessary improvements in methods and quality controls for DNA surface immobilization processes that influence analyte (i.e., DNA target) capture and that affect microarray assay signal reliability, reproducibility, and clinical translation.

■ ASSOCIATED CONTENT

Supporting Information

Additional information as noted in text. This material is available free of charge via the Internet at http://pubs.acs.org.

■ AUTHOR INFORMATION

Corresponding Author

*E-mail: david.grainger@utah.edu.

Present Address

[‖]Université Libre de Bruxelles, Belgium.

Notes

The authors declare no competing financial interest.

■ ACKNOWLEDGMENTS

The authors gratefully acknowledge support from NIH R01 EB-001473 (DWG) and NIH P41 EB002027 (NESAC/BIO), the Belgian American Educational foundation (NV) and the Fulbright commission (NV) for financial support. We also thank Dr. C. Rodesch (University of Utah) for assistance with epifluorescence imaging analysis.

■ REFERENCES

(1) Zou, S.; He, H.-J.; Zong, Y.; Shi, L.; Wang, L. *Standardization and Quality Assurance in Fluorescence Measurements II*; Resch-Genger, U., Ed.; Springer Series on Fluoresence; Springer-Verlag: Berlin, Heidelberg, Germany, 2008; Vol. 6, pp 215−237.

(2) Sasik, R.; Woelk, C. H.; Corbeil, J. *J. Mol. Endocrinol.* **2004**, *33* (1), 1−9.

(3) Vainrub, A.; Pettitt, B. M. *Phys. Rev. E: Stat., Nonlinear, Soft Matter Phys.* **2002**, *66* (4 Pt 1), 041905.

(4) Vainrub, A.; Pettitt, B. M. *Chem. Phys. Lett.* **2000**, *323* (1−2), 160−166.

(5) Halperin, A.; Buhot, A.; Zhulina, E. B. *J. Phys.: Condens. Matter* **2006**, *18* (18), S463−S490.

(6) Halperin, A. S.; Buhot, A.; Zhulina, E. B. *Biophys. J.* **2004**, *86* (2), 718−730.

(7) Xu, F.; Pellino, A. M.; Knoll, W. *Thin Solid Films* **2008**, *516* (23), 8634−8639.

(8) Yunker, P. J.; Still, T.; Lohr, M. A.; Yodh, A. G. *Nature* **2011**, *476* (7360), 308−311.

(9) Rouse, R. J.; Field, K.; Lapira, J.; Lee, A.; Wick, I.; Eckhardt, C.; Bhasker, C. R.; Soverchia, L.; Hardiman, G. *BMC Res. Notes* **2008**, *1*, 45.

(10) Lee, C. Y.; Harbers, G. M.; Grainger, D. W.; Gamble, L. J.; Castner, D. G. *J. Am. Chem. Soc.* **2007**, *129* (30), 9429−9438.

(11) Still, T.; Yunker, P. J.; Yodh, A. G. *Langmuir* **2012**, *28* (11), 4984−4988.

(12) Hu, H.; Larson, R. G. *J. Phys. Chem. B* **2006**, *110* (14), 7090−7094.

(13) Smalyukh, I. I.; Zribi, O. V.; Butler, J. C.; Lavrentovich, O. D.; Wong, G. C. L. *Phys. Rev. Lett.* **2006**, *96*, 177801.

(14) Park, J.; Moon, J. *Langmuir* **2006**, *22* (8), 3506−3513.

(15) Hu, H.; Larson, R. G. *Langmuir* **2005**, *21* (9), 3963−3971.

(16) Still, T.; Yunker, P. J.; Yodh, A. G. *Langmuir* **2012**, *28* (11), 4984−4988.

(17) Weon, B. M.; Je, J. H. *Phys. Rev. E: Stat., Nonlinear, Soft Matter Phys.* **2010**, *82* (1 Pt 2), 015305.

(18) Haw, M. D.; Gillie, M.; Poon, W. C. K. *Langmuir* **2002**, *18* (5), 1626−1633.

(19) Barash, L. Y.; Bigioni, T. P.; Vinokur, V. M.; Shchur, L. N. *Phys. Rev. E: Stat., Nonlinear, Soft Matter Phys.* **2009**, *79* (4 Pt 2), 046301.

(20) Ppoulard, C.; Damman, P. *Europhys. Lett.* **2007**, *80*, 64001.

(21) Ekins, R.; Chu, F. *Clin. Chem.* **1991**, *37* (11), 1955.

(22) Deegan, R. D.; Bakajin, O.; Dupont, T. F.; Huber, G.; Nagel, S. R.; Witten, T. A. *Phys. Rev. E: Stat. Phys., Plasmas, Fluids, Relat. Interdiscip. Top.* **2000**, *62* (1 Pt B), 756−765.

(23) Zhang, L.; Maheshwari, S.; Chang, H. C.; Zhu, Y. *Langmuir* **2008**, *24* (8), 3911−3917.

(24) Kaya, D.; Belyi, V. A.; Muthukumar, M. *J. Chem. Phys.* **2010**, *133* (11), 114905.

(25) Dugas, V.; Broutin, J.; Souteyrand, E. *Langmuir* **2005**, *21* (20), 9130−9136.

(26) Truskett, V. N.; Stebe, K. J. *Langmuir* **2003**, *19* (20), 8271−8279.

(27) Fang, X.; Li, B.; Petersen, E.; Seo, Y. S.; Samuilov, V. A.; Chen, Y.; Sokolov, J. C.; Shew, C. Y.; Rafailovich, M. H. *Langmuir* **2006**, *22* (14), 6308−6312.

(28) Seifert, J. L.; Connor, R. E.; Kushon, S. A.; Wang, M.; Armitage, B. A. *J. Am. Chem. Soc.* **1999**, *121* (13), 2987−2995.

(29) Armitage, B. A. *Top. Curr. Chem.* **2005**, *253*, 55−76.

(30) Ogul'chansky, T.; Losytskyy, M.; Kovalska, V. B.; Yashchuk, V. M.; Yarmoluk, S. M. *Spectrochim. Acta, Part A* **2001**, *57* (7), 1525−1532.

(31) Brockman, J. M.; Nelson, B. P.; Corn, R. M. *Annu. Rev. Phys. Chem.* **2000**, *51*, 41−63.

(32) Nagl, S.; Schaeferling, M.; Wolfbeis, O. S. *Microchim. Acta* **2005**, *151* (1−2), 1−21.
(33) Fielden, M. R.; Halgren, R. G.; Dere, E.; Zacharewski, T. R. *Bioinformatics* **2002**, *18* (5), 771−773.
(34) Ferguson, J. A.; Boles, T. C.; Adams, C. P.; Walt, D. R. *Nat. Biotechnol.* **1996**, *14* (13), 1681−1684.
(35) Repsilber, D.; Ziegler, A. *Methods Inf. Med.* **2005**, *44* (3), 400−404.
(36) Leung, Y. F.; Cavalieri, D. *Trends Genet.* **2003**, *19* (11), 649−659.
(37) Shi, L.; Tong, W.; Su, Z.; Han, T.; Han, J.; Puri, R. K.; Fang, H.; Frueh, F. W.; Goodsaid, F. M.; Guo, L.; Branham, W. S.; Chen, J. J.; Xu, Z. A.; Harris, S. C.; Hong, H.; Xie, Q.; Perkins, R. G.; Fuscoe, J. C. *BMC Bioinformatics* **2005**, *6* (Suppl. 2), S11.
(38) Graf, N.; Gross, T.; Wirth, T.; Weigel, W.; Unger, W. E. S. *Anal. Bioanal. Chem.* **2009**, *393* (8), 1907−1912.
(39) Boland, T.; Ratner, B. D. *Langmuir* **1994**, *10* (10), 3845−3852.
(40) May, C. J.; Canavan, H. E.; Castner, D. G. *J. Anal. Chem.* **2004**, *76* (4), 1114−1122.
(41) Dietrich, P. M.; Horlacher, T.; Girard-Lauriault, P. L.; Gross, T.; Lippitz, A.; Min, H.; Wirth, T.; Castelli, R.; Seeberger, P.; Unger, W. E. S. *J. Carbohydr. Chem.* **2011**, *30* (4−6), 361−372.
(42) Scurr, D. J.; Horlacher, T.; Oberli, M. A.; Werz, D. B.; Kroeck, L.; Bufali, S.; Seeberger, P. H.; Shard, A. G.; Alexander, M. R. *Langmuir* **2010**, *26* (22), 17143−17155.
(43) Tran, P. H.; Peiffer, D. A.; Shin, Y.; Meek, L. M.; Brody, J. P.; Cho, K. W. *Nucleic Acids Res.* **2002**, *30*, 12.
(44) Gong, P.; Grainger, D. W. *Surf. Sci.* **2004**, *570* (1−2), 67−77.
(45) Dandy, D. S.; Wu, P.; Grainger, D. W. *Proc. Natl. Acad. Sci. U.S.A.* **2007**, *104* (20), 8223−8228.
(46) Rao, A. N.; Rodesch, C. K.; Grainger, D. W. *Anal. Chem.* **2012**, *84*, 9379−9387.
(47) Grainger, D. W.; Greef, C. H.; Gong, P.; Lochhead, M. J. *Methods Mol. Biol.* **2007**, *381*, 37−57.
(48) Nguyen, V. X.; Stebe, K. J. *Phys. Rev. Lett.* **2002**, *88* (16), 164501.
(49) Barbulovic-Nad, I.; Lucente, M.; Sun, Y.; Zhang, M.; Wheeler, A. R.; Bussmann, M. *Crit. Rev. Biotechnol.* **2006**, *26* (4), 237−259.
(50) Petersen, D. W.; Kawasaki, E. S. *Adv. Exp. Med. Biol.* **2007**, *593*, 1−11.
(51) Pappaert, K.; Ottevaere, H.; Thienpont, H.; Van Hummelen, P.; Desmet, G. *BioTechniques* **2006**, *41* (5), 609−616.
(52) Draghici, S.; Khatri, P.; Eklund, A. C.; Szallasi, Z. *Trends Genet.* **2006**, *22* (2), 101−109.
(53) Peterson, A. W.; Heaton, R. J.; Georgiadis, R. M. *Nucleic Acids Res.* **2001**, *29* (24), 5163−5168.
(54) McQuain, M. K.; Seale, K.; Peek, J.; Levy, S.; Haselton, F. R. *Anal. Biochem.* **2003**, *320* (2), 281−291.
(55) Lee, K. S.; Ivanova, N.; Starov, V. M.; Hilal, N.; Dutschk, V. *Adv. Colloid Interface Sci.* **2008**, *144* (1−2), 54−65.
(56) Dias, R.; Rosa, M.; Pais, A. C.; Miguel, M.; Lindman, B. *J. Chin. Chem. Soc. (Taipei, Taiwan)* **2004**, *51* (3), 447−469.
(57) Zanchetta, G.; Nakata, M.; Buscaglia, M.; Bellini, T.; Clark, N. A. *Proc. Natl. Acad. Sci. U.S.A.* **2008**, *105* (4), 1111−1117.
(58) Liu, F.; Yang, J.; Huang, L.; Liu, D. *Pharm. Res.* **1996**, *13* (11), 1642−1646.
(59) Randolph, J. B.; Waggoner, A. S. *Nucleic Acids Res.* **1997**, *25* (14), 2923−2929.
(60) Lehmann, U. *Thin Solid Films* **1988**, *160* (1−2), 257−269.
(61) Linck, L.; Kapusta, P.; Resch-Genger, U. *Photochem. Photobiol.* **2012**, *88*, 867−875.
(62) Sobek, J.; Aquino, C.; Schlapbach, R. *Methods Mol. Biol.* **2007**, *382*, 33−51.
(63) Benvin, A. L.; Creeger, Y.; Fisher, G. W.; Ballou, B.; Waggoner, A. S.; Armitage, B. A. *J. Am. Chem. Soc.* **2007**, *129* (7), 2025−2034.
(64) Nazarenko, I.; Pires, R.; Lowe, B.; Obaidy, M.; Rashtchian, A. *Nucleic Acids Res.* **2002**, *30* (9), 2089−2195.
(65) Cox, W. G.; Beaudet, M. P.; Agnew, J. Y.; Ruth, J. L. *Anal. Biochem.* **2004**, *331* (2), 243−254.
(66) Laib, S.; Seeger, S. *J. Fluoresc.* **2004**, *14* (2), 187−191.
(67) Unruh, J. R.; Gokulrangan, G.; Lushington, G. H.; Johnson, C. K.; Wilson, G. S. *Biophys. J.* **2005**, *88* (5), 3455−3465.
(68) Di Fiori, N.; Meller, A. *Biophys. J.* **2010**, *98* (10), 2265−2272.
(69) Chhabra, R.; Sharma, J.; Wang, H.; Zou, S.; Lin, S.; Yan, H.; Lindsay, S.; Liu, Y. *Nanotechnology* **2009**, *20* (48), 485201.
(70) Fegan, A.; Shirude, P. S.; Balasubramanian, S. *Chem. Commun. (Cambridge, U.K.)* **2008**, No. 17, 2004−2006.
(71) Ng, J. H.; Ilag, L. L. *Biotechnol. Annu. Rev.* **2003**, *9*, 1−149.
(72) Lange, S. A.; Benes, V.; Kern, D. P.; Horber, J. K.; Bernard, A. *Anal. Chem.* **2004**, *76* (6), 1641−1647.
(73) Massey, M.; Algar, W. R.; Krull, U. J. *Anal. Chim. Acta* **2006**, *568* (1−2), 181−189.
(74) Landry, J. P.; Zhu, X. D.; Guo, X. W.; Gregg, J. P. *Mater. Res. Soc. Symp. Proc.* **2003**, *773*, 161−166.
(75) Relogio, A.; Schwager, C.; Richter, A.; Ansorge, W.; Valcarcel, J. *Nucleic Acids Res.* **2002**, *30* (11), e51.
(76) Wrobel, G.; Schlingemann, J.; Hummerich, L.; Kramer, H.; Lichter, P.; Hahn, M. *Nucleic Acids Res.* **2003**, *31* (12), e67.
(77) Dawson, E. D.; Reppert, A. E.; Rowlen, K. L.; Kuck, L. R. *Anal. Biochem.* **2005**, *341* (2), 352−360.
(78) Rao, A. N.; Eichinger, C. D.; Hlady, V.; Grainger, D. W. *Soft Matter* **2012**, in press.

High-resolution epifluorescence and TOF-SIMS chemical imaging comparisons of single DNA microarray spots

Archana N. Rao[1], Nicolas Vandencasteele[2,§], Lara J. Gamble[2] and David W. Grainger[1,3*]

* Corresponding author: David W. Grainger, david.grainger@utah.edu

Supporting Information

Abstract: The supporting information presented here describes further details from the experimental section (oligonucleotide sequences and layouts of printed DNA spots) and explanation of microarray printing methodology and epifluorescence imaging. The results and discussion section includes epifluorescence images pixel intensities for varying DNA and DNA-Cy3 dye concentrations, schematics of Marangoni flow for DNA spot drying, comparison of 200-micron spots using TOF-SIMS, epifluorescence and fluorescence scanner images, image orientation methods for cross-technique image comparisons, plots of spot RFU *vs.* DNA print concentration demonstrating non-linear RFU increase with increasing DNA and DNA-Cy3 fractions, method for measuring DNA spot dimensions with Image-J and their comparison to TOF images of the same 200-micron spot, and plots comparing DNA spot dimensions measured with epifluorescence and TOF-SIMS for 100- and 200- micron spots of varying DNA and DNA-Cy3 concentrations.

Data presented:

Materials and methods

- Table S-1: DNA oligonucleotide probe sequences and terminal modifications
- Figure S-1: Schematic layout of microarray prints with varying concentrations of DNA in distinct Cy3-labeled and unlabeled DNA probe mixed ratios in rows of 10 spots each. (Bold indicates spots of print buffers only).

Results and discussion:

- Table S- 2. Comparison of dimensions of identical printed DNA spot (100-micron diameter) with fluorescence scanner, epifluorescence imaging and corresponding (negative ion phosphate peak PO_3^-) TOF-SIMS imaging.
- Figure S-2: Comparison of pseudo-colored image (left) vs. gray scale image (right) of the same DNA spot.
- Figure S-3: Surface pixel intensity plots of dried DNA probe spots of varying DNA and DNA-Cy3 concentrations.
- Figure S-4: Schematics of DNA droplet drying process for printed droplets containing a mixture of DNA, salts and surfactants.
- Figure S-5: Comparison of DNA spots of 40μM DNA spotting concentrations containing increasing amounts of DNA-Cy3 with TOF-SIMS, epifluorescence and fluorescence scanner images of identical ~200 micron DNA spots.
- Figure S-6: Comparison of epifluorescence and fluorescence scanner images of dried DNA spots of RFU vs. pixel intensity.
- Figure S-7: Comparison of spot features in identical DNA spots (100μm spot diameter) with TOF-SIMS, epifluorescence and fluorescence scanner images.

- Figure S-8: Plot of RFU *vs.* DNA concentration with increase in the amount of DNA and the fractional amount of DNA-Cy3 per print using epifluorescence imaging of 100-micron and 200-micron spots.
- Figure S-9: Comparison of dimensions of identical printed DNA spot (100-micron diameter) using corresponding (negative ion phosphate peak (PO_2^-), TOF-SIMS image and epifluorescence imaging.
- Figure S-10: Illustration of measuring DNA spot dimensions from epifluorescence images using Image-J.
- Figure S-11: Comparisons of TOF-SIMS images and epifluorescence images of same ~200 micron DNA spot.
- Figure S-12A: Plot of DNA spot dimensions with varying DNA-Cy3 concentrations for 100-micron DNA spots as measured with TOF-SIMS and epifluorescence techniques,
- Figure S-12B: Plot of DNA spot dimension with varying DNA-Cy3 content (40μM total DNA concentration) for 100 and 200-micron DNA spots as measured with TOF-SIMS and epifluorescence techniques.

MATERIALS AND METHODS

Table S-1. DNA oligonucleotide probe sequences and terminal modifications

DNA	Identifier	5'-modification	Sequence	3'-modification
Probe	Oligo1-NH_2	--	CTGAACGGTAGCATCTTGAC	-C_6-NH_2
Probe	Cy3-Oligo1-NH_2	Cy3-C_6-	CTGAACGGTAGCATCTTGAC	-C_6-NH_2

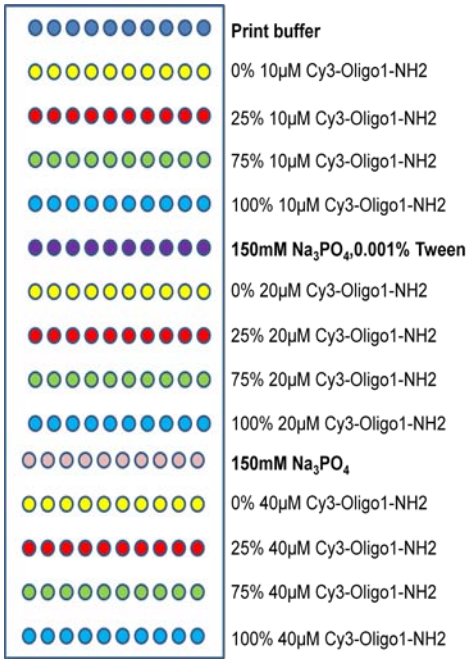

Figure S-1. Schematic layout of microarray prints with varying concentrations of DNA in distinct Cy3-labeled and unlabeled DNA probe mixed ratios in rows of 10 spots each. (Bold indicates spots of print buffers only).

Buffer salts, sarcosine, sodium dodecyl sulfate (SDS), Tween20 and ethanolamine (ACS grade) were purchased from Sigma-Aldrich (St. Louis, USA). Ultrapure water (UPW) was used for all solution preparations and rinsing printed slides (ASTM type I water, 18.2 MΩ-cm)

Microarray fabrication: Multiple Microarray Format SpoCLe Generator version 1.1.02 software (ArrayIt) was programmed to print multiple microarrays per slide substrate to obtain arrays of varying DNA-Cy3 concentrations. SMP4 pins spotting 1.1 nanoliters of DNA print solution produced dried spots with a diameter of ~135 microns and a spot-to-spot spacing of 160 microns. Larger SMP6 pins were used to dispense 1.8 nanoliters

to obtain larger spots of ~200 microns diameter with spot-to-spot spacing of 155 microns. Prior to starting each print run, pin print heads were calibrated according to manufacturer's recommended procedures with SNS4 or SNS6 solid calibrating pins for 135-micron and 200-micron diameter spots, respectively, to ensure standard print behavior on polymer-coated slides. Duplicate arrays were printed on separate slides to compare probe-only arrays. DNA spots were obtained by optimizing printing protocols including washing and drying cycles to prevent carryover of DNA print solutions between serial prints. To this end, spots were printed in replicates of 5 followed by a pin wash step (wash buffer containing 20% ethanol and 0.01% Tween20 in ultrapure water) and a dry cycle. Humidity during printing was maintained at approximately 60-65% with a built-in humidity chamber and printing was performed at ambient temperature (23°C). Fully printed slides were then incubated overnight (>12 h) at room temperature under 75% relative humidity using an in-house fabricated saturated salt water bath.

Post-print treatment of printed microarray slides: Briefly, slides were rinsed in sodium phosphate print buffer and then immersed in blocking solution (50mM ethanolamine in 0.1M Tris, pH 9.0) at 50°C for 30 min to consume residual amine-reactive groups. Subsequently, slides were rinsed thoroughly with UPW for 3 times followed by immersion in hybridization buffer (4X saline sodium citrate (SSC) containing 0.1% SDS at pH 7) at 50°C for 30 min. Slides were finally rinsed with UPW 3 times, blown dry with nitrogen, and immediately imaged for probe-only studies.

Detailed description of imaging with epifluorescence microscopy: For 40μM DNA spots, a 20X objective was employed, while for 20 and 10 μM print spots, a 40X objective was used since 40μM spots were slightly larger compared to the 20 and 10 μM spots. The environmental control stage maintained each slide at room temperature (23ºC) and 60-65% humidity during imaging. Images were captured with an exposure time of 100ms and binning was set to 2x2. Images were captured with Metamorph software as raw color images (36-bit) saved as 16-bit monochrome images, and then further processed with Image-J software (version 1.41). For clarity and interpretation, all the images are pseudo-colored and the contrast was adjusted using auto-scale function in Image J. The scale bar for both 20X and 40X images was measured from an imaged hemocytometer for converting pixels to microns to calculate DNA spot dimensions.

Detailed description of imaging with TOF SIMS: Printed, rinsed-blocked, dried spot sizes for TOF-SIMS images were determined using Image J software for fields of view determined from IONTOF software. The IONTOF instrument was calibrated following IONTOF protocols. Knowing the total image size and its resolution (256x256 pixels) allowed conversion of image pixels to microns. Spot sizes were measured by visually determining the spot diameter and counting numbers of pixels using Image J. Measurements performed on both positive ($C_5H_5O^+$) and negative (PO_2^-) images produced size variations between these 2 images of less than 5%."

RESULTS AND DISCUSSION

DNA concentration	% Cy3	Fluorescence scanner (μm)	Epifluorescence (μm)	TOF-SIMS (μm)
10μM	25	100	108	95
10μM	75	120	122	112
10μM	100	105	120	112
20μM	25	100	112	105
20μM	75	110	121	118
20μM	100	115	119	120
40μM	0	65	72	88
40μM	25	100	121	114
40μM	75	120	127	119
40μM	100	130	141	130

Table S-2. Comparison of dimensions of identical printed DNA spot (100-micron diameter) with fluorescence scanner, epifluorescence imaging, and corresponding (negative ion phosphate peak PO_3^-) TOF-SIMS imaging. The DNA spot has comparable gross printed morphology and size of distribution of Cy3-DNA using all three imaging techniques.

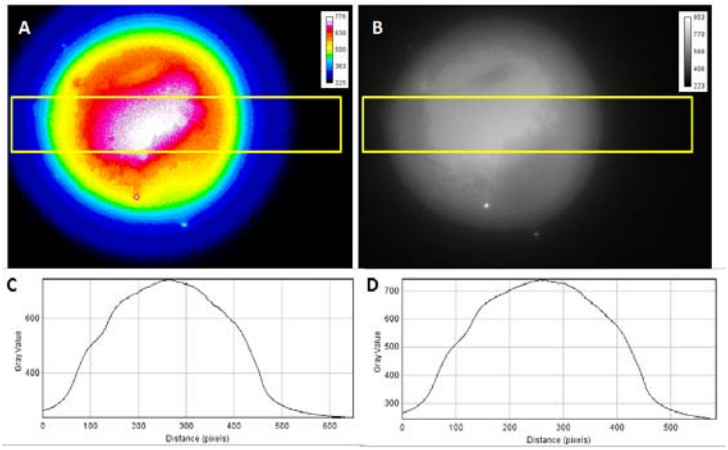

Figure S-2: Comparison of pseudo-colored image (left) vs. gray scale image (right) of the same DNA spot. A) The pseudo-colored DNA spot is shown with the intensity calibrator scale to depict fluorescent intensities. B) The gray scale image of the same spot has the same variation in pixel intensity as shown in intensity scale C) The spot line-scan intensity profile (below the pseudo colored image) shows variations in intensity across the spot. The Image J-plot profile was performed in the selected yellow rectangle region across the spot in each case. D) Gray scale radial pixel intensities showing similar plot intensity profile as colored image.

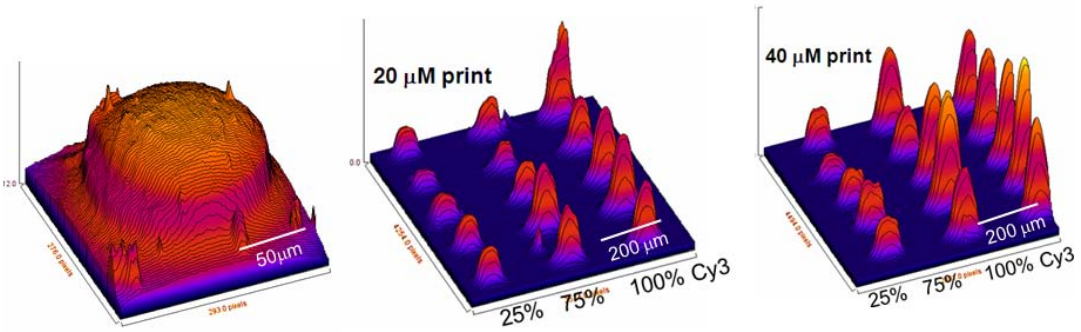

Figure S-3: Surface pixel 3-D intensity plots of dried DNA probe spots showing a single spot fluorescent heterogeneity (far left) and spot-to-spot DNA-Cy3 intensity (center, right) variations as a function of spot diameter, total DNA concentration and DNA-Cy3:DNA probe ratios. As the ratio of dye-labeled DNA probe increases from 25% to 75% to 100%, spot heterogeneity both within a single spot (left) and between spots (center, right) increases. This effect is also observed with increased total printed DNA probe concentrations (20μM, center, and 40μM, right).

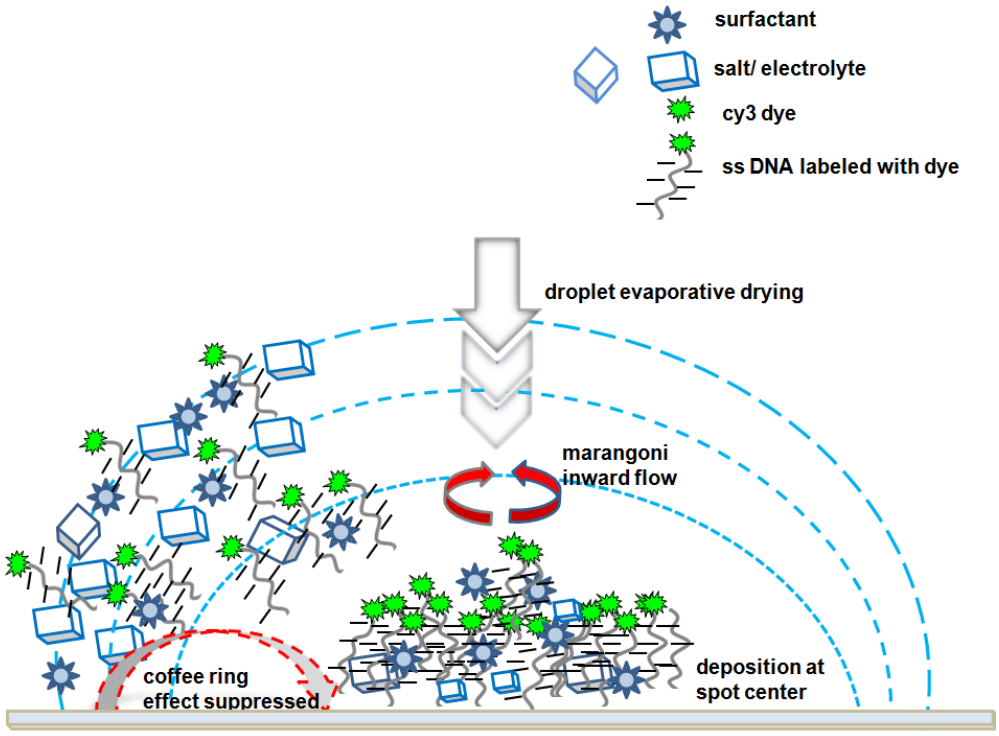

Figure S-4: Schematic of DNA microdroplet drying process for mixtures of DNA, salts and surfactants.

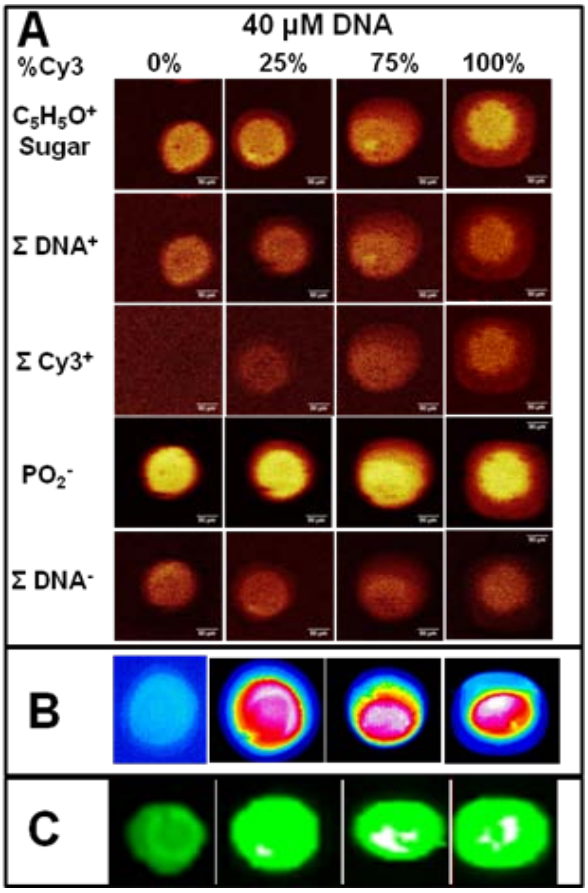

Figure S-5. Comparisons of DNA spots of 40µM DNA spotting concentrations containing increasing amounts of Cy3 dye-labeled DNA with TOF-SIMS, epifluorescence and fluorescence scanner images of identical ~200 micron DNA spots (compare each vertical column) of 40µM DNA concentration and fractional DNA-Cy3 dye label content (each vertical column) A) TOF-SIMS chemical images of different DNA chemical fragments (250 µm × 250 µm image sizes), B) epifluorescence images selecting DNA-Cy3 signal, images are 125µm × 125µm, and C) conventional fluorescence scanner images with filter set to excite Cy3.

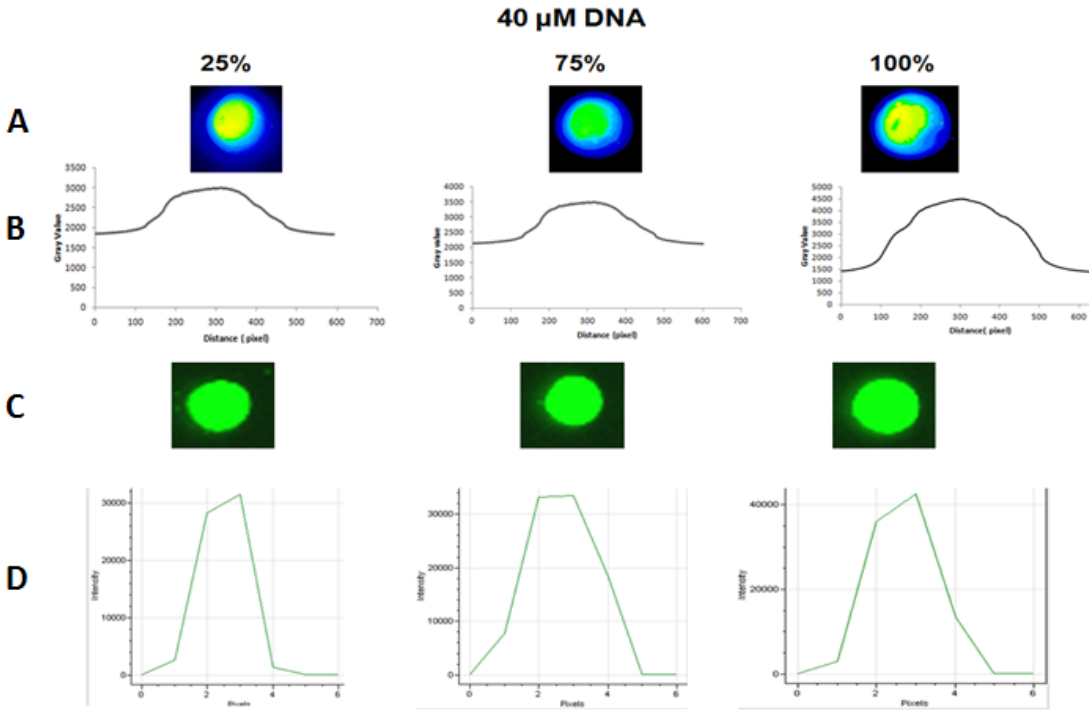

Figure S-6: Comparison of epifluorescence and fluorescence scanner images. A) Epifluorescence image of DNA spot; B) Image J- plot profile of fluorescence intensity vs. pixel across the spot. C) Fluorescence scanner images of the same DNA spot. D) Plot profile of the scanner images across the spot of RFU intensity vs. pixel at lower resolution than (B).

High-resolution epifluorescence and TOF-SIMS image comparisons of individual DNA microspots.

Specific distinguishing shape features of printed DNA droplets, including oval versus round morphologies, printed spikes, comet tailing or spot bulging, and internal intensity features were examined with both techniques at different magnifications based on spot sizes and image resolution. Both 20X (for 40μM DNA spots) and 40X (for 20μM and 10μM DNA spots) magnifications for identical DNA spots were directly compared with TOF-SIMS images and a single scanner image. For example, in Figure S-6A the bulge artifact at the spot edge of a same 100-micron diameter spot was a prominent, recognizable, distinguishing feature both in epifluorescence and TOF-SIMS images, irrespective of differences in spot image intensity. The drying artifact and distinguishing feature at the center within the 100-micron spot shown in Figure S-6B was comparable between the two techniques, and not observable in the scanner image. However, epifluorescence images show a graduation in fluorescence intensity across the spot whereas TOF-SIMS images reveal a high (spot center) and low intensity (spot edges) regions in the DNA spot.

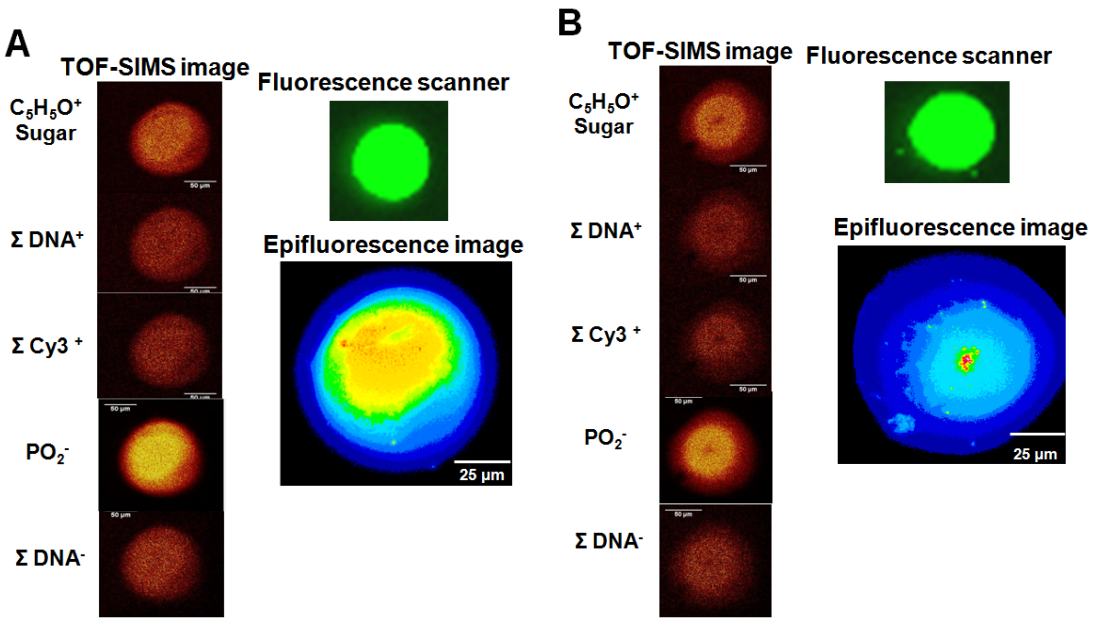

Figure S-7: Comparison of TOF-SIMS, epifluorescence and fluorescence scanner images of identical DNA spots. A) 100μm-diameter DNA spot (40μM DNA, 100% Cy3-DNA) exhibiting similar spot morphology for both epifluorescence and TOF-SIMS. The spot features and high intensity Cy3-DNA central region of the spot match. B) Similar comparisons with 200μm DNA spot (20μM, 75% Cy3-DNA). Epifluorescence images of 100-micron diameter spots are 125μm × 125μm and 200 micron spot are 200μm × 200μm; TOF-SIMS of 100 micron spot image was 200μm × 200μm and the 200micron spot was 250μm × 250μm.

Comparable features, intra-spot heterogeneities and artifacts created by spot drying were commonly identified between high-resolution imaging techniques irrespective of intensity differences. Only gross spot shapes lacking such detail are detectable with fluorescence scanner images (also shown in Figure 3). These results indicate that heterogeneous spot features obtained with high resolution epifluorescence images of DNA-Cy3 correlate well with TOF-SIMS chemical imaging for DNA and Cy3 features, providing complimentary information for common features. Significantly, none of these features are detectable in common commercial fluorescent scanner images.

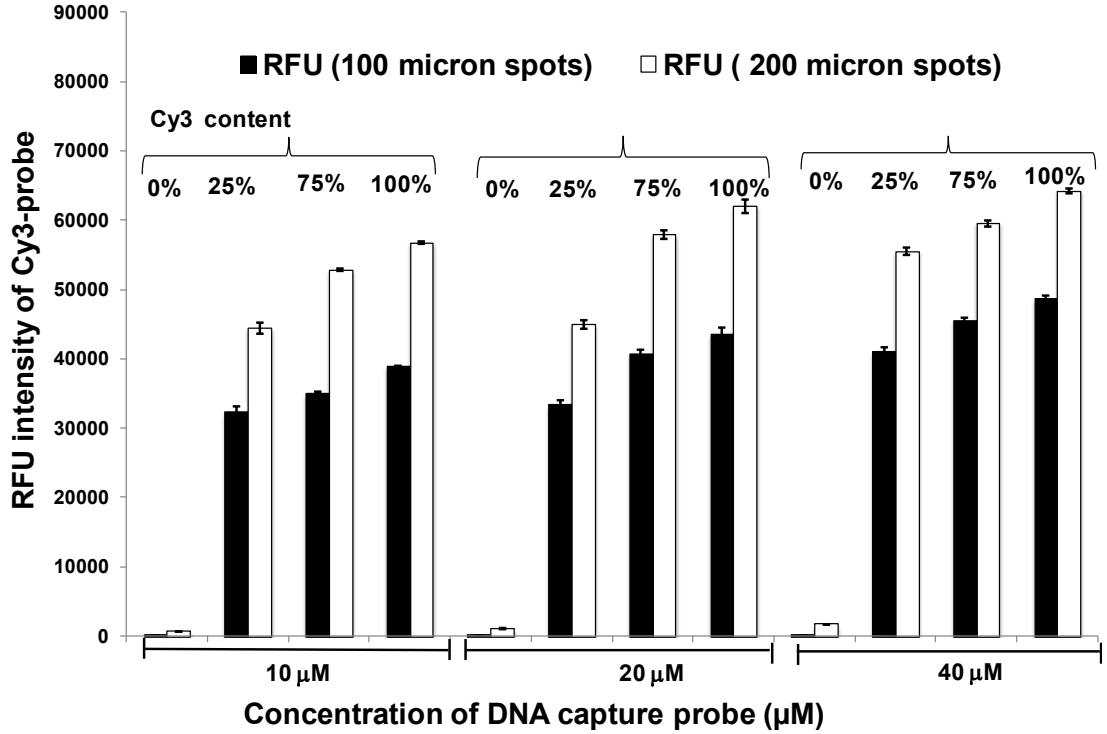

Figure S-8. Variations in spot integrated RFUs (relative fluorescence units) with increase in the total amount of DNA and also fractional amounts of DNA-Cy3 per print using epifluorescence imaging of 100-micron and 200-micron spots.

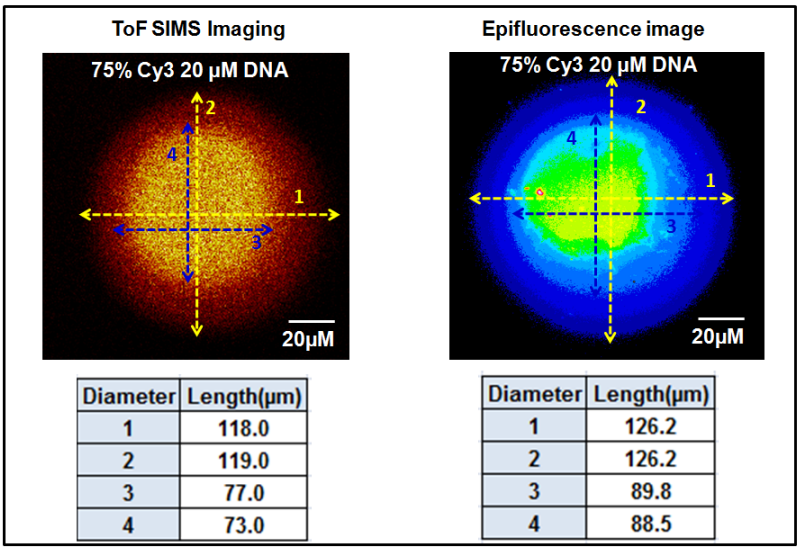

Diameter	Length(µm)
1	118.0
2	119.0
3	77.0
4	73.0

Diameter	Length(µm)
1	126.2
2	126.2
3	89.8
4	88.5

Figure S-9. Comparison of dimensions of identical printed DNA spot (100-micron diameter) using corresponding (negative ion phosphate peak (PO_2^-), TOF-SIMS image and epifluorescence imaging. The DNA spot has comparable gross printed morphology, size and distribution of Cy3-DNA using both imaging techniques.

Dimensions from both methods are comparable: orthogonal spot diameters of 118 µm and 126 µm for the same DNA spot (±10% across many images). These dimensions for epifluorescence high intensity DNA-Cy3 images (brighter) were comparable to higher intensity (i.e., yellow regions) TOF-SIMS regions mapping nucleotide phosphate fragment m/z 63 (PO_2^-). TOF-SIMS images reveal similar spot patterns for phosphate, DNA, and Cy3.

Data confirming accuracy of measurement of DNA-Cy3 distribution in epifluorescence imaging with Image-J software:

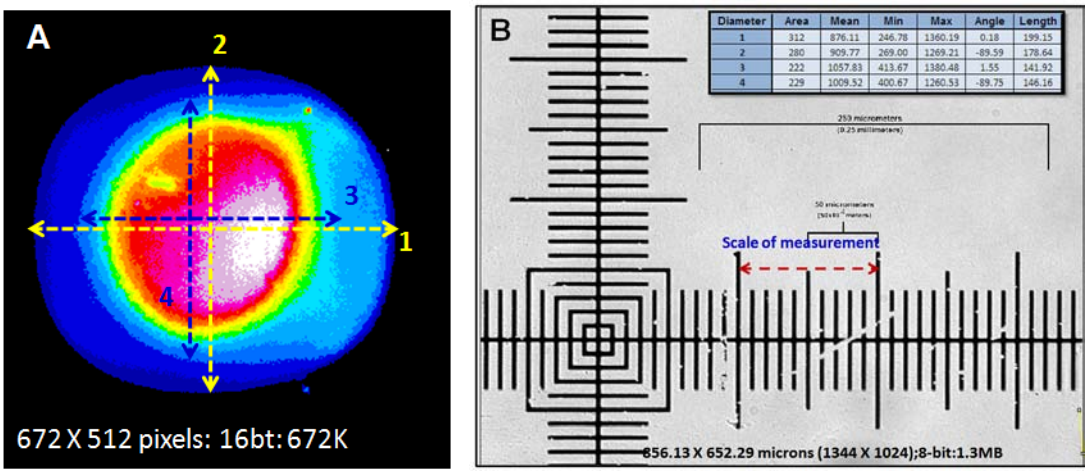

Figure S-10. Measurements of high intensity region of DNA-Cy3 distribution in single spot (pseudo-colored epifluorescence image) image of 40μM DNA with 100% DNA-Cy3 (~200 micron spot). A) Direct measurement of respective diameters for different regions of printed DNA spots. B) Image-J measurement of the different regions as captured on the epifluorescence microscope with 20X magnification.

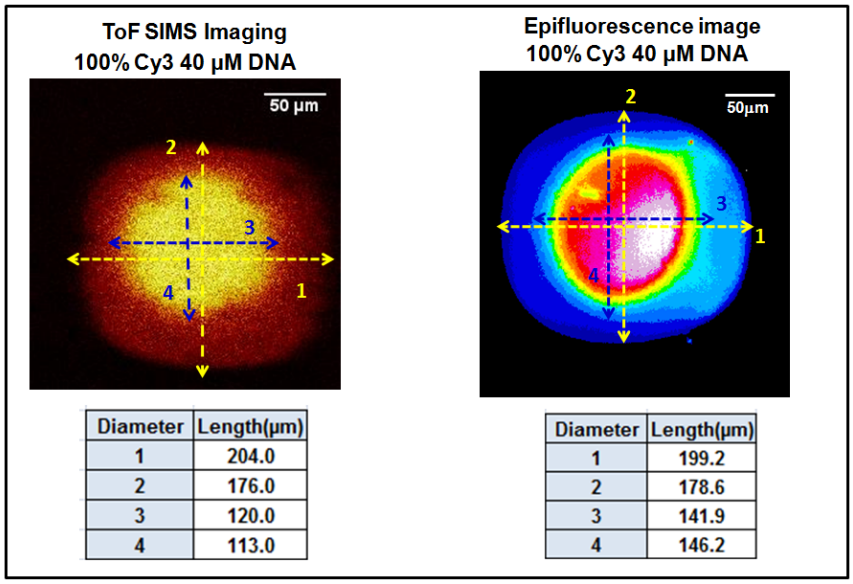

Diameter	Length(μm)
1	204.0
2	176.0
3	120.0
4	113.0

Diameter	Length(μm)
1	199.2
2	178.6
3	141.9
4	146.2

Figure S-11. Comparison of single spot TOF-SIMS images (m/z for negative ion phosphate peak PO_3^-) with identical epifluorescence images (40X magnification) for a ~200 micron diameter DNA spot; spots are comparable for geometry, orientation and size and DNA dye distribution due to drying and spreading.

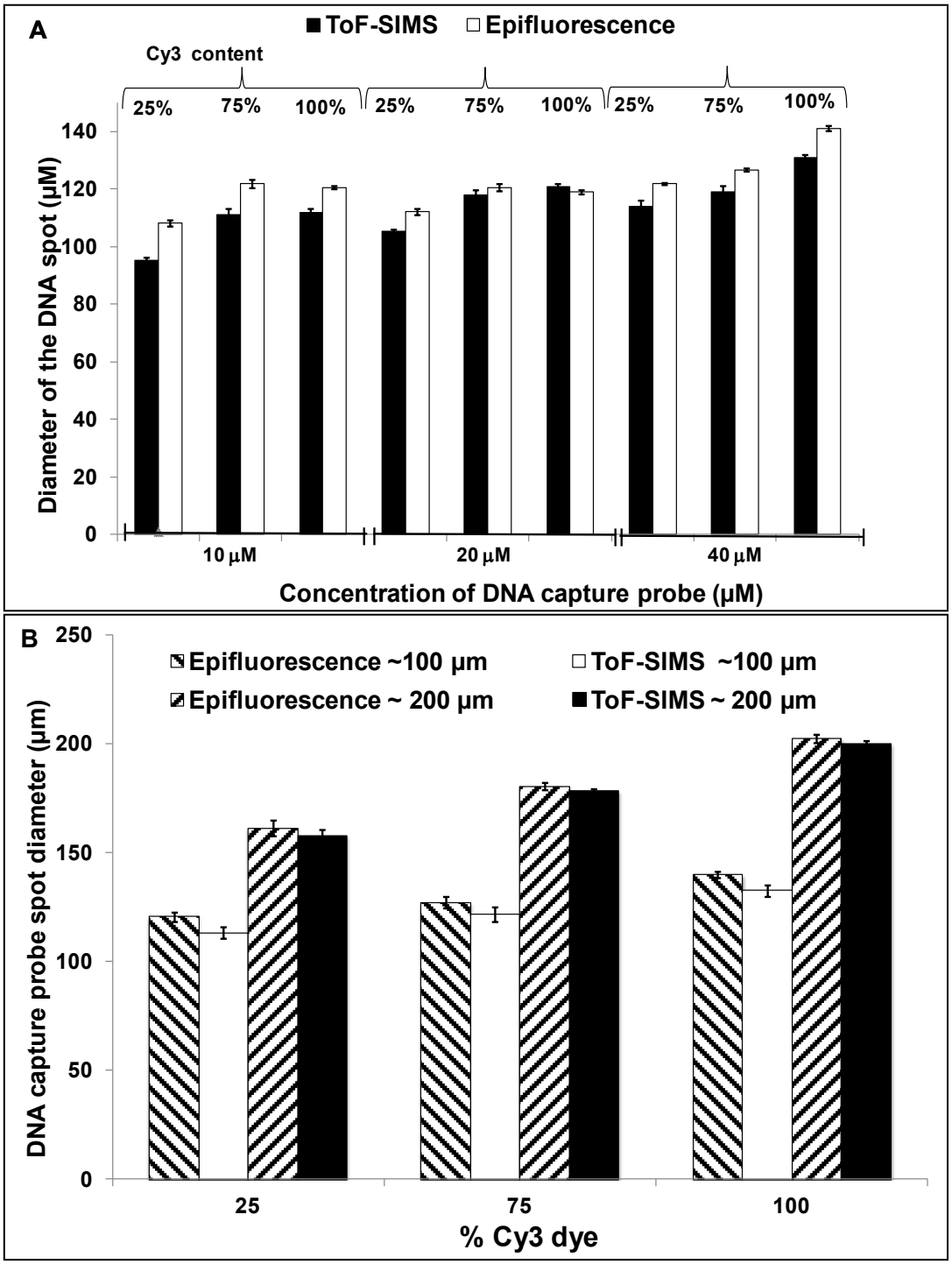

Figure S-12. Printed spot size dependence on total DNA concentration and DNA-Cy3 probe ratio. A) DNA spot size dependence with variations in DNA-Cy3 concentration for 100-micron DNA spots as measured with TOF-SIMS and epifluorescence techniques, and B) Close correlation of dried spot diameters for 200µm DNA spots using both TOF-SIMS and epifluorescence imaging of identical spots comprising 40µM DNA print concentrations with different ratios of DNA-Cy3 in the print solution.

CHAPTER-3

REAL-TIME FLUORESCENT IMAGE ANALYSIS OF DNA SPOT HYBRIDIZATION KINETICS TO ASSESS MICROARRAY SPOT HETEROGENEITY

Archana N. Rao[1], Christopher K. Rodesch,[2] and David W. Grainger[1,3*]

[1]Department of Pharmaceutics and Pharmaceutical Chemistry, University of Utah, Salt Lake City, UT 84112-5820 USA

[2] Health Sciences Core Research Facilities, School of Medicine, University of Utah, Salt Lake City, UT 84112 USA

[3]Department of Bioengineering, University of Utah, Salt Lake City, UT 84112 USA

**to whom correspondence should be addressed:* David W. Grainger, david.grainger@utah.edu

Keywords: DNA microarray, printing, confocal imaging, duplex, real-time hybridization, fluorescence resonance energy transfer, FRET, spot heterogeneity

---

Reprinted with kind permission from Analytical Chemistry: Anal. Chem., 2012, 84 (21), pp 9379–9387 DOI: 10.1021/ac302165h; Publication Date (Web): October 8, 2012

analytical chemistry

Article

pubs.acs.org/ac

Real-Time Fluorescent Image Analysis of DNA Spot Hybridization Kinetics To Assess Microarray Spot Heterogeneity

Archana N. Rao,[†] Christopher K. Rodesch,[‡] and David W. Grainger*[,†,§]

[†]Department of Pharmaceutics and Pharmaceutical Chemistry, [‡]Health Sciences Core Research Facilities, School of Medicine, and [§]Department of Bioengineering, University of Utah, Salt Lake City, Utah 84112, United States

Supporting Information

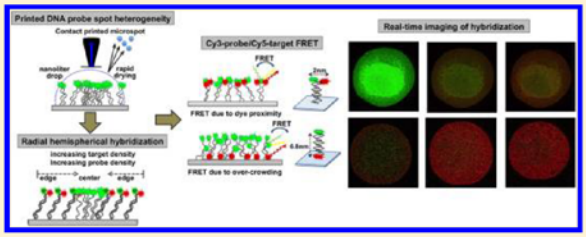

ABSTRACT: Current microarray assay technology predominately uses fluorescence as a detectable signal end point. This study assessed real-time in situ surface hybridization capture kinetics for single printed DNA microspots on solid array surfaces using fluorescence. The influence of the DNA target and probe cyanine dye position on oligo-DNA duplex formation behavior was compared in solution versus surface-hybridized single DNA printed spots using fluorescence resonance energy transfer (FRET) analysis. Fluorophore Cy3/Cy5 fluorescence intensities were analyzed both through the printed hybridized DNA spot thickness and radially across single-spot surfaces. Confocal single-spot imaging shows that real-time in situ hybridization kinetics with constant target concentrations changes as a function of the printed probe density. Target-specific imaging in single spots exhibits a heterogeneous printed probe radial density that influences hybridization spatially and temporally via radial hemispherical diffusion of dye-labeled target from the outside edge of the spot to the interior. FRET of the surface-captured target occurs irrespective of the probe/target fluorophore position, resulting from excess printed probe density and spot thickness. Both heterogeneous probe density distributions in printed spots and the fluorophore position on short DNA oligomers influence duplex formation kinetics, hybridization efficiencies, and overall fluorescence intensity end points in surface-capture formats. This analysis is important to understanding, controlling, and quantifying the array assay signal essential to reliable application of the surface-capture format.

DNA microarrays provide relative levels of expression for up to tens of thousands of genes in parallel on a single platform and are widely employed in genotyping, drug discovery, and gene expression profiling.[1] Accurate analysis and signal interpretation presents immense challenges to quantitative analysis and clinical translation.[2,3] Multiple sources of microarray spot heterogeneity, reproducibility, and repeatability are known, contributing to assay variability and inconsistency.[4−7] The DNA oligomer surface hybridization process with printed probes exhibits a complex kinetic and thermodynamic dependence on local interfacial environmental factors, including probe attachment modalities on solid supports,[8] surface probe density issues associated with steric and electrostatic interactions,[9] length and sequence specificities of the probe with the target,[10] increased nonspecific binding/cross-hybridization at higher probe densities, causing target cross-binding to neighboring probes,[11] and nonspecific influences.[12,13] Additional factors include surface chemistry to reduce nonspecific background noise, binding interference, and reliable probe immobilization and presentation.[14] Strategies to improve target−surface hybridization to solid supports include microspot size to overcome mass transfer limitations[15] and surface diluent spacers (e.g., mercaptohexanol,[16] 11-mercapto-1-undecanol,[17] oligoethylene glycols[17]) that reduce nonspecific probe−surface interactions, control electrostatic forces and steric issues between adjacent DNA probes, probe density, orientation and presentation to the incoming target analyte. Furthermore, increasing the ionic strength[18] during oligonucleotide probe deposition and electrostatic balance between the immobilized oligonucleotide charge density and solution ionic strength[19] can significantly increase the assay hybridization efficiency.

DNA hybridization at the solid−liquid interphase is complex: a stochastic process with nonlinear kinetics and analyte concentration dependence.[20] The simplest two-state model involving hybridization of matched complementary oligomer sequences is represented as a one-step reversible reaction model with forward and reverse rate constants and a binding equilibrium constant. Capture is influenced by DNA surface

Received: July 29, 2012
Accepted: October 8, 2012
Published: October 8, 2012

transport, adsorption/desorption, the probe/target length, the ionic strength, the extent of probe–target interactions, the 2-D diffusion coefficient, and the immobilized probe density.[13] Target binding is similar to ligand–receptor pairing: a hybrid of diffusion and reaction-controlled models with overall binding kinetics sensitive to both reaction rates and surface diffusion.[21] Various modifications of Langmuirian binding isotherms have been proposed for DNA hybridization on solid surfaces. Vainrub and Pettitt[22,23] account for repulsion between the target DNA and surface-immobilized oligonucleotide probes, producing a Coulombic blockage of target binding. Chan et al.[11] incorporated heterogeneous hybridization isotherms considering both the length and surface diffusion of the target with changing probe surface coverage. Further modification[24] considered competitive hybridization of surface vs bulk hybridization, entropic and enthalpic contributions[25] of the probe immobilized on an impenetrable surface, the polydispersity of the probe and target, and electrostatic interactions within the probe layers. A Langmuir-based hybridization model predicts two different mechanisms: direct hybridization from solution and hybridization by targets that first adsorb nonspecifically and then surface-diffuse to probes, showing that DNA hybridization on solid supports may be extremely efficient for physically realistic 2-D diffusion coefficients, target concentrations, and surface probe densities.[11] Langmuir models deviate from ideality with increasingly crowded probes and duplexes. Hybridization yields become insensitive to target concentrations at high ionic strengths and within densely tethered films.[26] Commercial microarray data under real-world conditions suggest that these nonidealities impact solid-phase hybridization versus identical sequences in solution.[27,28]

End-tethered single-stranded DNA (ssDNA) at a surface is characterized as a flexible polyanionic chain, while double-stranded DNA (dsDNA) is compared to a rigid polyanionic rod. This plays an important role in the kinetics and thermodynamics of the hybridization process. The dsDNA persistence length has been shown to be ~50 nm in salt concentrations greater than 10 mM, while that for ssDNA is ~1 nm. Hence, ssDNA is not only much more flexible than dsDNA, but also affected by conditions near a surface.[29,30] Moreover, the DNA persistence length increases with the strand length, temperature, and ionic strength, attributed to exaggerated end effects from shorter strands.[31] Increasing probe surface density creates a polyelectrolyte brush from collective crowding of nucleic acid tails. The ionic microenvironment within dense end-attached DNA oligonucleotides (i.e., DNA brushes) produces interfacial DNA brush electrostatics influencing target capture:[32] hybridization rates for longer oligomer lengths are reduced.[33] Therefore, tethered DNA strand dynamics and interfacial properties (flexibility, elasticity, and electrostatics all influencing steric contributions) affect the ssDNA conformation at surfaces and alter DNA target hybridization from solution.

Monitoring real-time DNA hybridization kinetics with different optical (ellipsometry,[34,35] evanescent wave methods,[36] and surface plasmon resonance[37]), physical or electrochemical (potentiometric stripping analysis,[38] amperometry[39]), and fluorescence (fluorescence resonance energy transfer (FRET),[40,41] fluorescence correlation spectroscopy[42]) analytical tools is common. Confocal fluorescence microscopy has been used in real-time detection of single oligonucleotides in solution.[43] FRET-based analysis for DNA in situ hybridization with donor–acceptor fluorophore pairs (i.e., Cy3-probe and Cy5-target) is extensively used[44,45] to report intermolecular fluorophore distances, conformations, molecular dynamics, and kinetics.[46] The FRET efficiency between Cy3 and Cy5 fluorophores attached to the different locations in DNA duplexes demonstrates a power law dependence on the separation distance and relative fluorophore dipole orientations.[47−49] FRET's orientational dependence is likely most significant when the fluorophores are constrained, such as for DNA bound to solid substrates where fluorophore motion is limited.[50] Acceptor photobleaching is also used to validate FRET, quantitatively determined by a "de-quenching" method comparing the intensities of Cy3-donor emission before and after photobleaching of the Cy5-acceptor.[51,52] Notably, cyanine dyes are predominately used for single-molecule FRET measurement and for DNA microarray analysis due to their favorable fluorescence quantum yields and photostabilities, low pH sensitivities, and ability to employ inexpensive diode lasers.[53] Additionally, repeated microarray optical scanning and other intense laser exposure can promote non-intentional dye photobleaching.[54]

In this study, we monitored real-time hybridization of a target to surface-tethered, dye-labeled DNA probes using confocal microscopy of individual printed DNA spots on array substrates. This analysis follows our recent comparisons of single printed probe microspots using epifluorescence and scanner-based imaging compared to mass spectrometry chemical imaging analysis of identical printed spots.[55] Real-time direct visualization of target hybridization within single spots follows fluorescent intensities for both the cyanine probe and target dyes in situ over time. Pronounced differences in hybridization kinetics to achieve spot target saturation were observed, although spot-to-spot hybridization kinetics for identical probe DNA concentrations and fractional probe DNA–fluorophore spot densities were comparable. Time-lapse images for spot hybridization show heterogeneous probe density distributions within printed DNA spots, resulting in time-dependent hybridization controlled by radial hemispherical diffusive flux of the target across the spot from the edge (less dense probe) to the center (denser probe). Also, spot hybridization is time-dependent with homogeneous probe densities due to transport limitations.[15] Moreover, Cy3-probe/Cy5-target FRET in printed spots using acceptor photobleaching over time and with spot depth showed little observable difference from the two distinct duplex-induced dye–dye orientations, possibly reflecting dense probe molecular environments and multiple nearest-neighbor donor–acceptor interactions in printed, micrometer-thick printed spots. By contrast, bulk solution-phase FRET readily distinguished the two different dye–dye duplex orientations, emphasizing distinct microenvironments for duplex formation in solution vs surface-bound assays. Furthermore, single-spot heterogeneity was probed by locally photobleaching the target-Cy5 dye over the spot thickness comprising the densely printed probe. Photobleaching studies also revealed a target-Cy5 signal at different depths in DNA microspots as shown by optical Z slices and additionally indicated that the photostability of Cy3/Cy5 pairings is critical to their analysis under multiple laser scans in microarray assays.

■ MATERIALS AND METHODS

Materials. HPLC-purified (≥90% purity) DNA oligomers with several different modifications (Table S-1, Supporting Information) were purchased from TriLink Biotechnologies

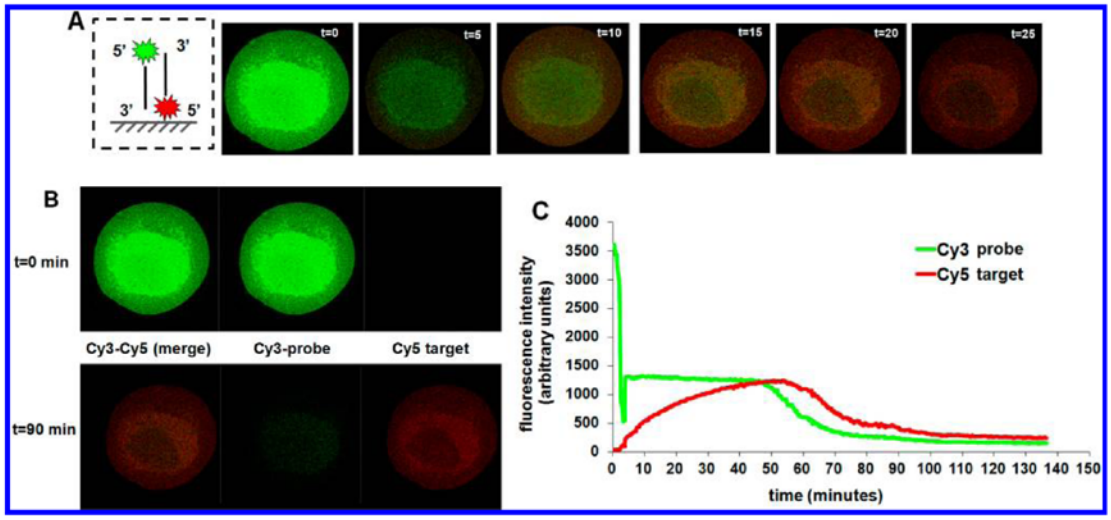

Figure 1. Real-time hybridization of a single DNA spot with dyes on opposite ends of the probe−target duplex: (A) schematic representation of the duplex, 5′-Cy3-Oligo1-probe with 5′-Cy5-Oligo2-target, and images of a DNA spot with merged Cy3 and Cy5 emission intensity at various time points; (B) images of spots in Cy3 or Cy5 or both filter channels during real-time imaging of single array spots before (t = 0) and after (t = 90 min) hybridization; (C) real-time hybridization of Cy3/Cy5 fluorescence intensity changes in single spots versus time. The duplex formation kinetics under this unstirred transport-limited regime follows pseudo-first-order kinetics (see the Supporting Information, Figure S-7). Note: microscopy image contrast has been digitally enhanced for the figures to better facilitate direct observation of the optical changes observed over time in situ.

(San Diego, CA). Ultrapure water (18.2 MΩ·cm) was used for all solutions and protocols. Cyanine Cy3 (probe) and Cy5 (target) fluorophores are incorporated at 5′ or 3′ oligonucleotide termini during synthesis using phosphoramidite reagents through a C6-linker to ssDNA.[56] All chemicals were used as received. Buffer salts, sarcosine, sodium dodecyl sulfate (SDS), and ethanolamine were ACS grade (Sigma-Aldrich, St. Louis, MO). Microarray slides (Slide H, amine-reactive 3D polymer-coated slides, Schott Nexterion, Louisville, KY) were used for DNA oligomer printing. New slides taken from the manufacturer's packaging were used without pre-treatment. Unused slides were stored under nitrogen at 4°C and used within a month to preserve the slide's ester reactivity.[57]

DNA Immobilization on Microarray Substrates Using Contact Printing. Microarrays were generated by printing multiple DNA probe concentrations (10, 20, and 40 μM) and different bulk solution ratios of Cy3-labeled (Cy3-Oligo1-NH_2) to unlabeled (Oligo1-NH_2) sequence-identical oligo-DNA probes (0:1, 1:3, 3:1, and 1:0 ratios) to provide printed rows containing no Cy3-labeled probes (0:1) with rows containing Cy3 gradient contents up to 100% Cy3-labeled probe (1:0). DNA probe solutions were prepared in print buffers containing 150 mM sodium phosphate, 0.001% Tween 20, and 0.001% sarcosine at pH 8.5. Spotted DNA arrays (5 × 4 spots of each probe concentration) with varying amounts of Cy3-DNA were printed in triplicate on separate slides to compare probe-only and hybridized duplex arrays. Contact printing was performed using a SpotBot2 contact printer and Stealth pins from Arrayit (Sunnyvale, CA). Further details of printing DNA spots and postprinting protocols are discussed in the Supporting Information.

Fluorescence Scanner Images of DNA Microarrays. Printed DNA microarray slides were scanned after blocking but prior to the hybridization steps (GenePix Microarray scanner 4100A, v.6 software) to record Cy3-DNA probe and Cy5-target DNA spot intensities. DNA-printed/hybridized slides were excited using two optical channels (535 and 635 nm for Cy3 and Cy5, respectively, laser power 100%, brightness and contrast 92%, PMT gain 400, pixel size 10 μm, line average set at 3).

Real-Time Confocal Imaging of Hybridization in Single DNA Spots. A fully automated Nikon A1R confocal microscope capable of capturing high-quality images was used to image real-time target hybridization, FRET, and photobleaching for single DNA microarray spots. Ultra-high-speed high-quality imaging scanned 512 × 512 pixels at 30 frames/s with a 40XELWD NA 0.80 air lens. Depth-dependent Z slice imaging in single printed spots was recorded with a 0.5 μm step size at 15 s intervals for 30 min time lapses. The slides were imaged with the printed side facing up and away from the objective to allow addition of hybridization buffer and target while imaging.

Real-Time Hybridization and FRET with Confocal Microscopy. To study real-time hybridization kinetics and FRET of DNA target oligomers with 5′-Cy3-labeled immobilized probe (i.e., a 5′-Cy3 dye position on oligonucleotide probes) and Cy5-labeled target (either 3′ or 5′ termini) in single spots, hybridization was performed in situ on the confocal microscope stage. Hybridization conditions typical of commercial microarray generation were adapted to study real-time imaging under confocal microscopy. A stage-mounted temperature-controlled humidity chamber (set to 23 °C and 60% humidity, Pathology Devices) was utilized, and 20 μL of 1 μM target DNA in hybridization buffer (4× saline sodium citrate (SSC) containing 0.1% SDS at pH 7) was added over the probe-printed surface slide, and a coverslip was overlaid to control evaporation. Following confocal imaging, the slides were washed with hybridization buffer solutions (4×, 2×, 1×, and 0.2× dilutions) for 5 min followed by a water wash. The samples were then blown dry with nitrogen and immediately

dx.doi.org/10.1021/ac302165h | Anal. Chem. 2012, 84, 9379−9387

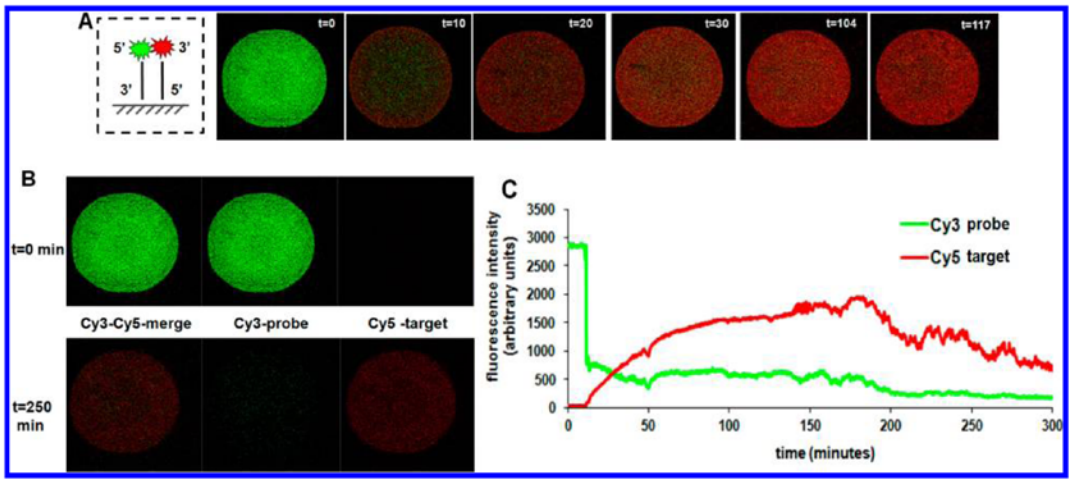

Figure 2. Real-time hybridization of a single DNA spot with dyes on the same end of the probe–target duplex: (A) schematic representation of the duplex, 5′-Cy3-Oligo1-probe with Oligo2-3′-Cy5-target and images of a DNA spot with merged Cy3 and Cy5 emission intensity at various time points; (B) images of spots in Cy3 or Cy5 or both filter channels during real-time imaging of single array spots before (t = 0) and after (t = 250 min) hybridization; (C) real-time hybridization of Cy3/Cy5 fluorescence intensity changes in single spots versus time. The duplex formation kinetics under this unstirred transport-limited regime follows pseudo-first-order kinetics (see the Supporting Information, Figure S-7). Note: microscopy image contrast has been digitally enhanced for the figures to better facilitate direct observation of the optical changes observed over time in situ.

scanned. Further details are discussed in the Supporting Information.

For Cy3–Cy5 FRET analysis, the target Cy5 emission signal was recorded under Cy3-specific excitation over time in single printed spots. To confirm FRET, acceptor photobleaching of Cy5 with 633 nm laser excitation was performed and then both Cy3 and Cy5 emission signals were recorded. In areas where FRET transfer between Cy3 and Cy5 is facilitated by duplex formation and sufficient dye proximity, photobleaching of the acceptor (Cy5) should result in an increase in the donor (Cy3) emission signal relative to that prior to bleaching. For FRET analysis, additional controls were performed to confirm FRET by monitoring changes in the intensities for different excitations and emissions of Cy3-probe and Cy5-target with unlabeled target DNA hybridized to a single spot.

DNA-Duplex-Induced Cy3–Cy5 FRET in Solution. FRET produced from DNA duplex formation in solution was assessed. Fluorescence emission spectra from 545 to 750 nm were obtained using a Cary Eclipse fluorescence spectrophotometer (Varian, Walnut Creek, CA). Excitation wavelengths for Cy3-DNA and Cy5-DNA were 547 and 644 nm, respectively, with emission wavelengths of 569 and 655 nm (λ_{max}), respectively. Further details are provided in the Supporting Information.

■ RESULTS AND DISCUSSION

Single-Spot Real-Time DNA Oligomer Hybridization Kinetics. Hybridization of immobilized 5′-Cy3-Oligo1-probe with 5′-Cy5-target-Oligo2 and Oligo2-3′-Cy5-target was analyzed in single printed probe spots in real time. To evaluate the dye–dye distance and steric influences on duplex formation, experiments were performed in different hybridization orientations shown in Figure S-1 (Supporting Information). Individual spots (40 μM probe DNA containing 50% Cy3-DNA duplex) with Cy5-target (1 μM containing 1% Cy5-DNA) were analyzed in different dye–duplex relative orientations depicted in Figure S-1 (also depicted in the schematics in Figures 1A and 2A).

Each single printed spot image in Figure 1A depicts an overlay of immobilized probe-Cy3 (green) and target-Cy5 (red) intensities versus time to assess distributions of Cy5-target captured in the same Cy3-DNA spot over time. Confocal spot images corresponding to the start (t = 0) and end (t = 90 min) of hybridization in different imaging channels are depicted in Figure 1B. However, Cy3/Cy5 intensities were recorded for up to 140 min total as indicated in Figure 1C. Figure 1A reveals a bright Cy3 emission (green) color at t = 0, and its intensity decreases after addition of Cy5-target DNA with a simultaneous increase in Cy5 emission (red) intensity. With increasing time, the Cy5 intensity (red) increases (e.g., t = 25 min), producing bright red spots at t = 90 min, indicating the expected increased target hybridization over time. Figure 1A also reveals a brighter Cy3 green intensity at the spot center compared to its peripheral intensity, indicating the nonuniformity of Cy3-DNA immobilized probe distribution. Previous work has detailed the causes of this microspot heterogeneity from printed spot drying dynamics.[55] The probe DNA density is high at spot centers as evidenced by the centralized green intensity, decreasing radially to the spot edges. This central green Cy3 emission intensity prevails throughout the Cy5-target hybridization process (although a relative decrease in intensity is observed); indicating limited duplex formation at the spot center.

Figure 1B compares Cy3-probe- and Cy5-target-only intensities of the same single DNA spot along with its Cy3–Cy5 merged intensity before and after hybridization (i.e., at t = 0 and t = 90 min). Contrasting intensities in DNA spots after hybridization are shown by mixing Cy3 and Cy5 signal intensities in the merged image for the spots. Increasing Cy5 intensity versus Cy3 intensity indicates probe–target duplex formation in the DNA spot after 90 min. Furthermore, hybridization completeness is confirmed by fluorescence scanner data. Figure 1C tracks relative spot-integrated emission intensities from each fluorophore over time, showing rapid

dx.doi.org/10.1021/ac302165h | Anal. Chem. 2012, 84, 9379–9387

decreases in the Cy3 fluorescence signal intensity immediately upon addition of Cy5-target, attributed to the altered Cy3 environment from the duplex formation, including quenching. This is confirmed using confocal imaging by corresponding decreases in the spot-integrated Cy3-probe emission intensity upon addition of unlabeled target DNA in hybridization buffer (4× SSC) (see Figure S-2, Supporting Information). Simultaneous increases in the Cy5-target intensity from the spot characterizes the onset of surface hybridization, occurring less than 2 min after addition of (unstirred) target solution over each spot. The in situ hybridization time-lapse imaging of single spots was performed over 30−60 min and shows that target emission intensity replaces probe emission intensity within the spot at ~6 min, seen both in the Figure 1A,B spot images and in the intensity-specific time plot in Figure 1C. At 45 min, a crossover of probe and target emission intensities (i.e., decreasing Cy3 intensity and increasing Cy5 intensity) is observed, attributed to increasing spot-based FRET (further confirmed in the following sections) from increasing densities of dye-labeled probe−target duplexes at high hybridization efficiencies. Figure 1C also indicates a higher intensity of Cy5 emission compared to Cy3 emission at the later time points, due to enhanced FRET, quenched Cy3, or a greater quantum yield from Cy5 vs Cy3 emitter on-spot. Steady signal intensities of Cy3 and Cy5 at longer times indicate saturation of the probes and completeness of hybridization for a 100 μm diameter spot at approximately 60 min. Similar experiments performed with 40 μM total DNA probe and 100%, 75%, or 25% fractional ratios of 5′-Cy3-Oligo1-probe with 5′-Cy5-Oligo2-target showed similar trends, though differences in time required to attain stability of the final Cy3 and Cy5 emission intensities were observed.

Figure 2 shows the case 2 (see Figure S-1 (Supporting Information) and the schematics in Figure 2A) situation for DNA duplexes forming with both fluorophores located at the same dsDNA terminus. These experiments show an emission kinetics plot and characteristic intensity−time changes for hybridization similar to those seen in Figure 1 for the case 1 antiparallel fluorophore duplex. Although hybridization begins within 2 min (similar to Figure 1), the spot exhibits Cy3−Cy5 emission intensity "crossover" more rapidly at 25 min. The Cy5-target emission intensity is higher compared to that of Cy3 and also plateaus due to completion of hybridization (assay saturation). Both signals then decrease beyond 160 min with eventual end point stabilization of both the Cy3-probe and Cy5-target emission intensities, with the final Cy5 signal again greater than that for Cy3 (Figure 2C).

The general trend in real-time kinetics of target binding to a surface-tethered probe with a dye label (shown in Figure S-3, Supporting Information) shows the initial rapid reduction in Cy3-probe emission intensity as target hybridization buffer (Cy5 DNA, 4× SSC) is added over the spot. Emission intensity reduction (over 50% reduction) is observed for both surface-array-phase (single-spot confocal image) and solution-phase (fluorescence spectrometry) hybridization involving the Cy3-probe. Previous reports indicate that the Cy3 fluorescence quantum yield is highest when attached to the 5′ terminus of single-stranded DNA (i.e., Cy3-5′-ssDNA) and decreases by a factor of 2.4 when the (unlabeled) complementary strand is annealed to form duplex DNA (Cy3-5′-dsDNA).[58] Control experiments for Cy3-ssDNA-Oligo1 hybridized with target-Oligo2 (i.e., no Cy5 dye label) confirm this reduction in Cy3 emission intensity from duplex formation (see Figures S-2 and S-4 (Supporting Information) for spot and bulk fluorophore behaviors). The observed fluorophore intensity crossover point where the Cy5-target signal intensity increases and the Cy3-probe signal decreases (i.e., shown in Figures 1 and 2) is speculated to result from FRET at higher degrees of hybridization when fluorophores are duplexed in close proximity.[59] Also, final signal saturation reflecting hybridization end points is further confirmed with fluorescence scanning data of spots with a homogeneous Cy5 signal (Figure S5, Supporting Information). Late-time-point reduced Cy3 and Cy5 emission is attributed to FRET, plus dye stacking due to overcrowding, dye−DNA and dye−DNA−dye induced self-quenching, and changes in the local fluorophore environments as a function of the spot hybridization density.[60]

Similar experiments performed with 10, 20, and 40 μM DNA with Cy3-DNA content (50%) for both case 1 and case 2 targets show the trend depicted in Figure S-6 (Supporting Information), with no remarkable differences in the crossover and saturation time points for hybridization using case 1 (antiparallel) and case 2 (parallel) dye positions on probes vs targets. The results are discussed in the Supporting Information. The assay incubation time (i.e., time to hybridization end point stabilization) can be very long (i.e., up to 14 h reported[9,20,61]) depending on the bulk composition, target concentration, ionic strength, and probe grafting density. Incubation times often vary, different even for similar concentrations of probe and target, but depending on the study conditions[25,62] and largely influenced by the probe density distributions.

Real-time hybridization imaging of single DNA probe spots shows evidence of spot fluorescence probe immobilization and density heterogeneities resulting from the probe printing and drying processes.[55] Printed dried probe spots often exhibit increased DNA density at spot centers compared to peripheries. This probe heterogeneity has implications for target uptake and resulting spot duplex heterogeneity as a consequence of the local differences in interfacial steric and Coulombic properties that affect target−probe pairing efficiencies and kinetics.[12,15] Figures 1 and 2 indicate the probe heterogeneity in each hybridized spot upon target introduction. Initially, increased probe DNA signal is evident at spot centers compared to the outer perimeter. Target hybridization therefore occurs from spot edges radially inward as indicated by increasing Cy5 emission spot intensity profiles (Figure 3). Both non-uniform radial probe density from spot drying[55] and target radial transport issues[15] produce non-homogeneous target hybridization with time. Target mass transport depends on the array format (static vs flow) and target concentration and diffusion coefficient.[15,63] Near spot centers, target is delivered to the probe surface solely through linear normal diffusion, whereas toward the outer edge, a lateral (radial) component of diffusive flux augments the normal linear transport component, producing hemispherical diffusion.[15] This results in spot outer edges accumulating more target through greater proximate fluid volume transport versus spot centers, depicted in the Figure 3A schematic. Figure 3B shows the observed increasing target-Cy5 emission intensity at the spot periphery initially, increasing radially toward the spot center over time as depicted from the time lapse. This validates the radial planar diffusion mechanism kinetically. It also shows that improving the uniformity of probe density across the spot feature could improve the assay signal consistency at any given assay end point, even prior to saturation. We recognize this

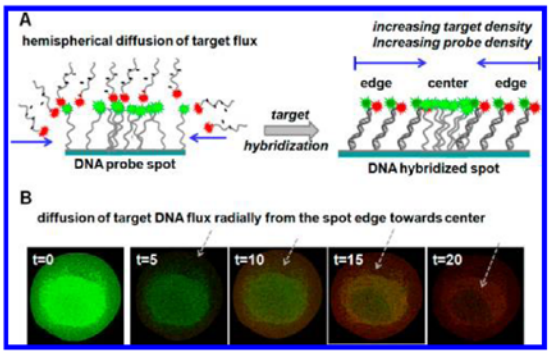

Figure 3. Mass-transfer-limited diffusion of target binding to an immobilized probe in a highly dense heterogeneous DNA spot:[15] (A) schematic representation of target DNA radial hybridization progress from the outside edge of the spot to the interior for a single DNA immobilized probe spot; (B) confocal images of real-time hybridization of a single printed DNA spot showing the Cy3−Cy5 overlay emission signal. The target Cy5 intensity increases from the spot edge initially and moves gradually radially into the spot center, supporting outside-to-inside mass-transport-mediated and probe-density-controlled spot hybridization. Note: microscopy image contrast has been digitally enhanced for the figures to better facilitate direct observation of the optical changes observed over time in situ.

duplex signal imbalance across the spot cannot be mitigated under target transport limitations in the assay, but might be addressed at long assay times approaching equilibrium by producing more uniform spot probe densities sufficiently low so that steric and Coulombic duplex hindrances are minimized and only target transport then remains kinetically limiting to signal generation. This is impossible currently in printed/dried spot formats and also could result in assay signal read-out thresholds below those for common scanners.

Kinetic modeling analysis was performed for DNA hybridization for both (case 1) antiparallel and (case 2) parallel dye positions of the duplex reactions from the confocal spot imaging data for Cy5 shown in Figures 1 and 2 (Figure S-7, Supporting Information). Both cases provide reliable fits for first-order reaction surface-capture kinetics ($R^2 > 0.996$). Probe-printed spot slides containing target in hybridization chambers are fixed and stationary, and analyte fluxes are not large enough to induce bulk flow (i.e., convection flow) and also sealed to prevent evaporative losses. The rate of target diffusion strongly affects hybridization rates and in an unstirred chamber is transport limiting. The hybridization reaction shows pseudo-first-order reaction kinetics when the concentration of bound probe strands is much greater than the concentration of corresponding target mobile strands in solution, similar to experimental conditions adapted in this work and in other previously published models. Previous observations demonstrate first-order and pseudo-first-order rate kinetics in time[64,65] and second-order in volume[15,66] for very similar target capture in probe spots.

Real-time in situ results for both case 1 and case 2 hybridizations (see Figures 1 and 2) indicate that irrespective of the relative Cy3−Cy5 duplex orientation, the Cy3 emission intensity decreases. The simultaneous increase in Cy5 emission intensity reflects FRET effects. Typically, FRET is most efficient when energy-matched fluorophores are within the Förster radius, typically several nanometers. Additionally, the FRET efficiency depends on the energy overlap between donor emission and acceptor excitation spectra, relative orientation of the fluorophore transition dipoles, donor quantum yield, extinction coefficient of the acceptor, and (sixth power of the) distance between fluorophores.[67] The 20-mer DNA oligomers used have substantial Cy3−Cy5 FRET potential[41,47] with a theoretical probe and target duplex with dyes in an antiparallel position with an end−end distance of 6.8 nm. In contrast to model thiolated DNA monolayers on gold surfaces,[17,18] DNA microarray spots printed on most commercial array surfaces dry under rapid nonequilibrium conditions, producing a dense, concentrated DNA film on the slide surface with buffer salts and additives and random orientations of many DNA probe layers, sometimes micrometers in thickness.[68] Rinsing however only partially removes the contents from this thick film, leaving multilayer DNA spots with random probe orientations. The target DNA analyte then hybridizes to this thick printed film with many differently

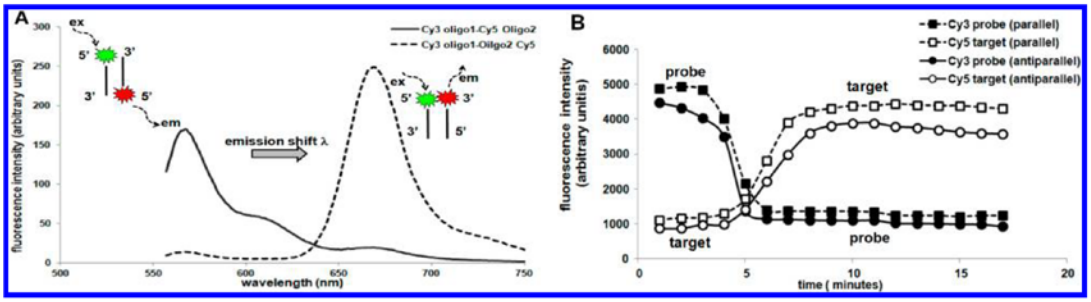

Figure 4. Comparison of FRET analysis in bulk (solution) and printed array spots on a solid substrate for two different orientations of dye (as described in Figure S-1, Supporting Information): (A) oligo-DNA target-Cy5 emission shift indicating FRET in bulk solution duplexes for 5′-Cy3-Oligo1-probe−Oligo2-3′-Cy5-target (case 2 dye on the same side of the duplexes indicated here by a dotted line) and not for 5′-Cy3-Oligo1-probe−5′-Cy5-Oligo2-target (case 1 with antiparallel dye duplexes indicated by a solid line); (B) single-spot analysis of fluorescence signals for Cy3-probe and Cy5-target emissions from surface-capture assays monitored in real time by confocal microscopy for the 5′-Cy3-Oligo1-probe−5′-Cy5-Oligo2-target parallel duplex (dotted lines) and for the 5′-Cy3-Oligo1-probe−Oligo2-3′-Cy5-target antiparallel duplex (solid lines) indicating FRET with increasing Cy5 emission intensity and simultaneously decreasing Cy3-probe intensity. Solution-phase FRET occurs in (A) for two fluorophores in close proximity (i.e., on the same duplex ends), whereas single-spot array assays (B) indicated FRET for both duplex dye orientations upon hybridization in printed spots.

oriented probes in uncontrolled densities. Irrespective of the labeling position of target-Cy5 during hybridization, the abundant duplex opportunities with dense, unoriented probe spots should facilitate FRET. In unstirred solutions, hybridization is observed to occur immediately (within seconds of target addition) and concludes in ~60 min. Each single spot scanned using a fluorescence scanner after 60 min indicates a peak Cy5 intensity and end point for hybridization in this format (see the Supporting Information, Figure S-5).

FRET in DNA Microarrays. The printed surface-capture array format should produce FRET when Cy3 and Cy5 dyes satisfy Förster conditions as depicted in Figure S-8 (Supporting Information). For dye–dye distances greater than 10 nm, FRET is unlikely to occur (Figure S-8). To confirm the assertion of FRET in the observed Cy3–Cy5 intensity crossover and further reduction in the Cy3 emission intensity (see Figures 1C and 2C), the FRET signal was compared in both the bulk solution phase (i.e., DNA–dye duplexes in solution) using spectrophotometry and surface capture (i.e., on printed microarrays) with confocal microscopy.

In solution, 5′-Cy3-Oligo1-probe duplexes with 5′-Cy5-Oligo2-target DNA (Figure 1A, dyes antiparallel) do not exhibit observable shifts in respective emission wavelengths (λ_{em}): duplexed dyes are theoretically approximately 7 nm apart). However, when both fluorophores are proximal in parallel duplexes (Figure 2A, dyes parallel; 5′-Cy3-Oligo1-probe–Oligo2-3′-Cy5-target, approximate theoretical separation of 2 nm), the Cy5 emission intensity increases, characteristic of FRET (see Figure 4A). Figure S-4 (Supporting Information) shows respective fluorescence excitation and emission spectra for all probe and target oligonucleotides in bulk solution duplex experiments.

On printed arrays, the Cy5-target emission intensity increases with decreasing Cy3 emission intensity upon addition of complementary Cy5-labeled target analyte to printed Cy3-probes (see Figures 1 and 2). In contrast to bulk duplex FRET studies, altered Cy5 and Cy3 emission is evident for both parallel and antiparallel dye orientations upon duplexing in printed spots (Figure 4). FRET is observed with both antiparallel and parallel dye–dye duplex orientations on arrayed single-spot studies (Figure 4B). We attribute this to a high probe density in dried multilayer printed spots, with many possible probe arrangements capable of duplexing Cy5-target. This produces high possibilities for energy transfer with multiple nearest neighbors or in duplexes between strands regardless of the relative Cy3–Cy5 orientations in the two duplex designs.

FRET is widely used to report nucleotide structures and dynamics transitions using the Cy3/Cy5 FRET pairing.[47,69−71] Optical complications involving multiple dye relaxation pathways are minimized since the absolute inter-dye distance is well within the FRET range (Förster radius 1–8 nm).[51] Moreover, orientational FRET dependence is significant when fluorophores are constrained on solid substrates.[50,71] Previous NMR evidence for Cy3 and Cy5 bound to DNA indicates dye stacking on the DNA helix terminus acts as an additional base pair signifying dependence on the fluorophore orientation for FRET efficiency. Various factors affect the fluorescence intensity in addition to complexity in analyzing FRET of dye–DNA bound to the surface of high-density probes. With parallel and antiparallel dye positions from probe–target hybridization (seen in real-time hybridization and FRET of DNA spots), we expect a high FRET probability, irrespective of the distances between dyes, due to heterogeneity in the probe density distribution facilitating abundant duplex opportunities with dense unoriented probes.

Duplex FRET Cy5-acceptor Photobleaching. Cy5-acceptor photobleaching in hybridized DNA single spots was used to investigate FRET in spots. This was achieved by comparing the donor fluorescence emission intensity in the same printed spot before and after deliberately photolyzing the Cy5-photoacceptor on the duplexed target. FRET was validated by analyzing the initial attenuation of Cy3 emission by energy transfer to Cy5, increasing the Cy5 emission. Upon selective Cy5 photobleaching, the Cy5-acceptor no longer accepts Cy3 emission energy. Cy3 emission therefore increases and Cy5 emission is attenuated. The FRET efficiency is quantified by $FRET_{eff} = 1 - (I_D/I_D')$, where I_D is the donor emission intensity during FRET and I_D' is the emission intensity after acceptor photobleaching.[51] Photobleaching experiments of hybridized DNA spots were performed within a region of a single DNA spot (region indicated by oval dotted line, Figure 5A). Cy3 and Cy5 emission intensities in the spots were

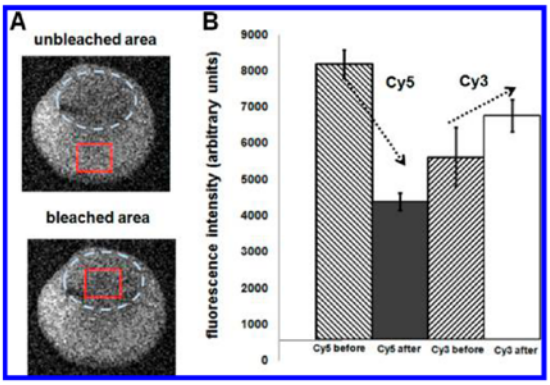

Figure 5. Photobleaching analysis of the FRET signal of a single hybridized DNA spot. Comparison of Cy3 and Cy5 emission intensities in unbleached and bleached regions of a single hybridized DNA microspot. (A) Images of both unbleached and bleached (oval dotted line) areas of the same DNA spot after confocal local photobleaching. Square indicates the region of interest for measurement of Cy3 and Cy5 intensity in the bleached and unbleached regions in the DNA spot. (B) Quantification of both Cy3-probe and Cy5-target emission intensities before and after photobleaching (solid squares) showing reduction of the Cy5-target signal and an increase in the Cy3-probe signal once Cy5 fluorophores are photolyzed, consistent with FRET effects.

recorded over time and compared with unbleached regions in the spots (indicated by the square zone, Figure 5A). The FRET efficiency in single hybridized DNA spots, depicted in Figure 5B, is about 18% before Cy5 photobleaching. The target Cy5 emission intensity decreases to approximately 30% with a significant increase in the Cy3 probe emission attributed to Cy5 acceptor photobleaching. These results confirmed FRET in single hybridized DNA spots.

DNA Spot Photobleaching Depth-Dependent Studies. To assess Cy5-DNA target penetration into printed probe microspots, photobleaching through the spot thickness in printed DNA spots was performed and both Cy3 and Cy5 emission intensities were collected at each depth (each Z slice ~0.5 μm) in single DNA spots. The intensities of Cy3 and Cy5

dx.doi.org/10.1021/ac302165h | Anal. Chem. 2012, 84, 9379−9387

emission in localized bleached areas in single spots were measured in each Z step (depth). Emission intensities for both Cy3 and Cy5 across a small bleached vs unbleached area in a single spot are shown in Figure S-9 (Supporting Information). Regions for analysis were chosen at spot corners since hybridization efficiencies are greater at edges than centrally, with more Cy5-DNA duplexed on spot peripheries as seen in Figure 3. Photobleaching of immobilized Cy5-target fluorophore is indicated by decreasing emission intensity through the Z series within bleached areas compared to unbleached areas in the same single DNA spot (Figure S-9B). The FRET phenomenon is observed in unbleached regions as the Cy5 emission intensity is higher compared to that from Cy3. In the different depth photobleached regions for DNA spots, the overlaid intensities of Cy3 and Cy5 emissions overlap, indicating decreasing Cy5 intensity compared to unbleached Cy3 intensity. Previous reports have shown that Cy5 is more sensitive to photobleaching than Cy3.[72] Cy3 dye has remarkable stability against photobleaching; however, it is much more sensitive than Cy5 to environmental factors such as temperature and local rigidity.[58,73] To improve assay signal detection and spot sensitivity, a higher excitation laser power is preferred. However, increased energy on-array leads to dye bleaching and reduced spot fluorescent signal emission during successive scans. Photobleaching studies reveal specific photolyzing of the dyes, penetration of target oligo-DNA into the printed probe spot during the hybridization process, and FRET in unbleached spots with signal intensities comparable to those of unbleached spots.

CONCLUSIONS

Fluorescence analysis of individual array-printed DNA microspots using fluorophore-labeled DNA probe–target pairings with confocal microscopy provides important new information regarding the spot molecular environment of immobilized probes, target hybridization processes to substrate-bound probe, and aspects of incubation time periods for duplex-forming assays. Single-spot image analysis and intensity measurements for immobilized Cy3-oligo-DNA probe and Cy5-oligo-DNA target compared for two different dye positions on the duplex showed few differences in real-time hybridization time points. The detailed image analysis of real-time hybridization for target DNA confirmed the mass-transfer-limited diffusion of target binding to the immobilized probe in highly dense but heterogeneous DNA spots. Though real-time hybridization (duplex formation) detection of the probe–target is challenging for surface-bound assays, FRET enables real-time monitoring of duplex formation and hybridization rates by monitoring Cy3/Cy5 signal intensities during hybridization processes. Hybridization in solution produced different FRET effects for the two different duplexed dye positions in contrast to DNA surface-capture assays that facilitate FRET in both positions in single DNA hybridized spots, attributed to high probe densities. In situ photobleaching of Cy3 and Cy5 within the spot's cross-section supports heterogeneous probe–target distribution in multilayer-thick printed spots. Overall, new confocal DNA hybridization data provide important new information supporting spot fluorescence signal intensity variations resulting from spot probe printing and drying. Real-time in situ fluorescence image analysis of hybridization supports nonuniform probe distribution density within each spot as a key influence on target binding kinetics and fluorescence signal ambiguities. Microarray assays based on spot printing and target capture should consider these sources of intrinsic variability and their influence on assay answer reliability.

ASSOCIATED CONTENT

Supporting Information

Additional information as noted in text. This material is available free of charge via the Internet at http://pubs.acs.org.

AUTHOR INFORMATION

Corresponding Author

*E-mail: david.grainger@utah.edu.

Notes

The authors declare no competing financial interest.

ACKNOWLEDGMENTS

Support from National Institutes of Health Grant EB001473 and assistance with imaging/intensity and data analysis from Dr. K. R. Carney (University of Utah) are both gratefully acknowledged.

REFERENCES

(1) Stears, R. L.; Martinsky, T.; Schena, M. *Nat. Med.* **2003**, *9* (1), 140–145.
(2) Šášik, R.; Woelk, C. H.; Corbeil, J. *J. Mol. Endocrinol.* **2004**, *33* (1), 1–9.
(3) Simon, R.; Radmacher, M. D.; Dobbin, K.; McShane, L. M. *J. Natl. Cancer Inst.* **2003**, *95* (1), 14–18.
(4) Wu, P.; Castner, D. G.; Grainger, D. W. *J. Biomater. Sci., Polym. Ed.* **2008**, *19* (6), 725–753.
(5) Zou, S.; He, H.-J.; Zong, Y.; Shi, L.; Wang, L. DNA Microarrays: Applications, Future Trends, and the Need for Standardization. *Standardization and Quality Assurance in Fluorescence Measurements II*; Springer Series on Fluorescence, Vol. 8; Springer: New York, 2008; pp 215–237.
(6) Shi, L.; Campbell, G.; Jones, W. D.; Campagne, F.; Wen, Z. *Nat. Biotechnol.* **2010**, *28* (8), 827–838.
(7) Shi, L. *Nat. Biotechnol.* **2006**, *24* (9), 1151–1161.
(8) Zammatteo, N.; Jeanmart, L.; Hamels, S.; Courtois, S.; Louette, P.; Hevesi, L.; Remacle, J. *Anal. Biochem.* **2000**, *280* (1), 143–150.
(9) Peterson, A. W.; Heaton, R. J.; Georgiadis, R. M. *Nucleic Acids Res.* **2001**, *29* (24), 5163–5168.
(10) Chou, C. C.; Chen, C. H.; Lee, T. T.; Peck, K. *Nucleic Acids Res.* **2004**, *32* (12), e99.
(11) Chan, V.; Graves, D. J.; McKenzie, S. E. *Biophys. J.* **1995**, *69* (6), 2243–2255.
(12) Dai, H.; Meyer, M.; Stepaniants, S.; Ziman, M.; Stoughton, R. *Nucleic Acids Res.* **2002**, *30* (16), e86.
(13) Heaton, R. J.; Peterson, A. W.; Georgiadis, R. M. *Proc. Natl. Acad. Sci. U.S.A.* **2001**, *98* (7), 3701–3704.
(14) Metzger, S. W.; Lockhead, M. J.; Grainger, D. W. Improving Performance in Protein-Based Microarrays: Surface Chemistries Enable Application of Protein Microarray Technologies to Diagnostics. *IVD Technol.* [Online] **2002**, Feature Articles, Manufacturing & Processing Technologies, p 10. http://www.ivdtechnology.com/article/improving-performance-protein-based-microarrays (accessed August 21, 2012).
(15) Dandy, D. S.; Wu, P.; Grainger, D. W. *Proc. Natl. Acad. Sci. U.S.A.* **2007**, *104* (20), 8223–8228.
(16) Levicky, R.; Herne, T. M.; Tarlov, M. J.; Satija, S. K. *J. Am. Chem. Soc.* **1998**, *120* (38), 9787–9792.
(17) Lee, C. Y.; Gong, P.; Harbers, G. M.; Grainger, D. W.; Castner, D. G.; Gamble, L. *J. Anal. Chem.* **2006**, *78* (10), 3316–3325.
(18) Demers, L. M.; Mirkin, C. A.; Mucic, R. C.; Reynolds Iii, R. A.; Letsinger, R. L.; Elghanian, R.; Viswanadham, G. *Anal. Chem.* **2000**, *72* (22), 5535–5541.

(19) Gong, P.; Levicky, R. *Proc. Natl. Acad. Sci. U.S.A.* **2008**, *105* (14), 5301−5306.
(20) Hassibi, A.; Vikalo, H.; Riechmann, J. L.; Hassibi, B. *Nucleic Acids Res.* **2009**, *37* (20), e132.
(21) Axelrod, D.; Wang, M. D. *Biophys. J.* **1994**, *66* (3), 588−600.
(22) Vainrub, A.; Pettitt, B. M. *J. Am. Chem. Soc.* **2003**, *125* (26), 7798−7799.
(23) Vainrub, A.; Pettitt, B. M. *Phys. Rev. E: Stat., Nonlinear, Soft Matter. Phys.* **2002**, *66* (4), 041905/1−041905/4.
(24) Halperin, A.; Buhot, A.; Zhulina, E. B. *J. Phys.: Condens. Matter* **2006**, *18* (18), S463−S490.
(25) Halperin, A. S.; Buhot, A.; Zhulina, E. B. *Biophys. J.* **2004**, *86* (2), 718−730.
(26) Irving, D.; Gong, P.; Levicky, R. *J. Phys. Chem. B* **2010**, *114* (22), 7631−7640.
(27) Held, G. A.; Grinstein, G.; Tu, Y. *Proc. Natl. Acad. Sci. U.S.A.* **2003**, *100* (13), 7575−7580.
(28) Ota, N.; Hirano, K.; Warashina, M.; Andrus, A.; Mullah, B.; Hatanaka, K.; Taira, K. *Nucleic Acids Res.* **1998**, *26* (3), 735−743.
(29) Mearns, F. J.; Wong, E. L. S.; Short, K.; Hibbert, D. B.; Gooding, J. J. *Electroanalysis* **2006**, *18* (19−20), 1971−1981.
(30) Ambia-Garrido, J.; Vainrub, A.; Pettitt, B. M. *Comput. Phys. Commun.* **2010**, *181* (12), 2001−2007.
(31) Morriss-Andrews, A.; Rottler, J.; Plotkin, S. S. *J. Chem. Phys.* **2010**, *132* (3), 035105.
(32) Shen, G.; Tercero, N.; Gaspard, M. A.; Varughese, B.; Shepard, K.; Levicky, R. *J. Am. Chem. Soc.* **2006**, *128* (26), 8427−8433.
(33) Halperin, A.; Buhot, A.; Zhulina, E. B. *Biophys. J.* **2005**, *89* (2), 796−811.
(34) Lassalle, N.; Vieil, E.; Correia, J. P.; Abrantes, L. M. *Biosens. Bioelectron.* **2001**, *16* (4−5), 295−303.
(35) Fritz, J.; Cooper, E. B.; Gaudet, S.; Sorger, P. K.; Manalis, S. R. *Proc. Natl. Acad. Sci. U.S.A.* **2002**, *99* (22), 14142−14146.
(36) Abel, A. P.; Weller, M. G.; Duveneck, G. L.; Ehrat, M.; Widmer, H. M. *Anal. Chem.* **1996**, *68* (17), 2905−2912.
(37) Peterlinz, K. A.; Georgiadis, R. M.; Herne, T. M.; Tarlov, M. J. *J. Am. Chem. Soc.* **1997**, *119* (14), 3401−3402.
(38) Wang, J.; Cai, X.; Tian, B.; Shiraishi, H. *Analyst* **1996**, *121* (7), 965−970.
(39) Siontorou, C. G.; Nikolelis, D. P.; Miernik, A.; Krull, U. J. *Electrochim. Acta* **1998**, *43* (23), 3611−3617.
(40) Gaylord, B. S.; Heeger, A. J.; Bazan, G. C. *J. Am. Chem. Soc.* **2003**, *125* (4), 896−900.
(41) Iqbal, A.; Arslan, S.; Okumus, B.; Wilson, T. J.; Giraud, G.; Norman, D. G.; Ha, T.; Lilley, D. M. J. *Proc. Natl. Acad. Sci. U.S.A.* **2008**, *105* (32), 11176−11181.
(42) Schwille, P.; Oehlenschlager, F.; Walter, N. G. *Biochemistry (Moscow)* **1996**, *35* (31), 10182−10193.
(43) Nie, S.; Chiu, D. T.; Zare, R. N. *Anal. Chem.* **1995**, *67* (17), 2849−2857.
(44) Clegg, R. M. *Rev. Mol. Biotechnol.* **2002**, *82* (3), 177−179.
(45) Sapsford, K. E.; Berti, L.; Medintz, I. L. *Angew. Chem., Int. Ed.* **2006**, *45* (28), 4562−4588.
(46) Clegg, R. M. *Curr. Opin. Biotechnol.* **1995**, *6* (1), 103−110.
(47) Clegg, R. M.; Murchie, A. I. H.; Zechel, A.; Lilley, D. M. J. *Proc. Natl. Acad. Sci. U.S.A.* **1993**, *90* (7), 2994−2998.
(48) Dale, R. E.; Eisinger, J.; Blumberg, W. E. *Biophys. J.* **1979**, *26* (2), 161−193.
(49) Stryer, L. *Annu. Rev. Biochem.* **1978**, *47*, 819−846.
(50) VanBeek, D. B.; Zwier, M. C.; Shorb, J. M.; Krueger, B. P. *Biophys. J.* **2007**, *92* (12), 4168−4178.
(51) Sabanayagam, C. R.; Eid, J. S.; Meller, A. *J. Chem. Phys.* **2005**, *122* (6), 061103−1−061103−5.
(52) Dinant, C.; Van Royen, M. E.; Vermeulen, W.; Houtsmuller, A. B. *J. Microsc.* **2008**, *231* (1), 97−104.
(53) Widengren, J.; Schwillle, P. *J. Phys. Chem. A* **2000**, *104* (27), 6416−6428.
(54) Leung, Y. F.; Cavalieri, D. *Trends Genet.* **2003**, *19* (11), 649−659.
(55) Rao, A. N.; Vandencasteele, N.; Gamble, L. J.; Grainger, D. W. *Anal. Chem.* **2012**, submitted for publication.
(56) Beaucage, S. L.; Caruthers, M. H. *Tetrahedron Lett.* **1981**, *22* (20), 1859−1862.
(57) Gong, P.; Grainger, D. W. *Surf. Sci.* **2004**, *570* (1−2), 67−77.
(58) Sanborn, M. E.; Connolly, B. K.; Gurunathan, K.; Levitus, M. *J. Phys. Chem. B* **2007**, *111* (37), 11064−11074.
(59) Didenko, V. V. *Biotechniques* **2001**, *31* (5), 1106−1121.
(60) Gregory Cox, W.; Beaudet, M. P.; Agnew, J. Y.; Ruth, J. L. *Anal. Biochem.* **2004**, *331* (2), 243−254.
(61) Toegl, A.; Kirchner, R.; Gauer, C.; Wixforth, A. *J. Biomol. Tech.* **2003**, *14* (3), 197−204.
(62) Carletti, E.; Guerra, E.; Alberti, S. *Trends Biotechnol.* **2006**, *24* (10), 443−448.
(63) Erickson, D.; Liu, X.; Krull, U.; Li, D. *Anal. Chem.* **2004**, *76* (24), 7269−7277.
(64) Stillman, B. A.; Tonkinson, J. L. *Anal. Biochem.* **2001**, *295* (2), 149−157.
(65) Gadgil, C.; Yeckel, A.; Derby, J. J.; Hu, W. S. *J. Biotechnol.* **2004**, *114* (1−2), 31−45.
(66) Bishop, J.; Blair, S.; Chagovetz, A. M. *Biophys. J.* **2006**, *90* (3), 831−840.
(67) Piston, D. W.; Kremers, G. J. *Trends Biochem. Sci.* **2007**, *32* (9), 407−414.
(68) Dugas, V.; Broutin, J.; Souteyrand, E. *Langmuir* **2005**, *21* (20), 9130−9136.
(69) Ha, T. *Methods* **2001**, *25* (1), 78−86.
(70) Murphy, M. C.; Rasnik, I.; Cheng, W.; Lohman, T. M.; Ha, T. *Biophys. J.* **2004**, *86* (4), 2530−2537.
(71) Selvin, P. R. *Nat. Struct. Biol.* **2000**, *7* (9), 730−734.
(72) Bilban, M.; Buehler, L. K.; Head, S.; Desoye, G.; Quaranta, V. *Curr. Issues Mol. Biol.* **2002**, *4* (2), 57−64.
(73) Aramendía, P. F.; Martín Negri, R.; San Román, E. *J. Phys. Chem.* **1994**, *98* (12), 3165−3173.

REAL-TIME FLUORESCENT IMAGE ANALYSIS OF DNA SPOT HYBRIDIZATION KINETICS TO ASSESS MICROARRAY SPOT HETEROGENEITY

Archana N. Rao[1], Christopher K. Rodesch[2] and David W. Grainger[1,3*]

* Corresponding author: David W. Grainger, david.grainger@utah.edu

SUPPORTING INFORMATION

Data Presented

Material and Methods

- Table S-1: Oligonucleotide sequences and terminal modifications used in this study.
- Detailed explanations for printing and post-printing methodologies; real time hybridization and FRET studies with both confocal microscopy and fluorescence spectrophotometry.

Results and Discussion

- Figure S-1: Schematics of real-time hybridization and FRET analysis of DNA duplexes in different probe-target dye orientations.
- Figure S-2: Confocal measurements of duplex formation with target on immobilized probe DNA spots: reduction in Cy3-DNA probe fluorescence emission intensities irrespective of target DNA with or without Cy5 dye label.
- Figure S-3: Plot of real-time DNA spot hybridization kinetics.
- Figure S-4: Plot of FRET in solution compared to controls of individual excitation and emission spectra for probe DNA (5'-Cy3 oligo1) and target DNA (5'-Cy5 oligo2) and (3'-Oligo2-Cy5).
- Figure S-5: Fluorescence scanner images for spot Cy3 fluorescence emission intensity before real time hybridization analysis with confocal and after completion of target hybridization: (Cy3) at 535nm and (Cy5) 635nm, respectively.

- Figure S-6. Increase in time to crossover of Cy3-Cy5 emission intensities, and time-to-signal saturation in single printed spots with increasing printed DNA probe concentration observed with real-time DNA single spot hybridization assays.
- Figure S-7. Plot of kinetics of DNA hybridization (Cy5 dye target vs. time in seconds).
- Figure S-8. Schematic of DNA microarray FRET assay using dye-labeled DNA with different dye orientations in duplexes of surface-bound single spot assays.
- Figure S-9. Fluorescence emission intensities of Cy3 probe and Cy5 target as a function of depth in single hybridized (bleached *vs.* unbleached) microspots using step-wise confocal z-slices of 0.5 μm.

Materials and Methods

Table S-1 Oligonucleotide sequences and terminal modifications

DNA	identifier	5'-modification	sequence	3'-modification
probe	Oligo1-NH_2	--	CTGAACGGTAGCATCTTGAC	--
probe	Cy3-Oligo1-NH_2	Cy3-C_6-	CTGAACGGTAGCATCTTGAC	C6-NH_2
target	Oligo2	--	GTCAAGATGCTACCGTTCAG	--
target	Cy5-Oligo2	Cy5-C_6-	GTCAAGATGCTACCGTTCAG	--
target	Oligo2-Cy5		GTCAAGATGCTACCGTTCAG	Cy5-C_6-

Fabrication of DNA probe microspots with contact printing

Multiple Microarray Format SpoCLe Generator version 1.1.02 software (ArrayIt) was used to print microarrays on commercial microarray polymer-coated slides (Slide-H, Schott-Nexterion). SMP4 pins were used to spot 1.1 nanoliters of DNA solution, yielding probe spots with dried diameters of approximately 135 microns and spot-to-spot spacing of 160 microns. DNA spots were printed with optimized pin wash and dry cycles to prevent pin carryover of DNA probe solution between prints. Spots were printed in replicates of 5 followed by a wash (wash buffer of 20% ethanol in water with 0.01% Tween 20) and dry cycle. Humidity during printing was approximately 60%. Printed slides were incubated overnight (>12 h) at room temperature under 75% relative humidity controlled by a saturated saltwater bath. Prior to starting a print run, the

print head was calibrated according to manufacturer's recommended procedure with SNS4 solid calibrating pins for 135-micron diameter spots.

Post-print array slide blocking

Printed slides were treated with a blocking solution to avoid non-specific DNA surface absorption in a stepwise protocol similar to recommendations from the manufacturer. Printed slides were rinsed in print buffer and then immersed in a blocking solution (50 mM ethanolamine in 0.1 M Tris, pH 9.0) at 50°C for 30 min to consume residual amine-reactive surface groups. Following blocking, slides were rinsed thoroughly with ultrapure water 3 times, blown dry with nitrogen and scanned in a fluorescence scanner to locate and record spot intensity and shape. Slides were then stored in glass slide containers filled with nitrogen and sealed in parafilm until analyzed with confocal microscopy.

Real-time hybridization and FRET with confocal microscopy

Real-time hybridization and FRET was performed similarly to well-established protocols for microarrays. Complementary target DNA (~20 μl volume) was added over single probe spots for real-time *in situ* hybridization studies. A transparent silicone gasket with adhesive on both sides (Grace Biolabs, specific for imaging) was placed around the probe array to contain the target DNA solution for hybridization. The slide was maintained at 60% humidity and 23°C to limit evaporation of small target solution volumes (consistent with most protocols). Sequential excitation/emission of Cy3 and Cy5 in the same spot location was measured during the time-lapse for real-time hybridization. Optimization of the signal intensity and array imaging in buffer was established using control spots prior to real-time detection with hybridization buffer on different spots.

Real-time 3D images of hybridization of Cy5-labeled DNA targets in hybridization buffer with immobilized Cy3-labeled DNA probes were collected. A single centrally located probe array spot was used to adjust the focus and Cy3 signal intensity. A 30-min time lapse was then recorded both Cy3 and Cy5 at single spot images every 15 seconds. Experiments were performed with various DNA probe concentrations (40μM, 20μM and 10μM) and varying amounts of printed Cy3-DNA probe fractions (100% 75%, 50%, 25% and 10%). Real-time hybridization

kinetics for single printed spots were recorded for two different cases of probe-target relative dye orientations: Cy3-probe dye-up:Cy5-target dye-down (ie., antiparallel dyes, case 1), and both probe and target dye-up (i.e., adjacent dyes, case 2) as illustrated in Figure 1. Hybridization of unlabeled probe (no Cy3 dye) with target was not performed due to the difficulty in finding/visualizing and focusing on unlabeled printed DNA spots after addition of bulk Cy5-target.

DNA duplex-induced Cy3-Cy5 FRET in solution

This experiment was performed using varied total DNA and dye-labeled DNA fractional concentrations in hybridization buffer at room temperature (23^0C). Initially Cy3 and Cy5 excitation and emission spectra were recorded separately to obtain the $\lambda_{ex,max}$ and $\lambda_{em,max}$ for Cy3-DNA probe with fluorophore at the 5' position and Cy5-DNA target having fluorophores at either 3' or 5' positions. FRET experiments were then performed for these same configurations. In cuvettes containing Cy3-DNA, Cy5-DNA was added with optical excitation set to 547 nm, and emission was recorded from 555-750nm over time. Optical excitation was then changed to 645 nm, and emission was recorded from 655-750nm. FRET was assessed by observing shifts in the wavelength or changes in the wavelength intensity of acceptor (Cy5) by energy transfer from the donor (Cy3).

Results and Discussion

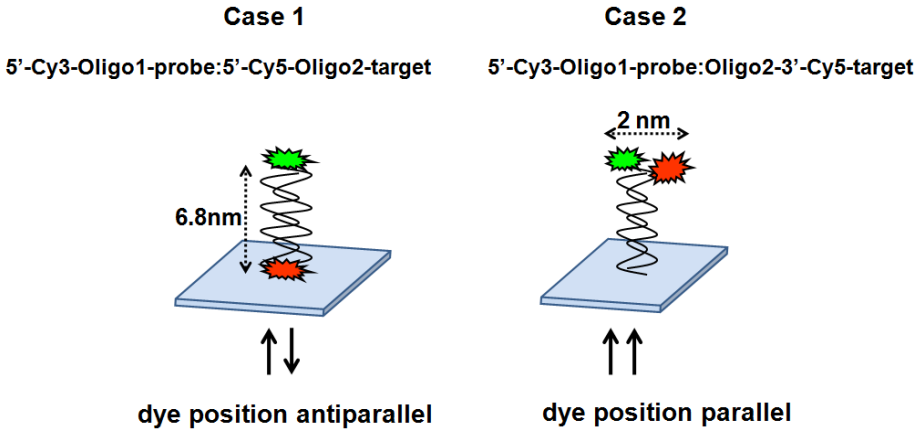

Figure S-1. Schematics for real-time hybridization and FRET analysis of DNA duplexes in different probe-target dye orientations. **Case 1**: Cy3 and Cy5 are oriented antiparallel after DNA duplex formation. **Case 2**: both dyes are located at the same duplex end after duplex formation.

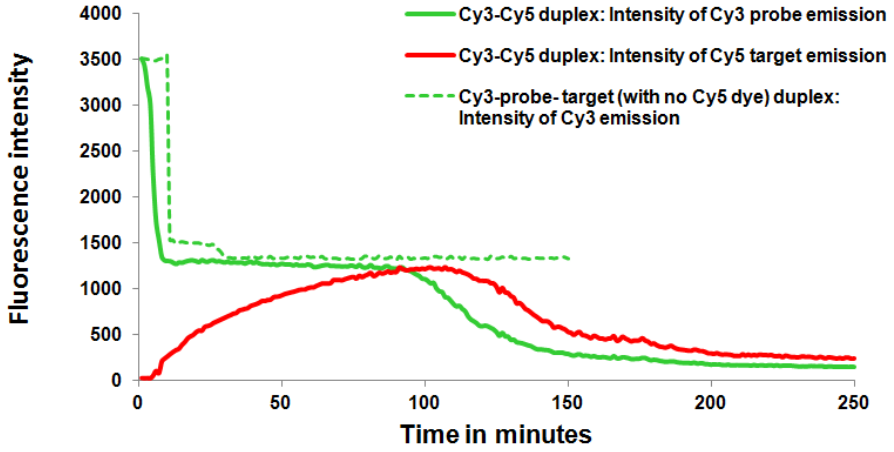

Figure S-2. Integrated Cy3 fluorescence emission intensity from a single printed Cy3-DNA probe spot after addition of target DNA in hybridization buffer both with (green solid line) and without (green dotted line) Cy5 dye labeled to target DNA. Resulting Cy5-target DNA emission signal is shown as red solid line. Addition of complementary DNA target with either no fluorophore or with Cy5 fluorophore in separate experiments both yield rapid decreases in probe Cy3 spot emission intensity with duplex formation in the spot. The real-time DNA duplex kinetics curve represented is for 100μM probe DNA spots containing Cy3-DNA probe fractions of 50%, and duplexed with Cy5-target (1μM containing 1% Cy5-DNA) with the dyes on the same end probe and target.

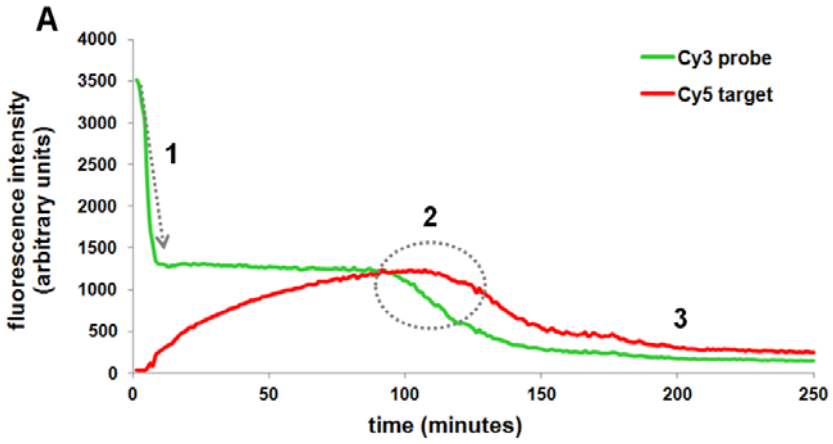

Figure S-3. Real-time DNA hybridization kinetics in printed spots showing 1) a rapid decrease in Cy3 DNA-probe intensity due to addition of the target solution, 2) slow increase in Cy5 intensity with simultaneous slower decrease in Cy3 due to FRET until a crossover point (circled), and 3) decrease in both Cy3 and Cy5 intensities from duplex formation, and final relatively constant signal intensity over time due to saturation/non-availability of probes. The real-time DNA kinetics curves were measured for 100μM probe DNA printed spots containing 50% Cy3-DNA, and duplexed with Cy5-target (1μM containing 1% Cy5-DNA). The hybridization curves and signals can be interpreted as follows: Point (1) the initial drastic decrease in Cy3 fluorescence emission (arrow) independent of FRET is due to the addition of target buffer solution as this effect occurs even in the presence of dye-less target (see Figure S-2). The initial increase in the number of hybridization events results in an initially progressive increase of Cy5 intensity. However, at this point, the average distance between Cy3 donors and Cy5 acceptors is still larger than the Förster distance required for inducing FRET, so only a slow decrease in the Cy3 intensity is observed due to the smaller number of local energy transfer events. Point (2): At ~100 minutes the average distance between donors and acceptors now falls below the Förster distance, yielding a precipitous decrease of Cy3 probe intensity due to FRET over time, while Cy5 intensity reaches its maximum. Point (3): The final decrease in Cy5 intensity is due to the self-quenching of this dye at its high surface concentration at the end stages of duplex formation.

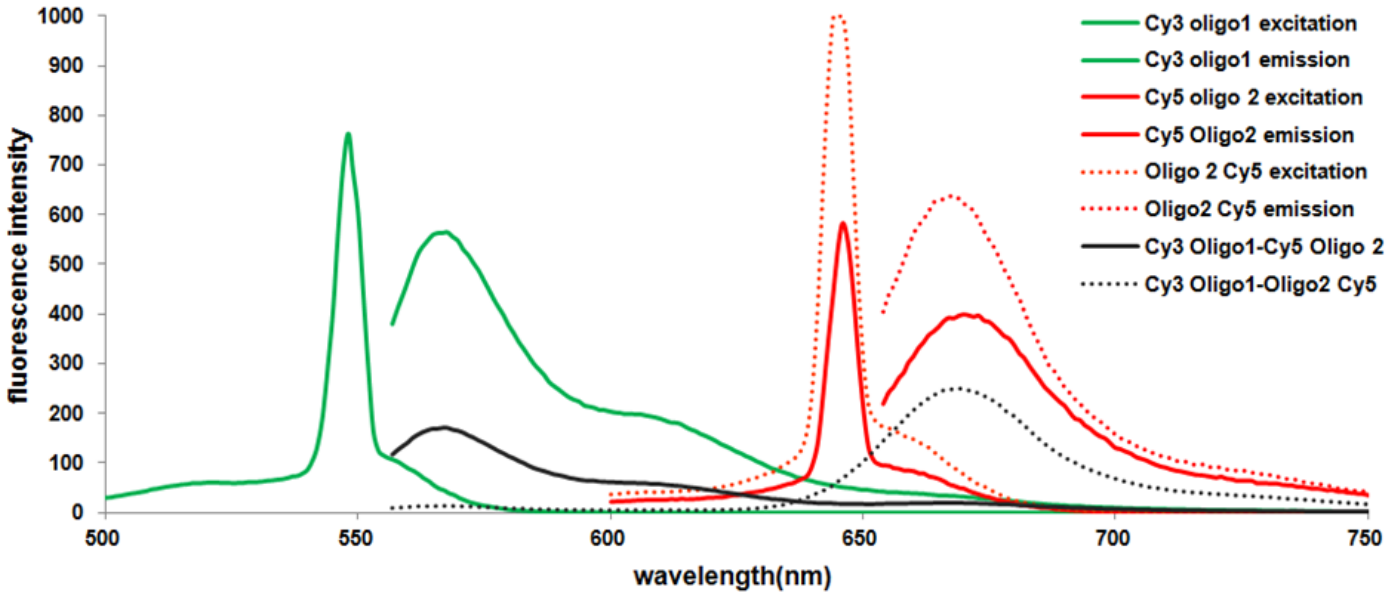

Figure S-4. Fluorescence excitation and emission spectra from solution phase Cy3 probe and Cy5 target DNA oligomers used for FRET analysis: Cy3-oligo1 excitation and emission spectra (green), Cy5-Oligo2 excitation and emission spectra and Oligo 2 Cy5 excitation and emission spectra (red) are also shown for both antiparallel and parallel duplex combinations of Cy3 and Cy5 dyes (black). Experiments were performed with 40μM 100% dye-labeled probes and targets in print buffer and hybridization buffer, respectively at 23°C. Using Cy3 excitation/emission at 547/569nm (5/10 nm slit width) and Cy5 excitation/emission 644/655nm, FRET was measured by exciting at 547nm and recording emission spectra from 557 to 750nm, and similarly exciting Cy5 at 644nm and measuring emission from 655-750nm

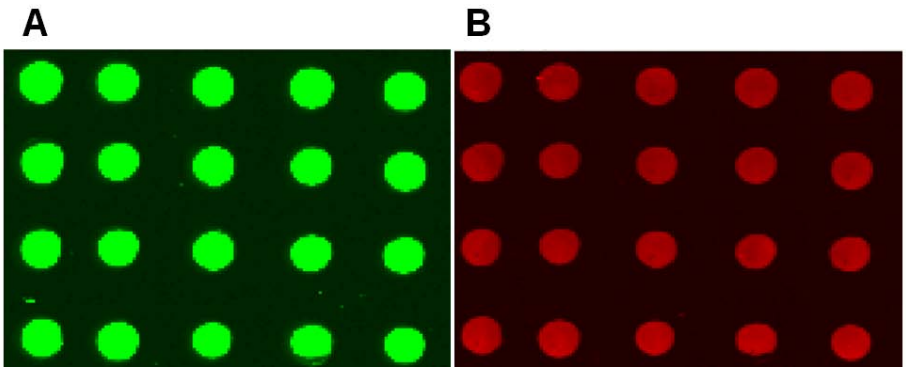

Figure S-5. Fluorescence scanner images of DNA spots immobilized on commercial polymer-coated arraying slide before and after real time hybridization analysis of individual microspots. A) Probe Cy3 fluorescence intensity at 535nm; B) The same set of spots after hybridization with complementary Cy5-target DNA (anti-parallel Cy3/Cy5 dye duplex orientations) and then scanned at 635nm.

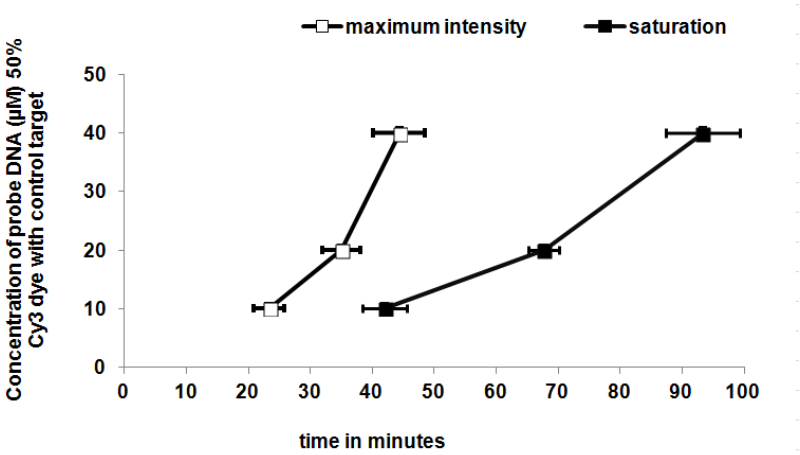

Figure S-6. Increase in time to crossover of Cy3-Cy5 emission intensities (open boxes, left)) for experiments as shown in Figure S-3, and time to signal saturation in single printed spots (filled boxes, right) with increasing printed DNA probe concentration. Each curve represents 10, 20 and 40μM DNA printed spots containing 50% Cy3-DNA and duplexed with Cy5-target (1μM containing 1% Cy5-DNA) for hybridization using case 1 (antiparallel, see Figure 1) relative Cy3/Cy5 dye positions on DNA probes vs. targets.

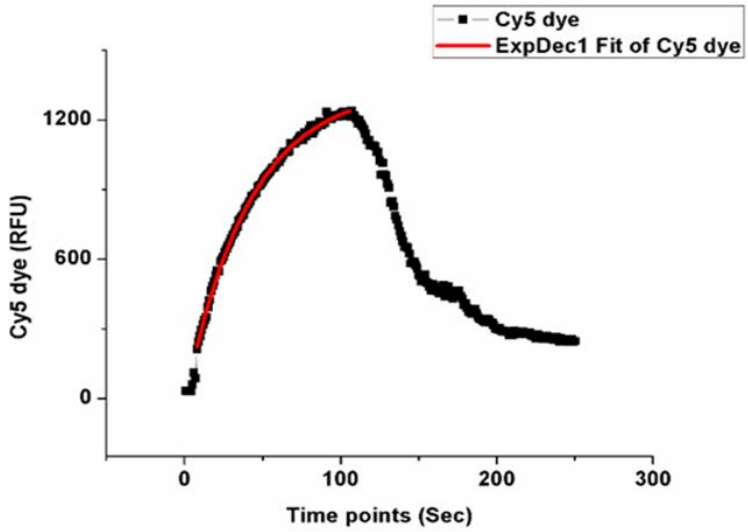

Figure S-7. DNA hybridization kinetics: plot of Cy5 intensity (change in concentration of bound target) vs. time (for case 1 antiparallel Cy3/Cy5 dye position hybridization; see Figure 1). The curve fit of data (red line) shows first-order kinetics with an on-rate constant of k_1= 0.0243sec^{-1}.

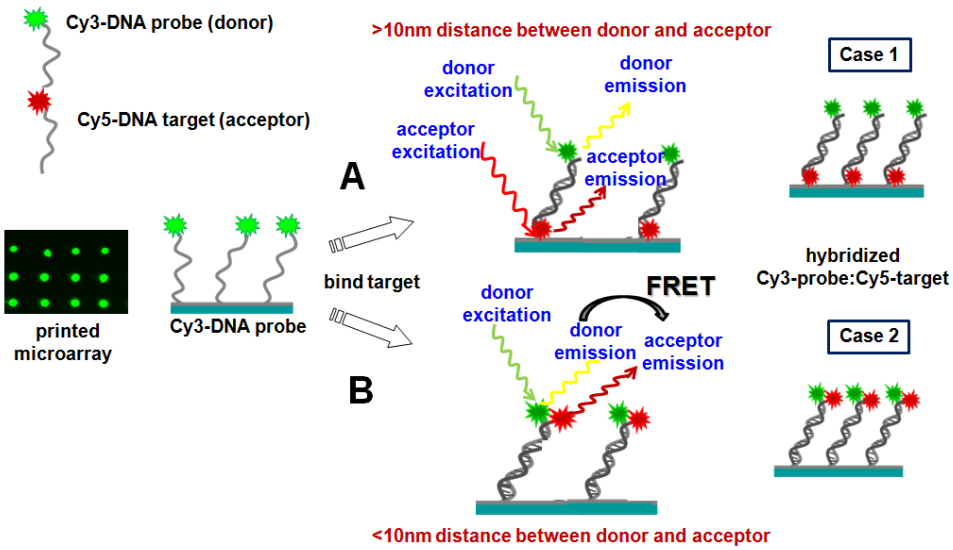

Figure S-8 Schematic of DNA microarray FRET assay designed with labeled-DNA dye with different dye orientations in duplex of surface-bound single spot assays. A) Case 1 (see Figure 1): no FRET anticipated from antiparallel duplex distances between Cy3/Cy5 positions; B) Case 2 (see Figure 1): FRET anticipated with Cy3-Cy5 fluorophores in close proximity with parallel pairing of the Cy3/Cy5 duplex in printed spots.

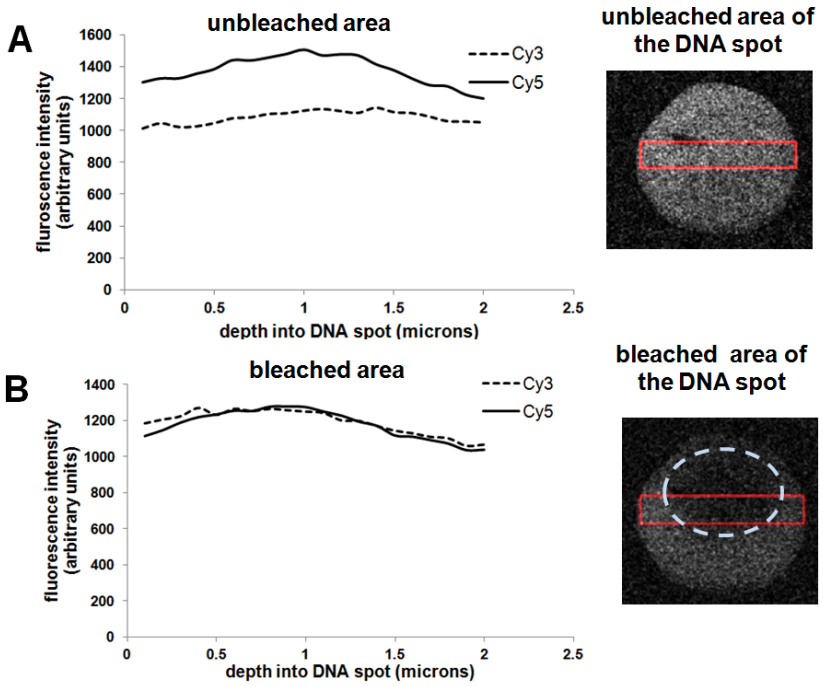

Figure S-9 Fluorescence emission intensities of Cy3 probe and Cy5 target as a function of depth in single hybridized microspots on surfaces using confocal z-slices of 0.5 μm each for: A) unbleached areas, and B) bleached areas (dotted oval, bleached as described in the Methods section) for the same single DNA spot. A) intensity in unbleached area is similar to real-time hybridization measurements with Cy5 intensity greater than Cy3 (FRET effects, see Figure S-3), whereas B) shows both decreased target Cy5 intensity compared to probe Cy3 after Cy5-specific photobleaching, as well as increased Cy3 emission intensity due to lack of FRET. Additionally, integrated Cy3 or Cy5 emission intensities (across solid rectangle shown) measured at different Z slice depths reflect probe Cy3 and target Cy5 emission signals in different depth regions of the DNA spot. Peak Cy5 emission intensity occurs at intermediate depth in spot (despite the confocal slice sampling thickness being thicker than the printed spot total thickness) in both A) and B). (Printed spot: 40μM printed probe DNA containing Cy3-DNA probe fractions of 10%, and duplexed with complementary Cy5-target (1μM containing 1% Cy5-DNA) with parallel (same end, Case 1, Figure 1) dye orientations).

CHAPTER-4

PRINTED SPOT HETEROGENEITY IN PNA MICROARRAYS

Archana N. Rao[1] and David W. Grainger[1,2*]

[1]Department of Pharmaceutics and Pharmaceutical Chemistry, University of Utah, Salt Lake City, UT 84112-5820 USA

[2]Department of Bioengineering, University of Utah, Salt Lake City, UT 84112 USA

**to whom correspondence should be addressed:* David W. Grainger, david.grainger@utah.edu

Keywords: microarray, peptide nucleic acid, betaine, epifluorescence imaging, spot heterogeneity, contact printing, evaporation

---

Submitted to Analytical Chemistry, ACS, February 2013

4.1 Abstract

Microarray printed spot heterogeneity, variable spot morphology, inter/intraspot non-reproducibility, and varying spot thickness are major challenges to the analytical fidelity of array technology. Improvements in slide surface chemistry, use of surfactants in print buffers, and manipulation of physicochemical properties of spot drying and wetting during evaporation have led to improvements in printed spot quality. Uncharged DNA analogs comprising peptide nucleic acid (PNA) oligomers have been used as an alternative DNA microarray capture probe to study printed spot features with the intent of providing more uniform immobilized probe capture density and distributions within printed spots. Fluorescently labeled (Cy3-PNA) amine-terminated probes were printed on commercial amine-reactive N-hydroxysuccinimide (NHS) polymer microarraying surfaces. Various surfactants and buffer solutions were used to study dried spot heterogeneity. Standard fluorescence scanner and epifluorescence images show nonuniform spots for print buffers containing betaine and sodium phosphate. Variation in spot morphology, geometry, drying patterns, and spot fluorescence intensities with different surfactants indicate that the dominant effect on spot quality is the time-scale of droplet evaporation rather than the print buffer chemistry. Printed droplet spreading is affected by buffer components, providing an original wetting “footprint” on the surface. Subsequent droplet evaporation begins immediately with printing and is largely complete within a few seconds, leaving solutes (salts, PNA) within the original wetted footprint at variable density. This has a dominant influence on final dried spot morphology and distribution of PNA probe is independent of print buffer surfactants, ionic strength, and pH. The heterogeneous array spots obtained affect the resulting hybridization with incoming target, resulting in variable signal generation on the surface and impacting the assay answer. Hence, PNA probes possess similar issues in printed spot heterogeneity with contact printing as DNA precedents due to the physicochemical properties of initial droplet spreading and then solute deposition during droplet evaporation.

4.2 Introduction

High-density printed nucleic acid-based microarrays for high-throughput genomics screening and lower-density microarrays for various diagnostics find wide-ranging applications in

cancer diagnostics, drug discovery, toxicology, pharmacogenomics and forensics (1, 2). Microarray fidelity as an analytical tool relies on natural base pairing of two short complementary nucleic acid strands on a capture surface (probe and target), converting this hybridization event into a measurable detection signal such as integrated fluorescence intensity within printed spots (3) . The specificity and selectivity, of probe-target duplex formation is crucial for the success of this technology (4). However, higher affinity, selectivity, and improved fabrication issues have favored replacing certain components of DNA microarrays with DNA analogs including peptide nucleic acids (PNA) (4, 5), morpholinos or phosphorodiamidate morpholino oligos (PMO) (6), and locked nucleic acids (LNA)(7) as capture reagents (i.e., surface-immobilized probes). PNA is a DNA analog in which the entire negatively charged sugar-phosphate biopolymer backbone is replaced with a neutral peptide-like backbone consisting of repeated N-(2-aminoethyl) glycine units linked by amide bonds (8, 9) (see supplementary Figure S-4.1). Given this unique structure, PNA's hybridization properties are unique compared to traditional oligonucleotides (10). PNA hybridization to complementary oligonucleotides obeys the Watson–Crick base-pairing rules with the PNA and DNA strands joined through hydrogen bond (8, 10, 11). Given PNA's uncharged backbone, PNA/DNA duplexes form independent of ionic strength and with high stability (12-14). At ambient temperature, PNA-DNA hybridization is 3-fold higher compared to DNA-DNA based duplexes. Also, the T_m values for a 15-base PNA-DNA versus DNA-DNA complex are 69°C and 53°C, respectively, permitting hybridization responses with PNA at elevated temperatures up to 50°C where DNA-DNA duplexes are unstable. The single-base mismatch DNA oligonucleotide provides 90% interference in DNA-DNA duplexes, but only 19% change for the analogous PNA-DNA pair. The strong enthalpy-entropy compensation (large entropy loss and enthalpy gain) (15) occurring in PNA-DNA duplexes with weakening of base-paired bonds (smaller $\Delta H°$) in the vicinity of the mismatch is compensated by a less rigid duplex structure (smaller $\Delta S°$) upon forming a less perfect sequence-matched duplex. This is attributed to changes in base pair formation, stacking, and the rearrangements of solvent molecules and ions (13). Observed decrease in T_m (i.e., destabilization) for PNA-DNA duplexes with increasing ionic strength in a concentration range of 0.01 to 0.5M is attributed to electrostatic effects dominant during counterion release

upon duplex formation. This contrasts the counterion association accompanying the formation of a DNA duplex. Also, at high salt concentration (>1M), where electrostatic contributions saturate, a decreased T_m observed for PNA-DNA and PNA-PNA duplexes were found to follow the Hofmeister series, underscoring the importance of hydrophobic interactions among nucleobases for PNA complex stability at high salt concentration (16). PNA microarrays have been fabricated using microcontact printing on glass slides modified with amine groups (17). PNA probes have also been spotted using noncontact printing at various concentrations ranging from 5 to 200μM in 1M betaine in water (pH 7) on maleimide-activated wafers and gold surfaces (5). The same authors also fabricated PNA microarrays with a contact printing technique utilizing split pins (18). Others have synthesized self-assembled monolayers (SAMs) of single-strand PNAs (ssPNA) on gold surfaces and demonstrated efficient capabilities for recognizing complementary ssDNA (19). PNA-DNA-based capture surfaces have been characterized by various optical (20) and surface analytical tools such as X-ray photoelectron spectroscopy (XPS), atomic force microscopy (AFM) (21), reflection absorption infrared spectroscopy (RAIRS) (22), surface plasmon resonance (SPR) (23), surface enhanced Raman scattering (SERS) (24), and time-of-flight secondary ion mass spectrometry (TOF- SIMS) (25, 26). Mateo-Marti et al. characterized PNA and PNA-DNA with XPS, providing chemical information and density of the molecular layers (22, 27). Additionally, TOF-SIMS measures the PO_2^- and PO_3^- concentrations in PNA-DNA hybridized duplexes; similarly, PO_2^- vibration frequency in RAIRS and nitrogen and phosphate binding energy using the XPS for detection since the nitrogen peak distorts upon PNA-DNA duplex formation (26).

Printed DNA probe individual spot heterogeneities and morphologies were documented with TOF-SIMS chemical and epifluorescence imaging techniques, and indicated that Marangoni drying patterns of DNA droplets influenced the final spot distribution of probe (28). Nanoliter volume DNA print droplets dispensed on array surfaces evaporate within seconds, leaving a heterogeneous, dried probe film on the surface (29). Since immobilized probe density is well-recognized to affect DNA target hybridization kinetics and also duplex efficiencies on surfaces (30, 31), the probe spotting and drying process is critical to controlling the target capture and consistent signals in printed spots (28, 32, 33). Real-time hybridization kinetics on spotted surface

demonstrate transport-controlled radial hemispherical diffusive transfer of target DNA to probe spots, with duplex fronts moving from the spot's outside (less dense probe) to the spot interior (more dense probe) as seen using confocal imaging (32, 33). Since probe density in spots can produce both steric hindrance and Coulombic blockade of incoming DNA target, PNA probes were hypothesized to improve DNA target capture behaviors by avoiding the large local electrostatic field issues that complicate DNA-DNA duplexes in high-density probe spots on surfaces. Experiments using RAIRS of ssPNA adlayers on gold show PNA lying flat on the surface. However, with increased PNA probe concentration, the ssPNA probe orients normal to the surface (22). Also, similar to tethered ssDNA, ssPNA molecules realign their molecular axes with the surface normal and form organized adlayers without co-immobilization of spacers or other backfilling molecules (18, 34). PNA printed in betaine, Tween 20, and sacrosine produced different microdroplet wetting, spreading, and spot drying patterns. With only water as the solvent without any additives or surfactants, printed PNA probes show more spreading and formation of noncircular spots. PNA printed spots in betaine solution produced spherical spots with sporadic distribution of ssPNA in the spots. PNA spots in sodium phosphate solution produced less uniform spots with a Marangoni drying pattern. These results indicate that drying and spreading dominate the effects of ionic strengths, type of additive, pH, and electrostatic interactions between probes. However, spot morphology or shape did not change after hybridization with DNA targets. Nonetheless, the additive systems in probe solution do not resolve the spot heterogeneity issues, meaning that high rates of droplet evaporation after it is dispensed on to a surface are the greater influence on final dried spot morphology, shape, and probe density that affect signal production.

4.3 Materials and methods

4.3.1 Materials

HPLC-purified grade (≥90% purity**)** DNA oligomers with several different terminal modifications (Table S-1) were purchased from TriLink Biotechnologies (San Diego, USA) (29, 35). Cy5 (target) fluorophores are incorporated at 3' oligonucleotide termini during synthesis using phosphoramidite reagents through a C6 linker to the ssDNA. PNA oligomers (>85% purity,

Biosynthesis,,USA) were synthesized similarly to peptides with Fmoc solid phase peptide synthetic chemistry with 2 O-linkers instead of the C6 linker for dye labeling to enhance the solubility of the dye-modified PNA (see supplementary information for all probe sequences, Table S-1).

Ultrapure water (UPW, ASTM type I water) was used for all solution preparations and protocols for microarray fabrication. All chemicals were used as received. Additives, salts, sarcosine, sodium dodecyl sulfate (SDS), betaine and ethanolamine were ACS grade (Sigma-Aldrich,, USA). Microarray slides (Slide H, amine-reactive 3D polymer-coated array slides, Schott Nexterion, Louisville, USA) were used for PNA oligomer probe printing, print buffer alone, and gold nanosphere spot printing. New slides taken from the manufacturer's packaging were used without any pre-treatment and unused slides were stored under nitrogen at 4°C and used within a month after opening the package to preserve their ester reactivity. Three kinds of PNA solutions were prepared in water-only (pH 7.5), betaine-only (1M) (pH 7.5) and sodium phosphate probe print solution (150mM sodium phosphate, 0.01% Tween 20 and 0.01% sarcosine at pH 8.5) (29, 35).

4.3.2 PNA probe immobilization on substrates with array contact printing

Microarrays (see layout shown in Figure S-2 and printing methodology in Supporting Information, similar to previous report(29)) were printed with multiple probe concentrations (10, 20 and 40 micromolar) and different molar ratios of Cy3 dye-labeled probe (Cy3-Oligo-Lys) to unlabeled probe (Oligo1-Lys) (i.e., 0:1, 1:3, 3:1, and 1:0). This yielded printed rows of spots containing no Cy3-labeled probe (0:1) progressing to printed rows of spots containing 100% Cy3-labeled probe (1:0). Non-specific polymer surface interactions (i.e., residual substrate primary amine chemical reactivity) were then blocked on PNA-printed slides using a step-wise protocol per manufacturer's recommendations (see Supporting Information for details). Non-complementary PNA probes were also printed with various buffer concentrations (10, 20 and 40μM). Humidity was maintained at 55-60% during print conditions, at ambient room temperature (23° C). After printing, the slides are placed in a salt water bath (fabricated in-house) to maintain 90% humidity for 12 hours (overnight). DNA spots were printed with the same conditions as PNA spots.

4.3.3 Postprint treatment and hybridization of printed microarray slides

Briefly, printed slides were rinsed in sodium phosphate print solution and then immersed in blocking solution (50mM ethanolamine in 0.1M Tris, pH 9.0) at 50°C for 30 minutes to consume residual surface amine-reactive NHS groups (36, 37). Subsequently, slides were rinsed thoroughly with UPW 3 times followed by immersion in hybridization solution (4X saline sodium citrate (SSC) containing 0.1% SDS at pH 7) at 50°C for 30 minutes. Slides were finally rinsed with UPW 3 times, blown dry with nitrogen, and immediately imaged with a fluorescence scanner for probe-only studies (details below). The hybridization process of PNA-DNA and DNA-DNA were similar to the above protocols.

Target hybridization was accomplished using Lifter slips (Erie Scientific no. 22x50I-2-4711) for microarray samples. Briefly, 1μM target DNA solution (1:99 Cy5-Oligo2:Oligo2) prepared in hybridization solution (4X SSC/0.01% SDS) was applied separately to the PNA and DNA probe spots for 4-hour incubations at room temperature and 100% relative humidity. After hybridization, slides were rinsed with hybridization solution followed by the solutions (2X SSC/0.1% SDS for 5 minutes, 0.2X SSC and 0.1X SSC for 1 minute each), and finally dried with nitrogen.

4.3.4 Fluorescence scanner images of printed DNA and PNA probe microarrays

Printed PNA microarray slides were fluorescently scanned after the blocking step and both before and after the hybridization step using a GenePix Microarray scanner 4100A, v.6 software. Slides of PNA printed and hybridized with target DNA were scanned using two optical channels (535 and 635 nm for Cy3 and Cy5, respectively). The following settings were used for all scans: laser power 100%, brightness and contrast 92%, PMT gain 400, pixel size range 5-100 micron, and line average set at 3. 4 print samples each of PNA and DNA were printed. 2 samples were further hybridized with DNA. 2 samples each of unhybridized (PNA probe only and DNA probe only) and 2 samples of PNA-DNA and DNA-DNA were hybridized for each type (water, betaine, and sodium phosphate). An average of 10 spots was analyzed for each concentration (40, 20, and 10μM) and

% of dye (100, 75, 25, and 0%). However, with PNA printed spots in betaine and water, 10μM and 20μM concentration spots were not visible in epifluorescence images, although with fluorescence scanner, spots were observable for all concentrations of probe and dye.

4.3.5 Epifluorescence imaging of single unhybridized PNA and DNA probe-only spots and hybridized PNA-DNA and DNA-DNA

High-resolution fluorescent images of single PNA spots were acquired (Olympus IX81 epifluorescence microscope, Prior Scientific motorized XYZ environmental stage, motorized shutter/filter wheel, and Photometrics CoolSnap-ES scientific CCD camera in 36-bit color mode, controlled by Metamorph V6.2r6 software). Successive fluorescent images of individual DNA spots were captured under motorized XYZ stage control. Autofocus was set initially for the DNA spot containing the highest dye intensity (e.g., 40μM DNA, 100% Cy3) to establish maximum image contrast and successively measured for all printed PNA spots in that array with the same optical parameters. Based on spot dye content, different microscope air objectives were used to maximize image information collection per spot (excitation filter 510-550 nm, dichroic long-pass filter from 510 nm, and emission band pass filter at 575-600 nm used for Cy3 image capture). For Cy5-DNA excitation, filter of 610-645 dichroic long pass filter from 610 nm and emission band pass filter at 665- 680 nm was used for Cy5 image capture. All images are pseudo-colored and image contrast was adjusted using the auto-scale function in Image J. This processing can produce concentric rings of different colors with defined rings most often being artifacts from the technique, hence, not real.

4.3.6 Contact angle measurement of DNA print solution on slide H

Contact angle measurements were performed on slide H with 3 different solutions - water, print solution, and Cy3 dye-labeled DNA in print solution to assess the variation in contact angle of the solution influencing the patterning of the DNA spot. The measurements were performed using KSV Cam101 Goniometer. The print solution was comprised of 150mM sodium phosphate, 0.01% tween, and 0.01% sarcosine and the DNA solution contained 100% Cy3 dye-

labeled 40μM DNA in the print solution. Contact angle measurements for each solution were performed on 3 different slide H samples (n = 3).

4.4 Results and discussion

4.4.1 Assessment of PNA (Cy3-PNA) probe-only spots and hybridized spots (Cy5-DNA) using fluorescence scanning

Scanned images (Figure 4.1) of PNA (Cy3-PNA) printed probe spots only show non-circular spots with little-to-no PNA present at spot centers. These spots also show higher spreading areas, with spots overlapping each other with a spot-spot center-center spacing distance of 125 microns. As expected, the 40μM spots exhibit highest Cy3 fluorescent intensities with spots gradually decreasing in fluorescence intensity and diameter with decreased DNA concentration (i.e., 20μM and 10μM) (data not shown) and with % DNA-dye content in the print solution. Hybridized PNA-DNA spots show similar printed spot morphology and size compared to PNA probe-only spots. PNA probe-only printed in betaine solutions produce uniform circular spots, but the camera PMT gain had to be increased (i.e., to 500) to observe these spots, indicating that the Cy3 fluorescence was diminished compared to other print conditions. The spot morphology is uniform with even distribution of intensity across the spot area (seen with 4 replicates of 15×10 print spots each). However, PNA-DNA spots show higher fluorescent intensities at spot edges compared to centers. Spot size and intensity for similar concentration (e.g., 40μM) with varying DNA-dye content (i.e., 25%, 75%, and 100%) did not show drastic differences in intensity or spot dimensions. PNA probe-only spots printed with sodium phosphate solution showed uniform circular spots with both PNA probe-only and PNA-DNA hybridized spots. Printed spots show increases in spot dimensions and intensities with increasing concentration of probe and DNA-dye fraction.

4.3.2 Epifluorescence image analysis of printed and hybridized spots printed from different probe print solutions

Single printed PNA probe-only spots in print solutions were evaluated for morphology, spot heterogeneity, and intensity. Spots after hybridization with target Cy5-DNA were also

analyzed. Probe spots printed with pure water, with evaporation/drying in the absence of salts and surfactants that influence drying patterns, spot dimension, and shape were compared to probe spots printed from salt- and surfactant- containing print solutions. Spot drying patterns are known to be largely influenced by initial wetting, mode of evaporation, temperature, humidity, surface chemistry, and the hydrophobicity/hydrophilicity of the substrate (38).

4.3.3 Epifluorescence imaging of PNA spot morphology assessed for PNA probe spots printed from water

Epifluorescence image analysis of single PNA printed spots in water revealed mostly noncircular spots with nonuniform distribution of the Cy3-PNA in the spots (Figure 4.2). Printed spot morphology showed more Cy3-PNA at the spot edges and less PNA at spot centers. Spot shapes were generally oval, not round, with spots overlapping each other's wetted footprint (125 micron center-center spacing). Spots with higher PNA concentrations (40μM) were visible but spots with lower concentrations and reductions in Cy3-DNA fraction were not visible by epifluorescence imaging. Also, intra- and interspot heterogeneity was observed across most printed spots. Intensity line scan profiles across probe-only single spots show higher intensities of Cy3 at spot edges compared to the spot center. However, DNA hybridization results in higher amounts of DNA target present in spot centers (depicted in line plot). Images for PNA-DNA hybridized spots were inconsistent, showing DNA at the spot center. Higher intensity of DNA at spot centers can result from higher hybridization there, perhaps due to lower probe density at spot centers that limits steric issues in duplex formation and Coulombic blockade (39). Probe-only spots also demonstrate an increase in spot dimensions and Cy3-fluorescence intensity with increasing concentrations of both PNA probes and amounts of Cy3-PNA fractional content in the print solution (Figure 4.3). More clearly distinguishable outer spot edges in hybridized spots may be attributed to a slight decrease in spot size.

4.4.4. Epifluorescence imaging of PNA spot morphology for PNA spots printed with betaine solutions

PNA printed spots printed from 1M betaine show different spot morphologies compared to those printed with water. The betaine-printed spots are more circular with drying and spreading patterns showing nearly perfect circles comparable with those observed in fluorescence scanner images. However, with epifluorescence imaging, a random distribution of Cy3-PNA dye in the spot is observed (Figure 2). The plot profiles for PNA probe-only spots show random distributions of Cy3-PNA throughout the spot. PNA-DNA hybridized spots exhibit more uniform spots, with higher Cy5 fluorescent intensity at outer edges (Figure 2). The PNA-DNA hybridized spots show coffee ring patterns for spot drying, with higher Cy5-intensity at the spot edges, as shown in intensity line scan profiles (Figure 2). Betaine is used as a surfactant to aid in contraction of the droplet to yield more reliable regular circular spots (40). Also, the addition of betaine is known to limit evaporation (at a concentration of 8M betaine, evaporation stops) by increasing the solution viscosity (41). However, Figure 2 shows that the intensity of Cy3-PNA fluorescence for the same volume of printed PNA probe was reduced compared to spots printed from water for identical PNA concentrations and amounts of Cy3-PNA dye. Betaine added in small amounts to SDS has been shown to increase the surface elasticity, with betaine converting from a zwitterionic to cationic additive, increasing the liquid surface tension (42). Additionally, PNA printed spots with betaine show reduced spot wetting and spreading with no overlap of printed spots. Reproducible diameters are also shown for Cy3-PNA spots printed with betaine for various amounts of Cy3-PNA labeling (25%, 75%, and 100%) compared to water or sodium phosphate.

4.4.5 Epifluorescence imaging of PNA spot morphology for PNA printed from sodium phosphate

PNA spots printed with print solutions comprising Tween 20 (nonionic) and sacrosine (zwitterionic) surfactants, commonly used species known to be driven to spot edges during evaporation (43, 44), exhibit a gradient in surfactant concentration along the liquid-solid interface due to flow (spreading) and recirculation to the drop center, resulting in solute deposition at the spot center relative to the edges (45). In the presence of salt solution, the salt-deposition pattern

dictates the mode of spreading and drying of the spots, with the probe deposition following the salting trace (46). Addition of surfactants greatly influences the spot diameter (increasing the spot size by reducing the contact angle and wetting energy for spreading) (38). PNA probe spots show similar spot dimensions compared to those from betaine for various concentrations of PNA probe. However, these spots show variations in spot dimensions for a particular PNA concentration with varying fractions of Cy3-PNA added (Figure 3). Intensity line scan profiles for single spots show high intensity of Cy3-PNA at spot centers. Hybridized PNA-DNA spots (Figure 3) display similar patterns with increased Cy3 intensity at spot centers.

4.4.6 Comparisons of PNA probe-only and DNA probe-only spots printed with sodium phosphate print solutions

PNA probe-only spots were compared with printed DNA probe-only spots under identical conditions. PNA probe-only spots exhibit similar morphology resulting from Marangoni drying patterns, with higher concentrations of Cy3-PNA at spot centers compared to edges (Figure 4A) (28). DNA spots show increased spot diameters and Cy3 fluorescent intensity compared to PNA spots at similar concentrations of probe and Cy3 dye content (Figure 4B and C). However, the drying pattern of the spots with both the probes (PNA and DNA) was similar, with similar distributions of probe intensities as shown by line scan analysis of individual spots.

Additives present in probe printing solutions alter printed spot wetting, spreading, spot morphologies, dried dimensions, and fluorescent intensity. Literature review shows betaine used often in print probe solution more often for PNA than DNA (4, 5). Betaine produced circular spots, but the distribution of Cy3-PNA was not uniform across the spot, leading to coffee ring-like patterns that become more prominent after hybridization with Cy5-DNA. Sodium phosphate with surfactant – a commonly used printing matrix (recommended by Perkin Elmer, CodeLink and Schott Nexterion technologies) – also produced circular spots. However, increased concentration of Cy3-PNA at spot centers, similar to that seen in printed Cy3-DNA spots is observed (32), due to Marangoni spreading and drying process (31, 32, 47). Without any additives, PNA probe (in water) produced nonuniform and noncircular spots, overlapping due to an increased wetting and spreading during spotting and drying. However, even with the addition of surfactants, all probe

printed spots exhibited heterogeneous fluorescence intensity distributions across spots, with intra- and interspot heterogeneity in morphology and nonuniform fluorescence intensity. Rapid spot evaporation and drying (i.e., within a few seconds after droplet deposit on the chemically reactive surface) is a dominant influence on final spot morphology, regardless of the print solution additives. Also, Cy3-PNA spots printed from water and betaine solutions at lower concentration were not readily visible in epifluorescence imaging. Evaporation processes accompanying printed spots with contact printing exert profound influences on final droplet shape and distribution of solute contents across the spot.

4.4.7 Contact angle measurement of DNA print solution on slide H

We obtained printed spots of DNA and PNA in sodium phosphate print solution leading to Marangoni droplet drying pattern with higher density of the probe at the center compared to the edges. It is well known that the Marangoni droplet drying patterns are influenced largely due to surface tension of the solution. Surface tension gradients in the solution lead to intensive mixing of the analyte during evaporation. This helps to overcome mass transport limitation countering the force forming coffee ring droplet drying. The contact angle measurement for water was ~60^{o} (60.36 ± 0.23 standard deviation), for print solution was ~55^{o} (55.45 ± 0.47 standard deviation), and for DNA in print solution again was ~60.5^{o} (60.57 ± 0.7standard deviation), (similar to water) (shown in Figure S-4.3). These results show that the contact angle is around ~60^{o} for different solutions indicating the slide H is hydrophilic. Since all the other factors in the experiment were the same except for the composition of the solution, it could be hypothesized that there is no significant change in the surface tension of the solution due to the addition of DNA (compared to water). Further experiments on measurement of surface tension of different probes (PNA/DNA) in different print solution needs to be conducted to investigate the influence of surface tension on spot drying patterns.

4.5 Conclusions

PNA was proposed as an alternative to printed DNA oligomers as it lacks formal charge and might avoid commonly encountered steric and electrostatic blockade issues affected by

uncontrolled DNA printed probe density in microarray printed spots. Spot morphology for PNA probe printed from different solutions systems with contact printing polymer arraying slides was studied to assess probe distributions and consistent spot features. Epifluorescence imaging of single spots provided new information on spot heterogeneity, fluorescence intensity for both probe and target in single spots, spot dimensions, and specifically drying patterns. Different spot morphologies result from different print solution compositions (e.g., surfactant, additives). The advantages of using print additives in producing consistent, homogeneous circular spots with defined edges are attractive altering the normal spot evaporation rates spots. However, rate of evaporation dominates over the role of these additives, temperature, and humidity in probe distributions within spots. This is important given the influence of probe distributions on target hybridization efficiencies and fluorescence analysis of integrated spot intensities when probes and targets are poorly distributed. Additionally, PNA spots from sodium phosphate solutions show similar spreading and drying effects comparable to analogous DNA probe spots previously reported (Chapter 2) to undergo strong convection oriented flow from Marangoni spot drying behavior. The electrostatic properties and chemical nature of probe had a small impact on the spot morphology and drying pattern observable for PNA and DNA. However, printed PNA probe spots had smaller spot dimensions for the same concentration of Cy3-labeled probe compared to analogous DNA probe spots. The reduced electrostatic and steric repulsion in PNA probe-only spots comparative to DNA could have attributed to smaller spot dimension observed in case of PNA probe-only spots. Microdroplet printing yields heterogeneous dried spots driven by many intersecting physical and chemical factors, with little alterations observed from the use of print solution additives to mitigate dominating influences from rapid evaporative drying patterns.

4.6 Acknowledgments

The authors gratefully acknowledge financial support from NIH grant R01 EB001473. The authors would also like to thank Tony Hsiao in Prof. Hlady's group (Univ. of Utah) for the help with contact angle measurements.

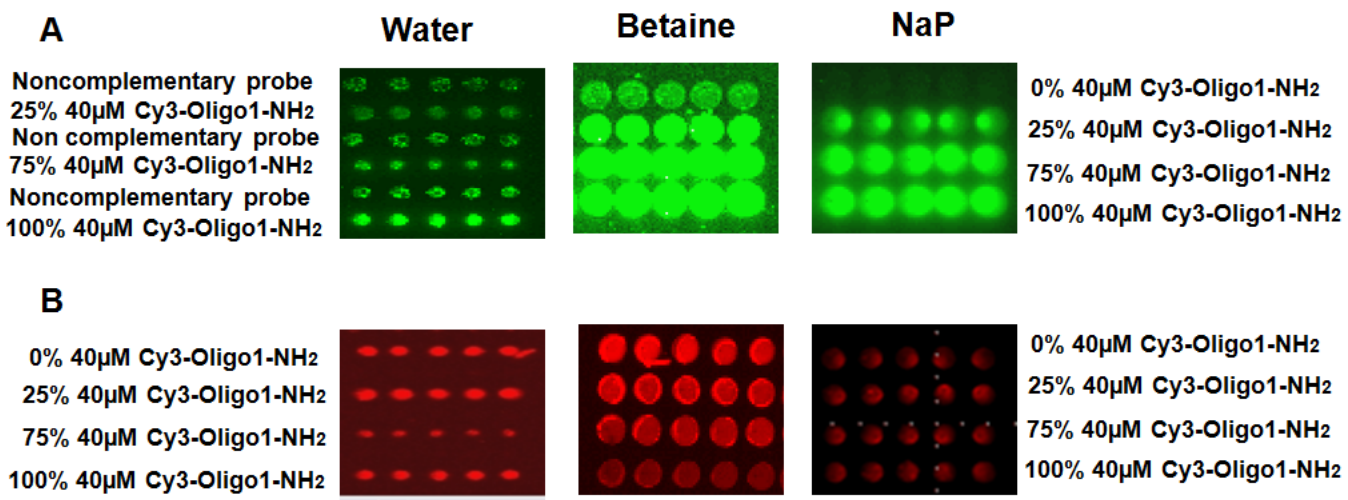

Figure 4.1. Fluorescence scanner images of PNA spots printed in different print solutions. **A)** Unhybridized (PNA-Cy3) (top row) printed in different buffer solutions (water only, betaine and sodium phosphate (NaP) and **B)** hybridized PNA-DNA spots (bottom row) (PNA-Cy3: DNA-Cy5); PNA-Cy3 hybridized with 1μM (1:99 Cy5-Oligo2:Oligo2) DNA-Cy5.

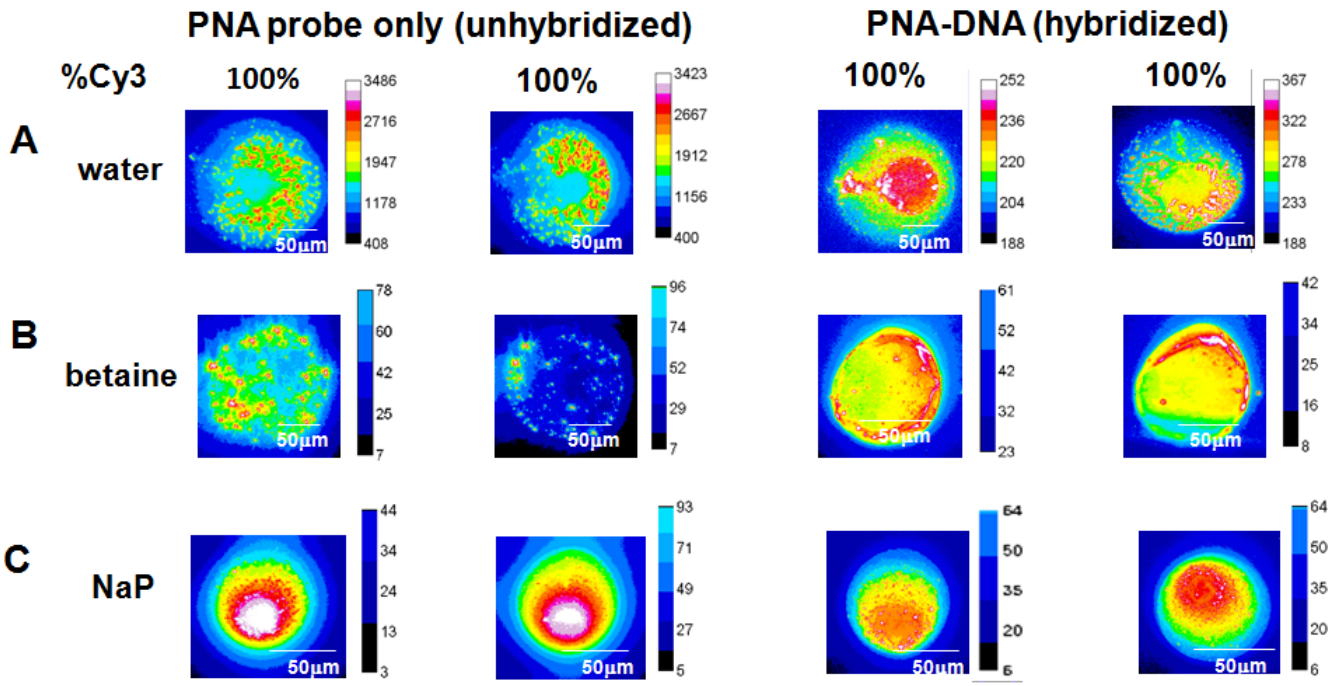

Figure 4.2. Epifluorescence images of single PNA probe spots (40µM 100% Cy3-PNA, left and resulting PNA-DNA hybridized spots, right) printed from different buffers. A) PNA probes printed from water; B) PNA probes printed from betaine; and C) PNA probes printed from 150 mM sodium phosphate with Tween and sarcosine. All images are pseudo-colored with intensity contrast adjusted using the auto-scale function in Image J to depict peak intensity for Cy3-PNA. (2 independent arrays analyzed, 10 different spots inspected, images shown are typical of most images seen). Scale bars in the images are 50µm.

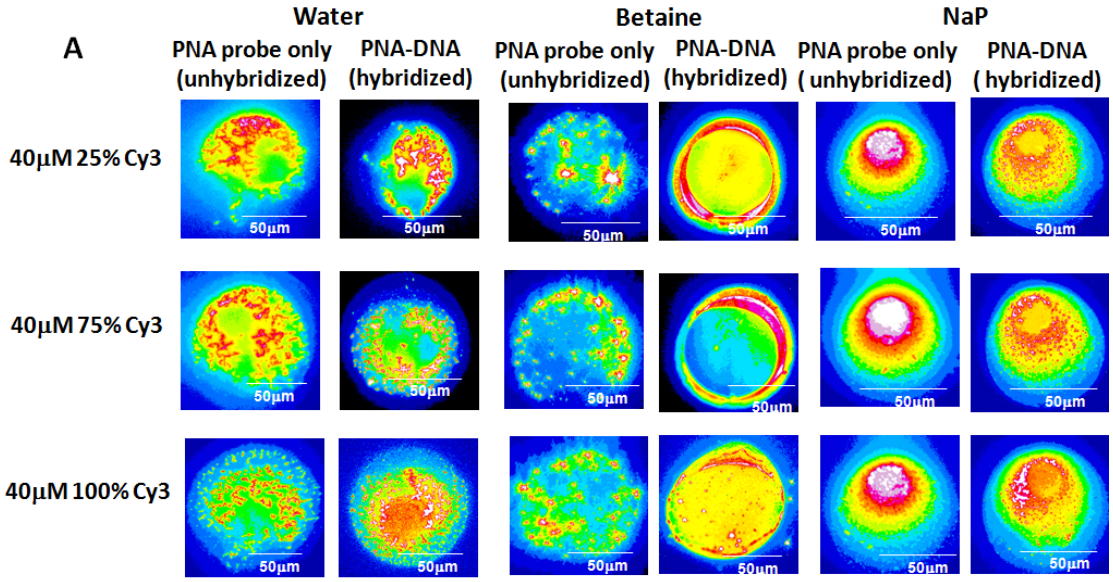

Figure 4.3. Comparison of printed spot morphologies from epifluorescence images, spot diameters, and fluorescence intensities for both unhybridized and hybridized PNA spots from print solutions. **A)** Comparison of epifluorescence images of 40μM PNA printed probe only (left) (printed in different buffer solution) for different concentration of Cy3 dye label (25%, 75%, and 100%) and PNA-DNA spots (right). Scale bars in the images are 50μm. **B)** Comparison of a printed spot diameter of 40μM PNA printed probe-only (printed in different print additives and surfactant solutions) for different concentrations of Cy3-PNA (25%, 75%, and 100%) and PNA-DNA hybridized spots. **C)** Comparison of RFU intensity of 40μM PNA probe-only (printed in different solutions) for different concentrations of Cy3-PNA (25%, 75%, and 100%) and PNA-DNA hybridized spots. (2 independent arrays analyzed, 10 different spots inspected, images shown in (A) are typical of most images seen; n=10 for (B) and (C)).

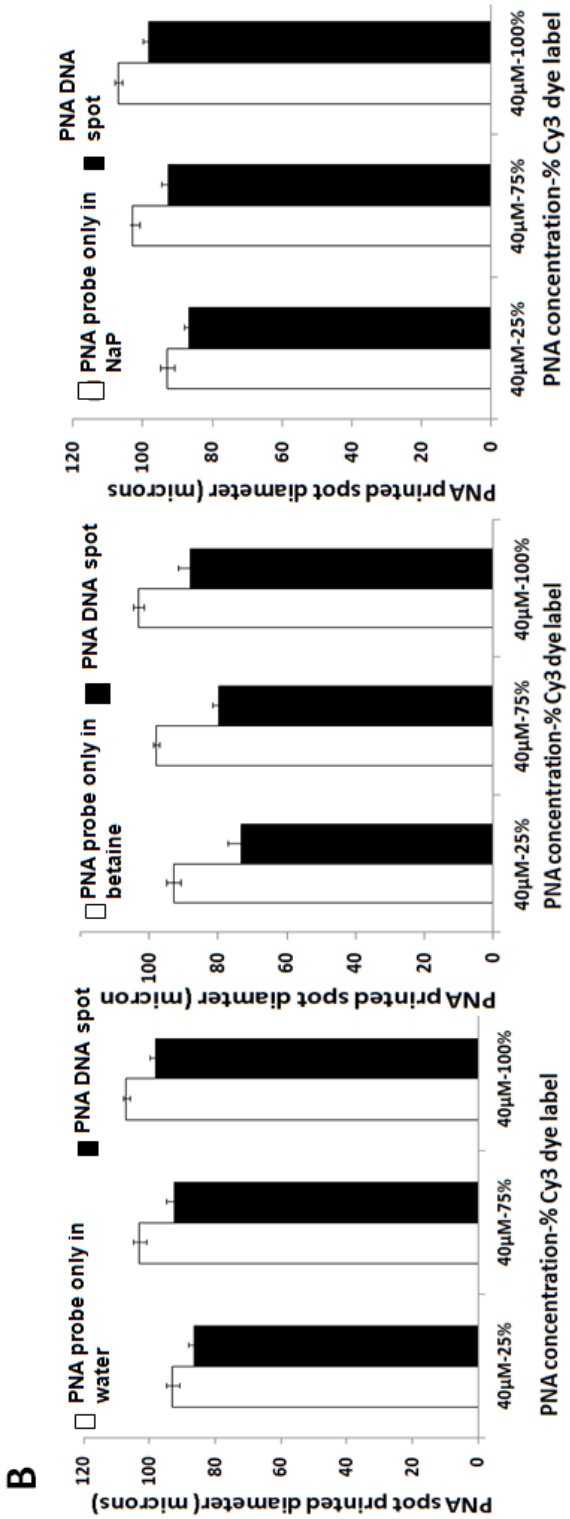

Figure 4.3. Continued

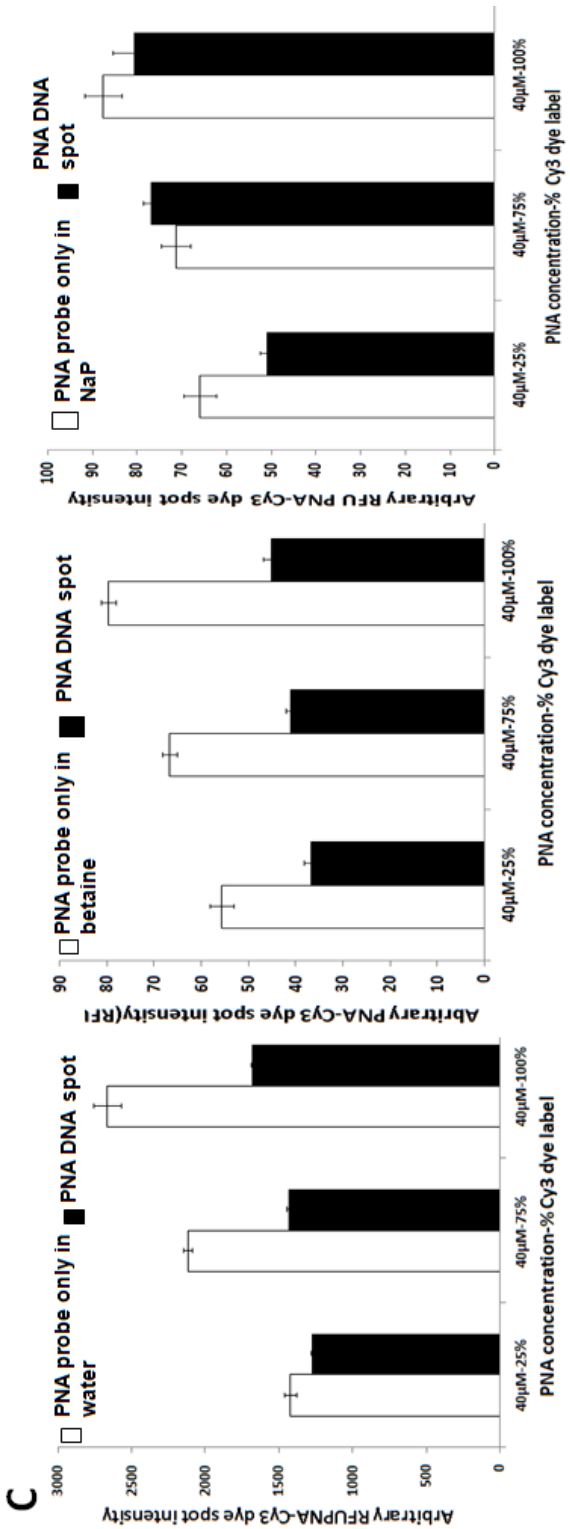

Figure 4.3. Continued.

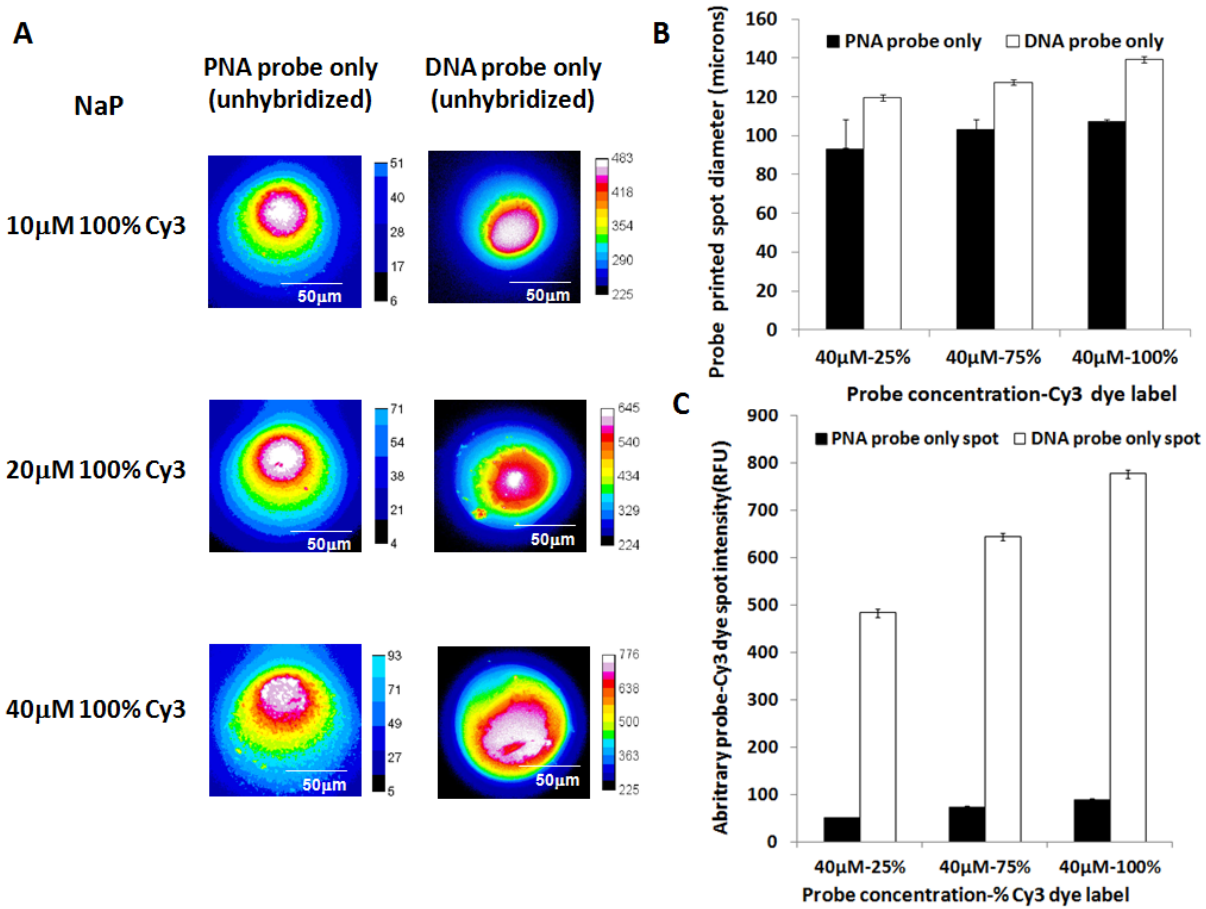

Figure 4.4. Comparison of spot morphology, dimensions, and RFU spot intensity for PNA probe-only and DNA probe-only spots printed from sodium phosphate/surfactant solutions. A) Epifluorescence images of both PNA and DNA probe spots for different concentrations of probe (10μM, 20μM and 40μM) with 100% Cy3-PNA or DNA fraction. Scale bars in images are 50μm. B) Spot dimensions for PNA probe-only and DNA probe-only spots. C) RFU intensity of PNA probe-only and DNA probe-only spots (2 independent arrays analyzed, 10 different spots inspected, images shown in (A) are typical of most images seen; n= 10 for (C).

4.8 References

1. Heller MJ. DNA microarray technology: Devices, systems, and applications. 2002. p. 129-53.

2. Stoughton RB. Applications of DNA microarrays in biology. 2005. p. 53-82.

3. Shalon D, Smith SJ, Brown PO. A DNA microarray system for analyzing complex DNA samples using two-color fluorescent probe hybridization. Genome Research. 1996;6(7):639-45.

4. Wang J. DNA biosensors based on peptide nucleic acid (PNA) recognition layers. A review. Biosensors and Bioelectronics. 1998;13(7-8):757-62.

5. Brandt O, Feldner J, Stephan A, Schröder M, Schnölzer M, Arlinghaus HF, et al. PNA microarrays for hybridisation of unlabelled DNA samples. Nucleic acids research. 2003;31(19).

6. Tercero N, Wang K, Gong P, Levicky R. Morpholino monolayers: Preparation and label-free DNA analysis by surface hybridization. Journal of the American Chemical Society. 2009;131(13):4953-61.

7. Tolstrup N, Nielsen PS, Kolberg JG, Frankel AM, Vissing H, Kauppinen S. OligoDesign: Optimal design of LNA (locked nucleic acid) oligonucleotide capture probes for gene expression profiling. Nucleic acids research. 2003;31(13):3758-62.

8. Egholm M, Buchardt O, Christensen L, Behrens C, Freier SM, Driver DA, et al. PNA hybridizes to complementary oligonucleotides obeying the Watson-Crick hydrogen-bonding rules. Nature. 1993;365(6446):566-8.

9. Nielsen PE, Egholm M, Berg RH, Buchardt O. Sequence-selective recognition of DNA by strand displacement with thymine-substituted polyamide. Science. 1991;254(5037):1497-500.

10. Brandt O, Hoheisel JD. Peptide nucleic acids on microarrays and other biosensors. Trends in Biotechnology. 2004;22(12):617-22.

11. Eriksson M, Nielsen PE. PNA-nucleic acid complexes. Structure, stability and dynamics. Quarterly Reviews of Biophysics. 1996;29(4):369-94.

12. Orum H, Nielsen PE, Jorgensen M, Larsson C, Stanley C, Koch T. Sequence-specific purification of nucleic acids by PNA-controlled hybrid selection. BioTechniques. 1995;19(3):472-80.

13. Ratilainen T, Holmén A, Tuite E, Nielsen PE, Nordén B. Thermodynamics of sequence-specifc binding of PNA to DNA. Biochemistry. 2000;39(26):7781-91.

14. Ratilainen T, Holmén A, Tuite E, Haaima G, Christensen L, Nielsen PE, et al. Hybridization of peptide nucleic acid. Biochemistry. 1998;37(35):12331-42.

15. Nielsen PE, Haaima G. Peptide nucleic acid (PNA). A DNA mimic with a pseudopeptide backbone. Chem Soc Rev. 1997;26(2):73-8.

16. Tomac S, Sarkar M, Ratilainen T, Wittung P, Nielsen PE, Norden B, et al. Ionic effects on the stability and conformation of peptide nucleic acid complexes. Journal of the American Chemical Society. 1996;118(24):5544-52.

17. Calabretta A, Wasserberg D, Posthuma-Trumpie GA, Subramaniam V, Van Amerongen A, Corradini R, et al. Patterning of peptide nucleic acids using reactive microcontact printing. Langmuir. 2011;27(4):1536-42.

18. Brandt O, Feldner J, Hellweg S, Schröder M, Stephan A, Arlinghaus HF, et al. Development towards label- and amplification-free genotyping of genomic DNA. Applied Surface Science. 2006;252(19):6935-40.

19. Briones C, Mateo-Martí E, Gómez-Navarro C, Parro V, Román E, Martín-Gago JA. Structural and functional characterization of self-assembled monolayers of peptide nucleic acids and its interaction with complementary DNA. Journal of Molecular Catalysis A: Chemical. 2005;228(1-2 SPEC. ISS.):131-6.

20. Epstein JR, Biran I, Walt DR. Fluorescence-based nucleic acid detection and microarrays. Analytica Chimica Acta. 2002;469(1):3-36.

21. Casero E, Darder M, Díaz DJ, Pariente F, Martín-Gago JA, Abruña H, et al. XPS and AFM characterization of oligonucleotides immobilized on gold substrates. Langmuir. 2003;19(15):6230-5.

22. Mateo-Martí E, Briones C, Román E, Briand E, Pradier CM, Martín-Gago JA. Self-assembled monolayers of peptide nucleic acids on gold surfaces: A spectroscopic study. Langmuir. 2005;21(21):9510-7.

23. Lao AIK, Su X, Aung KMM. SPR study of DNA hybridization with DNA and PNA probes under stringent conditions. Biosensors and Bioelectronics. 2009;24(6):1717-22.

24. Fabris L, Dante M, Braun G, Seung JL, Reich NO, Moskovits M, et al. A heterogeneous PNA-based SERS method for DNA detection. Journal of the American Chemical Society. 2007;129(19):6086-7.

25. Arlinghaus HF, Schröder M, Feldner JC, Brandt O, Hoheisel JD, Lipinsky D. Development of PNA microarrays for gene diagnostics with TOF-SIMS. Applied Surface Science. 2004;231-232:392-6.

26. Mateo-Marti E, Pradier CM. A Novel Type of Nucleic Acid-based Biosensors: the Use of PNA Probes, Associated with Surface Science and Electrochemical Detection Techniques. Intelligent and Biosensors. 2012.

27. Mateo-Martí E, Briones C, Pradier CM, Martín-Gago JA. A DNA biosensor based on peptide nucleic acids on gold surfaces. Biosensors and Bioelectronics. 2007;22(9-10):1926-32.

28. Rao AN, Vandencasteele N, Gamble LJ, Grainger DW. High resolution epifluorescence and TOF-SIMS chemical imaging comparisons of single DNA microarray spots. submitted to Analytical Chemsitry. 2012.

29. Lee CY, Harbers GM, Grainger DW, Gamble LJ, Castner DG. Fluorescence, XPS, and TOF-SIMS surface chemical state image analysis of DNA microarrays. Journal of the American Chemical Society. 2007;129(30):9429-38.

30. Peterson AW, Heaton RJ, Georgiadis RM. The effect of surface probe density on DNA hybridization. Nucleic Acids Research. 2001;29(24):5163-8.

31. Levicky R, Horgan A. Physicochemical perspectives on DNA microarray and biosensor technologies. Trends in Biotechnology. 2005;23(3):143-9.

32. Dandy DS, Wu P, Grainger DW. Array feature size influences nucleic acid surface capture in DNA microarrays. Proceedings of the National Academy of Sciences of the United States of America. 2007;104(20):8223-8.

33. Rao AN, Rodesch CK, Grainger DW. Real-Time Fluorescent Image Analysis of DNA Spot Hybridization Kinetics To Assess Microarray Spot Heterogeneity. Analytical Chemistry. 2012;84(21):9379-87. doi: 10.1021/ac302165h.

34. Lee CY, Gong P, Harbers GM, Grainger DW, Castner DG, Gamble LJ. Surface coverage and structure of mixed DNA/Alkylthiol monolayers on gold: Characterization by XPS, NEXAFS, and fluorescence intensity measurements. Analytical Chemistry. 2006;78(10):3316-25.

35. Rao AN, Vandencasteele N, Gamble LJ, Grainger DW. High resolution epifluorescence and TOF-SIMS chemical imaging comparisons of single DNA microarray spots. Analytical Chemistry. 2012:1-8.

36. Gong P, Grainger DW. Comparison of DNA immobilization efficiency on new and regenerated commercial amine-reactive polymer microarray surfaces. Surface Science. 2004;570(1-2):67-77.

37. Grainger D, Greef C, Gong P, Lochhead M. Current Microarray Surface Chemistries. In: Rampal J, editor. Microarrays: Humana Press; 2007. p. 37-57.

38. Fang X, Li B, Petersen E, Seo YS, Samuilov VA, Chen Y, et al. Drying of DNA droplets. Langmuir. 2006;22(14):6308-12.

39. Vainrub A, Pettitt BM. Coulomb blockage of hybridization in two-dimensional DNA arrays. Physical Review E - Statistical, Nonlinear, and Soft Matter Physics. 2002;66(4):041905/1-/4.

40. Dugas V, Broutin J, Souteyrand E. Droplet evaporation study applied to DNA chip manufacturing. Langmuir. 2005;21(20):9130-6.

41. Diehl F, Grahlmann S, Beier M, Hoheisel JD. Manufacturing DNA microarrays of high spot homogeneity and reduced background signal. Nucleic acids research. 2001;29(7).

42. Danov KD, Kralchevska SD, Kralchevsky PA, Ananthapadmanabhan KP, Lips A. Mixed solutions of anionic and zwitterionic surfactant (Betaine): Surface-tension isotherms, adsorption, and relaxation kinetics. Langmuir. 2004;20(13):5445-53.

43. Gorand Y, Pauchard L, Calligari G, Hulin JP, Allain C. Mechanical instability induced by the desiccation of sessile drops. Langmuir. 2004;20(12):5138-40.

44. Sefiane K. Effect of nonionic surfactant on wetting behavior of an evaporating drop under a reduced pressure environment. Journal of Colloid and Interface Science. 2004;272(2):411-9.

45. Truskett VN, Stebe KJ. Influence of surfactants on an evaporating drop: Fluorescence images and particle deposition patterns. Langmuir. 2003;19(20):8271-9.

46. Kaya D, Belyi VA, Muthukumar M. Pattern formation in drying droplets of polyelectrolyte and salt. Journal of Chemical Physics. 2010;133(11).

47. Bhardwaj R, Fang X, Attinger D. Pattern formation during the evaporation of a colloidal nanoliter drop: A numerical and experimental study. New Journal of Physics. 2009;11.

PRINTED SPOT HETEROGENEITY IN PNA MICROARRAYS

Archana N. Rao[1] and David W. Grainger[1,2*]

* *Corresponding author:* David W. Grainger, david.grainger@utah.edu

SUPPORTING INFORMATION

Results and discussion

- Table S-1: Oligonucleotide sequences and terminal modifications used in this study.
- Figure S-1: Schematic chemical model of PNA and DNA molecules showing different backbone linkages compared to DNA and DNA.
- Figure S-2: Schematic layout of microarray prints with varying concentrations of PNA in distinct Cy3-labeled and unlabeled DNA probe mixed ratios in rows of 10 spots each.
- Figure S-3: Contact angle measurement of different print solution on slide H.
- Scheme S-1: Chemical structures of surfactants used in print and wash solutions.

Table S-1. Oligonucleotide sequences and terminal modifications used in this study.

Nucleic acid type	identifier	5'-modification	Sequence	3'-modificiation
DNA probe	Oligo1-NH_2	--	CTGAACGGTAGCATCTTGAC	--
DNA probe	Cy3-Oligo1-NH_2	Cy3-C_6-	CTGAACGGTAGCATCTTGAC	C6-NH_2
DNA target	Oligo2	--	GTCAAGATGCTACCGTTCAG	--
DNA target	Cy5-Oligo2	Cy5-C_6-	GTCAAGATGCTACCGTTCAG	--
DNA target	Oligo2-Cy5		GTCAAGATGCTACCGTTCAG	Cy5-C_6-
PNA probe	Oligo1-NH_2		CTGAACGGTAGCATCTTGAC	Lys-NH_2
PNA probe	Cy3-Oligo1-NH_2	Cy3-OO-	CTGAACGGTAGCATCTTGAC	Lys-NH_2

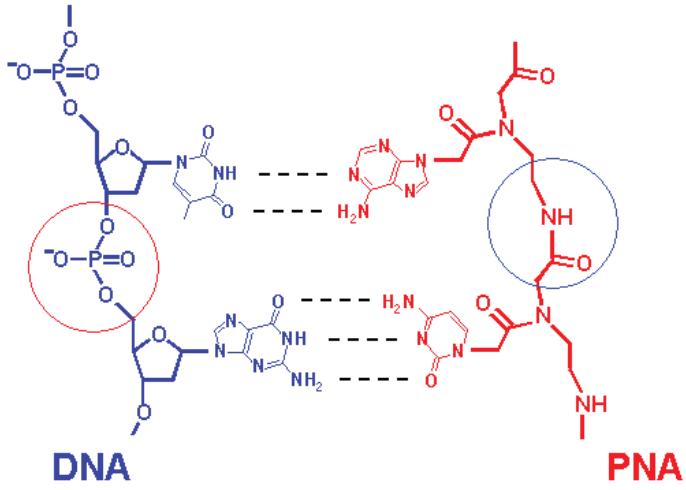

Figure S-1. Schematic chemical model of PNA and DNA molecules showing different backbone linkages compared to DNA and DNA (Reference 26).

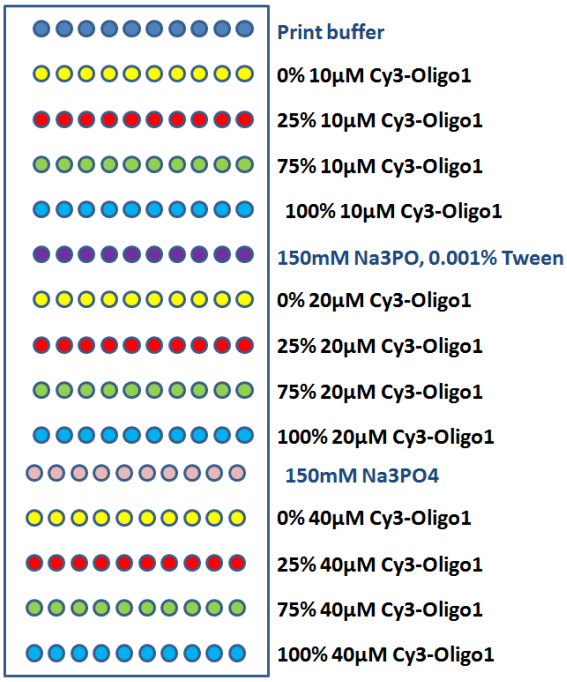

Figure S-2. Schematic layout of microarray prints with varying concentrations of PNA in distinct Cy3-labeled and unlabeled DNA probe mixed ratios in rows of 10 spots each. (Bold indicates spots of print buffers only). The print layout is indicated for the case of sodium phosphate print solution. Similar concentrations were prepared in water and betaine to obtain different arrays.

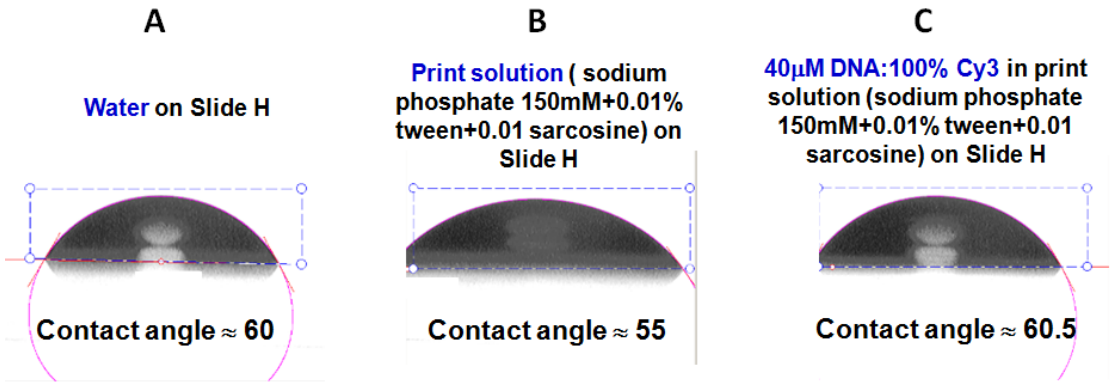

Figure S-3. Contact angle measurement of the DNA print solution on slide H. A) Contact angle of water on slide H. B) Contact angle of print solution on slide H and C) Contact angle of DNA in print solution.

Scheme S-1. Chemical structure of surfactants used in print and wash solutions.

1. **Betaine**

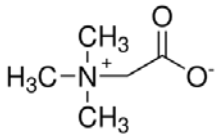

2. **Tween 20**

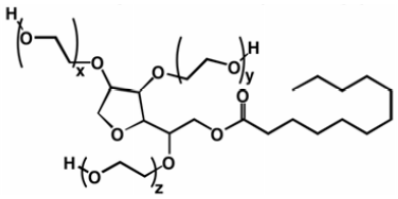

3. **Sarcosine**

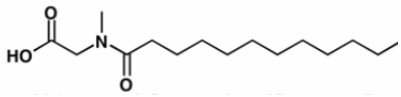

4. **Sodium dodecyl sulfate**

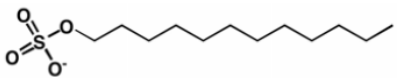

CHAPTER-5

SUMMARY OF RESEARCH AND SUGGESTED FUTURE WORK

This closing chapter presents a summary of the major results in addressing the motivation for the research, and selected technical recommendations for future studies on this topic addressed by chapter.

5.1 Chapter 2 – High-resolution epifluorescence and TOF-SIMS chemical imaging comparisons of single DNA microarray spots

5.1.1 Motivation for this work

Fluorescence signal is most frequently used to quantify fluorescently labeled DNA target capture in microarray assays. However, fluorescence cannot quantify absolute amounts of either probe or target DNA in immobilized spots. Additionally, signal quantitation is affected by numerous, known surface issues that confound reliable quantitative correlations of fluorescent assay signals spot-to-spot and comparisons experiment-to-experiment (1, 2). During imaging, high background noise on the slide substrate and local surface curvature affect fluorescence readings (3). These and other factors influence fluorescence intensity and therefore the significance of the signal recorded and it relationship to analyte abundance (4). Printed DNA microspot heterogeneity has been studied here using detailed chemical spatial and fluorescent imaging of dye-labeled probe and target distribution in spots deposited on well-characterized amine-reactive commercial microarray slides. Optically profiled single-spot heterogeneity obtained with epifluorescence techniques was complemented with time-of-flight secondary ion mass spectrometry (TOF-SIMS) chemical state imaging of the same spot. Principal component analysis (PCA) applied to TOF-SIMS imaging datasets demonstrated that the epifluorescence imaging technique provides information not readily observable in TOF-SIMS images alone,

particularly in identifying species associated with array spot nonuniformities. This provides new information regarding the nature of printed, dried array spot heterogeneity observed as fluorescent signal nonuniformities in printed spots and in signal variations after target capture.

5.1.2 Summary of research

Accurate metrics for captured DNA target signal rely upon uniform spot distribution of both probe and target DNA to yield reliable hybridized signal that reflects sample abundance. While often presumed, this is neither easily achieved nor often proven experimentally. High-resolution imaging techniques were used to determine spot heterogeneity in identical DNA array microspots comprising varied ratios of unlabeled and dye-labeled DNA probes contact-printed onto commercial arraying surfaces. Epifluorescence imaging data for individual array microspots were correlated with TOF-SIMS chemical state imaging of the same spots. Epifluorescence imaging intensity contours distinguished widely varying DNA densities distributed both within a given spot and from spot-to-spot. TOF-SIMS chemical analysis confirmed these heterogeneous printed DNA distributions by tracking bound Cy3 dye, DNA base, and phosphate-specific ion fragments often correlating to fluorescence patterns within identical spots. TOF-SIMS ion fragments originating from probe DNA and Cy3 dye are enriched in microspot centers, correlating to high fluorescence intensity regions. Both TOF-SIMS and epifluorescence analysis support Marangoni flow effects on spot drying, with high-density DNA-Cy3 located in spot centers and nonhomogeneous DNA distribution radially within printed spots. Microspot image dimensional analysis results for DNA droplet spreading show differing DNA densities across printed spots. Routine conventional fluorescence scanner images provide information for integrated spot pixel intensity, shape and morphology, but lack all details for intraspot DNA heterogeneity and intra-spot structural issues known to affect target capture and duplex hybridization kinetics critical to this assay's answer development and diagnostic reliability. This study directly supports different DNA probe chemical and spatial microenvironments within spots that yield spot-spot signal variations known to affect DNA target hybridization efficiencies and kinetics. These variations critically affect probe-target duplex formation and DNA array signal generation.

5.1.3 Critical assessments and suggested future work

Though TOF-SIMS and epifluorescence analysis provide ample proof of printed DNA spot intra- and interspot heterogeneity, the ability to overcome printed spot heterogeneity remains a challenge. Printed spot heterogeneity is a consequence of the fabrication technique, involving dispensing of nanoliter droplets onto surface that then evaporate quickly in a few seconds in non-equilibrium conditions, leaving behind a nonhomogenous dried spot. Many efforts to increase spot uniformity have been attempted: by increasing the viscosity of printed DNA solution, increasing printing humidity to reduce the rate of evaporation, and using anionic and nonionic surfactants to manipulate the spot wetting/drying process. However, this problem has not been resolved to date.

5.1.3.1 Altering fabrication techniques

A variety of techniques are available to immobilize DNA in patterns on surfaces for arraying. Contact printing, noncontact printing and immersing prepatterned gold substrates in DNA solution is a few such techniques. However, both contact and noncontact printing yield non-uniform droplets from coffee ring or Marangoni effects during droplet drying (3). The immobilization step is the most important aspect of fabrication of microarrays.

5.1.3.2 Improving immobilization of ssDNA to yield uniform DNA patterns

Immobilization of DNA probes on gold can lead to nonuniform distribution (5), random orientation, and islands of DNA probes which further influences the hybridization kinetics and isotherms. Steel et al. studies indicate that surface coverage decreases with increase in probe length (>24 bases) leading to less ordered arraignment of chains due to their density driven confirmations (5). Diluents are used to avoid DNA probe overcrowding and to orient probes to better bind target DNA to form duplex strands (6). Diluents such as alkylthiol, MCU, and OEG can be used to space the DNA probes for preferred orientation and spacing to enable increased hybridization efficiency which is critical to determine the analyte concentration and the assay end point result (7).

5.1.3.3 Label-free detection of ssDNA bound to surfaces and its hybridization

Fluorescence data in Chapter 2 show a nonlinear relationship of RFU intensity vs. printed DNA probe concentration. Fluorescent dye label quenching can occur due to various factors such as DNA-dye, dye-dye, and dye-surface interactions. The fluorescent signal output does not correlate to the abundance of the analyte. Label-free SPR techniques of measuring change in the refractive index of the medium directly in contact with sensor surface is well known for DNA detection in many formats (8, 9). However, the limitation with the SPR technique is the substrate should be gold and not a glass slide (10). Label-free assessment of DNA immobilization and hybridization requires use of complementary analytical tools such as XPS and TOF-SIMS to recognize array chemical signatures to assess the DNA probe distribution and densities, and target binding. Other label free techniques include electrochemical sensing based on the principles of oxidation/reduction reaction such as DNA hybridization sensors (Clinical Microsensors/ Motorola and Xanthon sensor) (11).

5.1.3.4 Controlling evaporation of DNA microdroplets during immobilization through electrowetting (EW)

Inkjet printing, spotting of biofluids, and coating technology all result in highly inhomogeneous deposition of DNA. The long-recognized “coffee stain” drying phenomenon produces a ring-like deposit driven by the combined actions of three-phase droplet contact line pinning and evaporation rate enhancement near this three-phase contact line. The Marangoni effect or convection-associated surface tension of the droplet, caused by concentration variation due to solvent evaporation, opposes coffee stain effects. Data in Chapter 2 show that DNA printed probe spots produce a Marangoni flow pattern with more DNA probe density at the spot center. However, this is correlated with reduced probe density in the periphery of the spot. These patterns result from various parameters such as concentration, size of the particles, viscosity of the print solution, temperature, humidity, type of surface (hydrophobic *vs.* hydrophilic), wetting and contact angle, and contact angle hysteresis of the substrate. It is possible to excite the drop

with alternating current (AC) in a broad frequency range (a few Hz to several kHz), preventing droplet contact line pinning during drying (12).

This results in a spots radius, somewhat larger than the radius in the absence of an applied voltage (13, 14). This phenomenon of EW (electrowetting) applied during droplet evaporation reduces the macroscopically measurable contact angle hysteresis, allowing mobilization of pinned contact lines while also preventing DNA from adsorbing to the substrate, thereby forming a uniform droplet (15) (16). Contradicting evidence of obtaining uniform and non-uniform spot are known due to variation in currents, solvent, and concentration used during manipulation of the spots. It was also observed that EW-controlled spots showed improved matrix-assisted laser desorption ionization mass spectroscopy signal indicating efficient droplet manipulation and characterization detection (15). However, it has been observed that for smaller particle sizes (<20nm), it is not possible to obtain uniform spots even at high applied voltages (300V). For larger particles, the adhesive force increases more weakly with increasing particle concentrations than the hydrodynamic force (17), indicating that for short DNA up to 40mers in length, it would be impossible to obtain uniform spots. However, >40mer DNA can be used. Figure 5.1 is the schematic of the design of EW incorporated into the DNA printing technique.

In future work, an electric circuit will be patterned on a glass slide to pass AC current underneath spin coated silica glass slide of an amine reactive surface. Platinum temperature sensors and heaters will be fabricated on the glass to manipulate the temperature (lower temperature) as the water droplet evaporates. In EW methodology described above, we will manipulate the droplet drying phenomena to obtain a uniformly distributed DNA probe density. Also, the NHS reactive slide will be coated in such a way that the coating diameter would be around 100 microns with a spacing of 200 microns (center-center distance) between adjacent spots to ensure that droplets are placed far apart from each other and can be bound only to NHS reactive sites within 100 microns. Unbound DNA will be washed off during the washing cycle. However, we also realize that electrowetting requires patterned electrode structure and corresponding complex interfacing to drive electronics (18). Also, the patterned electrodes restrict the droplet size. This problem of patterned electrodes can be overcome by the use of

opto-electrowetting in which a scanning laser beam of 405nm laser with a programmable mirror can be used to transport the droplet across the device to obtain uniform droplet drying (19).

These protocols can be used for immobilization of DNA probe on various surfaces such as glass, silicon, gold (with a photoconductive coating), and many more. This methodology will improve the probe distribution and improve hybridization with target analyte, while fluorescence labels can still be used for signal detection and can be more accurate due to uniform spot patterning.

5.2 Chapter 3 - Real-time fluorescent image analysis of DNA spot hybridization kinetics to assess microarray spot heterogeneity

5.2.1 Motivation for the work

Assessment of printed DNA spot heterogeneity inspires further studies of target binding kinetics, target flux diffusion in a highly crowded printed probe, influence of the position of dye-label on the probe/target in hybridization, and finally the fluorescence signal output. The hypothesis is that spot heterogeneity predominately occurs during immobilization and drying, and that heterogeneity is further increased during hybridization with the target analyte. Fluorescent dye-labeled target is routinely used in current microarray technology as a detectable signal end-point. Real-time *in situ* analysis of dye-labeled target hybridization in solution *vs.* in surface-capture assays can be used to elucidate the differences of hybridization kinetics and isotherms in bulk solution and on solid surfaces to improve microarray solid assays (tethered to surfaces).

Laser confocal microscopy is an excellent tool to study both the real-time hybridization and variation of signal intensity of Cy3-probe/Cy5-target during hybridization and photobleaching studies. Real-time *in situ* hybridization presents vital information of probing the mode of transport of target in printed spots with nonuniform probe density distribution across the spot. Photobleaching of dye-labeled DNA is an important aspect to understand, as the dye-labeled assays are often photobleached with high intensity laser during scanning. The position of the dye-labels on the oligomers affects the resulting signal based on the length of oligomers (probe/target), orientation of the fluorophore, and the position of the dye-label on the probe/target. The influence of dye-label positioning either parallel (close proximity) *vs.* antiparallel (dyes far

apart) in the duplex was studied to evaluate the dye distances affecting fluorescent signal output. Fluorescence resonance energy transfer (FRET) analysis of fluorophore (Cy3/Cy5) provides important information on the distance between the Cy3-probe and Cy5-target. FRET of Cy3/Cy5 fluorescent intensities were analyzed both in the printed hybridized DNA spot and in solution to investigate the proximity of dye-labeled probe-target in solid assays compared to that in solution. FRET provides significant evidence of overcrowding to the printed probe and the target binding to the nonuniform and disoriented probes. Data in Chapter 3 leverage the fluorescence information in capable of assessing printed spot hybridization and kinetics with real-time with confocal imaging technique.

5.2.2 Summary of research

Real-time *in-situ* surface hybridization capture kinetics of single printed DNA microspots on solid array surfaces using fluorescence provides important information regarding the molecular environment of immobilized probe spots, hybridization process of target binding to substrate-bound probe, and aspects of incubation time periods for duplex-forming assays. Confocal single-spot imaging shows that real-time *in-situ* hybridization kinetics with constant target concentration change for different printed probe densities. Target-specific imaging in single spots exhibits heterogeneous printed probe radial density that influences target hybridization via radial hemispherical diffusion of dye-labeled target from the spot's outside edge to its interior. Influence of DNA target and probe cyanine dye positions on oligo-DNA duplex formation behavior in solution vs. surface-hybridized single DNA spots using FRET analysis provides information of duplex formation and overcrowding of probes in the spot hybridized with the target. FRET of surface-captured target occurs irrespective of fluorophore position, resulting from excess printed probe density and spot thickness. Both heterogeneous probe density distributions in printed thick spots and fluorophore position on short DNA oligomers influence duplex formation kinetics, hybridization efficiencies, and overall fluorescence intensity end-point detection in surface-capture formats. This analysis is important for the understanding and quantification of an array's assay signal essential for surface-capture format.

5.2.3 Critical assessment and suggested future work

5.2.3.1 Influence of probe distribution to enhance hybridization efficiency

The methodology used here would be similar to that discussed in section 5.1.3. However, additional functionality will be integrated in the microchip of a silicon substrate and fabricated on the glass slide. A modified GMR (giant magnetoresistive sensor) composed of $Cu/Ni_{80}/Fe_{20}$ antiferromagnet will be micropatterned onto the glass slide (20). The magnetoresitive biosensor is patterned into spiral shaped line that covers the area of the DNA spot (100μm) and adjacent DNA spots are far apart (~200μm). Since NHS slide for probe immobilization will be used, no additional chemical modification for binding of DNA probes to the slide will be required. A schematic of the biosensor chip which incorporates electrical and the GMR techniques is shown in Figure 5.2.

5.2.3.2 Working principle of the sensor

The sensors include immobilization of the DNA probe with Fe_2O_3 'superparamagnetic' tags that are interactive with magnetic field but retain no residual magnetism after the field is removed (21). During the immobilization, the AC signal is ON and the magnetic pulse is generated to ensure the spreading of the droplet and its uniform drying. DNA tagged with iron oxide move specifically in the grids (22). This will ensure uniform distribution of the probes in a particular pattern, which will allow efficient target hybridization without crowding. Due to the binding of the negatively charged DNA, a change in the electrical signal output read out will ensure binding and the amount of bound DNA to the amplitude signal reduction bound state. The presence of both electric and magnetic sensing will help modulate orientation, spatial distribution, uniformity of probe distribution, and probe density of DNA. After probe immobilization, the target analyte containing MNT (magnetic nanotag)-labeled DNA are used for specific binding with the iron oxide-labeled probes in the absence of the magnetic field. This will ensure perfect duplex formation due to magnetic attraction between the labeled probe and target, and additionally due to uniformly patterned probe that has overcome the crowding issues. Each MNT bound target will produce a magnetic signal based on the magnetic moment that will give an appropriate amount of binding similar to a radioactive counter. The detection platform generates an offset signal that is proportional to the sensitivity of the GMR sensor and is independent of the magnetic particles.

Therefore, the signal change due to particles is determined relative to the offset signal of the GMR prior to binding (23).

5.2.3.3 Advantages of the DNA microarray based on AC pulse and GMR sensing

This technique improves selectivity and sensitivity of the DNA microarray sensor (24). Bound DNA alters the sensor resistance and generated electrical signals are directly measured with the integrated circuitry. The GMR biochip measures electrical signal directly from the sensor and makes a low-cost, highly portable device. The sensor can easily distinguish complementary and noncomplementary binding based on the magnetic moment and current which will be beneficial in complex milieu of biological samples wherein very low concentrations down to pg/μl can be detected due to improved selectivity and sensitivity. GMR-based biosensors have shown improved detection compared to fluorescent techniques due to improved specificity of binding and sensitivity in measuring signal of bound DNA. With magnetic markers, background noise is reduced drastically compared to fluorescent markers and additionally, the fluorescent markers are less stable during repeated measurements (20). Actuation of the GMR will increase the speed of the assay by reducing the diffusion limitation. Manipulation of the magnetic labels by the AC field will reduce the time of the assay to minutes (25). Thus, the advantage of using electrical and magnetic sensing improves the kinetics of the tag-capture detection of nucleic acid. Smaller superparamagnetic nanotags (50nm) give lower steric hindrance, and exhibit low nonspecific forces compared to larger tags. The sensitivity of smaller magnetic particles can also be manipulated by increasing the magnetic moment during detection (22). This detection will be accurate and can be compared to the efficiency of radiolabeled nucleic acid microarrays. However, careful consideration during fabrication of GMR to regulate the magnetic moment and the spin of the bound probe target should be considered for the accuracy in signal measurement (26). This technique can be extended to proteins, saccharides, and many more binding assays. It can also be extended to multiple analyte systems and complex biological milieu as the sensitivity in measurements is up to pg/ml range.

5.3 Chapter 4 - Epifluorescence imaging of printed spot heterogeneity and morphology of PNA microarray with different buffer systems

5.3.1 Motivation to the work

Chapter 4 of this dissertation described two approaches to overcome printed spot heterogeneity. DNA spot heterogeneity observed in both the optical and chemical high resolution techniques motivated us to overcome the long standing problem of probe immobilization -- printed spot heterogeneity. We adapted two approaches: changing the probe to PNA and the use of additives and surfactants to manipulate droplet wetting, spreading, and drying, anticipating an improvement in spot uniformity. Printing PNA probe instead of DNA probes addresses the local polyanion electrostatic fields or charge densities and the impact on subsequent DNA target capture produced by Coulombic blockade. In addition, the use of combinations of surfactant and buffer systems improves printed spot heterogeneity during droplet drying processes. Fast evaporation of the droplet (i.e., of nanoliter droplet drying within few seconds of being dispensed) dominates the time-scale required for chemical grafting of probes and the effect of surfactant chemistry influencing spot drying pattern in producing uniform spots.

5.3.2 Summary of research

Fluorescently labeled PNA was printed with sodium phosphate buffer containing tween and sarcosine using protocols similar to the DNA printing protocol in Chapter 2. Additionally, PNA probes were printed in betaine and compared with printed spots without any surfactant in water only. The spots were analyzed with fluorescence and epifluorescence imaging techniques. The spots were compared for morphology, spot-spot heterogeneity, spot shape, and diameter and fluorescence intensity. PNA probe printed in water alone (pH 7) produced spots which were non-spherical and heterogeneous. The spot size and RFU intensity increased with increase in concentration of DNA and dye label. However, PNA spots of 20μM and 10μM visible in fluorescence scanner were not visible with epifluorescence imaging. Both unhybridized and hybridized spots show same spot morphology. Fluorescence scanner images of PNA printed spots in betaine (pH 7) show circular spots with little or no variation in spot diameter with change

in amount of dye labeling but showed an increase in spot diameter with increase in DNA concentration. Epifluorescence images of unhybridized spots show sporadic distribution of PNA and the hybridized spots show coffee ring pattern of hybridized spots. The PNA probe printed in sodium phosphate (pH 8.5, containing 0.001% Tween and 0.001% sarcosine) are analogous to DNA printed spot in morphology and diameter for the same concentration probe and dye labeling. Both the probes show Marangoni pattern of drying with high intensity at spot center compared to the periphery as shown in profile plots with Image J. Thus, Chapter 5 of this dissertation emphasizes that altering the probe, surfactants, and buffer does not improve printed spot uniformity and thereby concludes the role of evaporation process of the droplet of spreading and drying has a dominant influence on printed spot morphology. Also, fluorescence scanner can only provide printed spot shape and cannot provide the details of probe distribution throughout the spot.

5.3.3 Critical assessment and suggested future work

5.3.3.1 PEG-linkers to bind PNA to polymer-coated slides

PNA with PEG linkers would address two spot issues: (1) increase the solubility of PNA for an enhanced distribution of PNA across the printed spot (2) to distance the hybridization portion of the PNA molecule from the surface for presentation to the incoming target DNA. Flexible spacer chains are utilized to enhance hybridization of terminally anchored oligonucleotide probes in DNA microarrays (27). It is known that the number of accessible chain configurations is reduced when a polymer is terminally anchored to an impenetrable surface such as a glass slide. Spacers mitigate this issue. Three advantages are apparent for using flexible spacers: 1) improvement in the hybridization efficiency, depending on various factors of hybridizing over short or long targets and probe densities (lower probe density leads to easier access of target to impenetrable surface); 2) additional possibility of labeling free ends allowing for determination of spatial distribution; and 3) formation of polymer brush regimes of probe with flexible spacers. These factors can contribute to improving spot uniformity and enhancing hybridization efficiency.

5.3.3.2 Summary of printing technology and alternative approach to DNA microarray printing technique

In conclusion, the printing technique has been known to yield nonuniform distribution of DNA probe in the spot, leading to either coffee rings or Marangoni drying patterns. Various efforts by researchers and industries to improve the printed spot morphology, including modification of surfaces, use of surfactants, buffers and additives (PEG, sucrose, etc.) in print solution, variations in temperature and humidity, and the application of electric current to move the DNA probes, have shown little or no improvement. Alternative methods of DNA sequencing techniques discussed in Chapter 1, such as “grafting to” and “grafting from”, provide site controlled immobilization of probes on the surface.

In “grafting to” technique, the DNA probe is bound to the surface by electrostatic interactions of the negatively charged DNA backbone to cationic substrate surfaces, or by combinations of polar and hydrophobic interactions (i.e., to nitrocellulose, silicon oxide, or polypropylene). In “grafting from” approach, fluidics, photolithography, and photochemistry are combined with automated microprocessing to sequentially add and spatially direct each individual DNA nucleotide to growing ssDNA probe chain ends across a patterned surface. The “grafting to” approach can be an appropriate methodology to spatially distribute DNA capture probes on the surface to improve order, reduce electrostatics and sterics due to overcrowding with the neighboring probes, and finally to increase the target hybridization efficiency. Various technologies to fabricate high-density arrays are well known such as Affymetrix, NimbleGen, and SMRT technology (Pacific Biosciences) of sequencing DNA. Incorporation of photolithography, maskless, and wave guide cell technology has known to improve the spatial distribution of the DNA probe resulting in improved sensitivity of the assay.

Microarrays must exhibit very high sensitivity for detecting extremely low concentrations of DNA bound to the surface to be possible to detect poorly expressed genes. The immobilization of primers with polymerase enzyme at appropriate locations at optimal density for efficient binding to reduce autofluorescence and minimize nonspecific binding of biomolecules to surfaces is important to obtain high-quality array fabrication. This technique is a suitable technology in DNA

microarray fabrication to overcome problems with heterogeneity in probe density distribution and low hybridization efficiency caused by printing. We have studied that spot drying features influence probe immobilization and density distribution which can be resolved with spatial placement of DNA probes on the surface. These techniques will enable high density DNA microarray with higher hybridization efficiency due to control over the placement of DNA probes. They will also overcome the problems with fluorescence quenching due to dye-dye interaction and dye surface interactions. The orderly arrangement will also overcome the mushroom or brush configurations of the DNA probes affecting the kinetics and thermodynamics hybridization with the target DNA.

Thus, an alternative approach rather than improvisation of the microarray printing technique should be adopted to improve probe spatial distribution and hybridization to enhance the quality of DNA microarray end point analysis.

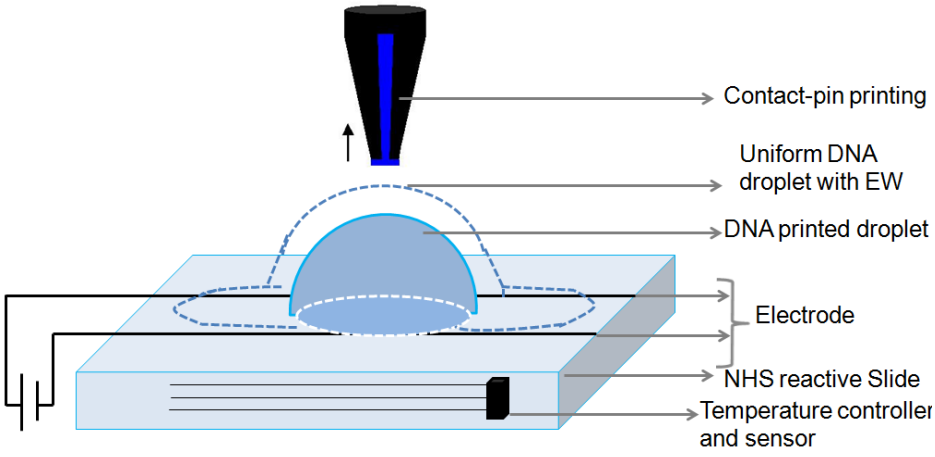

Figure 5.1. Manipulating the DNA droplet evaporation with EW to obtain DNA dried spot with uniform distribution of DNA probe density

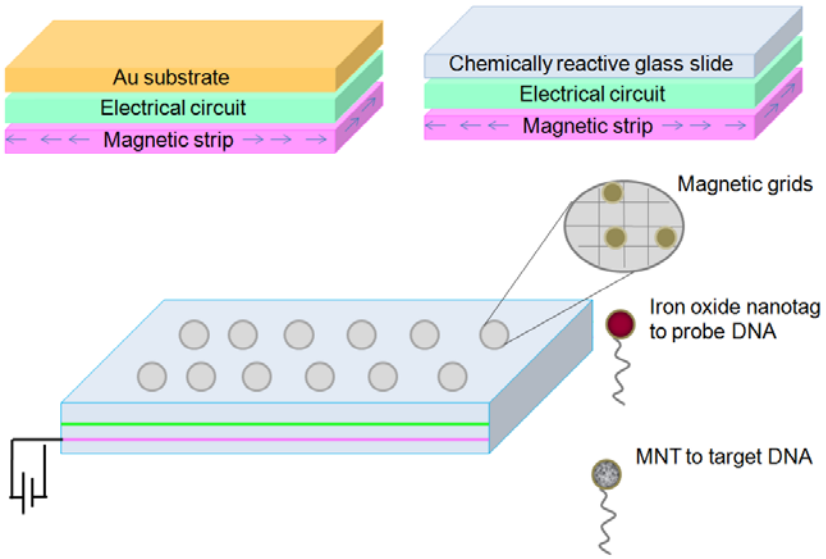

Figure 5. 2. Schematics of AC field current and GMR sensor-based microchip for immobilizationd and hybridization of the DNA-based sensors.

5. 5 References

1. Dudley AM, Aach J, Steffen MA, Church GM. Measuring absolute expression with microarrays with a calibrated reference sample and an extended signal intensity range. Proceedings of the National Academy of Sciences of the United States of America. 2002;99(11):7554-9.

2. Wu P, Castner DG, Grainger DW. Diagnostic devices as biomaterials: A review of nucleic acid and protein microarray surface performance issues. Journal of Biomaterials Science, Polymer Edition. 2008;19(6):725-53.

3. Dufva M. Fabrication of high quality microarrays. Biomolecular Engineering. 2005;22(5-6):173-84.

4. Draghici S, Khatri P, Eklund AC, Szallasi Z. Reliability and reproducibility issues in DNA microarray measurements. Trends in Genetics. 2006;22(2):101-9.

5. Steel AB, Levicky RL, Herne TM, Tarlov MJ. Immobilization of nucleic acids at solid surfaces: Effect of oligonucleotide length on layer assembly. Biophysical Journal. 2000;79(2):975-81.

6. Gong P, Lee CY, Gamble LJ, Castner DG, Grainger DW. Hybridization behavior of mixed DNA/alkylthiol monolayers on gold: Characterization by surface plasmon resonance and 32P radiometric assay. Analytical Chemistry. 2006;78(10):3326-34.

7. Lee CY, Gong P, Harbers GM, Grainger DW, Castner DG, Gamble LJ. Surface coverage and structure of mixed DNA/Alkylthiol monolayers on gold: Characterization by XPS, NEXAFS, and fluorescence intensity measurements. Analytical Chemistry. 2006;78(10):3316-25.

8. Kim SK, Cho H, Jeong J, Kwon JN, Jung Y, Chung BH. Label-free and naked eye detection of PNA/DNA hybridization using enhancement of gold nanoparticles. Chemical Communications. 2010;46(19):3315-7.

9. Scarano S, Mascini M, Turner APF, Minunni M. Surface plasmon resonance imaging for affinity-based biosensors. Biosensors and Bioelectronics. 2010;25(5):957-66.

10. Lee HJ, Goodrich TT, Corn RM. SPR imaging measurements of 1-D and 2-D DNA microarrays created from microfluidic channels on gold thin films. Analytical Chemistry. 2001;73(22):5525-31.

11. Paleček E. Past, present and future of nucleic acids electrochemistry. Talanta. 2002;56(5):809-19.

12. Mampallil D, Eral HB, Van Den Ende D, Mugele F. Control of evaporating complex fluids through electrowetting. Soft Matter. 2012;8(41):10614-7.

13. De Ruiter R, Wennink P, Banpurkar AG, Duits MHG, Mugele F. Use of electrowetting to measure dynamic interfacial tensions of a microdrop. Lab on a Chip - Miniaturisation for Chemistry and Biology. 2012;12(16):2832-6.

14. Cho SK, Moon H, Kim CJ. Creating, transporting, cutting, and merging liquid droplets by electrowetting-based actuation for digital microfluidic circuits. Journal of Microelectromechanical Systems. 2003;12(1):70-80.

15. Mugele F, Duits M, Van Den Ende D. Electrowetting: A versatile tool for drop manipulation, generation, and characterization. Advances in Colloid and Interface Science. 2010;161(1-2):115-23.

16. Pollack MG, Shenderov AD, Fair RB. Electrowetting-based actuation of droplets for integrated microfluidics. Lab on a Chip - Miniaturisation for Chemistry and Biology. 2002;2(2):96-101.

17. D. Mampallil HBE, D. Van de Ende and F. Mugele. Control of evaporating complex fluids through electrowetting. Soft Matter; Royal Society of Chemistry 2012. doi: 10.1039/c2sm26103k.

18. Yi UC, Kim CJ. Soft printing of droplets pre-metered by electrowetting. Sensors and Actuators, A: Physical. 2004;114(2-3):347-54.

19. Park SY, Teitell MA, Chiou EPY. Single-sided continuous optoelectrowetting (SCOEW) for droplet manipulation with light patterns. Lab on a Chip - Miniaturisation for Chemistry and Biology. 2010;10(13):1655-61.

20. Schotter J, Kamp PB, Becker A, Pühler A, Reiss G, Brückl H. Comparison of a prototype magnetoresistive biosensor to standard fluorescent DNA detection. Biosensors and Bioelectronics. 2004;19(10):1149-56.

21. Brzeska M, Panhorst M, Kamp PB, Schotter J, Reiss G, Pühler A, et al. Detection and manipulation of biomolecules by magnetic carriers. Journal of Biotechnology. 2004;112(1-2):25-33.

22. Han SJ, Xu L, Yu H, Wilson RJ, White RL, Pourmand N, et al., editors. CMOS integrated DNA microarray based on GMR sensors. 2006.

23. Koets M, van der Wijk T, van Eemeren JTWM, van Amerongen A, Prins MWJ. Rapid DNA multi-analyte immunoassay on a magneto-resistance biosensor. Biosensors and Bioelectronics. 2009;24(7):1893-8.

24. Ramli Ramli FH, Khairurrijal Khairurrijal and Mitra Djamal. GMR Biosensors for ClinicalDiagnostics, . 2011;Environment and Biosecurity(Biosensors for Health).

25. Megens M, Prins M. Magnetic biochips: A new option for sensitive diagnostics. Journal of Magnetism and Magnetic Materials. 2005;293(1):702-8.

26. Li G, Sun S, Wilson RJ, White RL, Pourmand N, Wang SX. Spin valve sensors for ultrasensitive detection of superparamagnetic nanoparticles for biological applications. Sensors and Actuators, A: Physical. 2006;126(1):98-106.

27. Halperin A, Buhot A, Zhulina EB. Hybridization at a surface: The role of spacers in DNA microarrays. Langmuir. 2006;22(26):11290-304.

APPENDIX

AFM ANALYSIS TO ASSESS PRINTED NUCLEIC ACID MICROARRAY FEATURES PRINTED ON POLYMER SUBSTRATES

Archana N. Rao[1] Colin D. Eichinger[2], Vladimir Hlady[2], and David W. Grainger[1,2*]

[1]Department of Pharmaceutics and Pharmaceutical Chemistry, University of Utah, Salt Lake City, UT 84112-5820 USA

[2]Department of Bioengineering, University of Utah, Salt Lake City, UT 84112-5820 USA

**to whom correspondence should be addressed:* David W. Grainger, david.grainger@utah.edu

Keywords: printed microspots, heterogeneity, nucleic acid arrays, atomic force microscopy

---

Submitted to RSC Soft Matter, ACS, March 2013

A.1 Abstract

DNA microarray technology has been plagued with analytical metric issues, false positives, and nonacceptance in clinical and diagnostic settings. DNA hybridization and the resulting consistent measurable signal is the basis of DNA microarray success. Variable signal from DNA array spots processed under similar conditions can be primarily attributed to spot heterogeneity resulting from array fabrication that leads to inaccurate and inconsistent signal generation upon hybridization. We have recently compared printed, fluorescently labeled DNA spot-heterogeneity and nonuniform probe density using optical techniques (epifluorescence and confocal microscopy), and chemical imaging (TOF-SIMS) where optical and chemical evidence of lateral heterogeneity and distribution of DNA probe was reported. The current study shows similar heterogeneity in spot morphologies for printed DNA microarray spots with contact printing using atomic force microscopy (AFM). Contact mode AFM provides dried spot morphologies for both unhybridized printed DNA probe, PNA (peptide nucleic acid), as well as for hybridized individual dried spots on commercial arraying slides. Printed microspot morphologies are comparable for different printed spot dimensions of DNA/PNA probes and unhybridized/hybridized microspots. AFM lateral force images show heterogeneity in the printed spot morphology and Marangoni drying phenomena. Printing technique, commonly used in diverse nucleic acid microarray fabrication strategies, is a major source of heterogeneity in deposited microspots. Printed spot heterogeneity affects hybridization rates and efficiencies of incoming target, resulting in variable array signal generation and answer variability for these formats.

A.2 Introduction

DNA microarrays represent a rapidly growing research and biomedical diagnostic tool (1, 2). However, a significant challenge for this assay format remains in satisfying rigorous requirements of array reliability and answer correlation to sample abundance to enable its translation from a laboratory bench assay to a clinical beside utility (3, 4). Nucleic acid array limitations include analyte specificity, sensitivity from complex samples, and quantitative metrics (5, 6). Large data sets generated by single chips have statistical and bioinformatics-related challenges and complexities (7, 8). Lack of standard protocols for microarray data analysis result in

repeatability and reproducibility issues among different platforms (9, 10). Array fabrication and processing shortcomings limit accurate measurement of absolute gene expression levels and reliable detection of low abundance genes, as well as direct sample-to-answer capabilities. Variable array answers (commonly fluorescence signal generation) reflect improper microarray design in choice of probes, probe lengths, print methods, and printed densities (11). Microarray performance requires that DNA probes be immobilized on a substrate while retaining their activity, orientation, accessibility to the target in solution, and low nonspecific adsorption to the substrate or other nonanalytes (12). These factors are governed by physico-chemical properties of DNA at interfaces (13, 14).

Thermodynamic and kinetic aspects of DNA surface hybridization depend on the electrostatic and steric environments of immobilized DNA probes at high grafting densities on a surface (15). DNA surface density affects immobilized DNA conformation and morphology (16). At low immobilized densities, isolated chains assume largely unperturbed mushroom conformations (17) or interact directly with the substrate (18). With increasing immobilized density, interchain spacing decreases, leading to electrostatic repulsion and resulting in a strongly stretched DNA brush layer extended away from the surface with reduced DNA-surface interactions (18). In the brush regime, hybridization is strongly suppressed due to DNA polyphosphate electrostatic repulsion and steric hindrance, overcome practically by using printing diluents or reduced density (18, 19). A consequence of high probe density is slower hybridization kinetics not reaching completion in practical timelines with a low concentration of the target analyte. On the contrary, lower surface probe densities lead to relatively fast kinetics but with absolute target number densities limited by the surface probe density (20). Knowledge and control of microspot DNA probe density and physical state is fundamentally important to interpreting changes in assay signal from label-free or labeled microarray assays, and to design highly efficient, reproducible assay formats.

Several fundamental methods commonly used to fabricate microarrays are DNA probe contact and noncontact printing, electrostatic nucleic acid adsorption, DNA-thiol adsorption to patterned coinage metals islands, and in situ nucleic acid synthesis (21). Microspotting techniques such as pin-based fluid transfer systems and the piezo-based inkjet dispenser systems produce

high-density, heterogeneous microspots on surfaces, leading to intra- and interspot variations in spot properties during immobilization and hybridization (11). Additionally, amine-terminated organosilane coatings provide cationic surfaces (similar to poly(L-lysine)-adsorbed surfaces) for electrostatically binding anionic DNA probes during microarray printing, the basis for several popular commercial silane-based glass microarray substrates (6). However, this leads to electrostatically bound DNA probes lying flat on the surface, limiting capabilities. Chemisorbed thiol-ssDNA frequently immobilizes DNA to gold, silver, and copper surfaces, yielding monolayers of DNA (22). However, immobilized ssDNA orientation can be profoundly influenced by backfilling the probe layer with small diluent organothiols to increase target hybridization efficiency (18)(23). Other preparation methods include photolithographic in situ high density nucleic acid probe synthesis (commercialized by Affymetrix), as well as multiplexed mirror-based photochemical addressing of microarray probe sites (developed by Nimblegen) (24).

Of these array fabrication methods, all but droplet spotting methods are expected to yield immobilized monolayers of nucleic acids on supports. Nonetheless, in situ probe synthesis is not 100% accurate, and precludes ready validation of the fidelity of the final probe synthesis on the surface (25). These microarrays therefore contain significant nucleotide chain defects distinct from the desired sequence (26). Printed microarrays use presynthesized oligonucleotides purified by capillary electrophoresis or high-performance liquid chromatography (HPLC) prior to array deposition of nearly homogeneous probe samples, increasing assay specificity. Notably, both inkjet contact and noncontact piezo-droplet deposition leads to DNA droplet-substrate wetting, spreading, and then drying anomalies in micron-sized spots, yielding nonuniform spot shapes and DNA radial distributions in spots (27, 28). Excess probe materials deposited with rapid drying results in aggregation of DNA probes with increasing ionic strength and resists rinsing upon drying (28, 29). Subsequent blocking and rinsing steps fail to remove excess aggregated material, leaving behind a faint residue from the spots (30).

DNA printed microspots from either contact or noncontact printing demonstrate classic coffee ring deposits (31) or Marangoni drying patterns (32), resulting in heterogeneous distribution of DNA residue across the dried spots. Hybridization with the target leads to a further heterogeneity

from radial hemispherical diffusion-limited transport (33, 34). It is important to note that target DNA can only hybridize with a probe exposed at spot surfaces and not those buried inside the dried spot residues. A previous report showed limited evidence for DNA oligomer penetration into dried probe microspots during hybridization from real-time imaging and 3D z-slice analysis with confocal microscopy, even with prolonged hybridization times (34). Ideally, printed DNA probes under assay should be uniformly accessible to the target, i.e, oriented upright away from the surface, with the height of the DNA film equal to probe length and with lateral density sufficient to minimize steric hindrance and electrostatic blockade of target in duplex formation. However, DNA probe specific and nonspecific surface binding due to both physisorption from rapid droplet evaporation and nucleotide base amine covalent attachment to NHS surface chemistry leads to heterogeneous printed spots (30). Hence, printed arrays also have several features confounding reliable signal/hybridization from inconsistent immobilization and inaccessible DNA buried within printed spots (34, 35).

The state of DNA probes immobilized on surfaces is critical to target capture, and also to assay sensitivity and reliability. It has been observed that random orientation and overcrowding of printed heterogeneous DNA spots leads to nonlinear dependence of the target fluorescence intensity with its concentration due to quenching of the dye signal via dye-dye, dye-DNA, and dye-surface interactions (28). Various reports assess immobilized DNA height with either labeled or unlabeled chromophores by measuring forces of DNA interactions with other biomolecules. AFM was used to assess DNA tethered length by attaching a large protein marker to genetically engineered pieces of human DNA (36). Force spectroscopy was applied to measure molecular interactions between the AFM probe tip and immobilized biomolecules. Such force analysis (compression, steric, and electrostatic) provides baseline information necessary to interpret the AFM image (37, 38).

DNA microarray performance is typically measured by parameters such as array geometry, spot density, spot characteristics (morphology, probe density, and hybridization density), background noise, target specificity, and sensitivity. Spotted probe heterogeneity and density dictate hybridization, hybridization efficiency, kinetics, and thermodynamics. Therefore, dried DNA

printed probe and hybridized DNA spot were assessed with AFM methods to evaluate printed spot morphologies. Previously reported Marangoni flow during printed spot drying phenomena leads to dried-state spot density heterogeneity, affecting target hybridization, thermodynamics, and kinetics (28, 34). In this study, we analyze dried printed DNA spot morphologies for both DNA and PNA probes. Spot uniformity is an important consideration for generating uniform printed microarrays that promote consistent, bound target amounts to yield more accurate, and reliable answers. Analysis of printed probe spots on commercial polymer array supports is required to understand this impact on known array assay answer and consistency problems.

A.3 Materials and methods

A.3.1 Materials

HPLC-purified (≥90% purity**)** DNA oligomers with several different terminal modifications (Table S-1) were purchased from TriLink Biotechnologies (San Diego, USA)(28, 29). Cyanine Cy3 (probe) and Cy5 (target) fluorophores are incorporated at 5' or 3' oligonucleotide termini during synthesis using phosphoramidite reagents through a C6 linker to the ssDNA. PNA oligomers (>85% purity) were procured from Biosynthesis (TX, USA). This PNA was synthesized similar to peptide with Fmoc SPPS (solid phase peptide synthesis) chemistry with 2 O-linkers instead of the C6 linker for dye labeling to enhance the solubility of the dye-modified PNA (see supplementary information for all probe sequences, Table S-1).

Ultrapure water (UPW, ASTM type I water, 18.2Ω M -cm) was used for all solution preparations and protocols for microarray fabrication. All chemicals were used as received. Buffer salts, sarcosine, sodium dodecyl sulfate (SDS), and ethanolamine were ACS grade, purchased from Sigma-Aldrich (St. Louis, USA). Microarray slides (Slide H, amine-reactive 3D polymer-coated array slides, Schott Nexterion, Louisville, USA) were used for DNA/PNA oligomer probe, print buffer, and gold nanosphere spot printing. New slides taken from the manufacturer's packaging were used without any pretreatment and unused slides were stored under nitrogen at 4°C and used within a month to preserve slide's ester reactivity. Gold nanospheres of 7nm (OD 1.1) and 49nm (OD 1.0) dispersed in citric acid stabilizer were purchased from Nanopartz (CO, USA) and were chosen as a printable controls for comparing printed spots.

A.3.2 DNA microarray immobilization on substrates with contact printing

Microarrays were generated by printing DNA probe solution (10μM concentration) with 1:1 Cy3-labeled (Cy3-Oligo1-NH_2) to unlabeled (Oligo1-NH_2) sequence-identical oligo DNA probes. DNA probe solutions were prepared in print buffers containing 150mM sodium phosphate, 0.001% Tween 20, and 0.001% sarcosine at pH 8.5 (28, 29). Spotted arrays (20x20 spots) of DNA were printed in triplicate on separate slides to facilitate comparison between probe-only and hybridized duplex arrays. Contact printing was performed using a SpotBot®2 contact printer with Stealth™ pins from Arrayit (Sunnyvale, USA). Spots were printed with a center-to-center spacing of 125μm to better raster and view printed spots with wide-scan AFM imaging.

A.3.3 PNA array immobilization with contact printing

PNA solutions (10μM total PNA solution with 1:1 Cy3-labeled PNA (Cy3-Oligo1-NH_2) to unlabeled (Oligo1-NH_2) sequence-identical oligoPNA probes) were prepared in UPW instead of print buffer. The printing and postprint processing was the same as described for DNA printing.

A.3.4 Printed buffer and gold nanosphere spots using contact printing technique

Print buffer containing sodium phosphate, 0.001 % Tween, and 0.001% sarcosine was printed with contact printing onto Slide H similarly to DNA and PNA. However, since the spots were printed buffer, slides were rinsed with water and dried without the additional blocking step. Gold nanospheres were printed as obtained from the supplier in citric acid buffer in a similar procedure that was followed for DNA and PNA except for postprint processing where the printed gold nanospheres spots were thoroughly rinsed in water and dried. All printed nanospheres were not conjugated with any chemical reactive group to avoid chemical reactivity with the slide.

A.3.5 Postprint treatment and hybridization of printed microarray slides

Briefly, printed slides were rinsed in sodium phosphate print buffer and then immersed in blocking solution (50mM ethanolamine in 0.1M Tris, pH 9.0) at 50°C for 30 minutes to consume residual surface amine-reactive NHS groups (14, 30). Subsequently, slides were rinsed thoroughly with UPW 3 times followed by immersion in the hybridization buffer (4X saline sodium citrate (SSC) containing 0.1% SDS at pH 7) at 50°C for 30 minutes. Slides were finally rinsed with UPW 3 times, blown dry with nitrogen, and immediately imaged with fluorescence scanner for probe-only studies. Target hybridization was accomplished using Lifter slips (Erie Scientific no. 22x50I-2-4711) for microarray samples. Briefly, 1μM target DNA solution (1:99 Cy5-Oligo2:Oligo2) prepared in hybridization buffer (4X SSC/0.01% SDS) was applied separately to the DNA probe spot and PNA probe spots for 4 h incubation at room temperature and 100% relative humidity. After hybridization, slides were rinsed with hybridization buffer and then by the following solvents (2X SSC/0.1% SDS (5 minutes), 0.2X SSC and 0.1X SSC (1 minute each), and finally dried with nitrogen.

A.3.6 Fluorescence scanner images of DNA and PNA microarrays

Printed DNA or PNA microarray slides were fluorescently scanned after blocking but before and after the hybridization steps using GenePix Microarray scanner (Model 4100A, v.6 software). DNA/PNA printed/hybridized slides were scanned using two optical channels (535 and 635 nm for Cy3 and Cy5, respectively). The following settings were used for all scans: laser power 100%, brightness and contrast 92%, PMT gain 400, pixel size 10μm, and line average set at 3.

A.3.7 AFM analysis of commercial polymer arraying substrates

Untreated array slides (Schott Nexterion) were analyzed with a Bruker Dimension ICON-PT atomic force microscope (AFM) in contact mode (peak force quantitative nanomechanical mapping). A Scanasyst Air (SiN) cantilever with a tip diameter of 2nm and a spring constant of 0.4N/m was used in air at ambient conditions. Sample scan rate was 1Hz with a pixel size of 1nm. The largest scan area possible on the was 90×90 μm^2 making it unsuitable to accommodate the large size of printed single DNA spots with a diameter of 150μm.

A.3.8 AFM analysis of printed spots

AFM images of printed, rinsed, blocked, and dried spots (DNA probe, DNA-DNA duplex, PNA probe, PNA-DNA hetero-duplex), and controls (print buffer only and gold nanospheres) were measured in air with a Topometric-TMX 2000 AFM operating in contact mode. A silicon cantilever with a tip radius of curvature R_c<10nm and a nominal spring constant of 0.01-0.08N/m was used. A scan area of 150μm^2 was generally used. However, for certain high-resolution imaging, the scan area was decreased as necessary. The printed samples were analyzed at room temperature 23^{o}C and relative humidity of 20%. A replicate of 6 spots were measured for each sample type. LFR (lateral force reverse) and LFF (lateral force forward) were measured. LFR was used for morphology and AFM image representation of the spots and processed with Image J and Adobe Photoshop (CS4, Version 11.0) for contrast and brightness adjustments.

A.4 Results and discussion

A.4.1 AFM analysis of untreated commercial arraying substrates

AFM measurement of the unprinted, as-supplied microarray slide substrate (without any pretreatment) exhibited an RMS surface roughness of about 0.27nm and RA roughness of 0.19nm as derived from the image shown in Figure A1. The 3D polymer coating on the array slide swells in water (44). Coating thickness for both hydrated (swollen) and dehydrated states using AFM and ellipsometry (39) showed dehydrated film thicknesses of 10-20nm with a peak-to-trough roughness of less than 1nm (rms roughness=0.29nm), similar to the surface of the underlying glass slide. Hydrated film thickness after 30 minutes stabilizes at 50-100nm with a final peak-to-trough roughness of approximately 10-20nm (rms roughness=3.20 nm) (39). Measurements of fresh untreated surfaces (RMS roughness of 0.27nm and RA roughness of 0.19nm) are very similar. The polymer-coated slide surface has very minimal surface roughness to influence the height of any immobilized nucleotides, or to interfere with AFM measurements.

A.4.2 Coating roughness results from swelling and de-swelling of the polymer coating in water

The coating comprises a polymer base component (NHS-PEG-aminosilane), matrix-forming component (nonionic surfactant containing ethylene oxide repeat units), and a cross-linking agent (azidosilane as a molecular cross-linker component) that are mixed together in a carrier solvent, spin-coated onto glass slides, and thermally cured to yield a thin, uniform polymer film as an NHS-active 3D polymer coating (40). Upon hydration, film topography and thickness change significantly, due to swelling of hydrated polymer and expansion during dehydration (40).

A.4.3 AFM analysis of printed unhybridized DNA probe and hybridized DNA-DNA spots

Printed-rinsed-blocked and dried single, fluorescently labeled DNA unhybridized probe spots were measured with AFM in air under contact mode. AFM LRF images show printed spot morphologies (Figures A2. A, C) comparable with epifluorescence images shown in Figure A2.B, D. Lateral force mode measures frictional forces between the tip and the surface and can be used to provide contrast between areas. These images show uniform printed circular DNA features of ~150μm diameter. The lateral force image also reveals a feature consistently observed when the printing pin makes surface contact during DNA droplet dispensing on the slide surface – a feature also observed in both profilometry and epifluorescence images of printed DNA dried spots (Figure AS.1). Printing and drying heterogeneity, and dried DNA aggregates in printed spots vary with printing techniques (methods, humidity, temperature, drying, blocking, etc.,) and slide surface chemistry, producing variable dried morphologies and thicknesses (34) (27, 31). Previously, TOF-SIMS chemical images of single dried DNA microspots were compared to epifluorescence optical images of identical spots to manifest such differences at spot centers, indicating heterogeneous DNA probe distribution within spots, with higher DNA density in the center due to Marangoni inward-flow drying patterns (see Figure AS.2) (28).

This printed-blocked-rinsed and dried DNA spot aggregate was shown previously to comprise mostly DNA, since salt ions from the print buffer after rinsing were not detected using TOF-SIMS (23, 28). Hence, the nonequilibrium, rapid drying experienced by printed droplets upon

deposition on the slide surface promotes ssDNA probe aggregation and insoluble transformation to a solid ssDNA deposit that resists normal array rinsing procedures. Further, upon hybridization, the spot morphologies reflect addition of target-forming duplex dsDNA across the spot surface. The duplex formation presumably occurs where probe ssDNA exposure in the aggregated printed spot allows hybridization upon spot rehydration in the hybridization chamber at elevated temperature. As the spot density across the spot is different, the hybridization occurs at lower density at the edges compared to spot center. The AFM spots show different morphology at center and the edge, as shown in the Figure A1 and A2. This was also observed with confocal images of DNA spots with high Cy3-DNA intensity at the center compared to the spot edges (25).

A.4.4 AFM analysis of printed unhybridized PNA probe and hybridized PNA-DNA spots

Similarly, AFM LFR images of printed ssPNA probe and PNA-DNA hybridized spots are shown in Figure A3. AFM measurements of morphologies show the same trends as in Figure A2, providing more features of spreading and drying of the spot. PNA binds to complementary DNA with high affinity due partially to the neutral PNA backbone alleviating the standard charge-charge polyphosphate backbone repulsion in DNA-DNA duplex formation (41). Relative to DNA–DNA duplexes, a hybrid PNA–DNA duplex is less dependent on ionic strength for stability and even at moderate salt levels, PNA-DNA is thermally more stable than DNA-DNA duplexes (42). The PNA-DNA duplex is similar to Watson-Crick base pairing and stacking patterns of DNA-DNA duplexes (43). The PNA-DNA duplex is somewhat unwound with a helical rise of 42Å and 13 bp per turn, and a slightly larger helix diameter of 23Å with a major groove wider and a minor groove narrower than those of the DNA-DNA duplex (44). In contrast, B-DNA has a helical rise of 33Å with 10.5 bp per turn and a helical diameter of 20Å. Hence, the height of the PNA-DNA duplex is slightly greater from this duplex helical disparity (45).

AFM morphological evidence from the printed unhybridized PNA spot shows spreading-drying patterns (depicted by arrows, Figure A3.A) consistent with Marangoni inward flow, similar to DNA spots (28, 34). Printed PNA spots show increased droplet spreading, as seen in epifluorescence images (Figure A2.B) for the same printing conditions. However, the absence of

print buffer for PNA (i.e., printed from pure water) alters droplet spreading and drying patterns compared to DNA. This pattern is still maintained in the hybridized spots, reflecting the influence of the dried spot patterns and probe distribution on target binding.

A.4.5 AFM analysis of printed control spots

Arrayed controls (print buffer only) were used to verify dried spot morphology changes from printing Figure A4.A. In our previous work, we faintly observe the printed buffer spots in epifluorescence and the fluorescence scanner images after rinsing, blocking, and drying (34, 37). Printed gold nanospheres of known sizes were also printed from citrate buffer and even after rinsing, citrate salt crystals are observed in all such spots in addition to gold nanoparticles. Printed gold nanospheres of 7nm (Figure A4.C) and 49nm (Figure A4.B) sphere diameters used as control samples. AFM images of spot morphology for printed 7nm gold nanospheres (Figure A4.C) display coffee ring drying effect and spreading patterns (46), with nanospheres distributed on spot peripheries as bright particles instead of at spot centers (shown by arrow). It is well-known that the shape, size, and presence of the buffer dictate the trade-off effects of coffee ring and Marangoni flows under drying (47). However, this coffee ring effect was not observed for spots comprising larger gold nanospheres of 49nm. High-resolution images of 7nm-diameter nanospheres show agglomerations (Figure A4.D). Similarly, 49nm-diameter gold nanospheres spots show agglomerations.

AFM surface morphology studies of individual array-printed DNA microspots using fluorophore-labeled DNA probe-target pairings provide information regarding the array spot's dried/rinsed shape, heterogeneous drying patterns, and spot pattern differences for unhybridized and hybridized spots. Previous reports have detailed DNA contact printing using both high-resolution fluorescence and chemical (TOF-SIMS) imaging of individual DNA spots, showing spot heterogeneity from Marangoni drying. These effects result in different ssDNA probe densities distributed within dried spots from rapid evaporation on these same arraying substrates (28). These observation signifies that hybridization, when directly observed in real-time in confocal images of spots, typically proceeds from the spot's outer edge radially toward the center with pseudo-first order capture kinetics (7, 34). These data confirm previous reports modeling the diffusive transport

of target across microspots as a function of spot size using hemispherical transport models (33). This leads to time-dependent completion for target-spot saturation, and therefore assay signal, that depends both on probe density and spot size. Ultimately, variable fluorescence signals occur due to both spot-spot and batch-batch variability. As spot size and probe printed density are observed to be poorly controlled and most target hybridization time-frames do not routinely approach equilibrium to mitigate, these kinetic target capture effects that alter spot signals.

Lateral heterogeneity within spots was shown to arise from spot evaporation and resulting competition between convective transport during droplet drying (28). AFM now shows similar spot morphology of printed array spots. This also has a profound impact on concepts involving hybridization efficiencies for printed spots. Aggregated printed DNA probes on these spots allow target binding only at sufficiently accessible probes exposed on spot surface regions, and likely not with probes buried in the spot's bulk interior. There is no evidence for spot swelling to facilitate target penetration during hybridization. AFM morphologies comparable with probe heterogeneities were previously reported using both optical (epifluorescence and confocal) and chemical (TOF-SIMS) imaging of individual spots (28), with higher ssDNA probe densities observed at spot centers compared to peripheries (Figure AS.2). Printed ssPNA probes produced comparable spot morphology to those from printed ssDNA with the exception of wetting/spreading differences (vida supra). Control spots using print buffer alone and gold nanospheres spots displayed aggregation as well, with different density at the center than the edges. These observations collectively indicate that printed microspot variability and heterogeneity of dried spots result from common array printing techniques for nano-droplet volumes of nucleic acids. Uniform arrayed spot sizes with homogeneous, well-controlled probe densities are proposed as necessary improvements to yield most reliable array signal generation, both spot-spot and batch-batch. This will be critical for achieving bioanalytical performance goals for these assays wherein measured fluorescent signals from such assay spots consistently and accurately represent analyte sample abundance.

A.5 Conclusions

AFM analysis of individual fluorescently labeled probe and probe-target hybridized nucleic acid spots demonstrates heterogeneous spot features that reflect variable probe-target distributions

due to drying phenomena after printing, rinsing, drying, blocking, and hybridization -- steps typical of routine microarray processing. This is attributed to printed deposition of excess probe, rapid drying, and solute aggregation upon drying that leads to poor spot rinsing efficiencies. Further spot heterogeneity increases with target hybridization appears to be surface-localized, not due to target penetration into printed spots. AFM data displayed spots with consistent morphologies at spot centers and edges, observed with ssDNA probes only, DNA-DNA duplexes, ssPNA probes only, PNA-DNA duplexes, print buffer, and printed gold nanospheres. This indicates that contact printing and subsequent rapid drying of the droplet leads to heterogeneous spots. Also, differences in electrostatics between DNA and PNA did not alter spot morphology, indicating that the droplet deposition and drying plays a major role in printed arrays. In addition, AFM images also provided morphology of printed single DNA spots comparable to high-resolution techniques. Thus, DNA microarray fluorescence signal discrepancies in end-point analysis are due to heterogeneous lateral probe density variations. This reduces target analyte binding to fewer accessible probes in these spots, poor control of probe spot morphologies on arrayed spots, variation in duplex efficiencies from spot-to-spot, and therefore intrinsic variability in microarray signal generation in these printed formats.

A.6 Acknowledgements

Support from NIH grant R01EB001473 (DWG), Utah's NSF-IGERT program, and assistance with AFM imaging and data analysis from Dr. B. Van Devener (University of Utah) are gratefully acknowledged.

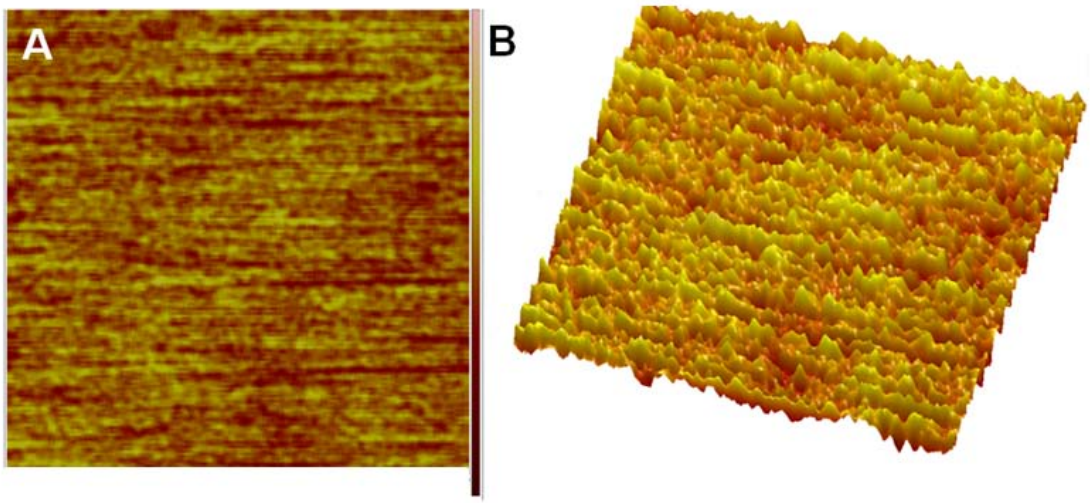

Figure A1. AFM images of the untreated polymer array substrate (Slide H) topography. A) 2D surface roughness of untreated slide. B) 3D image showing RMS surface roughness of 0.27nm

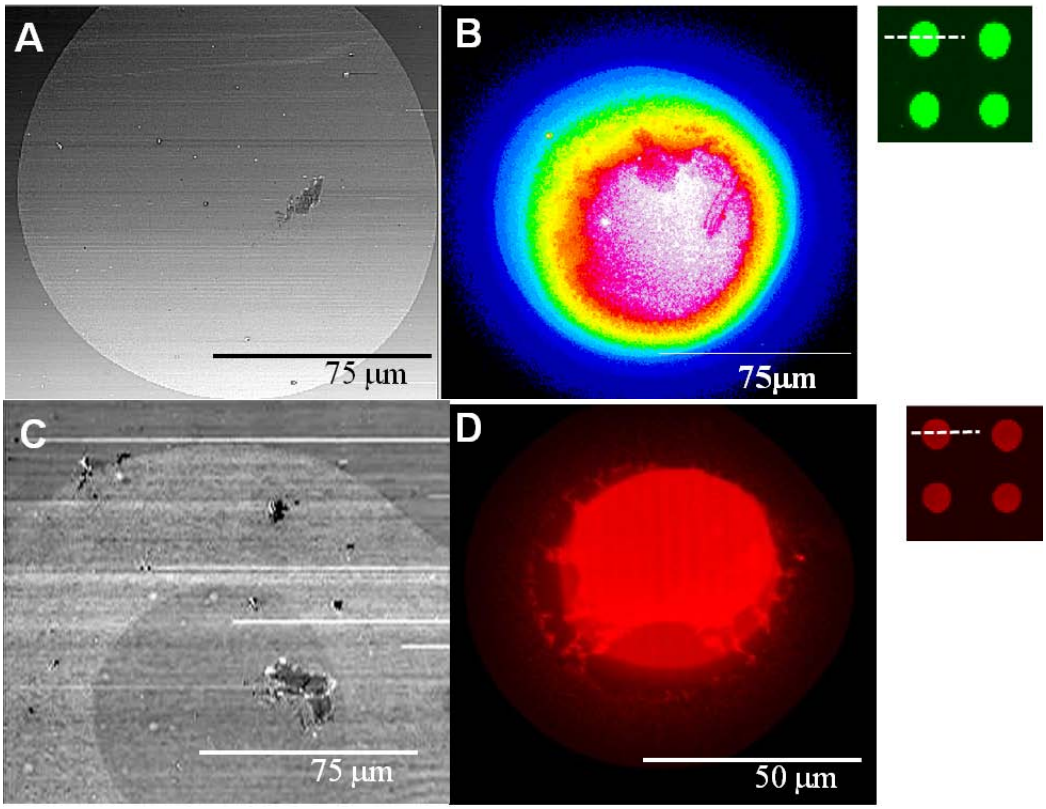

Figure A2. AFM images of spot morphology of unhybridized and hybridized DNA spots. A) AFM LFR image of printed ssDNA unhybridized spot B) Epifluorescence image of ssDNA unhybridized spot C) AFM LFR image of printed dsDNA duplex hybridized spot. D) Epifluorescence image of dsDNA (hybridized) spot. Insets (fluorescence scanner images) represent the AFM LFR scan across the spots from edge to edge.

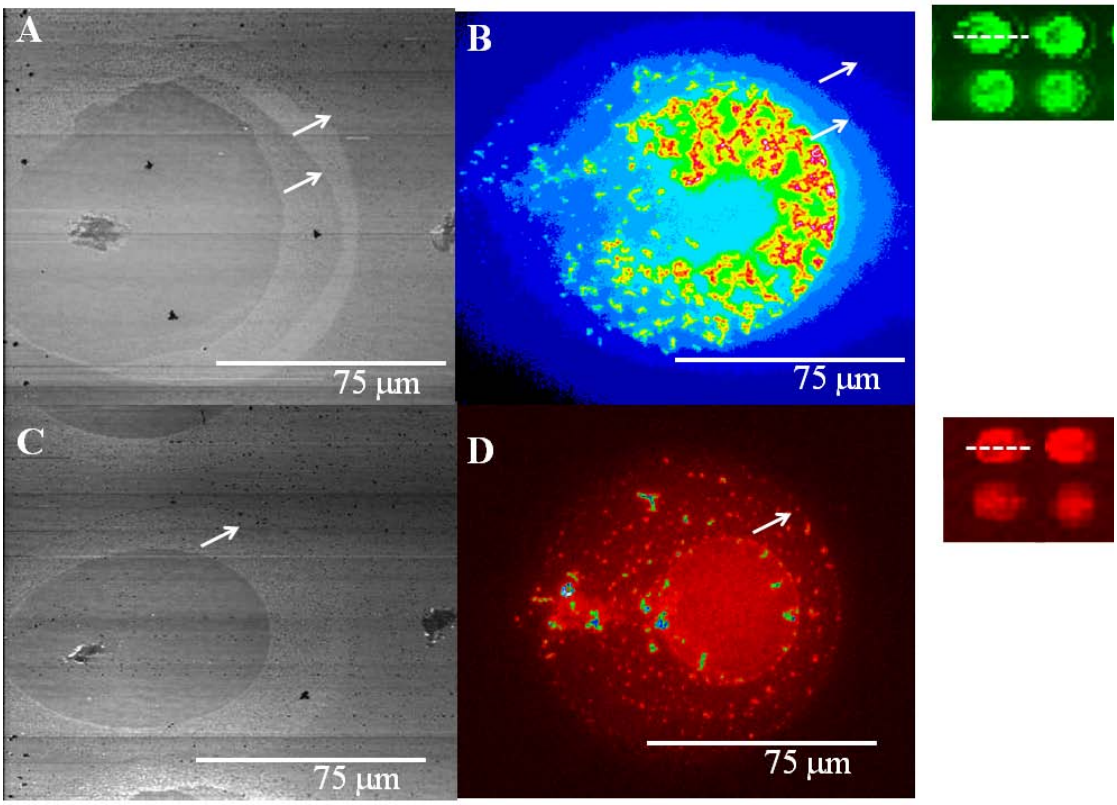

Figure A3. AFM images of spot morphology of unhybridized ssPNA and hybridized PNA-DNA spots. A) AFM image of printed ssPNA unhybridized spots showing different contours formed by drying and spreading indicated by arrows. B) Epifluorescence images of ssPNA spot. C) AFM image of printed PNA-DNA hybridized spot. Hybridized PNA-DNA spots retain different contours seen in printed spots. D) Epifluorescence image of hybridized PNA-DNA spot Insets (fluorescence scanner images) represent locations for AFM LFR measurements across the unhybridized and hybridized spots, respectively, from edge to edge.

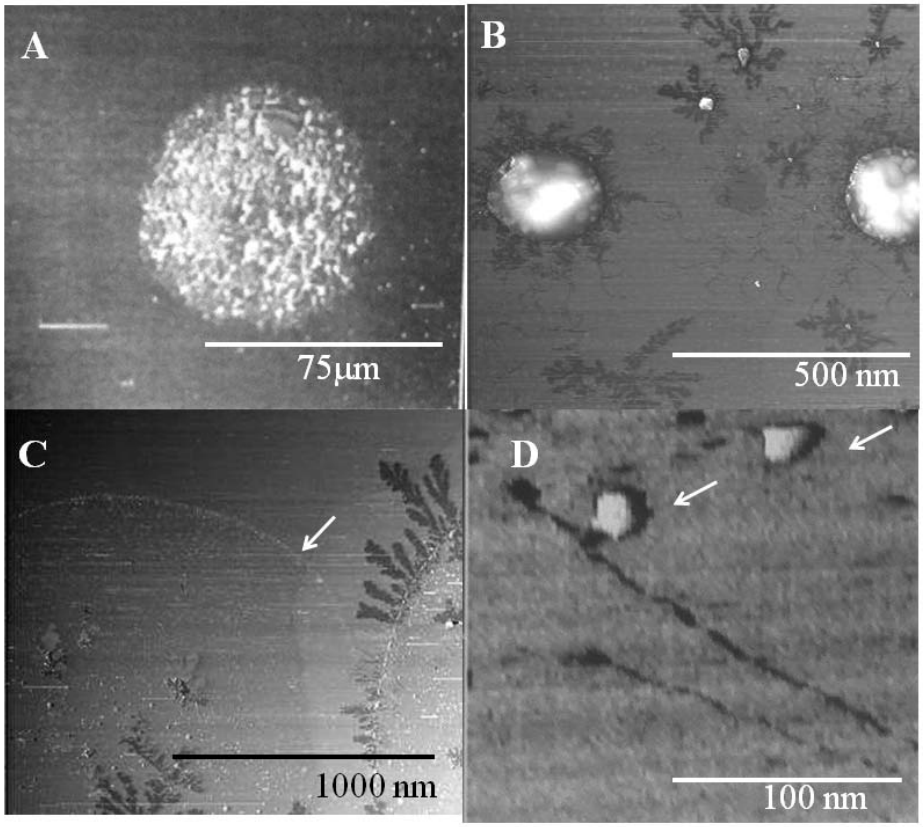

Figure A4. AFM LFR images of spot morphology of printed controls: blank print buffer and gold nanospheres. A) AFM image of dried print buffer spot after rinsing. B) printed/dried microspot of printed gold nanospheres (49nm diameter). C) Printed gold nanospheres (7nm diameter). D) Agglomeration of gold nanospheres (7-nm; rinsed-not blocked). AFM images shown are lateral force measurements.

A.7 References

1. Gershon D. Microarray technology: An array of opportunities. Nature. 2002;416(6883):885-91.

2. Stears RL, Martinsky T, Schena M. Trends in microarray analysis. Nature Medicine. 2003;9(1):140-5.

3. Abdullah-Sayani A, Bueno-de-Mesquita JM, van de Vijver MJ. Technology insight: Tuning into the genetic orchestra using microarrays - Limitations of DNA microarrays in clinical practice. Nature Clinical Practice Oncology. 2006;3(9):501-16.

4. Petricoin Iii EF, Hackett JL, Lesko LJ, Puri RK, Gutman SI, Chumakov K, et al. Medical applications of microarray technologies: A regulatory science perspective. Nature Genetics. 2002;32(5 SUPPL. DEC.):474-9.

5. Simon R, Radmacher MD, Dobbin K, McShane LM. Pitfalls in the use of DNA microarray data for diagnostic and prognostic classification. Journal of the National Cancer Institute. 2003;95(1):14-8.

6. Venkatasubbarao S. Microarrays - Status and prospects. Trends in Biotechnology. 2004;22(12):630-7.

7. Tilstone C. Vital statistics. Nature. 2003;424(6949):610-2.

8. Smyth GK, Speed T. Normalization of cDNA microarray data. Methods. 2003;31(4):265-73.

9. Draghici S, Khatri P, Eklund AC, Szallasi Z. Reliability and reproducibility issues in DNA microarray measurements. Trends in Genetics. 2006;22(2):101-9.

10. Wrong numbers? Nature Biotechnology. 2010;28(8):761.

11. Epstein JR, Biran I, Walt DR. Fluorescence-based nucleic acid detection and microarrays. Analytica Chimica Acta. 2002;469(1):3-36.

12. Sassolas A, Leca-Bouvier BD, Blum LJ. DNA biosensors and microarrays. Chemical Reviews. 2008;108(1):109-39.

13. Levicky R, Horgan A. Physicochemical perspectives on DNA microarray and biosensor technologies. Trends in Biotechnology. 2005;23(3):143-9.

14. Grainger D, Greef C, Gong P, Lochhead M. Current Microarray Surface Chemistries. In: Rampal J, editor. Microarrays: Humana Press; 2007. p. 37-57.

15. Wong IY, Melosh NA. An electrostatic model for DNA surface hybridization. Biophysical Journal. 2010;98(12):2954-63.

16. Elhadj S, Singh G, Saraf RF. Optical properties of an immobilized DNA monolayer from 255 to 700 nm. Langmuir. 2004;20(13):5539-43.

17. Halperin A, Buhot A, Zhulina EB. Brush effects on DNA chips: Thermodynamics, kinetics, and design guidelines. Biophysical Journal. 2005;89(2):796-811.

18. Gong P, Lee CY, Gamble LJ, Castner DG, Grainger DW. Hybridization behavior of mixed DNA/alkylthiol monolayers on gold: Characterization by surface plasmon resonance and 32P radiometric assay. Analytical Chemistry. 2006;78(10):3326-34.

19. Steel AB, Levicky RL, Herne TM, Tarlov MJ. Immobilization of nucleic acids at solid surfaces: Effect of oligonucleotide length on layer assembly. Biophysical Journal. 2000;79(2):975-81.

20. Halperin A, Buhot A, Zhulina EB. On the hybridization isotherms of DNA microarrays: The Langmuir model and its extensions. Journal of Physics Condensed Matter. 2006;18(18):S463-S90.

21. Barbulovic-Nad I, Lucente M, Sun Y, Zhang M, Wheeler AR, Bussmann M. Bio-microarray fabrication techniques - A review. Critical Reviews in Biotechnology. 2006;26(4):237-59.

22. Petrovykh DY, Kimura-Suda H, Whitman LJ, Tarlov MJ. Quantitative analysis and characterization of DNA immobilized on gold. Journal of the American Chemical Society. 2003;125(17):5219-26.

23. Gong P, Harbers GM, Grainger DW. Multi-technique comparison of immobilized and hybridized oligonucleotide surface density on commercial amine-reactive microarray slides. Analytical Chemistry. 2006;78(7):2342-51.

24. Miller MB, Tang YW. Basic concepts of microarrays and potential applications in clinical microbiology. Clinical Microbiology Reviews. 2009;22(4):611-33.

25. Ramakrishnan R, Dorris D, Lublinsky A, Nguyen A, Domanus M, Prokhorova A, et al. An assessment of Motorola CodeLink microarray performance for gene expression profiling applications. Nucleic Acids Research. 2002;30(7).

26. Dai H, Meyer M, Stepaniants S, Ziman M, Stoughton R. Use of hybridization kinetics for differentiating specific from non-specific binding to oligonucleotide microarrays. Nucleic Acids Research. 2002;30(16).

27. Singh KM, Brott LL, Grote JG, Naik RR, editors. Inkjet printing of DNA for use in bioelectronic applications. 2008.

28. Rao AN, Vandencasteele N, Gamble LJ, Grainger DW. High resolution epifluorescence and TOF-SIMS chemical imaging comparisons of single DNA microarray spots. Analytical Chemistry. 2012:1-8.

29. Lee CY, Harbers GM, Grainger DW, Gamble LJ, Castner DG. Fluorescence, XPS, and TOF-SIMS surface chemical state image analysis of DNA microarrays. Journal of the American Chemical Society. 2007;129(30):9429-38.

30. Gong P, Grainger DW. Comparison of DNA immobilization efficiency on new and regenerated commercial amine-reactive polymer microarray surfaces. Surface Science. 2004;570(1-2):67-77.

31. Dugas V, Broutin J, Souteyrand E. Droplet evaporation study applied to DNA chip manufacturing. Langmuir. 2005;21(20):9130-6.

32. Still T, Yunker PJ, Yodh AG. Surfactant-induced Marangoni eddies alter the coffee-rings of evaporating colloidal drops. Langmuir. 2012;28(11):4984-8.

33. Dandy DS, Wu P, Grainger DW. Array feature size influences nucleic acid surface capture in DNA microarrays. Proceedings of the National Academy of Sciences of the United States of America. 2007;104(20):8223-8.

34. Rao AN, Rodesch CK, Grainger DW. Real-time fluorescent image analysis of DNA spot hybridization kinetics to assess microarray spot heterogeneity. Analytical Chemistry. 2012:1-10.

35. Peterson AW, Heaton RJ, Georgiadis RM. The effect of surface probe density on DNA hybridization. Nucleic Acids Research. 2001;29(24):5163-8.

36. Murray MN, Hansma HG, Bezanilla M, Sano T, Ogletree DF, Kolbe W, et al. Atomic force microscopy of biochemically tagged DNA. Proceedings of the National Academy of Sciences of the United States of America. 1993;90(9):3811-4.

37. Rivetti C, Guthold M, Bustamante C. Scanning force microscopy of DNA deposited onto mica: Equilibration versus kinetic trapping studied by statistical polymer chain analysis. Journal of Molecular Biology. 1996;264(5):919-32.

38. Wang J, Bard AJ. Monitoring DNA immobilization and hybridization on surfaces by atomic force microscopy force measurements. Analytical Chemistry. 2001;73(10):2207-12.

39. Nexterion S. Three-dimensional thin film coating.

40. Harbers GM, Emoto K, Greef C, Metzger SW, Woodward HN, Mascali JJ, et al. Functionalized poly(ethylene glycol)-based bioassay surface chemistry that facilitates bio-immobilization and inhibits nonspecific protein, bacterial, and mammalian cell adhesion. Chemistry of Materials. 2007;19(18):4405-14.

41. Nielsen PE, Egholm M. An introduction to peptide nucleic acid. Current issues in molecular biology. 1999;1(1-2):89-104.

42. Ratilainen T. Thermodynamics of peptide nucleic acid interactions with DNA. 2000.

43. Briones C, Mateo-Martí E, Gómez-Navarro C, Parro V, Román E, Martín-Gago JA. Structural and functional characterization of self-assembled monolayers of peptide nucleic acids and its interaction with complementary DNA. Journal of Molecular Catalysis A: Chemical. 2005;228(1-2 SPEC. ISS.):131-6.

44. Eriksson M, Nielsen PE. Solution structure of a peptide nucleic acid-DNA duplex. Nature Structural Biology. 1996;3(5):410-3.

45. Eriksson M, Nielsen PE. PNA-nucleic acid complexes. Structure, stability and dynamics. Quarterly Reviews of Biophysics. 1996;29(4):369-94.

46. Deegan RD, Bakajin O, Dupont TF, Huber G, Nagel SR, Witten TA. Contact line deposits in an evaporating drop. Physical Review E - Statistical Physics, Plasmas, Fluids, and Related Interdisciplinary Topics. 2000;62(1 B):756-65.

47. Yunker PJ, Still T, Lohr MA, Yodh AG. Suppression of the coffee-ring effect by shape-dependent capillary interactions. Nature. 2011;476(7360):308-11.

SUPPORTING INFORMATION

AFM ANALYSIS TO ASSESS PRINTED NUCLEIC ACID MICROARRAY FEATURES PRINTED ON POLYMER SUBSTRATES

Archana N. Rao[1] Colin D. Eichinger[2], Vladimir Hlady[2], and David W. Grainger[1,2*]

* *Corresponding author:* David W. Grainger, david.grainger@utah.edu

Table AS.1. DNA and PNA oligonucleotide probe and target sequences and terminal modifications

Nucleic acid type	identifier	5'-modification	Sequence	3'-modification
DNA probe	Oligo1-NH_2	--	CTGAACGGTAGCATCTTGAC	--
DNA probe	Cy3-Oligo1-NH_2	Cy3-C_6-	CTGAACGGTAGCATCTTGAC	C6-NH_2
DNA target	Oligo2	--	GTCAAGATGCTACCGTTCAG	--
DNA target	Cy5-Oligo2	Cy5-C_6-	GTCAAGATGCTACCGTTCAG	--
DNA target	Oligo2-Cy5		GTCAAGATGCTACCGTTCAG	Cy5-C_6-
PNA probe	Oligo1-NH_2		CTGAACGGTAGCATCTTGAC	Lys-NH_2
PNA probe	Cy3-Oligo1-NH_2	Cy3-OO-	CTGAACGGTAGCATCTTGAC	Lys-NH_2

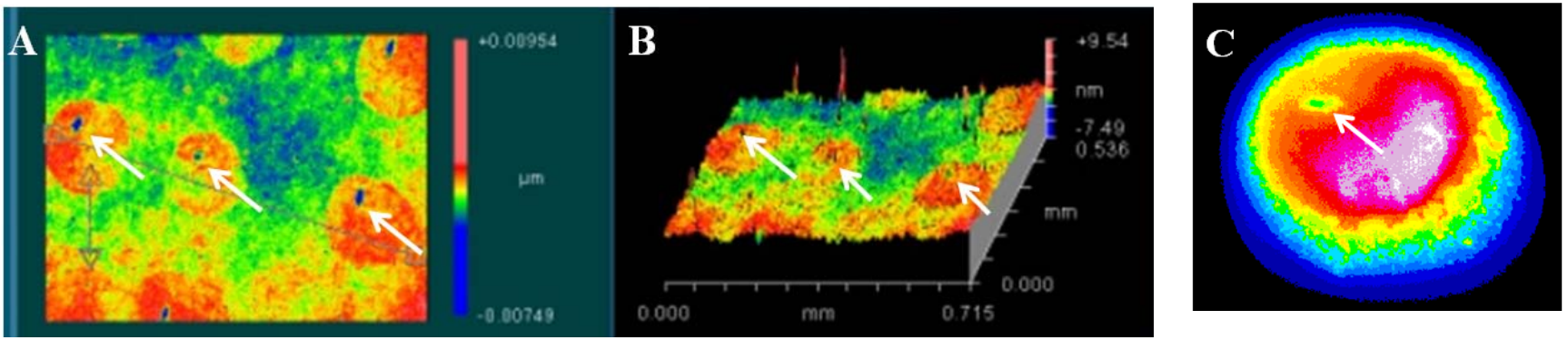

Figure AS.1. Zygo™ optical profilometer images of printed DNA probes array. Images A) and B) show blue spots (indicated with arrows) at the centers of spots depicting pin print head imprints left behind as observed in the dried spots. C) Epifluorescence image of printed DNA spot also showing the pin print feature (arrow).

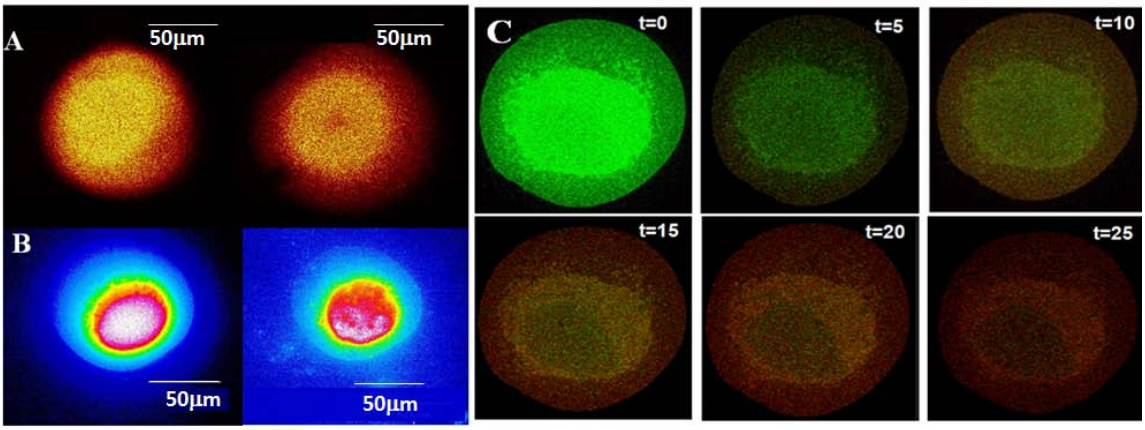

Figure AS.2. ToF-SIMS, epifluorescence, and confocal images of printed DNA spots showing printed spot heterogeneity. A) TOF-SIMS images of 10μM 75% (left) and 10μM 25% (right) DNA probe only spots shows higher density of DNA-Cy3 at spot center indicated by both spatial and chemical analysis of DNA. B) Same spots in Epifluorescence showing the similar phenomena with greater fluorescence intensity at spot center (Reference 28: Figure 3A and B). C) Confocal images of real time hybridization of Cy3 DNA probe spot (40μM 100% Cy3 DNA probe-only at t=0 to t=25 min) at various time points showing radial hemispherical distribution of DNA target (1μM 1% Cy5-DNA) from the outer edge of the spot moving towards the spot center (Reference 34: Figure 1B).